

**MODELING OF MODE-TRANSITION OF NATURAL
CONVECTION IN CAVITIES**

**MODELING OF FLOW MODE-TRANSITION OF NATURAL
CONVECTION IN INCLINED CAVITIES**

By

HONGDA WANG, B. Eng.

A Thesis

Submitted to the School of Graduate Studies

in Partial Fulfillment of the Requirements

for the Degree

Master of Applied Science

McMaster University

©Copyright by Hongda Wang, September, 2004

MASTER OF APPLIED SCIENCE (2004)

McMaster University

(Mechanical Engineering)

Hamilton, Ontario

**TITLE: Modeling of Flow Mode-Transition of Natural Convection
in Inclined Cavities**

**AUTHOR: Hongda Wang, B. Eng
(Tongji University, China)**

SUPERVISOR: Dr. Mohamed S. Hamed

NUMBER OF PAGES: xxxiv, 222

Abstract

Steady two-dimensional natural convection in air-filled, regular and irregular inclined enclosures has been investigated numerically.

The effect of various configurations of bidirectional temperature gradients on mode transition of thermal convection inside the cavity has been investigated. Numerical treatment of temperature discontinuity at the corner points of the cavity and its effect on the calculated Nusselt number has been discussed. Rayleigh numbers range between 10^3 and 10^4 , aspect ratio (width/height) = 1, 2, 4, and angle of inclination in the range between 0 and 90° . While the cavity bottom and top walls were kept at constant temperatures at T_h (heated) and at T_c (cooled), respectively, thermal conditions of end walls were varied. In addition to the base case of insulated end walls, seven different configurations of thermal conditions of the two side walls have been studied. Results show that numerically predicted heat transfer rates strongly depend on the numerical treatment of temperature discontinuities at cavity corner points. Results also indicate that thermal conditions of cavity end walls have a significant effect on mode-transition of thermal convection flows; and hence, on heat transfer effectiveness inside the cavity, and on the Hysteresis phenomenon occurred as the cavity angle of inclination varied from zero (horizontal position) to 90° (vertical position) and back to zero.

The effect of curved bottom is carried out by replacing flat bottom of the cavity with a curved one. Only insulated end walls were discussed in curved case. Results indicated that heat transfer rate and mode transition are strongly dependent on the height

of curvature of the bottom wall, which offers more flexibility in controlling flow mode-transition, and hence, effectiveness of heat transfer inside the cavity.

Acknowledgments

The author would like to express his deep and sincere gratitude to his supervisor Dr. Mohamed S. Hamed for his continuous guidance and advice. His patient, encouragement and assistance throughout this project have made the past two years a memorable experience.

Special appreciation is extended to Sharcnet for its high speed academic research computing network.

For there love and support, thanks: mom, dad, Meiyun Lin, Qinren Wang, my wife and son Ying Chen, William Wang...

Table of Contents

Chapter 1	Introduction and Literature Review.....	1
	1.1 Introduction.....	1
	1.2 Literature review.....	3
	1.2.1 Natural convection in vertical regular cavities.....	4
	1.2.2 Natural convection in horizontal regular cavities.....	7
	1.2.3 Natural convection in inclined regular cavities.....	13
	1.2.4 Natural convection in irregular-shaped cavities.....	19
	1.3 Present work.....	22
Chapter 2	Mathematical Formulation and Numerical Method.....	25
	2.1 Problem formulation.....	25
	2.2 Numerical algorithm:.....	28
	2.3 Convergence criterion.....	31
	2.4 Grid dependence check.....	32
	2.5 Energy balance test.....	36
	2.6 Relaxation factors.....	36
	2.7 Calculation of Nu number for cavity with flat bottom.....	36
	2.8 Grid distribution and calculation of Nu number for the case of curved bottom (irregular-shaped) cavity:.....	39
	2.8.1 Grid distribution.....	39
	2.8.2 Calculation of Nu number.....	40
	2.9 Accuracy of the algorithm.....	41

2.10 Numerical treatment of temperature discontinuity at corner points.....	42
2.11 Verification of numerical algorithm.....	47
2.11.1 Comparison with results reported by Corcione [12] –case of horizontal cavity.....	47
2.11.2 Comparison with results reported by Soong and Tzeng [21] – case of inclined cavity with insulated end walls (AA configuration).....	48
2.11.3 Comparison with benchmark problem reported in [27] – case of vertical cavity.....	50
2.11.4 Comparison with result reported by Ganzarolli and Milanez [11] – treatment of temperature discontinuity at corner points.....	51
Chapter 3 Numerical Results - Case of Square Cavity with Flat Bottom	54
3.1 AA configuration.....	54
3.1.1 Case of increasing γ	54
3.1.2 Case of decreasing γ	57
3.2 CH configuration.....	60
3.2.1 Case of increasing γ	60
3.2.2 Case of decreasing γ	62
3.3 HC configuration.....	63

3.3.1 Case of increasing γ	63
3.3.2 Case of decreasing γ	66
3.4 AC configuration.....	67
3.4.1 Case of increasing γ	67
3.4.2 Case of decreasing γ	70
3.5 CA configuration.....	71
3.5.1 Case of increasing γ	71
3.5.2 Case of decreasing γ	73
3.6 CC configuration.....	74
3.6.1 Case of increasing γ	74
3.6.2 Case of decreasing γ	77
3.7 LL configuration.....	78
3.7.1 Case of increasing γ	78
3.7.2 Case of decreasing γ	81

Chapter 4	Numerical Results - Case of Rectangular Cavity with Flat	
	Bottom.....	83
	4.1 Rectangular cavity with $A=2$.....	83
	4.1.1 AA configuration.....	84
	4.1.1.1 Case of increasing γ	84
	4.1.1.2 Case of decreasing γ	89

4.1.2' CH configuration.....	92
4.1.2.1 Case of increasing γ	92
4.1.2.2 Case of decreasing γ	95
4.1.3 HC configuration.....	96
4.1.3.1 Case of increasing γ	96
4.1.3.2 Case of decreasing γ	101
4.1.4 AC configuration.....	102
4.1.4.1 Case of increasing γ	102
4.1.4.2 Case of decreasing γ	106
4.1.5 CA configuration.....	107
4.1.5.1 Case of increasing γ	107
4.1.5.2 Case of decreasing γ	111
4.1.6 CC configuration.....	112
4.1.6.1 Case of increasing γ	112
4.1.6.2 Case of decreasing γ	115
4.1.7 LL configuration.....	116
4.1.7.1 Case of increasing γ	116
4.1.7.2 Case of decreasing γ	121
4.2 Rectangular cavity with higher aspect ratios.....	122
4.2.1 AA configuration.....	123
4.2.1.1 Cases of increasing γ	123

4.2.1.2 Cases of decreasing γ	129
4.2.2 CH configuration.....	130
4.2.2.1 Cases of increasing γ	130
4.2.2.2 Cases of decreasing γ	136
4.2.3 HC configuration:.....	138
4.2.3.1 Cases of increasing γ	138
4.2.3.2 Cases of decreasing γ	144
4.2.4 AC configuration.....	145
4.2.4.1 Cases of increasing γ	145
4.2.4.2 Cases of decreasing γ	151
4.2.5 CA configuration:.....	152
4.2.5.1 Cases of increasing γ	152
4.2.5.2 Cases of decreasing γ	158
4.2.6 CC configuration:.....	159
4.2.6.1 Cases of increasing γ	159
4.2.6.2 Cases of decreasing γ	168
4.2.7 LL configuration.....	169
4.2.7.1 Cases of increasing γ	169
4.2.7.2 Cases of decreasing γ	175

Chapter 5 Numerical Results - Case of Rectangular Cavity with Curved

Bottom.....	178
5.1 AAC configuration with SH=0.05	179
5.1.1 Case of increasing γ	179
5.1.2 Case of decreasing γ	187
5.2 AAC configuration with SH=0.25.....	189
5.2.1 Case of increasing γ	189
5.2.2 Case of decreasing γ	195
5.3 AAC configuration with SH=0.45.....	196
5.3.1 Case of increasing γ	196
5.3.2 Case of decreasing γ	202
5.4 AAC configuration with SH=0.65.....	202
5.4.1 Case of increasing γ	203
5.4.2 Case of decreasing γ	208
5.5 AAC configuration with SH=0.85.....	209
5.5.1 Case increasing γ	209
5.5.2 Case of decreasing γ	215
Chapter 6 Summary and Conclusions and Future Work.....	216
6.1 Summary and Conclusions.....	216
6.2 Future work.....	217
Reference	219

List of Figures

Figure 1.1	Isotherms and streamlines for $Pr=7.0$ and uniform temperature at the cavity floor. (a) $Ra=10^3$ Max stream function=1.09; (b) $Ra=10^5$, Max Stream function=19.16; (c) $Ra=10^6$, Max Stream function=43.35; (d) $Ra=10^7$, Max Stream functions=75.96.....	9
Figure 1.2	Thermal configuration of the cavity in [12].....	11
Figure 1.3	Isothermal lines and streamlines for different Ra numbers for $A=2$	12
Figure 1.4	Configuration of the cross force and upslope (down-slope) force in the inclined cavity.....	14
Figure 1.5	Different flow and thermal fields obtained using different initial thermal conditions in the cavity at $A=3$	17
Figure 1.6	Hysteresis phenomenon illustrated by average Nu numbers for Ra number ranged from 2×10^3 to 2×10^4	19
Figure 1.7	Configurations of thermal boundary conditions considered in the present study. In addition to the above three parameters, the present study will also investigate.....	23
Figure 2.1	Staggered grids used to calculate all independent variables...	30
Figure 2.2	Iterative procedure of the SIMPLE algorithm.....	31
Figure 2.3	Grid structure for curved bottom.....	39
Figure 2.4	Heat flux on curved bottom.....	40

Figure 2.5	Temperature at the corner (a) AA configuration; (b) CC configuration.....	42
Figure 2.6	Local Nu number at the bottom wall for (A) $L'=0.075$; (b) $L'=0.025$; (c) without the linear temperature distribution assumption.....	44
Figure 2.7	Results obtained using present algorithm considering different thermal boundary conditions at $A = 2$, $Pr = 0.7$, and $Ra=10^4$ and 10^5	48
Figure 2.8	Nu number Vs angle of inclination at different Ra numbers, $A = 4$, and $Pr = 0.7$. Results from present study (left) compared with those of reported in [21] (right).....	49
Figure 2.9	Nu VS γ for angle increasing and decreasing in various Ra numbers for AA configuration and $A=4$	50
Figure 2.10	Comparison with of calculated Nu number for cavities with various aspect ratios, $Pr = 0.7$ with those reported in [11]. (a) Results from present work; (b) Results reported in [11].....	52
Figure 2.11	Isothermal lines and Streamlines from present algorithm for different Ra numbers in left half of the cavity, $A = 2$, and $Pr=7.0$. To be compared with Fig 1.1.....	53
Figure 3.1	Normalized streamlines and isothermal lines for AA configuration at various angles of inclination and four Ra	

	numbers. (a) $Ra=1000$, (b) $Ra=3000$, (c) $Ra=5000$, (d) $Ra=10^4$. Positive values indicate rotation in clockwise direction.....	55
Figure 3.2	Variation of average Nu number (both top and bottom walls) with inclination angle at various Ra numbers for AA configuration and $A=1$	56
Figure 3.3	Average Nu number (bottom wall) as a function of inclination angle γ for angle increasing and decreasing at various Ra numbers for AA configuration and $A=1$	58
Figure 3.4	Results obtained using sweeping from right to left, AA configuration and $Ra=10^4$, (a) Streamlines and isotherms at $\gamma=0^\circ$. Positive values indicate rotation in clockwise. (b) Nu (bottom wall) Vs γ	60
Figure 3.5	Normalized streamlines and isothermal lines for CH configuration at various angles of inclination and four Ra numbers. (a) $Ra=1000$, (b) $Ra=3000$, (c) $Ra=5000$, (d) $Ra=10^4$. Positive values indicate rotation in clockwise direction.....	61
Figure 3.6	Variation of average Nu number (both top and bottom walls) with inclination angle at various Ra numbers for CH configuration and $A=1$	62
Figure 3.7	Average Nu number (bottom wall) as a function of inclination angle γ for angle increasing and decreasing at various Ra	

	numbers for CH configuration and $A=1$	63
Figure 3.8	Normalized streamlines and isothermal lines for HC configuration at various angles of inclination and four Ra numbers. (a) $Ra=1000$, (b) $Ra=3000$, (c) $Ra=5000$, (d) $Ra=10^4$. Positive values indicate rotation in clockwise direction.....	65
Figure 3.9	Variation of average Nu number (both top and bottom walls) with inclination angle at various Ra numbers for HC configuration and $A=1$	66
Figure 3.10	Average Nu number (bottom wall) as a function of inclination angle γ for angle increasing and decreasing at various Ra numbers for HC configuration and $A=1$	67
Figure 3.11	Normalized streamlines and isothermal lines for AC configuration at various angles of inclination and four Ra numbers, (a) $Ra=1000$, (b) $Ra=3000$, (c) $Ra=5000$, (d) $Ra=10^4$. Positive values indicate rotation in clockwise direction.....	69
Figure 3.12	Variation of average Nu number (both top and bottom walls) with inclination angle at various Ra numbers for AC configuration and $A=1$	70
Figure 3.13	Average Nu number (bottom wall) as a function of inclination angle γ for angle increasing and decreasing at various Ra numbers for AC configuration and $A=1$	71
Figure 3.14	Normalized streamlines and isothermal lines for CA	

	configuration at various angles of inclination and four Ra numbers. (a) Ra=1000, (b) Ra=3000, (c) Ra=5000, (d) Ra=10 ⁴ . Positive values indicate rotation in clockwise direction.....	72
Figure 3.15	Variation of average Nu number (both top and bottom walls) with inclination angle at various Ra numbers for CA configuration and A=1.....	73
Figure 3.16	Average Nu number (bottom wall) as a function of inclination angle γ for angle increasing and decreasing at various Ra numbers for CA configuration and A=1.....	74
Figure 3.17	Normalized streamlines and isothermal lines for CC configuration at various angles of inclination and four Ra numbers, (a) Ra=1000, (b) Ra=3000, (c) Ra=5000, (d) Ra=10 ⁴ . Positive values indicate rotation in clockwise direction.....	76
Figure 3.18	Variation of average Nu number (both top and bottom walls) with inclination angle at various Ra numbers for CC configuration and A=1.....	77
Figure 3.19	Average Nu number (bottom wall) as a function of inclination angle γ for angle increasing and decreasing at various Ra numbers for CC configuration and A=1.....	78
Figure 3.20	Normalized streamlines and isothermal lines for LL configuration at various angles of inclination and four Ra numbers, (a) Ra=1000, (b) Ra=3000, (c) Ra=5000, (d) Ra=10 ⁴ .	

	Positive values indicate rotation in clockwise direction.....	80
Figure 3.21	Variation of average Nu number (both top and bottom walls) with inclination angle at various Ra numbers for LL configuration and A=1.....	81
Figure 3.22	Average Nu number (bottom wall) as a function of inclination angle γ for angle increasing and decreasing at various Ra numbers for LL configuration and A=1.....	82
Figure 4.1	Normalized streamlines and isothermal lines for AA configuration at various angles of inclination and four Ra numbers, (a) Ra=1000, (b) Ra=3000, (c) Ra=5000, (d) Ra=10 ⁴ . Positive values indicate rotation in clockwise direction.....	87
Figure 4.2	Variation of average Nu number (both top and bottom walls) with inclination angle at various Ra numbers for AA configuration and A=2.....	88
Figure 4.3	Local velocity (in horizontal direction) distribution in x direction for various inclination angles.....	89
Figure 4.4	Average Nu number (bottom wall) as a function of inclination angle γ for angle increasing and decreasing at various Ra numbers for AA configuration and A=2.....	91
Figure 4.5	Normalized streamlines and isothermal lines for CH configuration at various angles of inclination and four Ra numbers, (a) Ra=1000, (b) Ra=3000, (c) Ra=5000, (d) Ra=10 ⁴ ,	

	Positive values indicate rotation in clockwise direction.....	94
Figure 4.6	Variation of average Nusselt number (both top and bottom walls) in the case of increasing angle of inclination at various Rayleigh numbers for CH configuration and $A=2$	95
Figure 4.7	Average Nu number (bottom wall) as a function of inclination angle γ for angle increasing and decreasing at various Ra numbers for CH configuration and $A=2$	96
Figure 4.8	Normalized streamlines and isothermal lines for HC configuration at various angles of inclination and four Ra numbers, (a) $Ra=1000$, (b) $Ra=3000$, (c) $Ra=5000$, (d) $Ra=10^4$. Positive values indicate rotation in clockwise direction.....	99
Figure 4.9	Variation of average Nu number (both top and bottom walls) with inclination angle at various Ra numbers for HC configuration and $A=2$	100
Figure 4.10	Average Nu number (bottom wall) as a function of inclination angle γ for angle increasing and decreasing at various Ra numbers for HC configuration and $A=2$	102
Figure 4.11	Normalized streamlines and isothermal lines for AC configuration at various angles of inclination and four Ra numbers. (a) $Ra=1000$, (b) $Ra=3000$, (c) $Ra=5000$, (d) $Ra=10^4$. Positive values indicate rotation in clockwise direction.....	105
Figure 4.12	Variation of average Nu number (both top and bottom walls)	

	with inclination angle at various Ra numbers for AC configuration and $A=2$	106
Figure 4.13	Average Nu number (bottom wall) as a function of inclination angle γ for angle increasing and decreasing at various Ra numbers for AC configuration and $A=2$	107
Figure 4.14	Normalized streamlines and isothermal lines for CA configuration at various angles of inclination and four Ra numbers, (a) $Ra=1000$, (b) $Ra=3000$, (c) $Ra=5000$, (d) $Ra=10^4$. Positive values indicate rotation in clockwise direction.....	109
Figure 4.15	Variation of average Nu number (both top and bottom walls) with inclination angle at various Ra numbers for CA configuration and $A=2$	110
Figure 4.16	Average Nu number (bottom wall) as a function of inclination angle γ for angle increasing and decreasing at various Ra numbers for CA configuration and $A=2$	112
Figure 4.17	Normalized streamlines and isothermal lines for CC configuration at various angles of inclination and four Ra numbers, (a) $Ra=1000$, (b) $Ra=3000$, (c) $Ra=5000$, (d) $Ra=10^4$. Positive values indicate rotation in clockwise direction.....	114
Figure 4.18	Variation of average Nu number (both top and bottom walls) with inclination angle at various Ra numbers for CC configuration and $A=2$	115

Figure 4.19	Average Nu number (bottom wall) as a function of inclination angle γ for angle increasing and decreasing at various Ra numbers for CC configuration and $A=2$	116
Figure 4.20	Normalized streamlines and isothermal lines for LL configuration at various angles of inclination and four Ra numbers, (a) $Ra=1000$, (b) $Ra=3000$, (c) $Ra=5000$, (d) $Ra=10^4$. Positive values indicate rotation in clockwise direction.....	119
Figure 4.21	Variation of average Nu number (both top and bottom walls) with inclination angle at various Ra numbers for LL configuration and $A=2$	120
Figure 4.22	Average Nu number (bottom wall) as a function of inclination angle γ for angle increasing and decreasing at various Ra numbers for LL configuration and $A=2$	122
Figure 4.23	Normalized streamlines and isothermal lines for AA configuration at various angles of inclination for $Ra=1000$ and $A=4$. Positive values indicate rotation in clockwise direction....	125
Figure 4.24	Normalized streamlines and isothermal lines for AA configuration at various angles of inclination for $Ra=3000$ and $A=4$. Positive values indicate rotation in clockwise direction...	126
Figure 4.25	Normalized streamlines and isothermal lines for AA configuration at various angles of inclination for $Ra=5000$ and $A=4$. Positive values indicate rotation in clockwise direction...	127

Figure 4.26	Normalized streamlines and isothermal lines for AA configuration at various angles of inclination for $Ra=10^4$ and $A=4$. Positive values indicate rotation in clockwise direction....	128
Figure 4.27	Variation of average Nu number (both top and bottom walls) with inclination angle at various Ra numbers for AA configuration and $A=4$	129
Figure 4.28	Average Nu number (bottom wall) as a function of inclination angle γ for angle increasing and decreasing at various Ra numbers for AA configuration and $A=4$	130
Figure 4.29	Normalized streamlines and isothermal lines for CH configuration at various angles of inclination for $Ra=1000$ and $A=4$. Positive values indicate rotation in clockwise direction...	132
Figure 4.30	Normalized streamlines and isothermal lines for CH configuration at various angles of inclination for $Ra=3000$ and $A=4$. Positive values indicate rotation in clockwise direction...	133
Figure 4.31	Normalized streamlines and isothermal lines for CH configuration at various angles of inclination for $Ra=5000$ and $A=4$. Positive values indicate rotation in clockwise direction...	134
Figure 4.32	Normalized streamlines and isothermal lines for CH configuration at various angles of inclination for $Ra=10^4$ and $A=4$. Positive values indicate rotation in clockwise direction...	135
Figure 4.33	Variation of average Nu number (both top and bottom walls)	

	with inclination angle at various Ra numbers for CH configuration and $A=4$	136
Figure 4.34	Average Nu number (bottom wall) as a function of inclination angle γ for angle increasing and decreasing at various Ra numbers for CH configuration and $A=4$	138
Figure 4.35	Normalized streamlines and isothermal lines for HC configuration at various angles of inclination for $Ra=1000$ and $A=4$. Positive values indicate rotation in clockwise direction...	140
Figure 4.36	Normalized streamlines and isothermal lines for HC configuration at various angles of inclination for $Ra=3000$ and $A=4$. Positive values indicate rotation in clockwise direction...	141
Figure 4.37	Normalized streamlines and isothermal lines for HC configuration at various angles of inclination for $Ra=5000$ and $A=4$. Positive values indicate rotation in clockwise direction...	142
Figure 4.38	Normalized streamlines and isothermal lines for HC configuration at various angles of inclination for $Ra=10^4$ and $A=4$. Positive values indicate rotation in clockwise direction...	143
Figure 4.39	Variation of average Nu number (both top and bottom walls) with inclination angle at various Ra numbers for HC configuration and $A=4$	144
Figure 4.40	Average Nu number (bottom wall) as a function of inclination angle γ for angle increasing and decreasing at various Ra	

	numbers for HC configuration and $A=4$	145
Figure 4.41	Normalized streamlines and isothermal lines for AC configuration at various angles of inclination for $Ra=1000$ and $A=4$. Positive values indicate rotation in clockwise direction...	147
Figure 4.42	Normalized streamlines and isothermal lines for AC configuration at various angles of inclination for $Ra=3000$ and $A=4$. Positive values indicate rotation in clockwise direction...	148
Figure 4.43	Normalized streamlines and isothermal lines for AC configuration at various angles of inclination for $Ra=5000$ and $A=4$. Positive values indicate rotation in clockwise direction...	149
Figure 4.44	Normalized streamlines and isothermal lines for AC configuration at various angles of inclination for $Ra=10^4$ and $A=4$. Positive values indicate rotation in clockwise direction...	150
Figure 4.45	Variation of average Nu number (both top and bottom walls) with inclination angle at various Ra numbers for AC configuration and $A=4$	151
Figure 4.46	Average Nu number (bottom wall) as a function of inclination angle γ for angle increasing and decreasing at various Ra numbers for AC configuration and $A=4$	152
Figure 4.47	Normalized streamlines and isothermal lines for CA configuration at various angles of inclination for $Ra=1000$ and $A=4$. Positive values indicate rotation in clockwise direction...	154

Figure 4.48	Normalized streamlines and isothermal lines for CA configuration at various angles of inclination for $Ra=3000$ and $A=4$. Positive values indicate rotation in clockwise direction...	155
Figure 4.49	Normalized streamlines and isothermal lines for CA configuration at various angles of inclination for $Ra=5000$ and $A=4$. Positive values indicate rotation in clockwise direction...	156
Figure 4.50	Normalized streamlines and isothermal lines for CA configuration at various angles of inclination for $Ra=10^4$ and $A=4$. Positive values indicate rotation in clockwise direction...	157
Figure 4.51	Variation of average Nu number (both top and bottom walls) with inclination angle at various Ra numbers for CA configuration and $A=4$	158
Figure 4.52	Average Nu number (bottom wall) as a function of inclination angle γ for angle increasing and decreasing at various Ra numbers for CA configuration and $A=4$	159
Figure 4.53	Normalized streamlines and isothermal lines for CC configuration at various angles of inclination for $Ra=1000$ and $A=4$. Positive values indicate rotation in clockwise direction...	162
Figure 4.54	Normalized streamlines and isothermal lines for CC configuration at various angles of inclination for $Ra=3000$ and $A=4$. Positive values indicate rotation in clockwise direction...	163
Figure 4.55	Normalized streamlines and isothermal lines for CC	

	configuration at various angles of inclination for $Ra=5000$ and $A=4$. Positive values indicate rotation in clockwise direction...	164
Figure 4.56	Normalized streamlines and isothermal lines for CC configuration at various angles of inclination for $Ra=10^4$ and $A=4$. Positive values indicate rotation in clockwise direction...	165
Figure 4.57	Variation of average Nu number (both top and bottom walls) with inclination angle at various Ra numbers for CC configuration and $A=4$	166
Figure 4.58	Average Nu on the top of the horizontal cavity for AA and CC configurations for Ra ranged between 1000 and 5000 with $A=4$, $Pr=0.7$	167
Figure 4.59	Velocity distribution in the horizontal cavity for AA, CC configurations in $y=0.5$ for $A=4$ and $Pr=0.7$ with $Ra=1000, 2000, 5000$, (a) AA case, (b) CC case.....	167
Figure 4.60	Local Nu distribution on the top wall of the horizontal cavity for CC configuration for $A=4$, $Pr=0.7$ with $Ra=1000, 2000, 5000$..	168
Figure 4.61	Average Nu number (bottom wall) as a function of inclination angle γ for angle increasing and decreasing at various Ra numbers for CC configuration and $A=4$	169
Figure 4.62	Normalized streamlines and isothermal lines for LL configuration at various angles of inclination for $Ra=1000$ and $A=4$. Positive values indicate rotation in clockwise direction...	171

Figure 4.63	Normalized streamlines and isothermal lines for LL configuration at various angles of inclination for $Ra=3000$ and $A=4$. Positive values indicate rotation in clockwise direction...	172
Figure 4.64	Normalized streamlines and isothermal lines for LL configuration at various angles of inclination for $Ra=5000$ and $A=4$. Positive values indicate rotation in clockwise direction...	173
Figure 4.65	Normalized streamlines and isothermal lines for LL configuration at various angles of inclination for $Ra=10^4$ and $A=4$. Positive values indicate rotation in clockwise direction...	174
Figure 4.66	Variation of average Nu number (both top and bottom walls) with inclination angle at various Ra numbers for LL configuration and $A=4$	175
Figure 4.67	Average Nu number (bottom wall) as a function of inclination angle γ for angle increasing and decreasing at various Ra numbers for LL configuration and $A=4$	177
Figure 5.1	Variation of average Nu number (bottom walls) with inclination angle at five Ra numbers for AA and AAC configuration for different SH. (a) AA configuration (b) SH=0.05, (c) SH=0.25, (d) SH=0.45, (e) SH=0.65, (f) SH=0.85.....	181
Figure 5.2	Variation of average Nu number (top walls) with inclination angle at five Ra numbers for AA and AAC configuration for different SH, (a) AA configuration (b) SH=0.05, (c) SH=0.25,	

	(d) SH=0.45, (e) SH=0.65, (f) SH=0.85.....	182
Figure 5.3	Normalized streamlines and isothermal lines for AAC configuration at various angles of inclination for Ra=1000 and SH=0.05. Positive values indicate rotation in clockwise direction.....	183
Figure 5.4	Normalized streamlines and isothermal lines for AAC configuration at various angles of inclination for Ra=3000 and SH=0.05. Positive values indicate rotation in clockwise direction.....	184
Figure 5.5	Normalized streamlines and isothermal lines for AAC configuration at various angles of inclination for Ra=5000 and SH=0.05. Positive values indicate rotation in clockwise direction.....	185
Figure 5.6	Normalized streamlines and isothermal lines for AAC configuration at various angles of inclination for Ra=10 ⁴ and SH=0.05. Positive values indicate rotation in clockwise direction.....	186
Figure 5.7	Distribution of velocity component in x-direction for angle increasing and angle decreasing at y=0.9, A=4 and Ra = 1000, AAC configuration.....	188
Figure 5.8	Average Nu number (bottom wall) as a function of inclination angle γ for angle increasing and decreasing at various Ra	

	numbers for AAC configuration and $SH=0.05$	189
Figure 5.9	Normalized streamlines and isothermal lines for AAC configuration at various angles of inclination for $Ra=1000$ and $SH=0.25$. Positive values indicate rotation in clockwise direction.....	191
Figure 5.10	Normalized streamlines and isothermal lines for AAC configuration at various angles of inclination for $Ra=3000$ and $SH=0.25$. Positive values indicate rotation in clockwise direction.....	192
Figure 5.11	Normalized streamlines and isothermal lines for AAC configuration at various angles of inclination for $Ra=5000$ and $SH=0.25$. Positive values indicate rotation in clockwise direction.....	193
Figure 5.12	Normalized streamlines and isothermal lines for AAC configuration at various angles of inclination for $Ra=10^4$ and $SH=0.25$. Positive values indicate rotation in clockwise direction.....	194
Figure 5.13	Average Nu number (bottom wall) as a function of inclination angle γ for angle increasing and decreasing at various Ra numbers for AAC configuration and $SH=0.25$	196
Figure 5.14	Normalized streamlines and isothermal lines for AAC configuration at various angles of inclination for $Ra=1000$ and	

	SH=0.45. Positive values indicate rotation in clockwise direction.....	198
Figure 5.15	Normalized streamlines and isothermal lines for AAC configuration at various angles of inclination for Ra=3000 and SH=0.45. Positive values indicate rotation in clockwise direction.....	199
Figure 5.16	Normalized streamlines and isothermal lines for AAC configuration at various angles of inclination for Ra=5000 and SH=0.45. Positive values indicate rotation in clockwise direction.....	200
Figure 5.17	Normalized streamlines and isothermal lines for AAC configuration at various angles of inclination for Ra=10 ⁴ and SH=0.45. Positive values indicate rotation in clockwise direction.....	201
Figure 5.18	Average Nu number (bottom wall) as a function of inclination angle γ for angle increasing and decreasing at various Ra numbers for AAC configuration and SH=0.45.....	202
Figure 5.19	Normalized streamlines and isothermal lines for AAC configuration at various angles of inclination for Ra=1000 and SH=0.65. Positive values indicate rotation in clockwise direction.....	204
Figure 5.20	Normalized streamlines and isothermal lines for AAC	

	configuration at various angles of inclination for $Ra=3000$ and $SH=0.65$. Positive values indicate rotation in clockwise direction.....	205
Figure 5.21	Normalized streamlines and isothermal lines for AAC configuration at various angles of inclination for $Ra=5000$ and $SH=0.65$. Positive values indicate rotation in clockwise direction.....	206
Figure 5.22	Normalized streamlines and isothermal lines for AAC configuration at various angles of inclination for $Ra=10^4$ and $SH=0.65$. Positive values indicate rotation in clockwise direction.....	207
Figure 5.23	Average Nu number (bottom wall) as a function of inclination angle γ for angle increasing and decreasing at various Ra numbers for AAC configuration and $SH=0.65$	209
Figure 5.24	Normalized streamlines and isothermal lines for AAC configuration at various angles of inclination for $Ra=1000$ and $SH=0.85$. Positive values indicate rotation in clockwise direction.....	211
Figure 5.25	Normalized streamlines and isothermal lines for AAC configuration at various angles of inclination for $Ra=3000$ and $SH=0.85$. Positive values indicate rotation in clockwise direction.....	212

Figure 5.26	<p>Normalized streamlines and isothermal lines for AAC configuration at various angles of inclination for $Ra=5000$ and $SH=0.85$. Positive values indicate rotation in clockwise direction.....</p>	213
Figure 5.27	<p>Normalized streamlines and isothermal lines for AAC configuration at various angles of inclination for $Ra=10^4$ and $SH=0.85$. Positive values indicate rotation in clockwise direction.....</p>	214
Figure 5.28	<p>Average Nu number (bottom wall) as a function of inclination angle γ for angle increasing and decreasing at various Ra numbers for AAC configuration and $SH=0.85$.....</p>	215

List of Tables

Table 2.1	Coefficients for variables in general integral governing equation 2.1.....	29
Table 2.2	Grid dependence check for different thermal boundary conditions (a). AA configuration, - 62X242; (b). AC configuration, - 82X322; (c). CA configuration – 62X42; (d). CC configuration, - 62X242.....	34
Table 2.3	Grid dependence check for different thermal boundary conditions (a). CH configuration, - 62X242; (b). HC configuration, - 62X242; (c). LL configuration, - 82X322; (d). AAC configuration, - 142X142.....	35
Table 2.4	Average Nu number calculated using different treatments temperature discontinuity for CC case. $A = 4$, $Pr = 0.7$, and $Ra = 5000$	46
Table 2.5	Comparison with results obtained for benchmark problem reported in [27].....	51

Nomenclature

H	cavity height
L	cavity length
SH	height of the curved bottom
A	aspect ratio = H/L
g	gravitational acceleration
p	pressure
P	dimensionless pressure = $\frac{p}{\rho U^{*2}}$
Pr	Prandtl number
Nu	Nusselt number
ψ	stream function
u	component of dimensionless velocity in x-direction = U/U^*
v	component of dimensionless velocity in y-direction = V/U^*
U^*	characteristic velocity (velocity scale) = v/H
X, Y	Cartesian coordinates
x, y	dimensionless coordinates = X/H , and Y/H , respectively.

Ra Rayleigh number = $\frac{g\beta(T_h - T_c)H^3}{\alpha\nu}$

Q_{in} sum of heat transferred from hot wall(s).

Q_{out} sum of heat transferred to cold wall(s).

Greek symbols

α thermal diffusivity

β coefficient of thermal expansion = $-\frac{(\partial\rho/\partial T)_P}{\rho}$

γ angle of inclination of cavity (measured from horizontal line).

θ dimensionless temperature = $\frac{(T - T_c)}{(T_h - T_c)}$

ρ density

Subscript

c cold surface

h hot surface

max maximum value

min minimum value

ave average value

x component in x-direction

y component in y-direction

Chapter 1

Introduction and Literature Review

1.1 Introduction

Natural convection has been extensively studied numerically and experimentally due to its existence in many engineering applications. Natural thermal convection arises through the interaction of a body force caused by gravity and density variations mostly caused by temperature gradients. The problem of natural convection can be classified into two main categories, namely, external and internal natural convection flows.

In the case of external natural convection, flow arises through an extensive medium due to local inhomogeneity in density at a location or at a surface without being confined by any other solid surfaces. External natural convection flows occur in many practical applications, such as systems involving horizontal or vertical heated surfaces, atmospheric and oceanic circulation, electronic power supplies, single windows, jets arising without any confining solid boundaries. In the case of internal natural convection, flow arises within a body of fluid contained in an enclosure or cavity. Internal natural convection flows might also encountered in many practical applications, such as: electric machinery, solar collectors, heating and cooling systems, etc.

External natural convection flows are, in most cases, affected by a single surface. In this case classical boundary-layer theory yields same conditions for external flow problems whose exterior regions are unaffected by the solid boundary. However, internal natural convection flows are normally affected by a group of enclosed surfaces, in which

case an exterior region of the flow field enclosed by solid boundaries is formed around a core region. The form of that core region depends not only on the thermal boundary conditions but also on the geometry of the enclosure. Therefore, internal natural convection flows are more complicated than external ones.

Most of the earliest research on natural convection was focused on external flow situations. Studies include: hot or cold, vertical or horizontal flat surfaces. These two cases were most extensively investigated [1, 2, 3, 4]. Natural convection from inclined and curved surfaces was also extensively studied [4]. Thermal plumes, such as fluid arisen from a horizontal heated wire with small diameter, and buoyant jets, which occurred when fluid was discharged into an ambient medium with different density, such as in smokestacks discharging hot gas into the atmosphere.

Early studies on internal natural convection flows were mainly experimental investigations. One of the earliest studies on the subject was carried out by Elenbass [5], who had experimentally studied natural convection from a group of vertical parallel plates heated using a common heater placed in the middle of a set of square vertical plates. Elenbass investigated the effect of plate size in the range from 5.95 X 5.95 cm to 24 X 24 cm, the effect of the distance between plates, b , in the range from 0 cm to 0.7cm, and the effect of plate temperature, θ_w , between 10°C and 350°C on the resulted heat transfer rates. His results indicated that, for small values of distance b up to a certain critical value, neighboring plates had a significant effect on rate of heat transfer from one another. In this case the natural convection problem can be regarded as an internal one. Increasing b beyond that critical value, natural convection from the vertical plates could no longer be

regarded as an internal flow problem. As b reached that critical value, each plate actually did not affect one another and the rate of heat transfer remained almost unchanged. As for the effect of plate temperature on the rate of heat transfer, at plate temperatures above 115°C , increasing plate temperature did not result in any significant enhancement in the rate of heat transfer.

1.2 Literature review

Due to the large number of studies found in the literature; and because natural convection in enclosures is the main focus of the present study, only research related to internal natural convection will be reviewed in the following sections.

Numerous investigations have been carried out concerning the effect of cavity orientation, cavity geometry (regular, i.e., with flat walls, or irregular; i.e., with curved walls), cavity dimensions (i.e., aspect ratio), Ra number, boundary conditions of cavity walls, and type of fluid inside the cavity (i.e., the value of Prandtl number) on flow and thermal fields and heat transfer rates inside the cavity. Based on cavity orientation with respect to the gravity vector, natural convection in cavities can be classified into three main groups: natural convection in vertical, in horizontal, and in inclined cavities. In the following sections, literature related to natural convection in regular cavities of these three orientations will be reviewed followed by a review of literature related to irregular cavities.

1.2.1 Natural convection in vertical regular cavities

Vertical cavities are defined as cavities with temperature gradients imposed in the horizontal direction. In this case, both the heated or cooled surfaces are parallel to the gravitational vector, and the resulted buoyancy force is perpendicular to it. In this case, natural convection flow begins immediately regardless of the value of the temperature gradient (i.e., for all values of Ra number). Assuming different thermal conditions for the two vertical walls, most of the research carried out on natural convection in vertical cavities was focused on cavities with insulated end (horizontal) walls. End walls were also sometimes assumed having a linear temperature distribution.

Davis [6] numerically studied two-dimensional natural convection in rectangular cavities, considering the effect of Ra number in the range between 10^3 and 1.5×10^5 and Prandtl number ranging from 0.1 to 1000. The top and bottom walls were chosen as either insulated or having linear temperature distribution. The two vertical walls were assumed differentially heated. The left wall was kept at a low constant temperature, T_c , and the right wall was at a higher constant temperature, T_h . The cavity height/width aspect ratio was varied in the range between 1 and 5.

Results indicated that thermal boundary conditions of horizontal walls and Ra number had a significant effect on both the resulted flow and thermal fields inside the cavity. Although Prandtl number did not cause much change in the calculated rate of heat transfer (within 7%) in the aforementioned configuration, it exerted a stabilizing influence on the numerical procedure.

Yin et al. [7] experimentally studied natural convection in rectangular, air-filled cavities with height/width aspect ratios in the range between 4.9 and to 78.7. The left wall was heated and kept at T_h , the right wall was cooled and assumed at T_c , and the top and bottom end walls were insulated. Grashof number, based on layer thickness, ranged from 1.5×10^3 to 7.0×10^6 .

Except for the area very close to the end wall, temperature distributions were linear as they were measured in major portion in vertical direction. For low Gr numbers, such as 4.96×10^3 or 5.43×10^3 , and for aspect ratios equal to 78.14 and 39.17, respectively, heat transfer from the hot plate to the cold plate was transported only by conduction across that major portion air layer.

For higher Gr number, such as 3.3×10^5 , and smaller aspect ratio, which was equal to 9.79, the results indicated that heat was mainly transported from the hot plate to the cold plate by convection. Conduction in the central regime was actually opposite to the overall direction of the heat transfer. Authors demonstrated that lower height-width aspect ratio would increase convection.

Finally, Yin et al showed the overall correlation equation: $Nu_D = C(Gr_D)^a (L/D)^b$, where $C=0.210$, $a=0.269$, $b=-0.131$. The results had an average deviation of less than 7.6% and also with 94.4% of the data within $\pm 20\%$ of the values.

Studies considering vertical cavities with boundary conditions other than those considered by Davis [6] and Yin et. al. [7] were also carried out.

Aydin et al.[8] numerically investigated natural convection in rectangular cavities with aspect ratios equal to 1, 2 and 4. Boundary conditions used in this study were: high

temperature at the left wall, low temperature at the top wall, and the other two walls were assumed insulated. Considering this set of boundary conditions, temperature discontinuity appeared at the cavity top left corner point and required a special numerical treatment. Aydin et al. assumed that the temperature at that corner point is equal to the average of the hot and cold walls temperatures. This numerical treatment is very common in such cases of mixed boundary conditions; and has been used in other studies [9,12] as will be discussed later. The assumption of the average temperature taken at the corner point leaves the numerical solution grid dependent, i.e., values of the calculated rates of heat transfer (Nu number) will vary with the grid size. In order to deal with this grid dependence problem, Aydin et al. assumed that the temperature profile between the nodal point at the corner and the one next to it is linear. Whereas, they did not mention how much the distance among these nodal points they used was; and the effect of the size of such distance on the calculated Nu numbers. Results of average Nu number Vs. Ra number were reported for Ra number ranged from 10^3 to 10^7 , and for aspect ratios from 1 to 4. Their results indicated that the effect of aspect ratio at high Ra numbers, such as 10^6 and 10^7 is more significant than that at lower Ra numbers. Heat transfer rates were shown to, as expected, increase with the increase of Ra numbers.

Shiralkar and Tien [9] studied the effect of vertical temperature gradients on natural convection flows in an air-filled, differentially-heated square cavity. Left and right walls were heated and cooled, respectively. The effect of vertical temperature gradients was investigated by considering the top and bottom walls having various temperatures. Results indicated that vertical temperature gradients have a significant

effect on natural convection flows. When the temperature of the bottom wall was higher than that of the top wall, heat transfer rates in horizontal direction would decrease as this difference increased. As this difference reached 5 times of the temperature difference between left and right walls, Nu number decreased as Ra increased from 10^3 to 10^4 . As for the temperature on the top wall was higher than bottom wall, heat transfer in both horizontal and vertical direction increased as temperature gradient in vertical direction increased, i.e. Nu numbers were increase function of the Ra numbers.

1.2.2 Natural convection in horizontal regular cavities

As indicated before, regular indicates that all cavity walls are flat, not curved. Similar to the case of vertical cavity, horizontal means that the cavity is bounded by two, differentially heated, horizontal walls. The two end (vertical) walls are usually assumed to be either insulated or having linear temperature profiles. Buoyancy force produced by vertical temperature gradient in the case of horizontal cavity is parallel to the gravitational vector. As will be discussed later, in this case, in order for natural convection flow to take place inside the cavity, Raleigh number has to be above a certain critical value, below which heat transfer inside the cavity will be entirely dominated by conduction. Research carried out on horizontal cavities also focused on investigating the effect of different boundary conditions, of Ra number, of cavity aspect ratio, and the effect of Prandtl (Pr) number.

Studies considering low Pr numbers were related to certain industrial applications, such as, cooling systems of nuclear reactors using liquid metals, processing of molten

metals, and crystal growth of electrical semiconductors from melt phases. Ozoë and Ukeba [10] investigated numerically the effect of Pr number on natural convection flows inside horizontal cavities heated from the bottom, cooled from the top wall, and having insulated end walls. Values of Pr number considered in this study were all below 1.0. Results indicated that heat transfer rates greatly depend on Pr number in the range between 0.0003 and 0.72, which was not same as results reported by Davis [6] in the case of vertical cavities at Pr numbers in the range between 0.1 and 1000. The critical value of Ra number at which convection get into play was investigate for all Pr numbers considered. Value of $Ra_c=1709$ reported by Ozoë and Ukeba [10] agrees with value reported in [14].

Studies considering horizontal cavities with boundary conditions other than those considered by Ozoë and Ukeba [10] were also carried out.

Ganzarolli and Milanez [11] studied numerically natural convection inside a horizontal cavity heated from below (isothermal or constant heat flux), insulated on the top and cooled from the two vertical end walls. Ra numbers based on the cavity height ranged between 10^3 and 10^7 , Pr numbers varied from 0.7 to 7 and length to height ratio of the cavity ranged from 1 to 9.

As Ra number increased, the fluid was accelerated by a stronger buoyancy force and tended to occupy the whole cavity, so isothermal lines and streamlines were compressed closer toward the wall, which resulted in a thinner boundary layer thinner as shown in Fig. 1.1 [11].

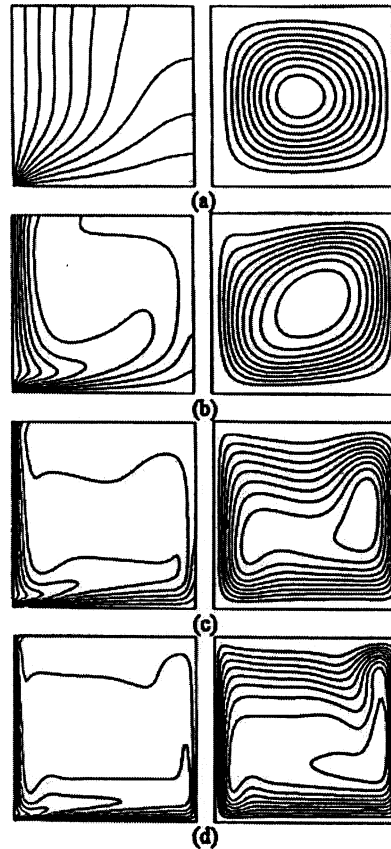


Fig 1.1 Isotherms and streamlines for $Pr=7.0$ and uniform temperature at the cavity floor. (a) $Ra=10^3$ Max stream function=1.09; (b) $Ra=10^5$, Max Stream function=19.16; (c) $Ra=10^6$, Max Stream function=43.35; (d) $Ra=10^7$, Max Stream functions=75.96 [11].

It seemed that fluid fields would keep same when aspect ratio greater than a critical value due to maximum effective distance by the side wall for the isothermal bottom. For example, isotherms and streamlines for $A=7$ and 9 are same as $Ra=10^5$ as bottom surface was isothermal.

Due to temperature discontinuity at the two lower corner points, similar to the method used by Aydin et al.[8], Ganzarolli and Milanez assumed that the temperature at those corner points is equal to the average of the temperatures of the hot and cold walls.

bottom. For example, isotherms and streamlines for $A=7$ and 9 are same as $Ra=10^5$ as bottom surface was isothermal.

Due to temperature discontinuity at the two lower corner points, similar to the method used by Aydin et al.[8], Ganzarolli and Milanez assumed that the temperature at those corner points is equal to the average of the temperatures of the hot and cold walls. In a practical situation and physically, there should be a temperature profile between the temperature at each corner point and that of the two intersecting walls. Authors assumed a linear temperature profile between the corner point and small distance from this corner, however, there was no mention of how long this distance was.

Horizontal cavities heated from below and cooled from above have drawn a lot of attention due to its special character and flow instability associated in such cases. Rather than the commonly developed unicell flow structure, in this case, natural convection flows are characterized by multi-cell flow structures.

Corcione[12] numerically studied the effect of different boundary conditions, various aspect ratios between 1 and 8, Ra numbers from 10^3 to 10^6 on natural convection in air-filled horizontal cavities. Six configurations of boundary conditions of the cavity end walls were considered as shown in Fig. 1.2.

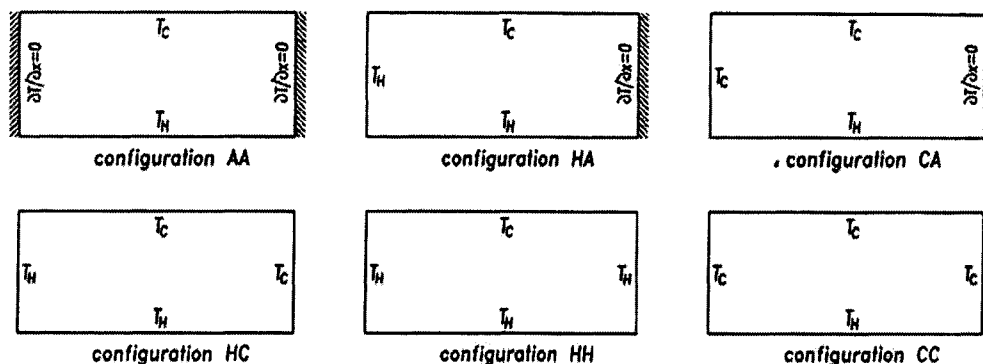


Fig 1.2 Thermal configuration of the cavity in [12].

Corcione concluded that end wall boundary conditions have significant effect on the resulted flow and thermal fields inside the cavities as shown in Fig. 1. 3. Author set AA as reference. As each insulated end walls was replaced by a cooled, heat transfer rate on the bottom wall would increase. A opposite phenomenon could be observed for the top wall. Whereas, as each insulated end walls was replaced by a heated wall, heat transfer rate on the bottom wall would decrease. The effect of aspect ratio was investigated by fixing Ra number for all the thermal conditions. Results showed average heat transfer rate tended to be the same value with the increase of aspect ratio for all the investigated thermal conditions as Ra number was kept in a same value. However, local heat fluxes from top and bottom walls only depended on the thermal boundary conditions.

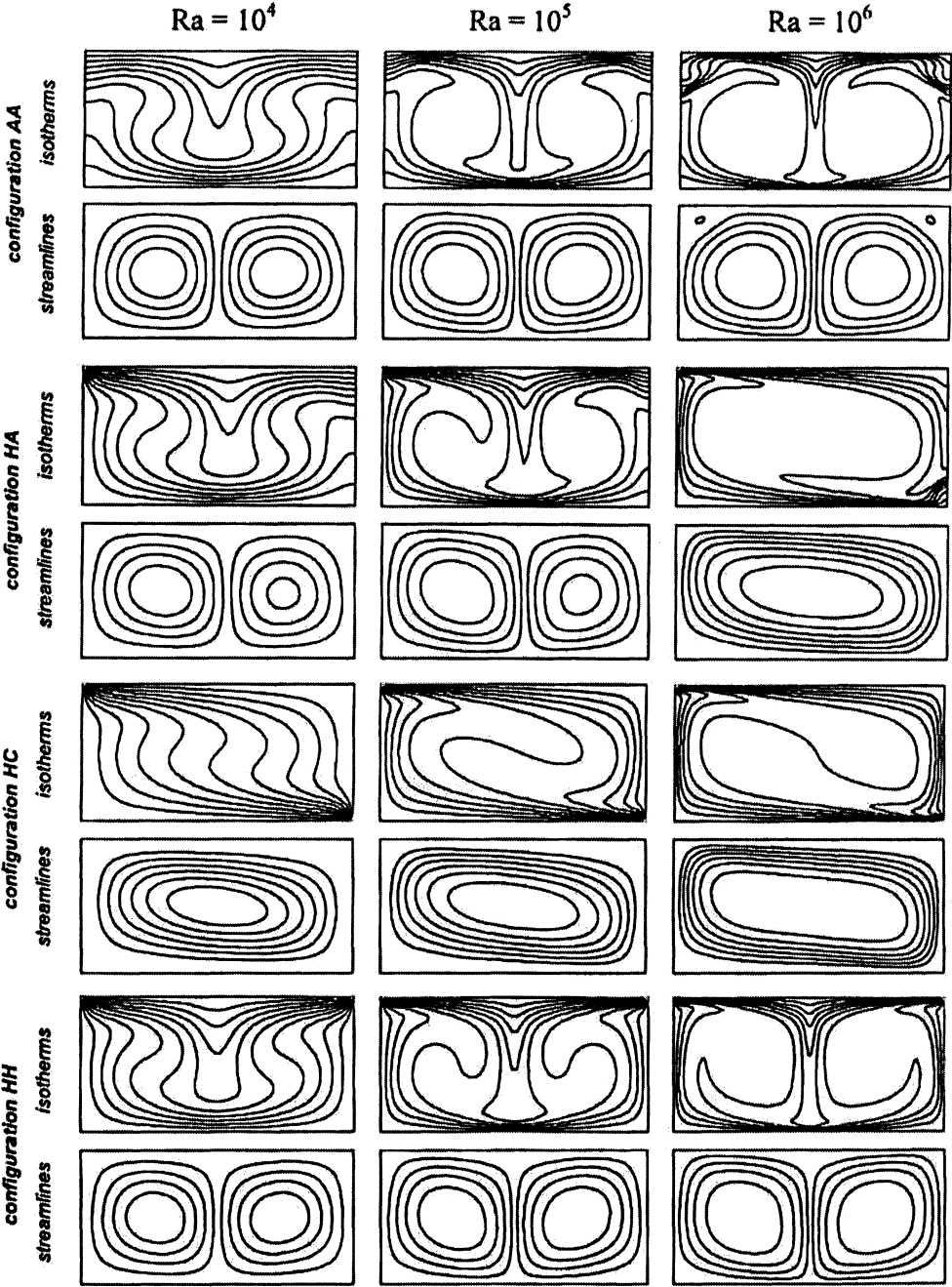


Fig 1.3 Isothermal lines and streamlines for different Ra numbers for A=2 [12].

For configurations with temperature discontinuity at corner points, Corcione employed the same numerical treatment used in [8 and 10], i.e., assumed temperature at

corner points equal to the average of the temperatures of the two intersecting walls. However, Corcione did not use any linear temperature profile as in [8 and 10], without which his results are expected to be grid-dependent. No mention of the effect of grid size on calculated Nu numbers was given. Some of the reported results indicated that the conservation of energy was not satisfied. For example, results reported for the HA case at $Ra = 1000$, have an error in the balance of Q_{in} and Q_{out} of about 20%.

1.2.3 Natural convection in inclined regular cavities

The study of thermal natural convection in inclined enclosures is motivated by a desire to find out what effect slope would have on certain thermally driven flows which are found in many engineering applications. These applications include: building systems containing multi-layered walls, double windows, and air gaps in unventilated spaces; energy systems such as solar collectors, storage devices, furnaces, heat exchanges, and nuclear reactors; material processing such as melting processes and crystal growth reactors. Thermally driven flows in inclined enclosures are also found in large scale geophysical, astrophysical, and environmental phenomena.

In the case of an inclined cavity, there is an angle between buoyancy force and the gravity vector, thus buoyancy force can be divided into two components. One component is parallel to the direction normal to the bottom of the cavity, and will be denoted here as the cross force. The other component is tangent to the bottom of the cavity, and will be denoted as the upslope or down-slope force, see Fig. 1.4.

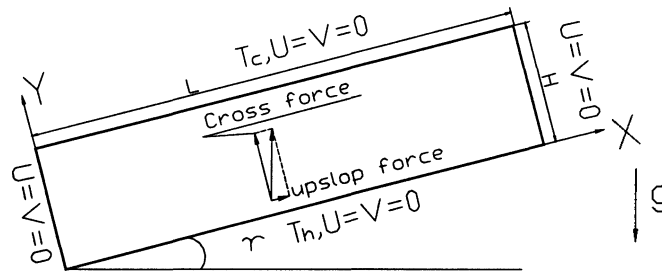


Fig 1.4 Configuration of the cross force and upslope (down-slope) force in the inclined cavity.

As shown in Fig 1.4, the angle of inclination (γ) of the cavity is measured from the horizontal direction, i.e., when $\gamma = 0^\circ$, the cavity is in the horizontal position. When γ is greater than 0° at some values of Ra numbers, convection would produce some motion in the fluid by the upslope (or down-slope) force. Whereas, no convective heat transfer is produced, and heat is transferred across the cavity only by conduction, if Ra number is below a certain critical value. In case of horizontal cavities, that critical value of Ra number was found to depend on the cavity aspect ratio and thermal conditions of end walls. In case of inclined cavities, as will be discussed later, in addition to these parameters, the critical value of Ra number also depends on the cavity angle of inclination.

Flow caused by upslope force in inclined cavities without convective heat transfer was first described by Batchelor [13] and was called “base-flow” by Hollands and Konicek [14], who carried out an experimental study to determine the critical value of Ra number (Ra_c) in inclined rectangular cavities. When $Ra < Ra_c$, no convective heat transfer

was observed. Experiments were performed in a shallow air-filled cavity with width-to-height aspect ratio equal to 44, which was differentially heated in vertical direction and insulated in the other direction. For horizontal cavities, i.e., $\gamma = 0^\circ$, results reported by Hollands and Konicek have 0.9% difference from those reported by Unny [15] and Hart [16]. When cavity was inclined, their results have about maximum 20% difference with those predicted in [15 and 16].

Hamady et al [17] experimentally studied local heat transfer characteristics in air-filled, square enclosures heated and cooled in the vertical direction and insulated in the other sides. Ra number ranged between 10^4 and 10^6 and inclination angle varied from 0° to 180° . Local Nu number was reported and the flow pattern was shown to give the flow and heat transfer behavior. Results showed that Ra number and angle of inclination strongly affect rate of heat transfer.

Different boundary conditions were also studied in inclined cases. Ben and Bilgen [18] numerically investigated natural convection in an inclined cavity bounded by a solid wall with its outer boundary at uniform temperature while the opposite side had a constant heat flux with the other two sides insulated. Heat transfer rate and fluid field were reported. Results showed that heat transfer rate was an increasing function of Ra number and decrease function of thickness of the solid wall. This function would be more significant at higher Ra numbers or better wall conductivity. The Maximum heat transfer happened as inclination angle equal to 80° .

Arnold et al. [19] experimentally investigated the effect of cavity aspect ratio and inclination on natural convection in inclined enclosures. The cavity was initially cooled

on the bottom and heated on the top with two insulated end walls. Ra numbers ranged from 10^3 to 10^6 and aspect ratio was set 1, 3, 6 and 9. Inclination angles varied from 0 to 180° . Results indicated that heat transfer reached a maximum value at inclination angle equal to 90° . After that it decreased and reached a minimum value at a certain angle and then increased again. These phenomena were more significant in low aspect ratios, such as 1 and 3. The angle of minimum heat transfer rate occurred closer to 180° as aspect ratio got closer to 0. It would reach an asymptote at 110° as aspect ratio increased from 12 to higher values.

While, Elsherbiny [20] experimentally studied natural convection in inclined shallow cavities with width-height aspect ratios ranged from 20 to 80. The air filled cavity was initially heated from below and cooled on the top wall with two perfectly conducting end walls. Ra number ranged from 10^2 to 2×10^6 and inclination angles varied from 0 to 180° . Results showed that heat transfer rate was a decrease function of the inclination angle.

Soong and Tzeng [21] numerically investigated mode transition in inclined enclosures heated from below, cooled from above with insulated end walls. This study investigated the effect of initial conditions on mode transition of natural convection flows inside inclined cavities. Depending on cavity aspect ratio and angle of inclination, two totally different flow patterns were observed. A unicell flow mode and a multi-cell flow mode. Even in the cases where the multi-cell mode was normally expected, results indicated that, depending on the initial condition of the fluid inside the cavity whether it

is initially cold ($T_i = T_c$ or $\theta_i = \frac{T - T_c}{T_h - T_c} = 0$), at the average temperature of the top and bottom walls ($\theta_i = 0.5$), or hot ($\theta_i = 1$), different steady solutions could be obtained, as shown in Fig. 1.5.

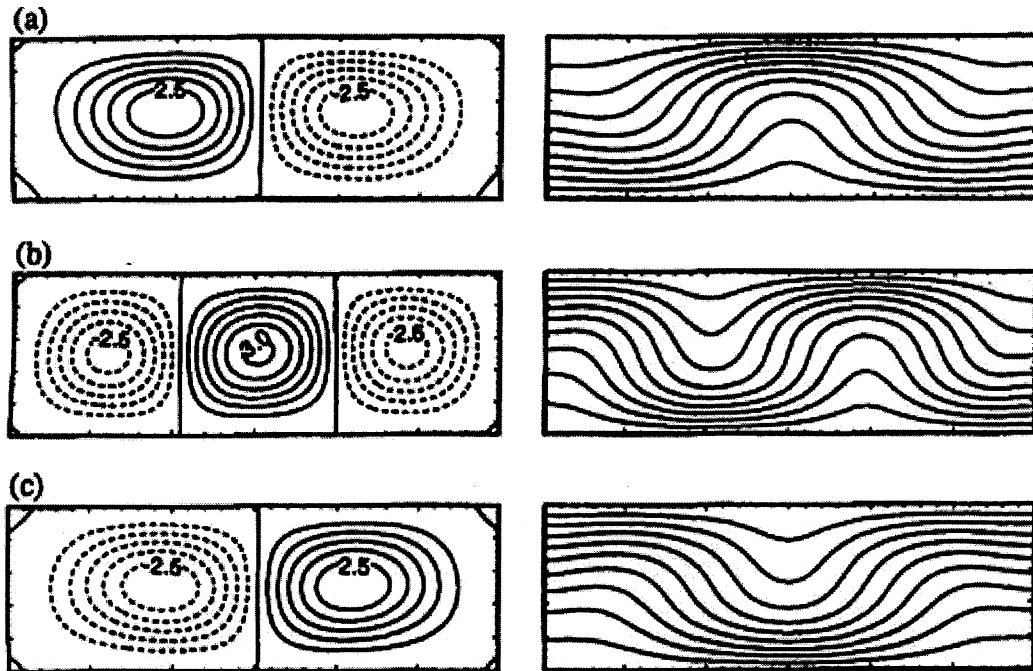


Fig 1.5 Different flow and thermal fields obtained using different initial thermal conditions in the cavity at $A=3$ [21].

The reasons for the multi solutions for different initial conditions are also indicated in [21]. For the case with initially cold fluid, the fluid near the hot bottom wall was heated and tried to go up due to the buoyancy force. Since the fluid next to the side walls were stuck due to the viscous force at the wall, the ascending motion was more stronger in the central region. Finally, as shown in Fig1.5a, the central fluid rose and an anticlockwise cell on the left and clockwise cell on the right part of the cavity appear. In the case of initially hot fluid, the fluid was initially at the same temperature as that of the

hot wall and was cooled by the top cold wall. The cooled fluid near the top wall tended to descend and, for relatively stronger viscous effect near the side walls, the fluid in central region tended to move down. Cells rotating in opposite direction to those formed in Fig 1.5a are obtained. In case of fluid initially at average temperature of the hot and cold walls, due to the lower temperature gradient between the walls and the fluid, a flow field with lower average velocities has developed. Lower velocity means that the fluid is not accelerated enough to occupy the same space in the cavity. As a result of that three (more) cells have been developed in this case, as shown in Fig1.5b.

Due to the inherent non-linearity of the problem and the possibility of having multi-flows, or in other words, having a hysteresis phenomenon, as explained above. Soong and Tzeng reported a detailed investigation of the cavity angle of inclination on such phenomenon. The sequence of numerical calculations was specified clearly. In calculations with γ increasing from 0° (horizontal) to 90° (vertical), flow and temperature fields at a constant Ra and $\gamma = 0^\circ$ were first calculated using 0 as initial guess for the velocity and the temperature fields. The $\gamma = 0^\circ$ solution was then used as initial condition for solution of the subsequent case of inclination with $\gamma = 5^\circ$, which was then used as an initial condition for the subsequent case of $\gamma = 10^\circ$, and so on. As the value of γ at which mode transition occurs was determined, say between 30° and 35° , calculations were then repeated starting from 30° with increments of 1° in order to locate mode-transition angle within 1° accuracy. A similar procedure was employed for calculations with γ decreasing starting from 90° back to 0° using the 90° solution obtained from the γ increasing case as

an initial condition. Hysteresis phenomena of the mode transition for $A = 4$ for some Ra numbers reported in [21] is shown in Fig. 1.6.

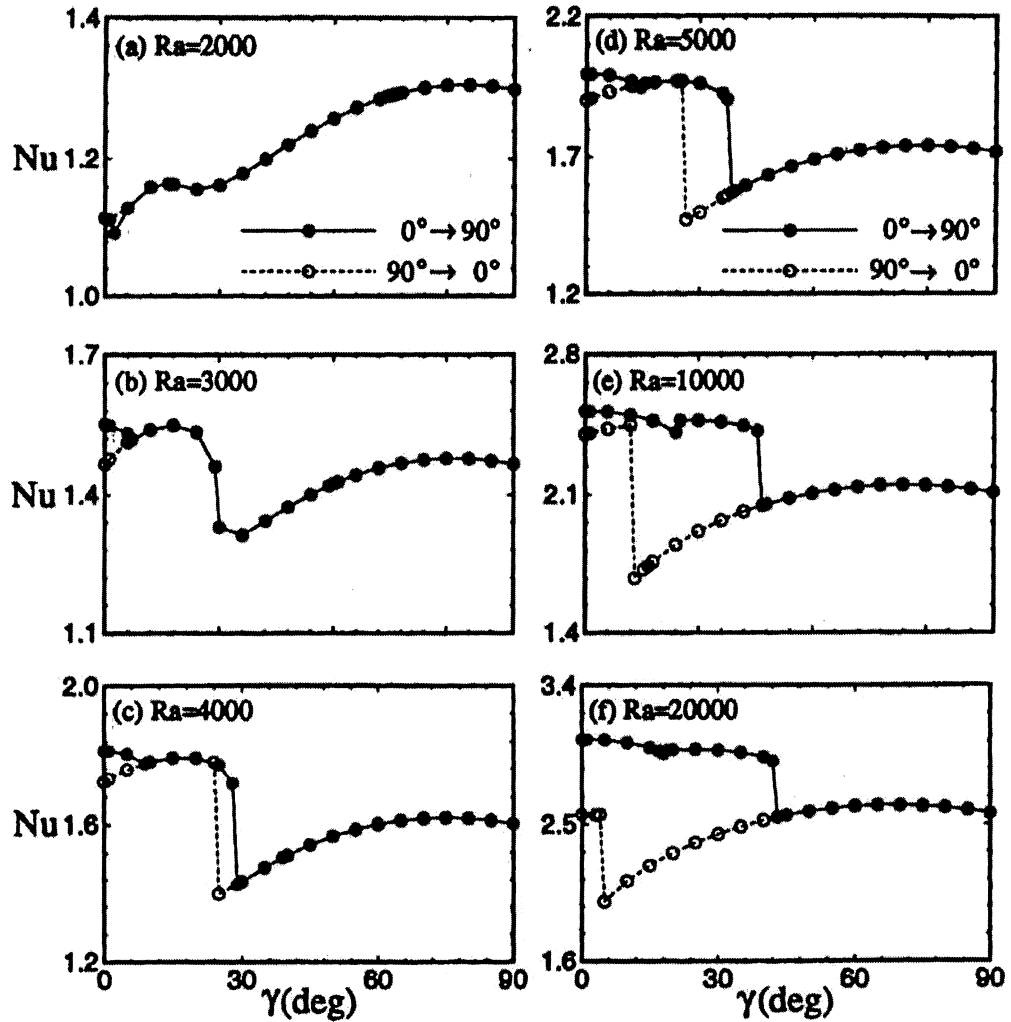


Fig 1.6 Hysteresis phenomenon illustrated by average Nu numbers for Ra number ranged from 2×10^3 to 2×10^4 [21].

1.2.4 Natural convection in irregular-shaped cavities

Although many engineering applications where natural convection plays an important role occur not necessary in regular shaped cavities, only a few numerical or

experimental studies have been carried out considering irregular shaped cavities (i.e., cavities with curved walls).

Lewandowski and Khubeiz [22] experimentally investigated natural convection in glycerine filled cylindrical cavities with various convex and concave bottoms. Ratio of diameter of the hemisphere to diameter of cylinder bottom wall ranged from 0 to 1. Number of convex or concave cells on the bottom varied between 1 and 7. Ra numbers between 10^5 and 10^7 were investigated.

For concave hemispherical bottom with diameter ratio equal to 1, the bottom concavity inhibited fluid flow and motionless flow field dominated both corners between the curved bottom and vertical walls, where heat was transferred only by conduction. With the dead space effect, heat transfer was greatly reduced at these corners, which could be applied to the honey comb cells in solar collectors and insulating cellular material for building engineering. In the case of bottom wall with smaller concavity, free convective flux (flume) would be generated. Heat transfer was enhanced. More concave cells would expectedly increase heat transfer looked like more flumes heating on the bottom, especially for cavity with small height.

Morsi and Das [23] numerically studied natural convection in cavities with dome-shaped top walls. The dome was formulated by circular, elliptical, parabolic, or hyperbolic shapes. Ra numbers ranged between 10^3 and 10^5 , and $Pr = 1.0$. The cavities were heated on the left wall and cooled on the right side wall with two insulated top and bottom walls. Solution has been carried out indicating the effect of the height, shape of the dome and Ra number on the heat transfer and flow patterns. An increase of Ra

number resulted in dominance of the convection, therefore, thicker boundary layer could be observed close to the hot and cold walls. As Ra number further increased, zero or even opposite temperature gradients could be observed in the central of the cavity, which is the same conclusion as in [10]. As Ra number increased, peak horizontal velocity shift to the top of the hot wall and bottom of the cold wall.

When dome shape was replaced with a rectangular cap, heat transfer rate was greatly increased. Increase in the eccentricity of dome would result in decrease of heat transfer rate. As the height of dome was less than 0.3, eccentricity did not affect heat transfer greatly. However, as it was greater than 0.3 at higher Ra number, great difference could be observed in various shapes.

Chen and Cheng [24] numerically and experimentally investigated natural convection in an inclined arc-shape enclosure. The arc-shaped cavity was cooled on the flat top wall and heated on the curved bottom wall. Due to the temperature discontinuity at corners between surfaces with high and low temperature, linear temperature distribution was assumed to avoid temperature discontinuity. However, no details of temperature profile were given at the corner. Grashoff number (Gr) varied from 10^5 to 10^7 . Inclination angle ranged between 0 (curved surface on the bottom) to π . Pr number was kept constant at 0.7. A flow-visualization technique using smoke was applied to observe the flow pattern.

Flow fields produced from numerical simulations were in good agreement with experimental results for various inclination angles from 0 to π at $Gr = 10^5$. Increasing Gr number from 10^4 to 10^5 did not cause too much difference in Nu number. As $Gr > 10^5$,

except at inclination angle equal to π , where the cavity was heated from the top wall, heat transfer rate increased as the developing of Gr number. Except for $Gr \leq 10^5$, heat transfer rate was inversely proportional to the inclination angle.

In light of the above, due to the added effect of cavity irregularity, natural convection heat transfer in irregular cavities has more complex characteristics as compared with in regular cavities. Although natural convection in irregular shaped is more practical, only a few studies have been reported in this field.

1.3 Present work

As indicated in sections 1.2.2 and 1.2.3, Corcoine [12] investigated the effect of various boundary conditions on flow and thermal fields in regular cavities. However, he considered only the case of horizontal, regular, cavities. Soony and Tzeng [21] studied the effect of angle of inclination and initial conditions on mode transition and flow and thermal fields in inclined, regular, cavities. However, they only studied the case of insulated end walls.

In practical applications, end walls may not be perfectly insulated and the cavities may always have some angle of inclination. In addition to that the cavity is not always regular. The main objectives of this study are to investigate the combined effect of:

1. Various thermal conditions of the cavity end walls, Fig1.7.
2. Angle of inclination,
3. Width-to-height aspect ratio.

on flow mode-transition, and hence on the effectiveness of heat transfer in regular-shaped cavities. The intended outcome of such study is developing a better understanding of thermally driven flows under these conditions, which should allow us to control or device heat transfer rates in any desired way by varying the aforementioned parameters.

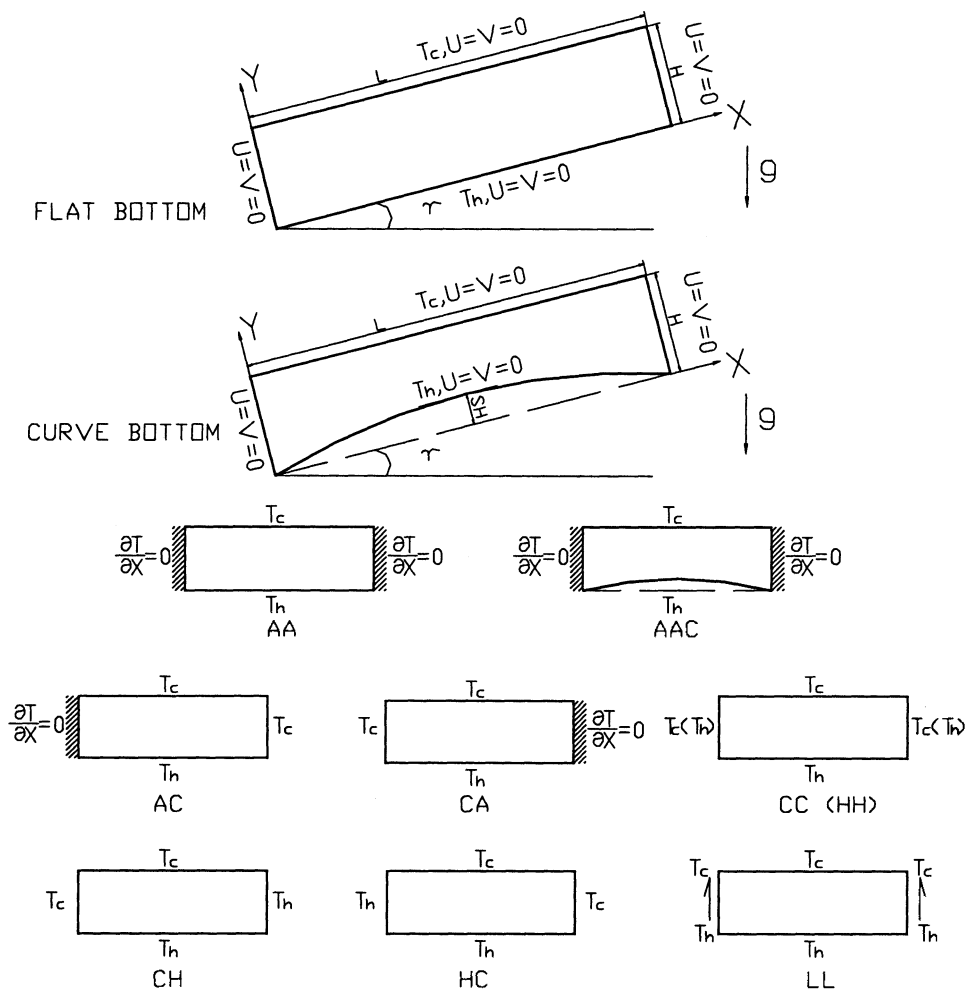


Fig 1.7 Configurations of thermal boundary conditions considered in the present study. In addition to the above three parameters, the present study will also investigate.

In addition to the above three parameters, the present study will also investigate the effect of cavity irregularity on mode-transition and on the resulted flow in inclined

cavities by considering cavities with curved bottoms denoted by configuration AAC in Fig 1.7. In this case only the case of cavity heated from below, cooled on the top with insulated side walls will be investigated. Effect of bottom wall curvature will be investigated by assuming that the shape of the bottom wall is defined by $y = (|x - L/2| + 2)^2 \times SH / 2^2$, where SH is the maximum height at $x = L/2$ as shown in Fig. 1-7. Investigations will be carried out to study the effect of various values of SH, namely, SH = 0.05, 0.25, 0.45, 0.65, and 0.85. Results will be compared with those obtained for the corresponding regular shape cavity, i.e., the AA configuration, shown in Fig. 1.7 as well.

Chapter 2

Mathematical Formulation and Numerical Method

2.1 Problem formulation

Consider a regular-shaped cavity (i.e., having flat walls) of width L and height H as shown in Figure 1.7. The cavity is differentially heated in the vertical direction, i.e., the bottom wall and the top wall are maintained at T_h and T_c , respectively. Depending on the thermal condition of the two end walls, eight configurations are to be considered in the present study, denoted by AAC, AA, AC, CA, CC, CH, HC, HH, and LL, as shown in Fig 1.7.

For all these configurations, the first letter of its name denotes the thermal condition of the left end wall, while the second letter denotes that of the right end wall. A “C” or an “H” is used to denote a wall that is kept insulated or at T_c or T_h , respectively. This naming system is used for all of the eight configurations shown in Fig 1.7, except for the case LL configurations. In the LL configuration, the two end walls are assumed to have linear temperature profiles.

As was outlined in section 1.3, the effect of cavity irregularity on natural convection flows will also be investigated in the present study by considering a cavity with a curved bottom, denoted by AAC configuration in Fig 1.7. In the case of the AAC configuration, the flat bottom wall in AA is replaced with a curved wall while keeping thermal conditions of the two end walls unchanged as in the AA case.

For the case of an inclined cavity, gravity vector has two components:

in X-direction: $g\text{Sin}\gamma$

in Y-direction: $g\text{Cos}\gamma$

The steady, two-dimensional natural convection inside the cavity, assuming constant properties and employing the Boussinesq approximation for the gravity term, is governed by the following set of equations:

Conservation of mass

$$\frac{\partial V}{\partial Y} + \frac{\partial U}{\partial X} = 0 \quad 2.1$$

Momentum equations with Boussinesq assumption:

X – direction:

$$\rho_{\infty} \left(U \frac{\partial U}{\partial X} + V \frac{\partial U}{\partial Y} \right) = \mu \left(\frac{\partial^2 U}{\partial X^2} + \frac{\partial^2 U}{\partial Y^2} \right) - \frac{\partial P}{\partial X} + \rho_{\infty} \beta (T - T_{\infty}) g \text{Sin}\gamma \quad 2.2$$

Y – direction:

$$\rho_{\infty} \left(U \frac{\partial V}{\partial X} + V \frac{\partial V}{\partial Y} \right) = \mu \left(\frac{\partial^2 V}{\partial X^2} + \frac{\partial^2 V}{\partial Y^2} \right) - \frac{\partial P}{\partial Y} - \rho_{\infty} \beta (T - T_{\infty}) g \text{Cos}\gamma \quad 2.3$$

Energy equation:

$$\rho_{\infty} c_p \left(U \frac{\partial T}{\partial X} + V \frac{\partial T}{\partial Y} \right) = k \left(\frac{\partial^2 T}{\partial X^2} + \frac{\partial^2 T}{\partial Y^2} \right) \quad 2.4$$

Dimensionless variables are defined by:

$$x = \frac{X}{H}, \quad y = \frac{Y}{H}$$

$$u = \frac{U}{V}, \quad v = \frac{V}{V}, \quad \theta = \frac{T - T_c}{T_h - T_c}$$

$$p = \frac{P}{\rho_{\infty} \left(\frac{v}{H}\right)^2}$$

$$A = \frac{L}{H} \tag{2.5}$$

Substituting dimensionless variables defined in 2.5 in equations 2.1-2.4 results in the following set of dimensionless equations:

Non-dimensional continuity equation:

$$\frac{\partial v}{\partial y} + \frac{\partial u}{\partial x} = 0 \tag{2.6}$$

Non-dimensional momentum equations with Boussinesq assumption:

x – direction:

$$u \frac{\partial u}{\partial x} + v \frac{\partial u}{\partial y} = -\frac{\partial p}{\partial x} + \left(\frac{\partial^2 u}{\partial x^2} + \frac{\partial^2 u}{\partial y^2} \right) + Ra \times \frac{1}{Pr} \times \theta \times \sin \gamma \tag{2.7}$$

y – direction:

$$u \frac{\partial v}{\partial x} + v \frac{\partial v}{\partial y} = -\frac{\partial p}{\partial y} + \left(\frac{\partial^2 v}{\partial x^2} + \frac{\partial^2 v}{\partial y^2} \right) - Ra \times \frac{1}{Pr} \times \theta \times \cos \gamma \tag{2.8}$$

Non-dimensional energy equation:

$$u \frac{\partial \theta}{\partial x} + v \frac{\partial \theta}{\partial y} = \frac{1}{Pr} \left(\frac{\partial^2 \theta}{\partial x^2} + \frac{\partial^2 \theta}{\partial y^2} \right) \tag{2.9}$$

The above set of dimensionless equations 2.6-2.9 is subject to the following set of boundary condition:

Velocity condition:

x=0 and A, u=0, v=0;

$y=0$ and 1 , $u=0$, $v=0$.

Thermal condition:

Horizontal walls for all cases: $y=0, \theta=1$; $y=1, \theta=0$;

As for vertical walls:

AA: $x=0, \frac{\partial \theta}{\partial x} = 0$; $x=A, \frac{\partial \theta}{\partial x} = 0$.

CH: $x=0, \theta=0$; $x=A, \theta=1$.

AC: $x=0, \frac{\partial \theta}{\partial x} = 0$; $x=A, \theta=0$.

CA: $x=0, \theta=0$; $x=A, \frac{\partial \theta}{\partial x} = 0$.

CC: $x=0, \theta=0$; $x=A, \theta=0$.

HC: $x=0, \theta=1$; $x=A, \theta=0$.

LL: $x=0, \theta=0-1$; $x=A, \theta=0-1$. (Linear distribution from 1 on the bottom to 0 on the top)

AAC: no slip condition for all walls.

Left and right end walls were insulated; Top wall is cooled and curved bottom wall is heated

2.2 Numerical algorithm:

The numerical algorithm used in the present study was developed based on the well known SIMPLE algorithm proposed by Patankar [25].

Dimensionless equations 2.6 – 2.9 can be written in the following general form:

$$\frac{\partial(\rho\phi)}{\partial t} + \text{div}(\rho\phi u) = \text{div}(\Gamma \text{grad}\phi) + S_\phi \tag{2.10}$$

where ϕ represents a general independent variable. Γ is a general diffusion coefficient, and S_ϕ is a general source term. Values of ϕ , Γ , and S_ϕ based on the corresponding governing equation that equation 2.10 represents are listed in Table 2.1.

Table 2.1 Coefficients for variables in general integral governing equation 2.10.

Equation	ϕ	Γ	S_ϕ
Continuity	1	1	0
x-Momentum	u	1	$-\frac{\partial p}{\partial x} + Ra \times \frac{1}{Pr} \times \theta \times \text{Sin}\gamma$
y-Momentum	v	1	$-\frac{\partial p}{\partial y} - Ra \times \frac{1}{Pr} \times \theta \times \text{Cos}\gamma$
Energy	θ	$\frac{1}{Pr}$	0

Integrating equation 2.10 over a general control volume gives:

$$\int_{cv} \frac{\partial(\rho\phi)}{\partial t} dV + \int_A \bar{n} \cdot (\rho\phi u) dA = \int_A \bar{n} \cdot (\Gamma \text{grad}\phi) dA + \int_{cv} S_\phi dV \tag{2.11}$$

A staggered grid shown in Fig. 2.1 below is employed in the SIMPLE algorithm to couple the two momentum equations and the continuity equation. Solid lines in Fig. 2.1 represent grids used for temperature θ and pressure p, while dash lines represent grids used for calculating velocity components u and v.

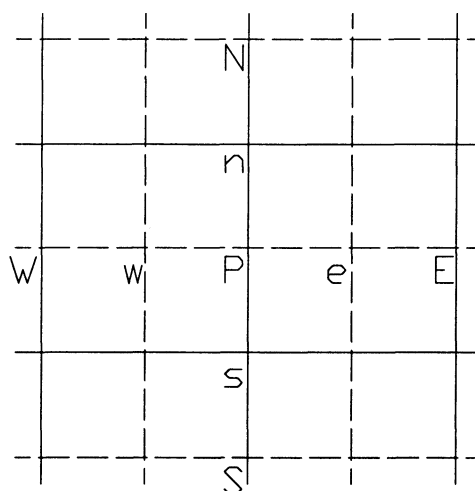


Fig 2.1 Staggered grids used to calculate all independent variables.

The computer program used to solve the above problem is based on finite volume method developed by Patankar [25], which is based on the discretization of the governing equations using central differencing in space. The discretized equations were solved by using the Gauss-Seidel method. The iteration method used in this program is a line by line procedure, which is a combination of the direct method and the resulting Tri Diagonal Matrix Algorithm (TDMA). The procedure used by Patankar is to solve simultaneously the continuity and momentum equations and then the energy equation. The iteration is stopped according to a certain criteria as will be discussed later. Figure 2.2 shows an outline of the iterative procedure used in the SIMPLE algorithm.

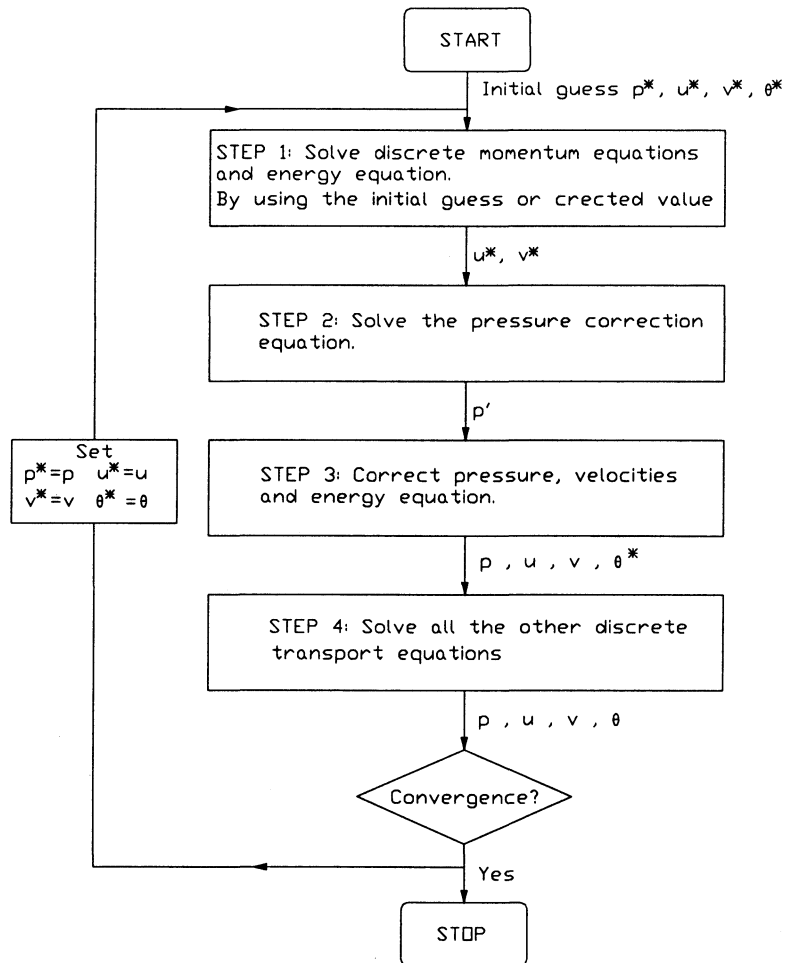


Fig 2.2 Iterative procedure of the SIMPLE algorithm.

2.3 Convergence criterion

Iterative procedure outlined in Fig 2.2 was regarded converged when the maximum difference in all independent variables and the maximum deviation in the average Nu number between two successive iterations, was less than 10^{-5} .

2.4 Grid dependence check

Although, non-uniform grids are normally preferred to be used since they allow one to use substantially fewer grid points, it was difficult to determine appropriate arrangements of any non-uniform grids before solving each case. This difficulty arises due to complex and variable structures of the calculated flow and thermal fields. Multi modes were expected for different configurations and at various inclination angles besides that, mode transition was expected to take place at various unknown angles of inclination. Due to this difficulty, uniform grids were used in all calculations performed in the present study.

In order to minimize calculation time, number of grid points used should be reduced as much as possible. However, using fewer grid points reduces the accuracy of the results. The main purpose of carrying out a grid dependence test is to achieve a reasonable balance between these two conflicting factors and to make sure that results do not depend on the number of grid points.

If n is the number of grid points used in the y -direction, $n \times A$ grid points were used in the x -direction for flat bottom case. For curved bottom, both x and y direction used n as grid number. The grid dependence test is performed by carrying out several runs considering the same set of parameters and only increasing the number of grid points “ n ” by 20 in each consecutive. For example, starting with $n = 50$ in the first run, $n = 70$ would be used in the next run, and so on. The appropriate number of grid points was determined by comparing results obtained from several runs and confirming that the

difference between calculated values of all independent variables and calculated average Nu numbers obtained from two consecutive runs were less than 1%. In other words,

$$\frac{|\phi_{m+1} - \phi_m|}{|\phi_{m+1}|} < 1\% \quad \text{and} \quad \frac{|Nu_{m+1} - Nu_m|}{|Nu_{m+1}|} < 1\% \quad 2.12$$

where ϕ stands for u, v, p, and θ and m is an index indicating run number. If conditions in equation 2.12 were satisfied, grid used in run number m was regarded appropriate and was used for all further calculations.

For thermal convection problems grid density depends strongly on the Ra number. For an inclined enclosure, it also depends on flow patterns, which depend strongly on the angle of inclination. A grid check was performed for the cases of $Ra = 10^4$ and for all thermal boundary conditions considering four different angles of inclination at $\gamma = 0, 30, 60$ and 90° .

Results shown in Tables 2.2 and 2.3 indicate that using $n = 60/\text{unit}$ was appropriate for the AA, CA, CC, CH, and HC configurations, while more grid points were needed for the AC and LL at which case $n = 80/\text{unit}$ was needed. For the case of the AAC configuration, even more grid points had to be used in order to resolve the curved bottom. $n = 140$ was used in that case to also satisfy energy conservation, which will be discussed below.

Table 2.2 Grid dependence check for different thermal boundary conditions (a). AA configuration, - 62X242; (b). AC configuration, - 82X322; (c). CA configuration – 62X42; (d). CC configuration, - 62X242.

a(AA)

Value for the Grid Check										Difference Between the Grids in same angle %								
Angle	Grid	Nu-left	Nu-right	Nu-top	Nu-bottom	Umax	Vmax	Wmax	$(Q_{wall})_{Q_{wall}}$	Nu-left	Nu-right	Nu-top	Nu-bottom	Umax	Vmax	Wmax		
0	22X 82	0.00	0.00	2.545	2.546	44.068	38.375	12.032	0.915					0.292	0.307	-2.177	-3.291	-1.715
30	22X 82	0.00	0.00	2.461	2.461	37.805	58.872	15.717	0.005					26.006	26.011	88.657	-14.616	-16.113
60	22X 82	0.00	0.00	2.167	2.168	22.194	70.481	22.108	0.005					0.969	0.974	1.361	-1.482	0.459
90	22X 82	0.00	0.00	2.141	2.141	20.429	68.189	21.479	0.020					1.019	1.028	1.314	-1.434	0.501
0	42X162	0.00	0.00	2.536	2.536	45.069	38.681	12.242	-0.001					0.051	0.051	-0.232	-0.427	-0.407
30	42X162	0.00	0.00	1.977	1.977	19.933	58.590	18.736	0.000					-20.246	-20.246	-47.435	14.502	19.183
60	42X162	0.00	0.00	2.147	2.147	21.896	71.541	22.008	0.000					0.182	0.182	0.252	0.057	0.073
90	42X162	0.00	0.00	2.119	2.119	20.164	70.175	21.372	0.000					0.189	0.189	0.229	-0.083	0.075
0	82X322	0.00	0.00	2.537	2.537	45.174	38.851	12.282	0.000					0.820	0.820	-8.144	-8.419	-8.154
30	82X322	0.00	0.00	2.478	2.478	37.821	52.834	15.723	0.000					0.816	0.820	0.813	-8.190	8.886
60	82X322	0.00	0.00	2.143	2.143	21.841	71.590	21.982	0.000					0.865	0.865	0.868	-8.182	8.818
90	82X322	0.00	0.00	2.115	2.115	20.118	70.249	21.338	0.000					0.868	0.868	0.868	8.876	8.828
0	82X322	0.00	0.00	2.536	2.536	45.228	40.915	12.311	0.000					0.012	0.012	-0.002	-0.082	-0.089
30	82X322	0.00	0.00	2.478	2.478	37.916	52.966	15.722	0.000					0.012	0.008	0.013	0.913	0.032
60	82X322	0.00	0.00	2.141	2.141	21.828	71.573	21.988	0.002					0.028	0.028	0.041	-0.854	0.009
90	82X322	0.00	0.00	2.114	2.114	20.108	70.187	21.350	0.001					0.028	0.033	0.045	-0.873	0.009
0	102X402	0.00	0.00	2.536	2.536	45.240	40.948	12.322	0.000					0.008	0.008	-0.022	-0.872	-0.841
30	102X402	0.00	0.00	2.478	2.478	37.911	52.879	15.717	0.000					0.004	0.004	0.004	-8.151	-0.040
60	102X402	0.00	0.00	2.141	2.141	21.819	71.587	21.986	-0.002					0.014	0.019	0.028	0.021	0.009
90	102X402	0.00	0.00	2.113	2.113	20.097	70.238	21.348	-0.002					0.019	0.014	0.040	-8.004	0.005
0	122X482	0.00	0.00	2.536	2.536	45.250	40.977	12.327	0.000									
30	122X482	0.00	0.00	2.478	2.478	37.879	52.158	15.734	-0.001									
60	122X482	0.00	0.00	2.140	2.140	21.813	71.582	21.984	-0.002									
90	122X482	0.00	0.00	2.113	2.113	20.089	70.241	21.347	0.002									

b(AC)

Value for the Grid Check										Difference Between the Grids in same angle %									
Angle	Grid	Nu-left	Nu-right	Nu-top	Nu-bottom	Umax	Vmax	Wmax	$(Q_{wall})_{Q_{wall}}$	Nu-left	Nu-right	Nu-top	Nu-bottom	Umax	Vmax	Wmax			
0	22X 82	0.00	2.428	2.510	3.100	44.600	41.200	12.900	-0.287					-0.412	0.400	0.000	-2.193	-3.286	-1.527
30	22X 82	0.00	2.430	2.100	2.700	28.800	56.500	17.800	-0.280					0.478	0.478	0.000	0.752	-1.224	0.565
60	22X 82	0.00	3.340	1.810	2.640	22.400	68.800	21.800	-8.184					-0.290	0.558	0.380	1.357	-1.690	0.000
90	22X 82	0.00	4.400	1.570	2.670	28.800	72.900	22.000	-0.068					0.000	0.641	0.376	1.132	-1.486	0.444
0	42X162	0.00	2.420	2.500	3.100	45.600	42.600	13.100	-8.141					0.413	0.000	-0.322	-0.219	-0.467	-0.758
30	42X162	0.00	2.440	2.080	2.700	28.600	57.200	17.700	-8.146					0.412	0.000	0.000	0.377	0.000	0.000
60	42X162	0.00	3.350	1.800	2.630	22.100	71.000	21.800	-8.120					0.000	0.559	0.000	0.465	0.000	0.461
90	42X162	0.00	4.400	1.590	2.660	28.500	74.000	22.500	-0.082					0.000	0.000	0.377	0.379	0.000	0.000
0	82X322	0.00	2.420	2.500	3.110	45.700	42.800	13.200	-8.089					0.000	0.000	0.000	0.000	-0.465	0.000
30	82X322	0.00	2.430	2.080	2.700	28.500	57.200	17.700	-0.068					-5.647	-11.814	-10.299	-35.680	16.260	19.595
60	82X322	0.00	3.350	1.790	2.620	22.000	71.000	21.700	-8.085					0.299	0.000	0.000	0.000	-0.141	0.000
90	82X322	0.00	4.400	1.580	2.650	28.400	74.000	22.500	-0.072					0.000	0.000	0.000	0.380	0.000	0.448
0	82X322	0.00	2.428	2.508	3.118	45.700	43.800	13.200	-8.884					0.888	0.888	0.888	0.888	0.888	0.888
30	82X322	0.00	2.578	2.378	3.018	41.200	48.200	14.800	-8.882					0.888	0.888	0.888	0.888	0.888	0.888
60	82X322	0.00	3.348	1.798	2.638	22.800	71.900	21.700	-8.883					0.888	0.888	0.888	0.888	0.888	0.888
90	82X322	0.00	4.408	1.588	2.668	28.300	74.800	22.400	-8.887					0.888	0.888	0.888	0.888	0.888	0.888
0	102X402	0.00	2.428	2.500	3.118	45.700	43.000	13.200	-8.049					0.000	0.000	0.000	0.000	-0.232	0.000
30	102X402	0.00	2.578	2.378	3.018	41.200	48.200	14.800	-8.048					0.000	0.000	0.000	0.243	0.204	0.000
60	102X402	0.00	3.340	1.790	2.630	22.000	71.100	21.700	-8.050					0.000	0.000	0.000	0.000	0.000	0.000
90	102X402	0.00	4.400	1.580	2.650	28.300	74.000	22.400	-8.046					0.000	0.000	0.000	0.000	-0.135	0.000
0	122X482	0.00	2.428	2.500	3.118	45.700	43.100	13.200	-8.048										
30	122X482	0.00	2.578	2.378	3.018	41.100	48.100	14.800	-8.048										
60	122X482	0.00	3.340	1.790	2.630	22.000	71.100	21.700	-8.041										
90	122X482	0.00	4.400	1.580	2.650	28.300	74.100	22.400	-8.037										

c(CA)

Value for the Grid Check										Difference Between the Grids in same angle %									
Angle	Grid	Nu-left	Nu-right	Nu-top	Nu-bottom	Umax	Vmax	Wmax	$(Q_{wall})_{Q_{wall}}$	Nu-left	Nu-right	Nu-top	Nu-bottom	Umax	Vmax	Wmax			
0	22X 82	2.428	0.000	2.510	3.100	44.600	41.200	12.900	-0.287					-0.412	0.400	0.000	-2.193	-3.286	-1.527
30	22X 82	2.170	0.000	2.460	2.980	37.900	51.000	15.800	-0.539					13.021	24.873	22.041	78.774	-14.286	-15.508
60	22X 82	1.860	0.000	2.150	2.610	22.200	70.200	22.000	-0.403					-1.587	0.939	0.385	1.370	-1.404	0.457
90	22X 82	1.860	0.000	2.120	2.570	20.200	68.700	21.300	-0.406					-1.587	1.435	0.391	0.468	-1.285	0.472
0	42X162	2.430	0.000	2.500	3.100	45.600	42.600	13.100	-8.141					0.413	0.000	-0.322	-0.219	-0.467	-0.758
30	42X162	1.920	0.000	1.970	2.450	21.200	58.500	18.700	-8.193					-19.592	-18.080	-44.646	13.985	18.354	10.000
60	42X162	1.890	0.000	2.130	2.600	21.900	71.200	21.800	-8.187					0.000	0.000	0.000	0.000	0.000	0.000
90	42X162	1.890	0.000	2.090	2.560	20.100	69.800	21.200	-8.187					0.000	0.000	0.000	-0.143	0.000	0.000
0	82X322	2.438	0.000	2.598	3.118	45.700	42.800	13.200	-8.089					0.888	0.888	0.888	-8.485	8.888	0.888
30	82X322	2.198	0.000	2.458	2.998	38.300	52.900	15.800	-8.888					0.888	0.888	0.888	0.888	0.888	0.888
60	82X322	1.898	0.000	2.138	2.608	21.800	71.300	21.988	-8.115					0.888	0.888	0.888	0.888	0.888	0.888
90	82X322	1.898	0.000	2.098	2.568	20.000	69.700	21.388	-8.116					0.888	0.888	0.888	8.144	8.888	0.888
0	82X322	2.430	0.000	2.500	3.110	45.700	43.000	13.200	-8.884					0.000	0.000	0.000	0.000	0.000	0.000
30	82X322	2.190	0.000	2.450	2.990	38.300	52.900	15.800	-8.888					0.000	0.000	0.000	0.000	0.000	0.000
60	82X322	1.890	0.000	2.130	2.600	21.900	71.200	21.900	-8.079					0.472	0.386	0.000	-8.140	0.000	0.000
90	82X322	1.890	0.000	2.090	2.560	20.100	69.800	21.200	-8.080					0.000	0.000	0.000	-8.143	0.000	0.000
0	102X402	2.428	0.000	2.500	3.118	45.700	43.000	13.200	-8.049					0.000	0.000	0.000	-8.232	0.000	0.000
30	102X402	2.190																	

Table 2.3 Grid dependence check for different thermal boundary conditions
 (a). CH configuration, - 62X242; (b). HC configuration, - 62X242; (c). LL configuration, - 82X322; (d). AAC configuration, - 142X142.

a (CH)

Value for the Grid Check										Difference Between the Grids in same angle %									
Angle	Grid	No-left	No-right	No-top	No-bottom	Umax	Vmax	Wmax	$Q_{tot}/Q_{tot,s}$	No-left	No-right	No-top	No-bottom	Umax	Vmax	Wmax			
0	22X 82	2.520	2.310	2.950	2.960	38.500	43.800	13.700	0.005	-0.420	-0.858	-0.338	0.000	0.000	-2.242	-0.725			
30	22X 82	1.900	1.800	2.450	2.450	21.000	58.400	18.800	0.005	-13.626	-14.480	-17.220	-17.220	-43.806	14.804	18.745			
60	22X 82	1.870	1.870	2.580	2.580	21.800	66.700	21.800	-0.002	-1.950	-1.858	0.388	0.388	1.380	-1.554	0.458			
90	22X 82	1.870	1.880	2.550	2.540	18.100	68.000	21.900	-0.008	-1.050	-1.053	0.394	0.395	1.596	-1.306	0.476			
0	42X162	2.520	2.230	2.960	2.960	38.500	44.000	13.800	0.001	0.000	0.000	0.000	0.000	0.000	-0.224	-0.719			
30	42X162	2.200	2.210	2.960	2.960	38.500	51.700	15.700	0.000	0.000	0.000	0.000	0.000	0.000	-0.365	0.000			
60	42X162	1.890	1.890	2.580	2.580	21.800	70.800	21.800	0.000	0.000	0.000	0.000	0.000	0.465	0.000	0.000			
90	42X162	1.890	1.920	2.540	2.530	18.800	69.300	21.000	-0.001	0.000	0.000	0.395	0.395	0.535	-1.145	0.000			
0	62X242	2.520	2.320	2.960	2.960	38.500	44.700	13.900	0.000	0.000	0.000	0.000	0.000	0.000	-0.223	0.000			
30	62X242	2.280	2.210	2.960	2.960	38.500	51.900	15.700	0.000	0.000	0.000	0.000	0.000	0.000	-0.182	0.000			
60	62X242	1.890	1.890	2.580	2.580	21.800	70.800	21.800	0.000	0.000	0.000	0.000	0.000	0.000	0.000	0.000			
90	62X242	1.890	1.900	2.530	2.530	18.700	69.800	21.000	0.000	0.000	0.000	0.000	0.000	0.000	0.000	0.000			
0	82X322	2.520	2.320	2.960	2.960	38.500	44.800	13.900	0.000	0.000	0.000	0.000	0.000	0.000	0.000	0.000			
30	82X322	2.200	2.200	2.960	2.960	38.500	52.000	15.700	0.000	0.000	0.000	-0.337	0.000	0.000	0.000	0.000			
60	82X322	1.890	1.890	2.580	2.580	21.500	70.800	21.800	0.001	0.000	0.000	0.000	0.000	0.000	-0.141	0.000			
90	82X322	1.890	1.900	2.530	2.530	18.700	69.000	21.000	0.001	0.000	0.000	0.000	0.000	0.000	0.000	0.000			
0	102X402	2.520	2.320	2.960	2.960	38.500	44.900	13.900	0.000	0.000	0.000	0.000	0.000	0.000	0.000	0.000			
30	102X402	2.220	2.200	2.970	2.960	38.500	52.000	15.700	0.000	0.000	0.000	0.000	0.000	0.000	0.000	0.000			
60	102X402	1.890	1.890	2.580	2.580	21.500	70.900	21.800	0.000	0.000	0.000	0.000	0.000	0.000	0.141	0.000			
90	102X402	1.890	1.900	2.530	2.530	18.700	69.000	21.000	0.000	0.000	0.000	0.000	0.000	0.000	0.000	0.000			
0	122X482	2.520	2.320	2.960	2.960	38.500	44.900	13.900	0.000	0.000	0.000	0.000	0.000	0.000	0.000	0.000			
30	122X482	2.200	2.200	2.970	2.960	38.500	52.000	15.700	0.000	0.000	0.000	0.000	0.000	0.000	0.000	0.000			
60	122X482	1.890	1.890	2.580	2.580	21.500	70.900	21.800	-0.002	0.000	0.000	0.000	0.000	0.000	0.000	0.000			
90	122X482	1.890	1.900	2.530	2.530	18.700	69.000	21.000	0.002	0.000	0.000	0.000	0.000	0.000	0.000	0.000			

b (HC)

Value for the Grid Check										Difference Between the Grids in same angle %									
Angle	Grid	No-left	No-right	No-top	No-bottom	Umax	Vmax	Wmax	$Q_{tot}/Q_{tot,s}$	No-left	No-right	No-top	No-bottom	Umax	Vmax	Wmax			
0	22X 82	2.318	2.320	2.950	2.960	38.500	43.800	13.700	0.005	-0.828	-0.428	-0.338	0.000	-2.242	-0.725				
30	22X 82	2.480	2.500	2.750	2.750	33.100	52.800	16.500	0.002	-0.402	0.000	-0.362	-0.362	-0.301	-0.037	0.000			
60	22X 82	3.380	3.380	2.280	2.280	22.300	69.100	21.600	0.002	-0.287	-0.287	0.441	0.441	1.828	-1.847	0.000			
90	22X 82	4.420	4.410	2.100	2.100	26.500	75.400	23.500	0.006	0.228	0.000	0.000	0.478	1.145	-1.567	0.027			
0	42X162	2.520	2.230	2.960	2.960	38.500	44.000	13.800	0.001	0.000	0.000	0.000	0.000	0.000	-0.224	-0.719			
30	42X162	2.480	2.500	2.760	2.760	33.200	54.000	16.500	0.000	0.000	0.000	0.000	0.000	0.000	-0.380	0.000			
60	42X162	3.378	3.378	2.278	2.278	21.900	70.400	21.600	0.000	0.000	0.000	0.000	0.000	0.000	0.000	0.000			
90	42X162	4.428	4.418	2.100	2.080	26.200	76.000	23.400	0.001	0.227	0.000	0.478	0.000	0.000	0.000	0.000			
0	62X242	2.520	2.320	2.960	2.960	38.500	44.700	13.900	0.000	0.000	0.000	0.000	0.000	0.000	-0.223	0.000			
30	62X242	2.480	2.500	2.760	2.760	33.200	54.200	16.500	0.000	0.000	0.000	0.000	0.000	0.000	0.000	0.000			
60	62X242	3.378	3.378	2.278	2.278	21.900	70.500	21.500	0.000	0.000	0.000	0.000	0.000	0.000	0.000	0.000			
90	62X242	4.418	4.418	2.080	2.080	26.300	76.600	23.400	0.001	0.000	0.227	0.000	0.000	0.380	0.000	0.000			
0	82X322	2.520	2.320	2.960	2.960	38.500	44.800	13.900	0.000	0.000	0.000	0.000	0.000	0.000	0.000	0.000			
30	82X322	2.480	2.490	2.760	2.760	33.200	54.200	16.500	-0.001	0.000	0.000	0.000	0.000	0.000	0.000	0.000			
60	82X322	3.378	3.378	2.278	2.278	21.900	70.400	21.500	0.000	0.000	0.000	0.000	0.000	0.459	-0.142	0.000			
90	82X322	4.418	4.400	2.080	2.080	26.100	76.000	23.400	0.001	0.000	-0.227	0.000	0.000	0.000	0.000	0.000			
0	102X402	2.520	2.320	2.960	2.960	38.500	44.900	13.900	0.000	0.000	0.000	0.000	0.000	0.000	0.000	0.000			
30	102X402	2.480	2.490	2.760	2.760	33.200	54.200	16.500	-0.001	0.000	0.000	0.000	0.000	0.000	0.000	0.000			
60	102X402	3.378	3.378	2.278	2.278	21.800	70.500	21.500	0.000	0.000	0.000	0.000	0.000	0.000	0.000	0.000			
90	102X402	4.418	4.418	2.080	2.080	26.100	76.600	23.400	0.002	0.000	0.000	0.000	0.000	0.000	0.000	0.000			
0	122X482	2.520	2.320	2.960	2.960	38.500	44.900	13.900	0.000	0.000	0.000	0.000	0.000	0.000	0.000	0.000			
30	122X482	2.480	2.490	2.760	2.760	33.200	54.200	16.500	-0.002	0.000	0.000	0.000	0.000	0.000	0.000	0.000			
60	122X482	3.378	3.378	2.278	2.278	21.800	70.500	21.500	-0.001	0.000	0.000	0.000	0.000	0.000	0.000	0.000			
90	122X482	4.418	4.418	2.080	2.080	26.100	76.600	23.400	-0.003	0.000	0.000	0.000	0.000	0.000	0.000	0.000			

c (LL)

Value for the Grid Check										Difference Between the Grids in same angle %									
Angle	Grid	No-left	No-right	No-top	No-bottom	Umax	Vmax	Wmax	$Q_{tot}/Q_{tot,s}$	No-left	No-right	No-top	No-bottom	Umax	Vmax	Wmax			
0	22X 82	1.917	1.917	1.810	2.508	43.089	38.025	12.082	0.871	-7.422	-7.427	0.124	-0.713	-2.332	-3.824	-2.216			
30	22X 82	1.738	2.441	1.810	1.794	18.415	58.105	18.854	-0.005	3.724	-0.919	0.993	0.586	1.387	-0.408	0.452			
60	22X 82	3.158	4.710	1.916	1.918	21.919	71.721	22.483	0.000	1.484	2.274	0.752	0.794	1.708	-1.454	0.447			
90	22X 82	3.641	5.866	1.895	1.887	26.229	71.918	22.438	-0.001	1.875	2.648	0.696	0.754	1.578	-1.695	0.547			
0	42X162	2.071	2.071	2.178	2.524	44.118	38.537	12.365	0.819	-1.858	-1.858	-0.037	-0.221	-4.595	-0.768	-0.531			
30	42X162	1.876	2.411	1.792	1.794	18.163	58.346	18.870	0.000	-34.175	-38.859	-21.362	-21.677	-51.478	14.402	18.742			
60	42X162	3.112	4.805	1.902	1.902	21.551	72.778	22.383	-0.001	0.167	0.316	0.147	0.153	0.619	-0.067	0.072			
90	42X162	3.574	5.528	1.882	1.883	23.853	73.137	22.317	-0.001	0.174	0.344	0.138	0.154	0.511	-0.022	0.065			
0	62X242	2.118	2.118	2.178	2.520	44.342	38.643	12.432	0.800	-0.846	-0.846	-0.023	-0.111	-0.274	-0.480	-0.233			
30	62X242	2.545	3.502	2.279	2.278	37.428	55.639	18.009	0.005	-0.023	0.018	0.009	0.021	-0.117	0.006				
60	62X242	3.107	4.981	1.889	1.890	21.485	72.739	22.387	0.001	0.005	0.009	0.047	0.058	0.161	-0.125	0.018			
90	62X242	3.567	5.501	1.889	1.889	23.778	73.153	22.298	0.000	0.028	0.087	0.048	0.059	0.156	-0.067	0.027			
0	82X322	2.128	2.128	2.178	2.522	44.464	38.887	12.481	0.805	-0.846	-0.846	-0.013	-0.063	-0.398	-0.118	-0.128			
30	82X322	2.545	3.503	2.278	2.277	37.418	55.638	18.009	0.000	-0.008	0.013	-0.004	-0.003	-0.067	-0.064				
60	82X322	3.106	4.987	1.889	1.889	21.472	72.823	22.383	-0.001	0.010	0.026	0.021	0.026	0.042	-0.095	0.009			
90	82X322	3.566	5.486	1.879	1.879	23.742	73.184	22.282	0.000	-0.006	0.035	0.021	0.027	0.191	-0.107	0.009			
0	102X402	2.128	2.128	2.178	2.524	44.504	38.971</												

2.5 Energy balance test

The difference in energy balance of the whole cavity was calculated from:

$$Q_{error} = \left| \frac{|Q_{out}| - |Q_{in}|}{\text{Min}(|Q_{out}|, |Q_{in}|)} \right| \quad 2.13$$

and $Q_{error} < 1.5\%$ was regarded as an additional condition required to consider the procedure convergent and the grid size used appropriate.

2.6 Relaxation factors

Convergence of the iterative procedure outlined in Fig 2.2 above can be speeded up by an over-relaxation factor, or slowed down, by an under-relaxation factor. Values of these relaxation factors are usually different for each independent variable and normally depend on the nature of the problem.

In all cases considered in the present study, under-relaxation factors were used. For Ra numbers less or equal to 5000, 0.4 was used as relaxation factor for velocities, pressure, and temperature. However, for $Ra=10^4$ and $A=4$, convergence for some configurations, such as AC, CC, and HC, was more difficult to achieve. Under-relaxation factors equal to 0.1 were used for these cases.

2.7 Calculation of Nu number for cavity with flat bottom

Nu number is derived from the following condition:

$$\text{x - direction} \quad h(\theta_w - \theta_\infty) \cdot \text{area} = k \frac{\Delta\theta}{\Delta y} \Big|_{\text{wall}} \cdot \text{area} \quad 2.14$$

$$y - \text{direction} \quad h(\theta_w - \theta_\infty) \cdot \text{area} = k \left. \frac{\Delta\theta}{\Delta x} \right|_{\text{wall}} \cdot \text{area} \quad 2.15$$

And Nu number is defined as:

$$Nu \Big|_x = \left| \frac{h \cdot l}{k} \right|$$

Here, $l = \frac{L}{L} = 1$, from Equations 2.14 and 2.15 local Nu number can be calculated from:

$$Nu_x = \frac{h \cdot 1}{k} = \frac{\theta_{nwall} - \theta_{wall}}{y_2 - y_1} \Big|_{\text{wall}} \cdot \frac{1}{(\theta_{wall} - \theta_\infty)} \quad 2.16$$

$$Nu_y = \frac{h \cdot 1}{k} = \frac{\theta_{nwall} - \theta_{wall}}{x_2 - x_1} \Big|_{\text{wall}} \cdot \frac{1}{(\theta_{wall} - \theta_\infty)} \quad 2.17$$

Here θ_{nwall} is the temperature at a node next to the wall.

Assuming unit distance in the z-direction, rate of heat transfer can be calculated from:

$$x\text{-direction:} \quad Q \Big|_{\text{wall-x}} = h \cdot (\theta_{wall} - \theta_\infty) \cdot 1 \cdot A \quad 2.18$$

$$y\text{-direction:} \quad Q \Big|_{\text{wall-y}} = h \cdot (\theta_{wall} - \theta_\infty) \cdot 1 \cdot 1 \quad 2.19$$

From equations 2.16 and 17 into equations 2.18 and 19

$$Q \Big|_{\text{wall-x}} = \frac{\theta_{nwall} - \theta_{wall}}{y_2 - y_1} \Big|_{\text{wall}} \cdot A \cdot k \quad 2.20$$

$$Q \Big|_{\text{wall-y}} = \frac{\theta_{nwall} - \theta_{wall}}{x_2 - x_1} \Big|_{\text{wall}} \cdot k \quad 2.21$$

In case where $\theta_{wall} = 1$ θ_∞ is taken as 0. When $\theta_{wall} = 0$, θ_∞ is taken as 1. Accordingly, equations 2.16, 17, 20 and 21 can be simplified as,

$$Nu \Big|_x = \left| \frac{\theta_{nwall} - \theta_{wall}}{y_2 - y_1} \right|_{wall} \quad 2.22$$

$$Nu \Big|_y = \left| \frac{\theta_{nwall} - \theta_{wall}}{x_2 - x_1} \right|_{wall} \quad 2.23$$

$$Q \Big|_{wall-x} = \left| \frac{\theta_{nwall} - \theta_{wall}}{y_2 - y_1} \right|_{wall} \cdot A \cdot k \quad 2.24$$

$$Q \Big|_{wall-y} = \left| \frac{\theta_{nwall} - \theta_{wall}}{x_2 - x_1} \right|_{wall} \cdot k \quad 2.25$$

When the end wall is assumed having a linear temperature profile (i.e., θ at the wall varies from 1 to 0), θ_{wall} is not constant now. Equations 2.24 and 2.25 can still be used. However, Nu number defined in equations 2.22 and 23 can only be used for isothermal boundary conditions, which can be integrated as equations 2.26 and 27. For thermal conditions of linear temperature profiles, only equations 2.16 and 17 can be used for the calculation of Nu number.

Average Nu numbers were calculated from:

x-direction:

$$Nu_{ave-x} = \frac{1}{A} \int_0^1 \frac{\partial \theta}{\partial y} \Big|_{wall} dx \quad 2.26$$

y-direction:

$$Nu_{ave-y} = \int_0^1 \frac{\partial \theta}{\partial x} \Big|_{wall} dy \quad 2.27$$

2.8 Grid distribution and calculation of Nu number for the case of curved bottom (irregular-shaped) cavity:

2.8.1 Grid distribution

In this case, same grid number was used in both the x- and y- directions. Uniform grid was used in both x- and part of the y-directions as shown in Fig. 2.3. However, number of grid points used in y-direction was split into two parts. One was used for $y \leq SH$ and the other was for $y > SH$. Intersection between each mesh line in x-direction and the curved bottom was used to determine the location of mesh lines in y-direction. For example, uniform grid was used in x direction, say using 60 grid points. Intersection with which determines the size of the first 30 grid lines in y-direction for $y \leq SH$. At $y > SH$, the other 30 grid points was arranged uniformly.

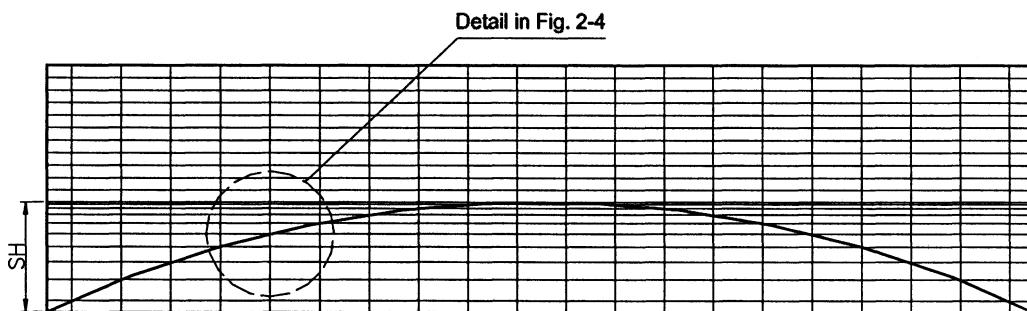


Fig. 2.3 Grid structure for curved bottom.

In order to impose the no-slip and no penetration (i.e., $u=v=0$) as well as $T = T_h$ boundary conditions at the curved bottom, values of S_ϕ in equation 2.10 corresponding to the two momentum and energy equations were assumed equal to 10^{30} for all nodal points located at or below the intersecting line of the curved bottom and grid lines in the x-

direction. Patankar [25] proposed this technique as a possible method of dealing with irregular geometries.

2.8.2 Calculation of Nu number

In this case Nu number is calculated from (see Fig. 2.4):

$$\overline{Nu} = \frac{\sum_1^{\text{int}(n/2)} \sqrt{q_{xi}^2 + q_{yi}^2} \cdot L_i + \sum_{\text{int}(n/2)+1}^n \sqrt{q_{x(n-i)}^2 + q_{yi}^2} \cdot L_i}{L_c} \quad 2.28$$

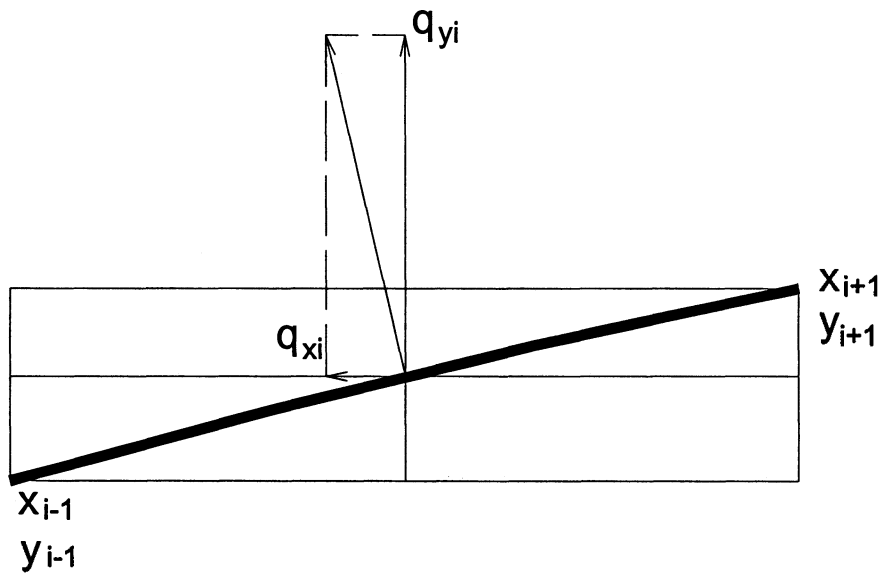


Fig. 2.4 Heat flux on curved bottom.

Where

$$q_{xi} = \left| \frac{\theta_{i+1,i} - \theta_{i-1,i}}{x_{i+1} - x_{i-1}} \right| \quad \text{and} \quad q_{yi} = \left| \frac{\theta_{i,i+1} - \theta_{i,i-1}}{y_{i+1} - y_{i-1}} \right| \quad 2.29$$

where n in equations 2.28 and 2.29 is the total number of grid points, L_c is the total length of the curved bottom and L_i is the local distance from i to $i-1$.

2.9 Accuracy of the algorithm

The algorithm used in the present study has a theoretical second order accuracy. However, the actual accuracy could be lower, so actual accuracy should be determined.

Assuming the real order of accuracy of numerical result is ‘ ξ ’, the difference between the calculated and the exact value of the general parameter ϕ can be expressed by the following equation:

$$\phi_{\text{exa}} - \phi_{\text{cal}} = c (\Delta x)^\xi \quad 2.30$$

where c is a constant., ϕ_{exa} is the exact value, ϕ_{cal} is the calculated value.

In order to calculate ξ , three runs were carried out using 10 grid points / unit length, 20 grid points / unit length, and 40 grid points / unit length. Results of all these runs were substituted in equation 2.30 giving the following equation.:

$$\frac{\phi_3 - \phi_2}{\phi_2 - \phi_1} = \frac{(\Delta x_3)^\xi - (\Delta x_2)^\xi}{(\Delta x_2)^\xi - (\Delta x_1)^\xi} \quad 2.31$$

Solving equation 2.31 for ξ , ξ can be calculated as:

$$\xi = \frac{\ln\left(\frac{\phi_1 - \phi_2}{\phi_2 - \phi_3}\right)}{\ln 2} \quad 2.32$$

Calculation of ξ was performed for the case of AA configuration for $A=4$ at inclination angle $\gamma=0^\circ$. The values of ξ are 1.509 and 1.893 for Nu number of the top and bottom walls, respectively.

2.10 Numerical treatment of temperature discontinuity at corner points

Most of previous studies were focused on the case of differentially heated cavities only in one direction with insulated end walls. In such cases, temperature discontinuity problem at corner points did not exist. For example, in the AA configuration (Fig 2.5 a), the left and right end walls are insulated, and temperature at corner points can be assumed equal to that of the respective horizontal wall. Whereas, for example, in the case of the CC configuration, corner point 3 is located at the intersection of two walls having two different temperatures, Fig. 2.5b.

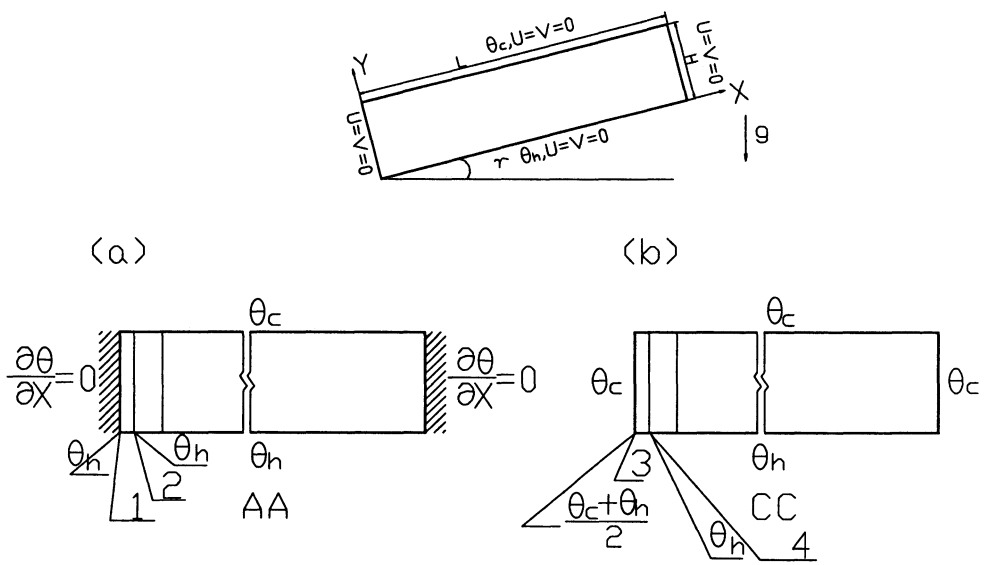


Fig. 2.5 Temperature at the corner (a) AA configuration; (b) CC configuration.

Although temperature discontinuities at corner points has found to have no influence on the numerically calculated flow and internal temperature fields (see values of u_{\max} , v_{\max} , and ψ_{\max} in Table 2.4), it was found to have a significant effect on the calculation of average Nu number. As was well demonstrated by Nansteel et.al. [26], due to temperature discontinuity, the calculated heat flux exhibits a non-integrable singularity at corner points and consequently the overall rate of heat transfer turns out to be unbounded. Accordingly, Nu number becomes larger and larger as the grid is refined. Some authors, e.g., Corcione [11], adopted the simple, but grid dependent, procedure by taking the temperature at the corner point as the average temperature of the two intersecting walls and keeping the temperatures of the adjacent nodal points at the respective wall temperatures. The numerical treatment of temperature discontinuity at corner points in the present study is carried out by introducing a well defined temperature distribution for the transition from the temperature of one wall to the temperature of the other. A linear temperature profile between the corner nodal point and the small distance close to this point is assumed. The effect of this small distance (L' in Fig. 2.6) was investigated. As shown in Fig 2.6, at 0.025, this distance gave reasonable results in terms of grid size dependency and its effect on the calculated average Nu number, and hence was used in all cases.

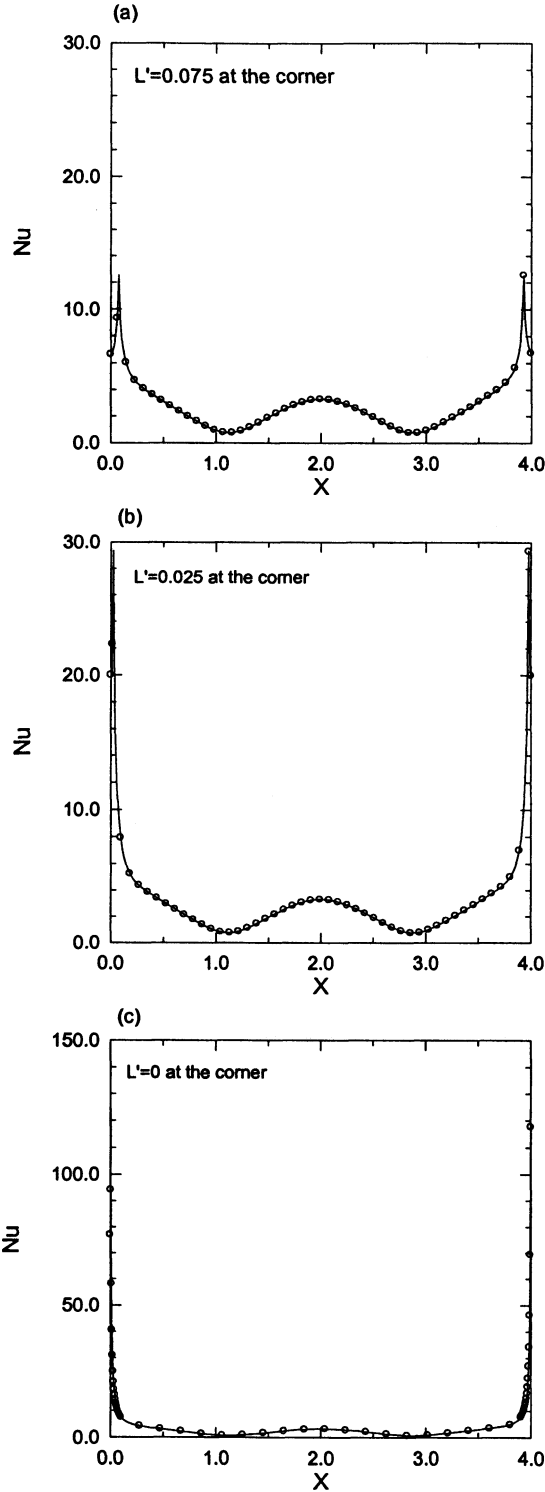


Fig 2.6 Local Nu number at the bottom wall for (A) $L'=0.075$; (b) $L'=0.025$; (c) without the linear temperature distribution assumption.

In a typical practical application, the actual temperature distribution at the corner can be measured and used in the numerical calculations. For the sake of the present study, the introduction of such treatment prevented any dependency of the calculated Nu number on the grid size. A comparison between results with and without such treatment is presented in Fig. 2.6 and Table 2.4. Results confirm that the introduction of such linear temperature profile did not cause any significant changes in the predicted flow field nor in the internal thermal field.

Table 2.4 Average Nu number calculated using different treatments temperature discontinuity for CC case. $A = 4$, $Pr = 0.7$, and $Ra = 5000$.

With linear temperature distribution starting at 0.075 from the corner

Inclined Angle	Grid	Nu-left	Nu-right	Nu-top	Nu-bottom	Umax	Vmax	Ψ_{max}	$(Q_{w, \text{max}} - Q_{w, \text{min}}) / Q_{w, \text{min}}$ %
0	62X242	1.67 (-29.54)	1.67 (-29.54)	1.97 (0.00)	2.80 (-10.83)	26.30 (0.00)	25.50 (0.00)	8.13 (0.00)	-0.03
5	62X242	1.65 (-29.49)	1.69 (-29.29)	1.96 (0.00)	2.80 (-10.83)	26.30 (0.00)	26.90 (0.00)	8.52 (0.00)	-0.03
10	62X242	1.62 (-30.17)	1.72 (-28.93)	1.95 (0.00)	2.78 (-11.18)	26.10 (0.00)	28.20 (0.00)	8.87 (0.00)	-0.03
15	62X242	1.60 (-30.13)	1.75 (-28.28)	1.93 (0.00)	2.76 (-11.25)	25.70 (0.00)	29.30 (0.00)	9.19 (0.00)	-0.03
20	62X242	1.57 (-30.63)	1.77 (-28.34)	1.89 (0.00)	2.72 (-11.40)	25.10 (0.00)	30.40 (0.00)	9.48 (0.00)	-0.03
25	62X242	1.38 (-33.98)	1.70 (-29.17)	1.64 (0.00)	2.40 (-12.73)	15.50 (-0.64)	33.20 (0.00)	10.40 (0.00)	-0.04
30	62X242	1.35 (-34.15)	1.76 (-28.16)	1.63 (0.00)	2.40 (-12.73)	15.70 (0.00)	35.10 (0.00)	11.00 (0.00)	-0.04
35	62X242	1.34 (-33.99)	1.82 (-27.49)	1.61 (0.00)	2.40 (-12.41)	15.70 (0.00)	36.90 (0.00)	11.60 (0.00)	-0.04
40	62X242	1.32 (-34.85)	1.90 (-26.92)	1.58 (0.00)	2.38 (-12.82)	15.40 (0.00)	38.70 (0.00)	12.10 (-0.82)	-0.04
45	62X242	1.31 (-34.83)	2.05 (-25.18)	1.53 (0.00)	2.37 (-12.55)	15.00 (0.00)	40.40 (0.00)	12.70 (0.00)	-0.04
50	62X242	1.30 (-35.00)	2.31 (-23.26)	1.45 (0.00)	2.35 (-12.98)	15.00 (0.00)	42.10 (0.00)	13.20 (0.00)	-0.04
55	62X242	1.29 (-35.18)	2.56 (-21.23)	1.40 (0.00)	2.36 (-12.59)	14.90 (0.00)	43.60 (0.00)	13.60 (0.00)	-0.03
60	62X242	1.29 (-34.85)	2.74 (-20.35)	1.37 (0.00)	2.37 (-12.87)	14.80 (0.00)	44.80 (0.00)	14.00 (0.00)	-0.03
65	62X242	1.28 (-35.35)	2.88 (-19.55)	1.34 (0.00)	2.38 (-12.82)	14.70 (0.00)	45.80 (0.00)	14.30 (0.00)	-0.03
70	62X242	1.28 (-35.35)	3.00 (-18.92)	1.32 (0.00)	2.39 (-12.45)	15.00 (0.00)	46.40 (0.00)	14.50 (0.00)	-0.03
75	62X242	1.28 (-35.35)	3.10 (-18.21)	1.30 (0.00)	2.39 (-12.77)	15.80 (0.00)	46.80 (0.00)	14.60 (0.00)	-0.03
80	62X242	1.29 (-34.85)	3.18 (-18.04)	1.28 (0.00)	2.40 (-12.41)	16.70 (0.00)	46.90 (0.00)	14.60 (0.00)	-0.03
85	62X242	1.29 (-34.85)	3.25 (-17.72)	1.26 (0.00)	2.39 (-12.77)	17.60 (0.00)	46.80 (0.00)	14.50 (0.00)	-0.03
90	62X242	1.29 (-35.18)	3.32 (-17.21)	1.24 (0.00)	2.39 (-12.45)	18.50 (0.00)	46.40 (0.00)	14.40 (0.00)	-0.02

With linear temperature distribution starting at 0.025 from the corner

0	62X242	2.37	2.37	1.97	3.14	26.30	25.50	8.13	-0.17
5	62X242	2.34	2.39	1.96	3.14	26.30	26.90	8.52	-0.17
10	62X242	2.32	2.42	1.95	3.13	26.10	28.20	8.87	-0.17
15	62X242	2.29	2.44	1.93	3.11	25.70	29.30	9.19	-0.17
20	62X242	2.26	2.47	1.89	3.07	25.10	30.40	9.48	-0.17
25	62X242	2.06	2.40	1.64	2.75	15.60	33.20	10.40	-0.19
30	62X242	2.05	2.45	1.63	2.75	15.70	35.10	11.00	-0.19
35	62X242	2.03	2.51	1.61	2.74	15.70	36.90	11.60	-0.19
40	62X242	2.02	2.60	1.58	2.73	15.40	38.70	12.20	-0.19
45	62X242	2.01	2.74	1.53	2.71	15.00	40.40	12.70	-0.19
50	62X242	2.00	3.01	1.45	2.70	15.00	42.10	13.20	-0.19
55	62X242	1.99	3.25	1.40	2.70	14.90	43.60	13.60	-0.19
60	62X242	1.98	3.44	1.37	2.72	14.80	44.80	14.00	-0.19
65	62X242	1.98	3.58	1.34	2.73	14.70	45.80	14.30	-0.18
70	62X242	1.98	3.70	1.32	2.73	15.00	46.40	14.50	-0.18
75	62X242	1.98	3.79	1.30	2.74	15.80	46.80	14.60	-0.18
80	62X242	1.98	3.88	1.28	2.74	16.70	46.90	14.60	-0.18
85	62X242	1.98	3.95	1.26	2.74	17.60	46.80	14.50	-0.18
90	62X242	1.99	4.01	1.24	2.73	18.50	46.40	14.40	-0.18

Without linear temperature distribution

0	73X289	3.21 (35.44)	3.21 (35.44)	1.95 (-1.02)	3.57 (13.69)	26.20 (-0.38)	25.30 (-0.78)	8.05 (-0.98)	0.24
5	73X289	3.18 (35.90)	3.23 (35.15)	1.95 (-0.51)	3.56 (13.38)	26.00 (-1.14)	26.80 (-0.37)	8.43 (-1.06)	0.24
10	73X289	3.16 (36.21)	3.28 (34.71)	1.94 (-0.51)	3.55 (13.42)	25.80 (-1.15)	28.00 (-0.71)	8.79 (-0.80)	0.24
15	73X289	3.13 (36.68)	3.28 (34.43)	1.92 (-0.52)	3.53 (13.50)	25.40 (-1.17)	29.20 (-0.34)	9.12 (-0.78)	0.24
20	73X289	3.11 (37.81)	3.31 (34.01)	1.88 (-0.53)	3.49 (13.68)	24.80 (-1.20)	30.30 (-0.33)	9.42 (-0.63)	0.24
25	73X289	2.90 (40.78)	3.24 (35.00)	1.83 (-0.81)	3.18 (15.84)	15.60 (0.00)	33.10 (-0.30)	10.40 (0.00)	0.26
30	73X289	2.89 (40.98)	3.29 (34.29)	1.82 (-0.81)	3.18 (15.84)	15.70 (0.00)	35.00 (-0.28)	11.00 (0.00)	0.26
35	73X289	2.88 (41.87)	3.36 (33.86)	1.81 (0.00)	3.17 (15.69)	15.70 (0.00)	36.90 (0.00)	11.60 (0.00)	0.27
40	73X289	2.88 (41.58)	3.44 (32.31)	1.58 (0.00)	3.16 (15.75)	15.40 (0.00)	38.70 (0.00)	12.10 (-0.82)	0.27
45	73X289	2.85 (41.79)	3.59 (31.02)	1.52 (-0.65)	3.14 (15.87)	15.10 (0.67)	40.40 (0.00)	12.60 (-0.79)	0.28
50	73X289	2.84 (42.00)	3.85 (27.91)	1.45 (0.00)	3.13 (15.93)	15.00 (0.00)	42.10 (0.00)	13.20 (0.00)	0.28
55	73X289	2.83 (42.21)	4.09 (25.85)	1.40 (0.00)	3.14 (16.30)	14.90 (0.00)	43.60 (0.00)	13.60 (0.00)	0.29
60	73X289	2.83 (42.93)	4.28 (24.42)	1.36 (-0.73)	3.15 (15.81)	14.90 (0.68)	44.80 (0.00)	14.00 (0.00)	0.29
65	73X289	2.82 (42.42)	4.42 (23.46)	1.34 (0.00)	3.16 (15.75)	14.80 (0.68)	45.80 (0.00)	14.20 (-0.70)	0.29
70	73X289	2.82 (42.42)	4.53 (22.43)	1.32 (0.00)	3.17 (16.12)	15.10 (0.67)	46.40 (0.00)	14.40 (-0.69)	0.29
75	73X289	2.82 (42.42)	4.63 (22.16)	1.30 (0.00)	3.17 (15.89)	15.90 (0.63)	46.80 (0.00)	14.50 (-0.68)	0.29
80	73X289	2.82 (42.42)	4.71 (21.39)	1.28 (0.00)	3.17 (15.69)	16.70 (0.00)	47.00 (0.21)	14.60 (0.00)	0.30
85	73X289	2.83 (42.93)	4.79 (21.27)	1.26 (0.00)	3.17 (15.69)	17.60 (0.00)	46.80 (0.00)	14.50 (0.00)	0.30
90	73X289	2.83 (42.21)	4.85 (20.95)	1.24 (0.00)	3.16 (15.75)	18.50 (0.00)	46.50 (0.22)	14.40 (0.00)	0.30

2.11 Verification of numerical algorithm

In order to validate the numerical algorithm developed to be used in solving the problem of interest in the present study, the algorithm was used to solve problems reported in the literature.

2.11.1 Comparison with results reported by Corcione [12] –case of horizontal cavity

As was indicated in chapter 1, Corcione [12] carried out a numerical study of the effect of different boundary conditions on natural convection in air-filled horizontal cavities having various aspect ratios between 1 and 8 considering Ra numbers from 10^3 to 10^6 . Cavities were heated from bottom, cooled from top and thermal conditions of end walls were varied according to the six configurations shown in Fig. 1.2. Although good agreement between flow fields and internal temperature distributions calculated using the present numerical algorithm and those reported in [12], for $\gamma = 0^\circ$, was found, Nu numbers reported in [12], did not agree with those obtained in the present study. This might be attributed to the difference in the way temperature discontinuities at corner points have been treated in [12], as explained above. Fig 2.7 presents sample results obtained using the present algorithm for $A = 2$ and $Ra = 10^4$ and 10^5 . Results reported in [12] for the same case were given in Fig. 1.3.

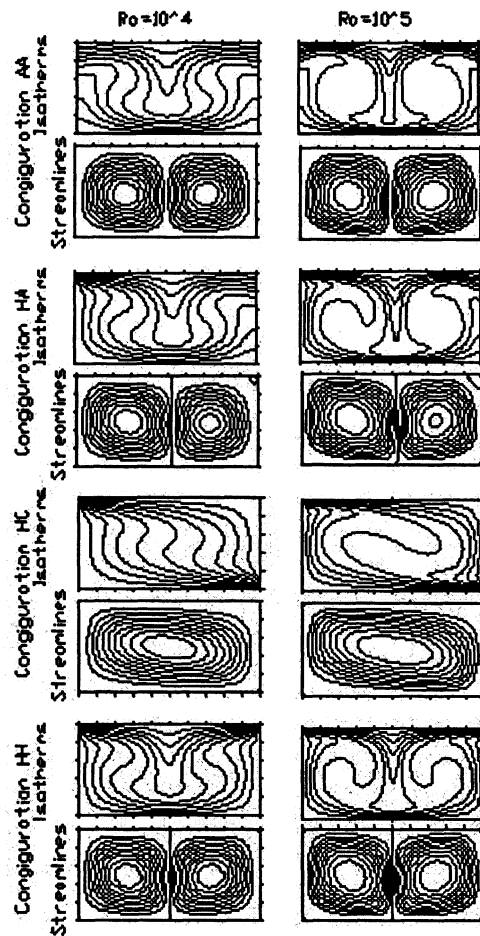


Fig 2.7 Results obtained using present algorithm considering different thermal boundary conditions at $A = 2$, $Pr = 0.7$, and $Ra = 10^4$ and 10^5 .

2.11.2 Comparison with results reported by Soong and Tzeng [21] – case of inclined cavity with insulated end walls (AA configuration)

Fig 2.8 presents results obtained for an air-filled inclined cavity heated from the bottom, cooled from the top, and with insulated end walls at $A = 4$ for various Ra Numbers and the case of increasing angle of inclination from 0° to 90° .

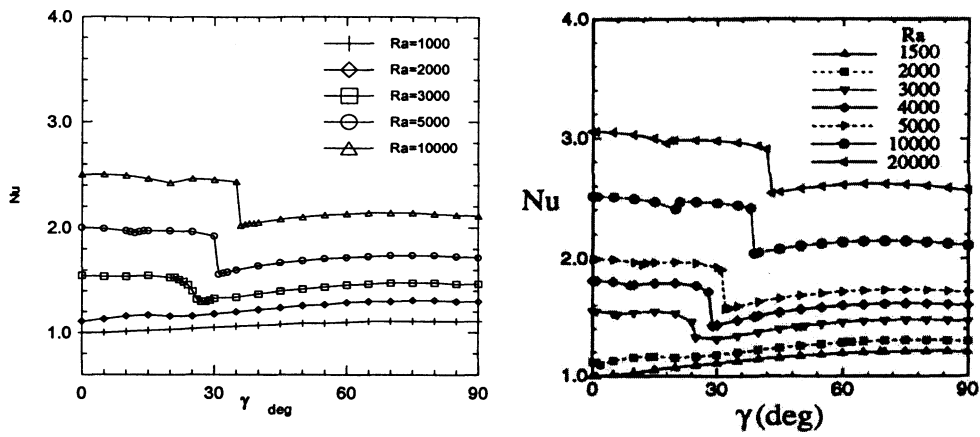


Fig. 2.8 Nu number Vs angle of inclination at different Ra numbers, $A = 4$, and $Pr = 0.7$. Results from present study (left) compared with those of reported in [21] (right).

Soong and Tzeng [21] investigated hysteresis phenomenon associated with increasing and decreasing cavity angle of inclination. Fig. 2.9 shows present results of hysteresis phenomenon for $Ra=1000, 3000, 5000$, and 10^4 , heat transfer rate, and values of angle of inclination at which mode transition took place. Results shown in Fig 2.9 compare very well with those reported in [21] shown in Fig. 1.6.

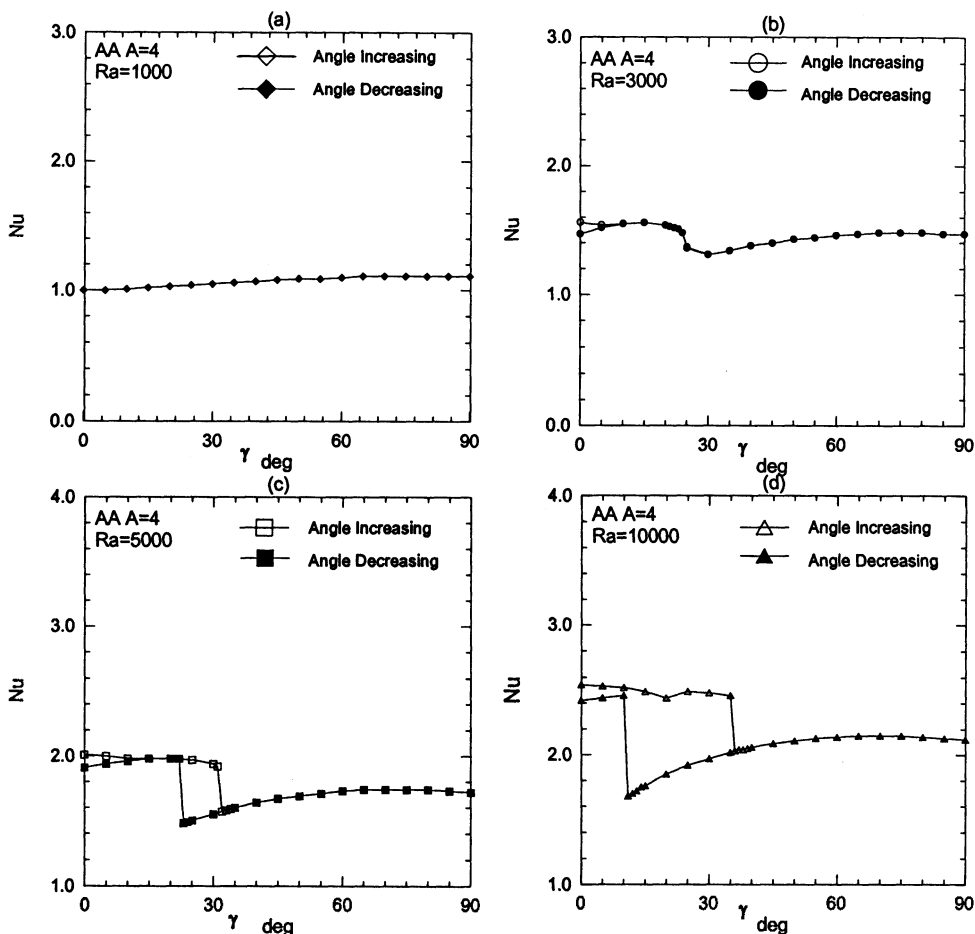


Fig. 2.9 Nu VS γ for angle increasing and decreasing in various Ra numbers for AA configuration and $A=4$.

2.11.3 Comparison with benchmark problem reported in [27] – case of vertical cavity

The present numerical algorithm has been used to solve benchmark problem reported by Davis and Jones [27]. The problem is to numerically calculate natural convection flows in an air-filled square cavity, heated on left wall and cooled from right wall, with insulated top and bottom surfaces. Ra number ranged from 10^3 to 10^6 . Table

2.5 shows a comparison between results flow and thermal fields obtained using the present algorithm with those reported in [27]. Maximum difference is 3.0%.

Table 2.5 Comparison with results obtained for benchmark problem reported in [27].

Quantities	Benchmark	Present	Deviation(%)
$Ra=10^3$			
U_{max}	3.649	3.649	-0.01
V_{max}	3.697	3.707	0.26
Nu_{ave}	1.117	1.119	0.17
Nu_{max}	1.505	1.506	0.09
Nu_{min}	0.692	0.695	0.39
$Ra=10^4$			
U_{max}	16.178	16.202	0.15
V_{max}	19.617	19.674	0.29
Nu_{ave}	2.238	2.242	0.20
Nu_{max}	3.528	3.526	-0.05
Nu_{min}	0.586	0.596	1.77
$Ra=10^5$			
U_{max}	34.730	35.773	3.00
V_{max}	68.590	68.772	0.27
Nu_{ave}	4.509	4.512	0.07
Nu_{max}	7.717	7.714	-0.04
Nu_{min}	0.729	0.745	2.23
$Ra=10^6$			
U_{max}	64.630	65.300	1.04
V_{max}	219.360	220.000	0.29
Nu_{ave}	8.817	8.790	-0.31
Nu_{max}	17.925	17.400	-2.93
Nu_{min}	0.989	1.000	1.11

2.11.4 Comparison with result reported by Ganzarolli and Milanez [11] – treatment of temperature discontinuity at corner points

The present numerical algorithm was also used to solve problem considered by Ganzarolli and Milanez who carried out a numerical study of natural convection inside a horizontal cavity heated from below, insulated from the top, and cooled from the two vertical end walls. Ra numbers based on the cavity height ranged between 10^3 and 10^7 , Pr numbers varied from 0.7 to 7 and length to height ratio of the cavity ranged from 1 to 9.

Fig. 2.10 presents results obtained for Ra number ranging from 10^3 to 10^6 . and aspect ratios from 1 to 9 with those reported in [11]. Small differences in Nu numbers between the present work and results in [11] can be observed. However, the trend of the data is the same. This small difference might be attributed to the different distance of linear temperature distribution used treating the temperature discontinuity at corner points. This distance was not explicitly stated in [11].

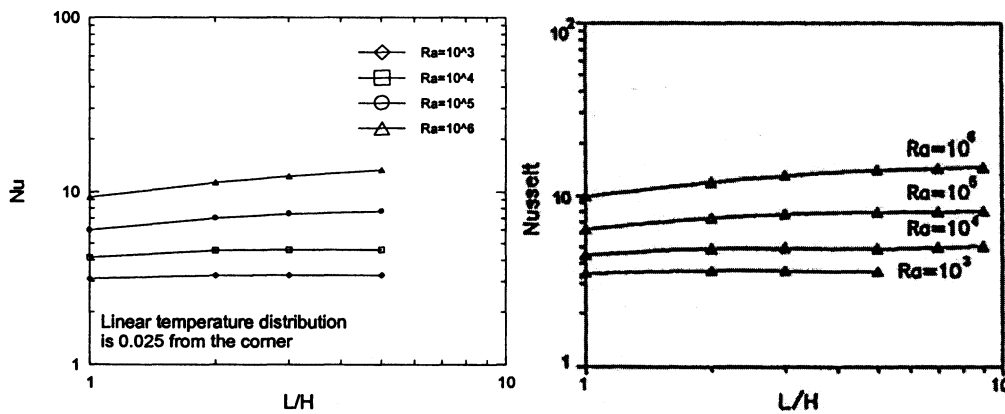


Fig. 2.10 Comparison with of calculated Nu number for cavities with various aspect ratios, Pr = 0.7 with those reported in [11]. (a) Results from present work; (b) Results reported in [11].

Calculated flow and thermal fields using the present algorithm are shown in Fig. 2.11. They compare very well with those reported in [11] given in Fig. 1.1.

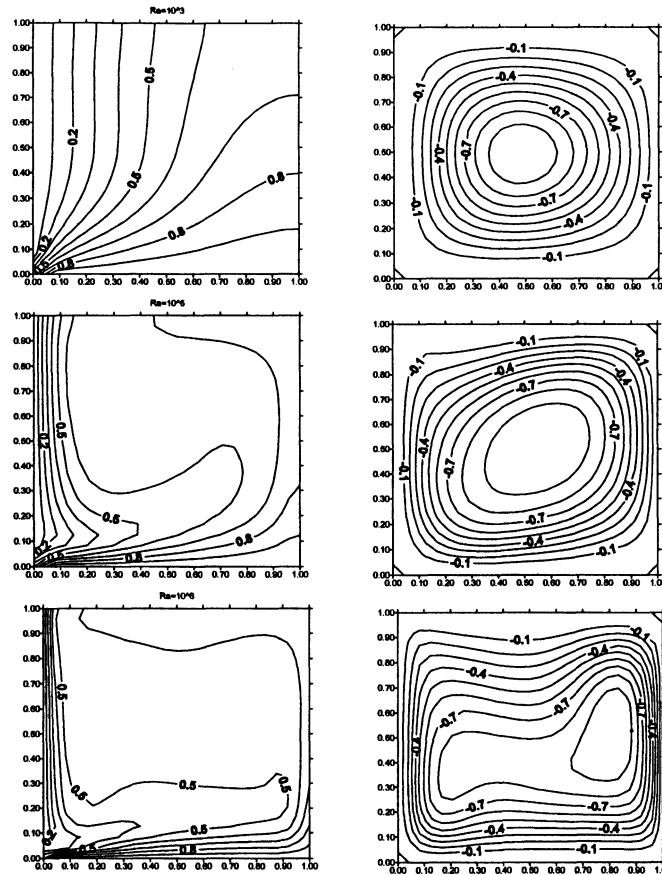


Fig. 2.11 Isothermal lines and Streamlines from present algorithm for different Ra numbers in left half of the cavity, $A = 2$, and $Pr=7.0$. To be compared with Fig 1.1.

All the aforementioned comparisons demonstrate that the present model can be used for solving different problems considering various thermal boundary conditions, angles of inclination, and initial conditions.

Chapter 3

Numerical Results - Case of Square Cavity with Flat Bottom

In the present chapter, results obtained for the case of square cavities with flat bottoms are presented considering seven different configurations of end wall thermal conditions, Ra number in the range between 10^3 and 10^4 , Pr number constant at 0.7, and two cases of changing cavity angle of inclination: increasing from $\gamma = 0^\circ$; and decreasing from $\gamma = 90^\circ$.

3.1 AA configuration

3.1.1 Case of increasing γ

As was reported in [10,14], in all cases of horizontal cavities heated from bottom, cooled from above, and with two insulated end walls, natural convection is not expected to take place until Ra number reaches or exceeds a certain critical value, below which heat transfer in the cavity will be entirely by conduction. That critical value for cavity with different aspect ratio as will be discussed in chapter 4 where results for cases of rectangular cavities (i.e., $A > 1$) will be presented.

Fig. 3.1 presents the normalized streamlines and isothermal lines in the case of AA configuration at various angles of inclination γ for the case of increasing γ from 0° to 90° and the case of decreasing γ back to 0° . Numerical results obtained for four Ra numbers; namely, $Ra = 1000, 3000, 5000, \text{ and } 10^4$. At each angle of inclination, streamlines were normalized using the corresponding absolute maximum value of the stream function, $|\psi_{\max}|$. As shown in Fig 3.1, at $\gamma = 0^\circ$ and for $Ra \leq 3000$, there is no

convection motion observed and heat transfer in these cases is primarily by conduction, as evident from the shape of the isothermal lines being parallel to the horizontal direction. A convective cell rotating in the anticlockwise direction is produced as γ increased above 0° . Average Nu numbers as function of angles of inclination calculated for the case of increasing γ and four Ra numbers shown in Fig 3.1 are presented in Fig. 3.2.

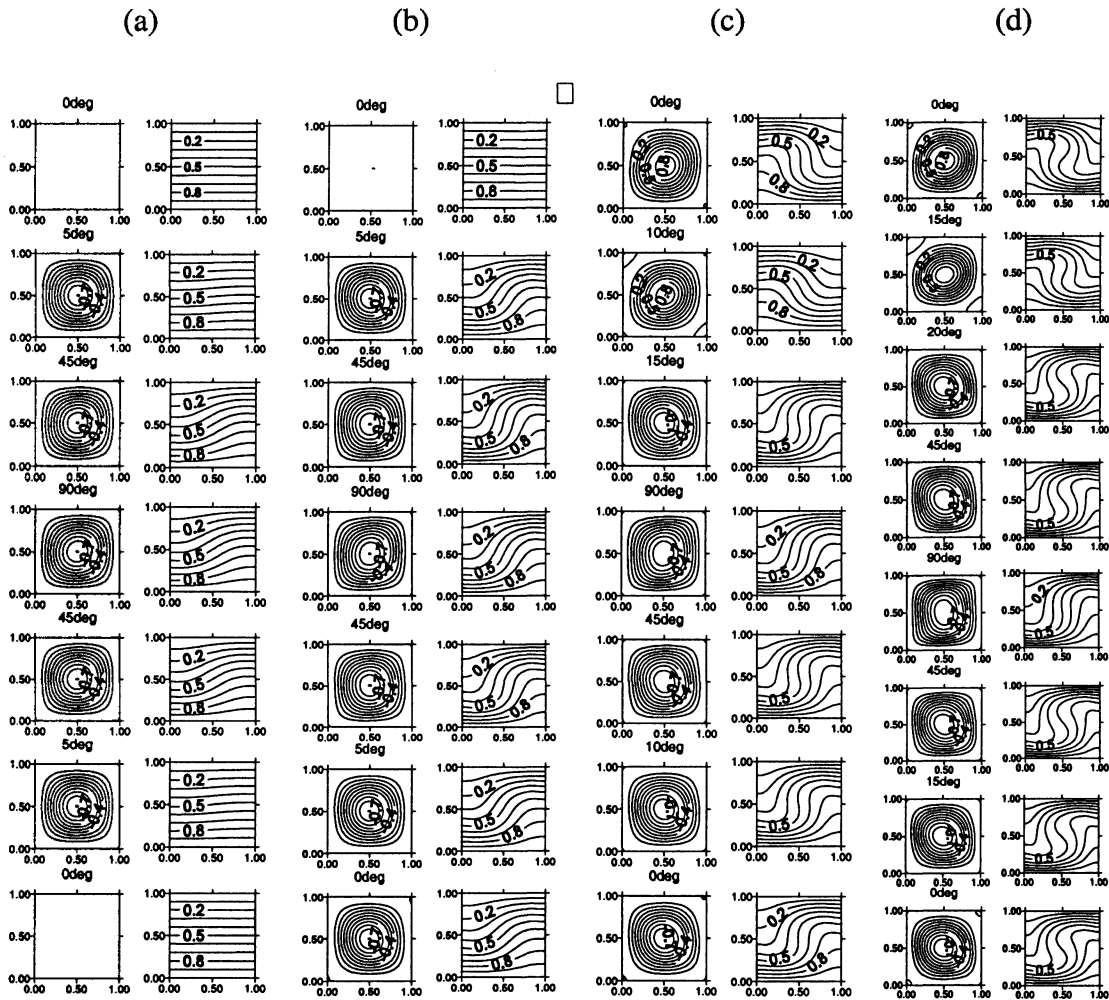


Fig. 3.1 Normalized streamlines and isothermal lines for AA configuration at various angles of inclination and four Ra numbers. (a) Ra=1000, (b) Ra=3000, (c) Ra=5000, (d) Ra=10⁴. Positive values indicate rotation in clockwise direction.

At Ra = 1000, and for angles of inclination $\gamma > 0^\circ$, although convection did take place and became stronger as the angle of inclination increased up to 90° , this convective

motion did not cause big enhancement in the rate of heat transfer, as shown in Fig 3.2. At $\gamma = 0^\circ$, average Nu number is still equal to 1, i.e., natural convection did not cause any increase in the rate of heat transfer, not until $\gamma=5^\circ$, as shown in Fig 3.2. As compared with its value at $\gamma = 0^\circ$, the rate of heat transfer increased by about 13% and reached its maximum value at $\gamma = 60^\circ$. Its value remained almost unchanged up to $\gamma = 90^\circ$. For $Ra = 3000$, convection took place at $\gamma \geq 5^\circ$. The rate of heat transfer increases by about 64% and reached its maximum value at $\gamma = 45^\circ$, (as compared with its value at $\gamma = 0$), and decreased slightly between $\gamma = 45^\circ$ and 90° .

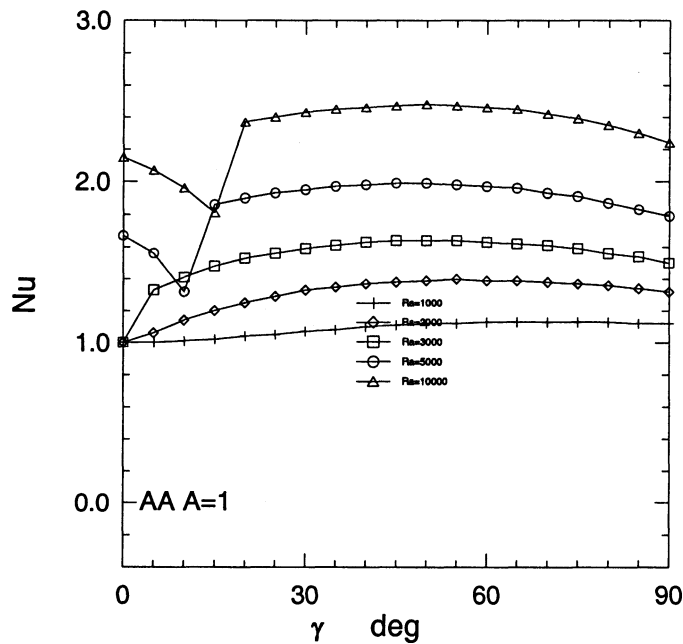


Fig. 3.2 Variation of average Nu number (both top and bottom walls) with inclination angle at various Ra numbers for AA configuration and A=1.

In the case of $Ra = 5000$, beside the fact that natural convection took place in this case even at $\gamma= 0$ and produced much stronger cells than those produced at lower Ra numbers, more important observations are worth noting. Convective cells produced at $\gamma =$

0° are rotating in the clockwise direction, not in the anticlockwise direction, as was observed in the two cases of $Ra = 1000$ and 3000 . As the angle on inclination of the cavity increased, component of buoyancy force in the upslope direction increased, while its component in the cross stream direction (named hereafter as cross force) decreased. Because of that effect the main convective cell changed direction of rotation at $\gamma = 10^\circ$. That change in direction was associated with a sudden drop in the value of the average Nu number, as shown in Fig 3.2.

Two small corner cells are observed at two opposite corners of the cavity depending on the direction of rotation of the main core cell. As γ further increased the main core cell became much stronger and bigger in size, and therefore, the size of these two small cells decreased.

The case of $Ra = 10^4$ is somewhat similar to that at $Ra = 5000$ except that the change in direction of the core cell was delayed until $\gamma = 15^\circ$. As Ra increased, the cross force increased and was able to sustain the anticlockwise core cell further than in the case of $Ra = 5000$.

3.1.2 Case of decreasing γ

Calculations for the case of γ decreasing started from $\gamma = 90^\circ$ back to 0° , using the 90° solution obtained from the γ increasing case as an initial condition for $\gamma = 85^\circ$ and so on. Figure 3.3 shows calculated average Nu number for the two cases of increasing and decreasing γ . At $Ra = 1000$, Fig 3.3a, no significant difference between results obtained in the two courses of changing γ was observed. However, At $Ra = 3000$, Fig 3.3b, two solutions deviate in a small region of inclination around $\gamma < 10^\circ$. In this case, initial

conditions with higher velocities from the solution at $\gamma = 5^\circ$ resulted in a strong anticlockwise cell at $\gamma = 0^\circ$ and an average Nu number 18% higher than that obtained at $\gamma = 0^\circ$ in the case of angle increasing.

At $Ra = 5000$ and 10^4 numbers, hysteresis region extends to higher angles of inclination $\gamma \leq 15^\circ$ and $\gamma \leq 20^\circ$, respectively. However, heat transfer rates are exactly the same at $\gamma = 0^\circ$, Figs. 3.3c and 3.3d.

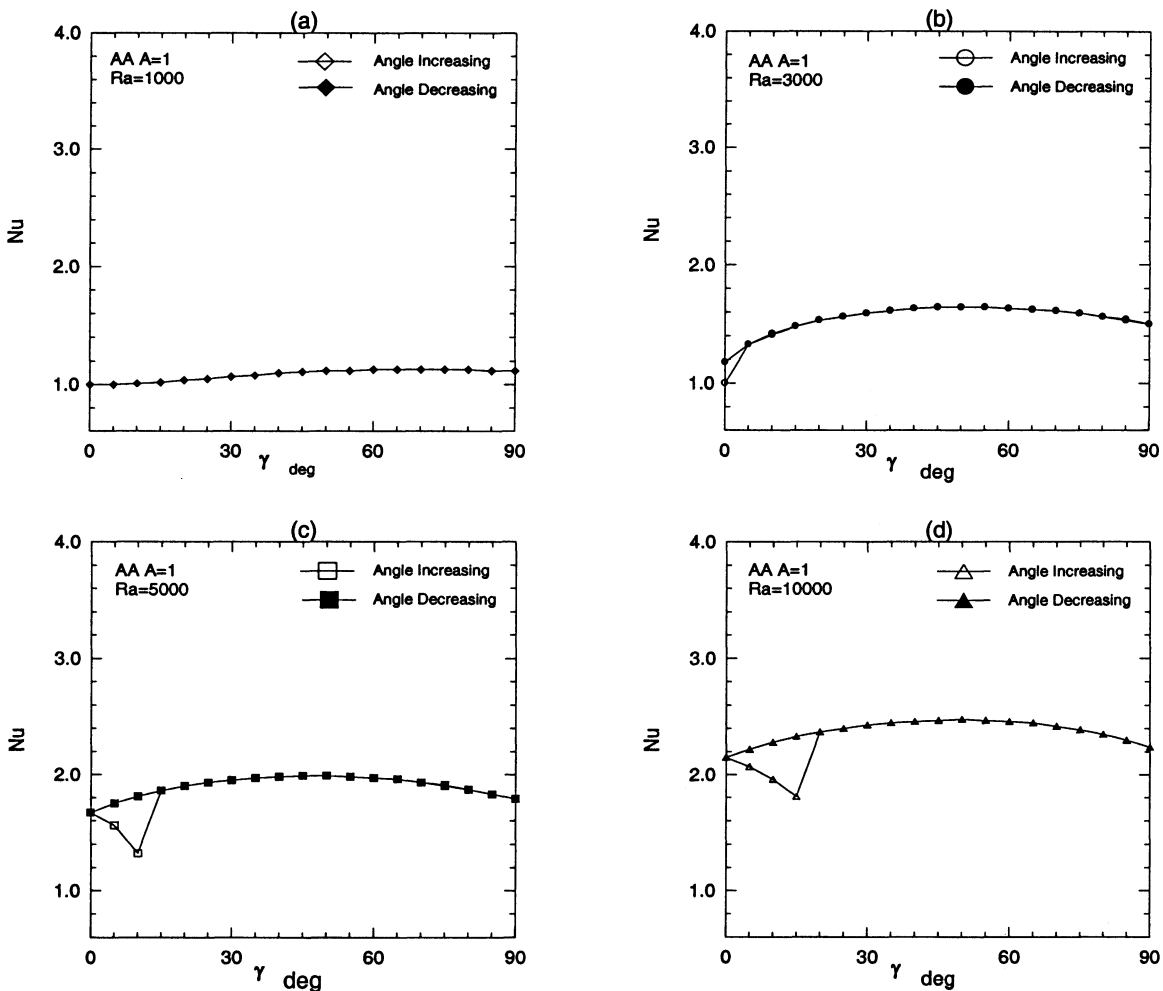


Fig. 3.3 Average Nu number (bottom wall) as a function of inclination angle γ for angle increasing and decreasing at various Ra numbers for AA configuration and A=1.

As mentioned in section 3.1.1, for the case of γ increasing, at small angles of inclination, much stronger cells were produced at $Ra=5000$ and 10^4 . However, these cells

were in the opposite direction to those observed at $Ra \leq 3000$. Due to the symmetry of all boundary conditions in the case of AA configuration, rotating cells in either clockwise or anti-clockwise directions comprise two possible and expected solutions. Soong and Tzeng [21] introduced an artificial unbalance in initial conditions and found that it would greatly affect their numerical solutions. Whether the change in the results shown in Figs 3.2 and 3.3 was due to a physical or a numerical unbalance is worth noting and investigating. The effect of the sweeping direction of the iterative method used to solve the set of discretized equations was investigated for the case of $Ra=10^4$. Results shown in Figs. 3.1, 3.2 and 3.3 were produced using sweeping from left to right. Changing sweeping direction from right to left produced a convection cell rotating in the anticlockwise direction for all values of γ , as shown in Fig 3.4a. These results indicate that the present problem is very sensitive to any kind of unbalance in boundary or initial conditions, as confirmed by [21]. Values of average Nu number shown in Fig 3.4b do not have any sharp drops as those indicated in Fig. 3.3 due to change in direction of rotation of core cell. In a practical situation any slight unbalance in boundary conditions or in initial conditions might result in situations favoring one of the two possible solutions. In such cases, results shown in Figs 3.2 and 3.3 might still be applicable.

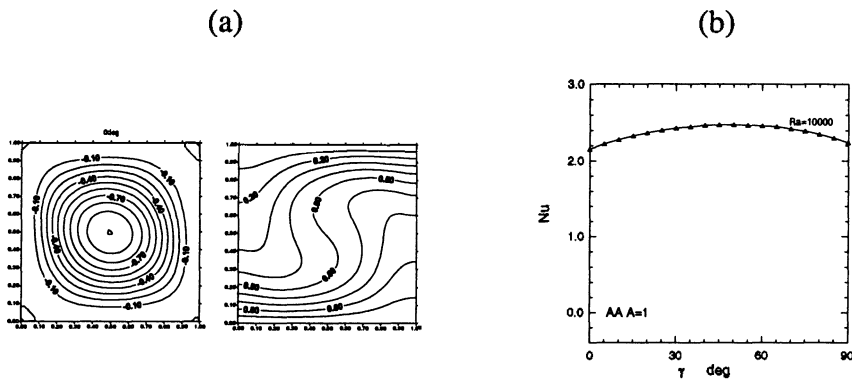


Fig. 3.4 Results obtained using sweeping from right to left, AA configuration and $Ra=10^4$, (a) Streamlines and isotherms at $\gamma=0^\circ$. Positive values indicate rotation in clockwise. (b) Nu (bottom wall) Vs γ .

3.2 CH configuration

3.2.1 Case of increasing γ

Due to thermal conditions of the left and the right end walls, temperature gradients are now parallel and perpendicular to the gravity vector. Similar to the case of vertical cavities, natural convection occurs at any Ra numbers, i.e., there is no critical value of Ra number in the case of CH configuration. Also, temperature gradients at the left and right end walls produce a downward and an upward buoyancy forces, respectively. In this case, there is only one possible solution and flow fields for all Ra numbers start at $\gamma = 0^\circ$ with an anticlockwise unicell supported by the upward force at the left end wall and the downward force at the right end wall, see Fig. 3.5.

As the cavity angle of inclination increased, buoyancy forces at all cavity walls kept the produced convective cell rotating in the same direction, which also resulted in values of average Nu number gradually decreasing as γ increased after certain inclination angle, see Fig 3.6. As the cavity was going from the horizontal to the vertical position, Nu number decreased due to stratification of hot and cold air near the top/right

and the bottom/left corners, respectively. The amount of decrease in the value of Nu number increased as Ra number increased. At Ra = 1000, average Nu number of bottom wall calculated while the cavity was at the horizontal position was about 2% higher than that calculated at the vertical position. At Ra=2000, 3000, 5000, and 104, Nu numbers calculated at the horizontal position were 6%, 9%, 11.2%, and 12.4% higher than those obtained at the vertical position, respectively, see Fig. 3.6.

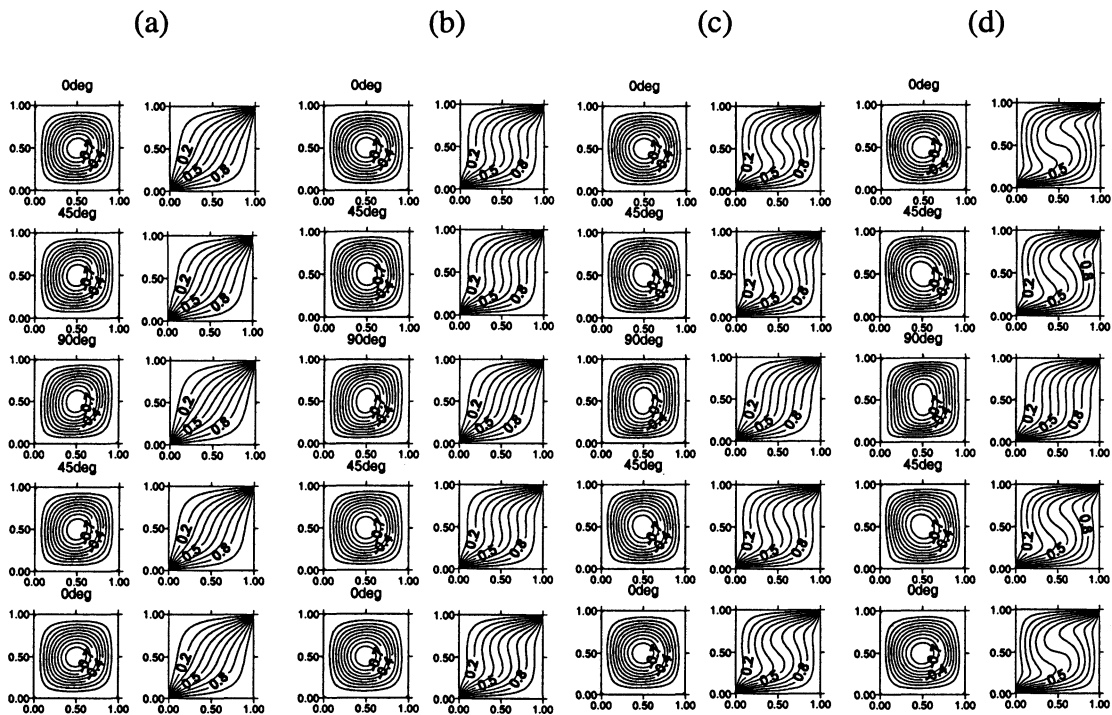


Fig. 3.5 Normalized streamlines and isothermal lines for CH configuration at various angles of inclination and four Ra numbers. (a) Ra=1000, (b) Ra=3000, (c) Ra=5000, (d) Ra=10⁴. Positive values indicate rotation in clockwise direction.

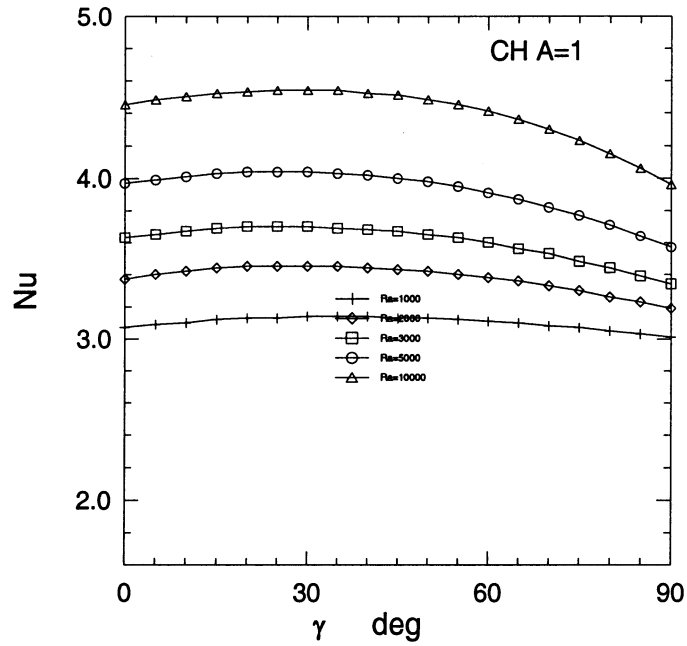


Fig. 3.6 Variation of average Nu number (both top and bottom walls) with inclination angle at various Ra numbers for CH configuration and $A=1$.

3.2.2 Case of decreasing γ

No hysteresis phenomena could be observed in the case of CH configuration as indicated by Fig. 3.7.

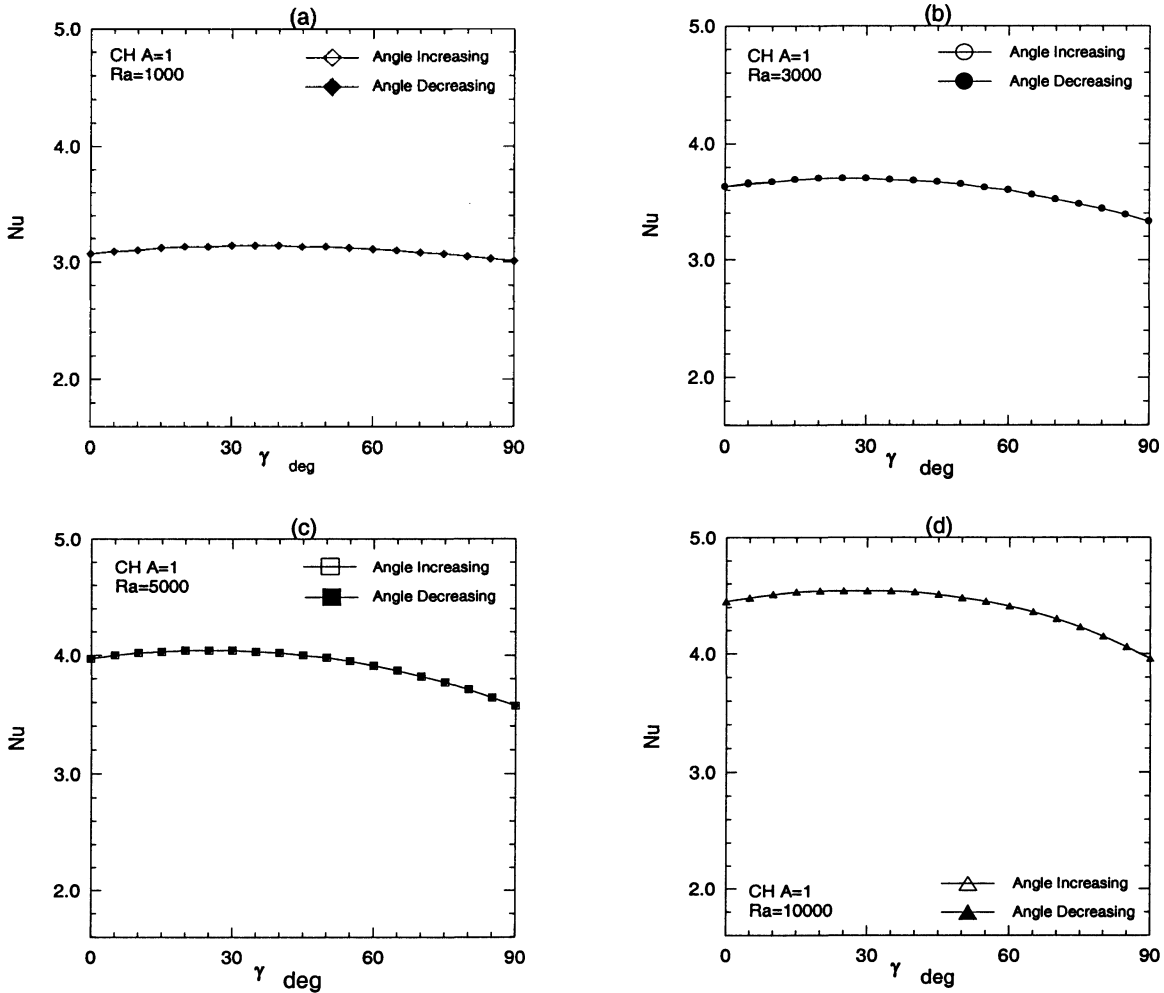


Fig. 3.7 Average Nu number (bottom wall) as a function of inclination angle γ for angle increasing and decreasing at various Ra numbers for CH configuration and A=1.

3.3 HC configuration

3.3.1 Case of increasing γ

At $\gamma = 0^\circ$, although convective cells are rotating in opposite directions in the cases of HC and CH configurations. Due to symmetry of cavity geometry, same rates of heat transfer were observed, see Figs. 3.6 and 3.9. In CH configuration, Fig 3.5, cells were rotating in the same direction all the way as γ increased. However, in HC configuration, rotating direction had to be reversed from clockwise at $\gamma = 0^\circ$ to anticlockwise at $\gamma = 90^\circ$. At $\gamma = 0^\circ$, upward force at the heated left wall and downward force at the cold right wall

produced a clockwise cell, which enhances the rate of heat transfer rate of the top and bottom walls similar to the case in CH configuration, as compared with AA configuration, see Figs. 3.9 and 3.2.

For $Ra < 3000$, only upward and downward forces from end walls and upslope and downslope force from top and bottom walls work on the fluid motion. At $\gamma = 45^\circ$, all these four forces are equal to each other resulting in a flow pattern having four cells, Fig. 3.8. At $Ra=5000$ and 10000 , cross force has greater effect on the rotating cells, which affects the balance of the aforementioned forces, so that flow pattern with four co-existing cells can not be observed at $\gamma = 45^\circ$. While cell changes its direction to anticlockwise, fluid is preheated at the left side wall and pre-cooled at the right side wall resulting in a sudden drop in Nu number of the top and bottom walls. Nu number on both top and bottom walls decreased by 20.6% for $Ra = 5000$ and by 21.7% for $Ra=10^4$, Fig. 3.9.

At $\gamma = 90^\circ$, Nu number did not significantly change with Ra number and ranged between 2.5 and 2.8, still higher than the AA configuration.

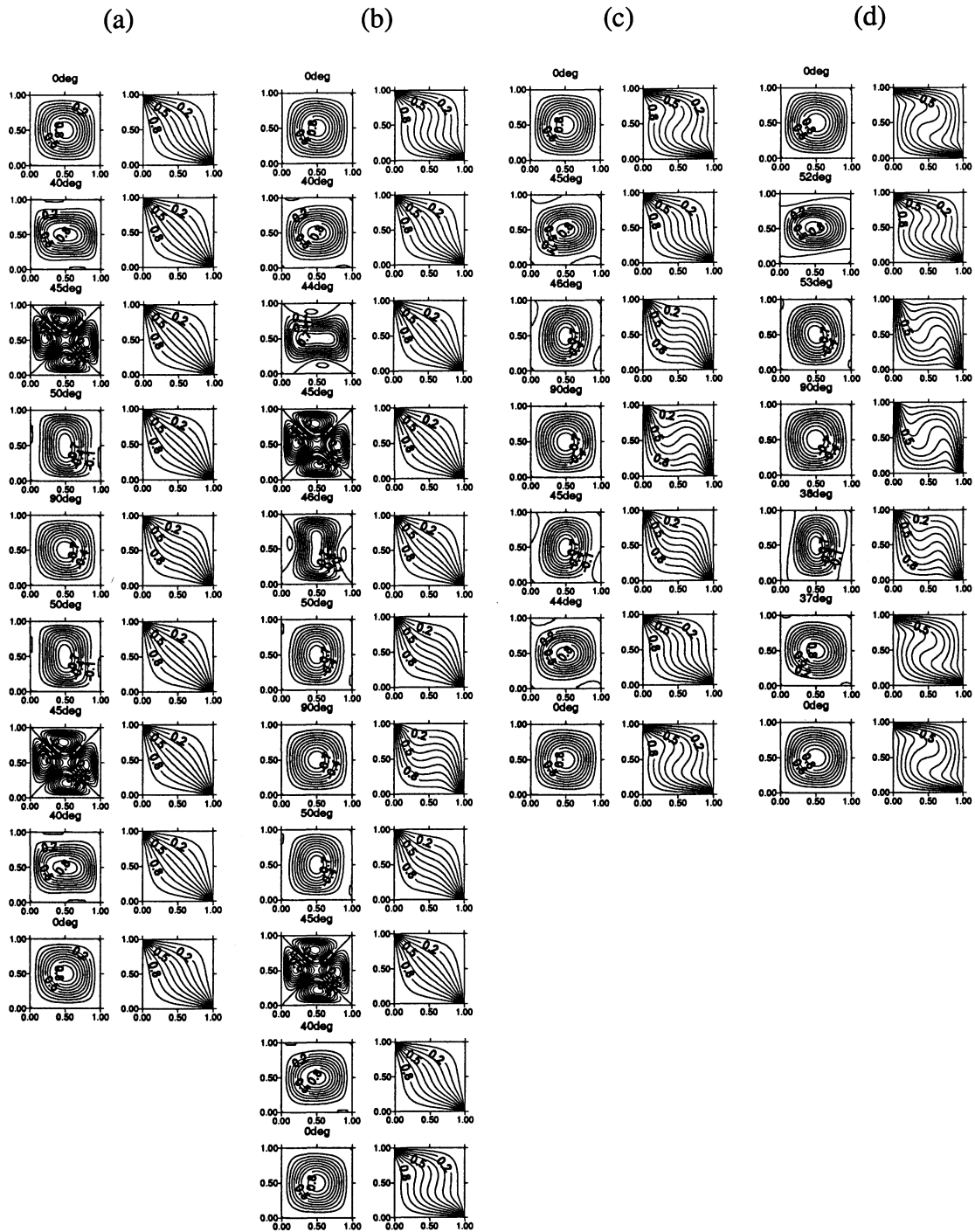


Fig. 3.8 Normalized streamlines and isothermal lines for HC configuration at various angles of inclination and four Ra numbers. (a) Ra=1000, (b) Ra=3000, (c) Ra=5000, (d) Ra=10⁴. Positive values indicate rotation in clockwise direction.

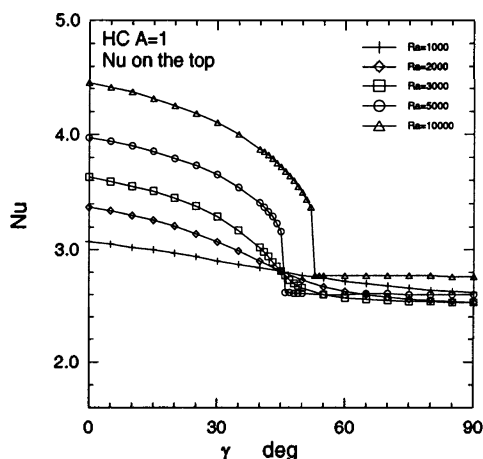


Fig. 3.9 Variation of average Nu number (both top and bottom walls) with inclination angle at various Ra numbers for HC configuration and A=1.

3.3.2 Case of decreasing γ

No hysteresis was observed for $Ra \leq 3000$. For $Ra \geq 5000$, drastic changes in Nu number could be observed similar to those observed for angle increasing when convective cell reversed its direction of rotation. Fig. 3.10 shows sudden drops in Nu number for $Ra = 5000$ very close between angle increasing and decreasing. Therefore, a small hysteresis region exists in this case. At $Ra=10^4$, a much bigger hysteresis region exists between $\gamma = 40^\circ$ and 53° .

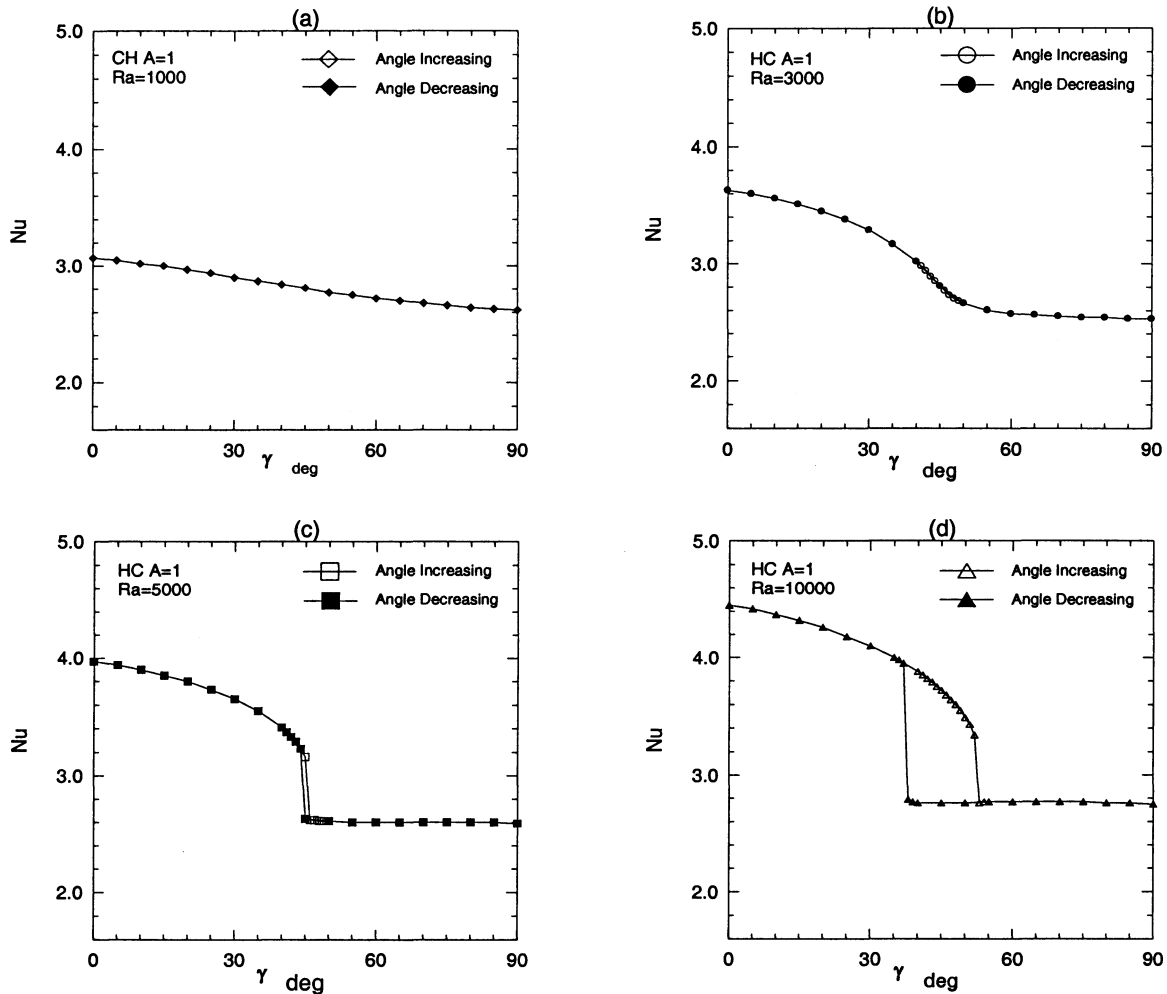


Fig. 3.10 Average Nu number (bottom wall) as a function of inclination angle γ for angle increasing and decreasing at various Ra numbers for HC configuration and A=1.

3.4 AC configuration

3.4.1 Case of increasing γ

In the case of AC configuration, a downward force produced at the cold right end wall impels a cell rotating in the clockwise direction at all values of Ra numbers, i.e., no critical value of Ra number exists in this case. Fig 3.11 presents normalized streamlines and isothermal lines at various Ra numbers. As γ increased, an upslope force at the bottom hot wall and a down slope force at the top cold wall produce another cell in the anticlockwise direction beside the original one. As γ increased further, the anticlockwise

cell is getting stronger and bigger, whereas the clockwise cell is getting weaker and smaller. The later eventually disappears as the cavity assumes its vertical position. At low Ra numbers, $Ra \leq 2000$, the change in Nu number is gradual and not as significant due to low velocity magnitudes, Fig 3.12.

At $Ra = 3000$, Nu number on the top wall encountered a 27% drop at γ between 20° and 25° , Fig. 3.12. At $\gamma = 25^\circ$ the anticlockwise cell became much stronger and the one rotating in the clockwise direction completely disappeared as shown in Fig. 3.11b. At $\gamma = 20^\circ$, the clockwise cell dominated the flow field, and so fluid was heated from the bottom and went directly to the cold top wall, which allowed the top wall to have higher rate of heat transfer. However, at $\gamma = 25^\circ$, the anticlockwise cell dominated the flow field, so fluid was pre-cooled from the right end wall, which greatly reduced rate of heat transfer from the top wall as shown in Fig. 3.12. As far as the rate of heat transfer from the bottom wall, at $\gamma \leq 20^\circ$, the clockwise cell was dominating the cavity. This cell opposed the upslope flow at the bottom wall, so Nu number at the bottom decreased and reached its lowest value at $\gamma = 20^\circ$. When γ further increased, the anticlockwise cell at the left side of the cavity became stronger and promoted the upslope flow at the bottom wall, which increased the rate of heat transfer from the bottom.

At $Ra=5000$ and 10^4 , mode transition was more abrupt than at $Ra=3000$ and occurred at higher angles of inclination. The change in Nu numbers at the bottom and top walls followed the same trend as in the case of $Ra = 3000$, except that the sudden drop in Nu was more pronounced as Ra increased.



Fig. 3.11 Normalized streamlines and isothermal lines for AC configuration at various angles of inclination and four Ra numbers. (a) Ra=1000, (b) Ra=3000, (c) Ra=5000, (d) Ra=10⁴. Positive values indicate rotation in clockwise direction.

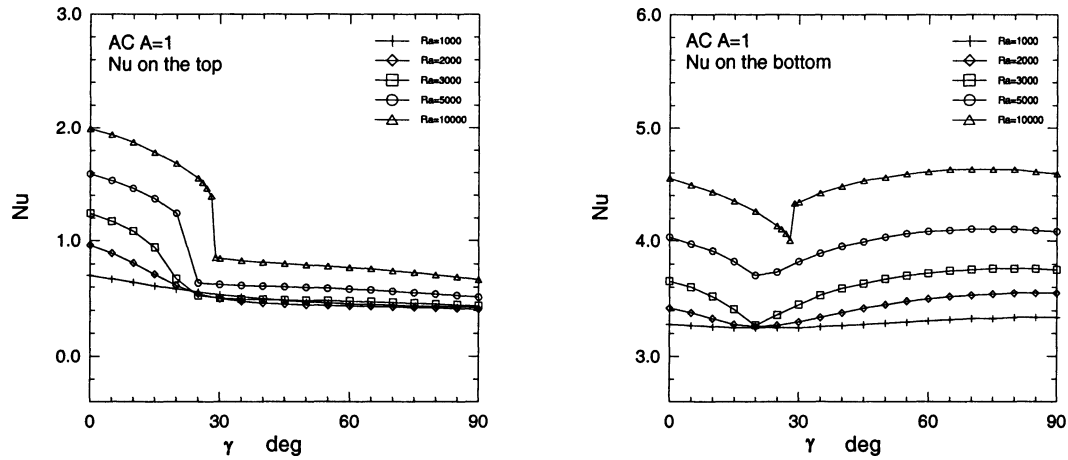


Fig. 3.12 Variation of average Nu number (both top and bottom walls) with inclination angle at various Ra numbers for AC configuration and A=1.

3.4.2 Case of decreasing γ

For angle decreasing, at $Ra \leq 3000$, no hysteresis phenomena could be observed as shown in Figs. 3.11, and 3.13. At $Ra=5000$ two solutions deviate in a small region of inclination around $20^\circ < \gamma < 25^\circ$, Fig 3.13c. At $Ra = 10^4$, hysteresis region extends to a wider range of γ between 15° and 30° , see Fig. 3.13d.

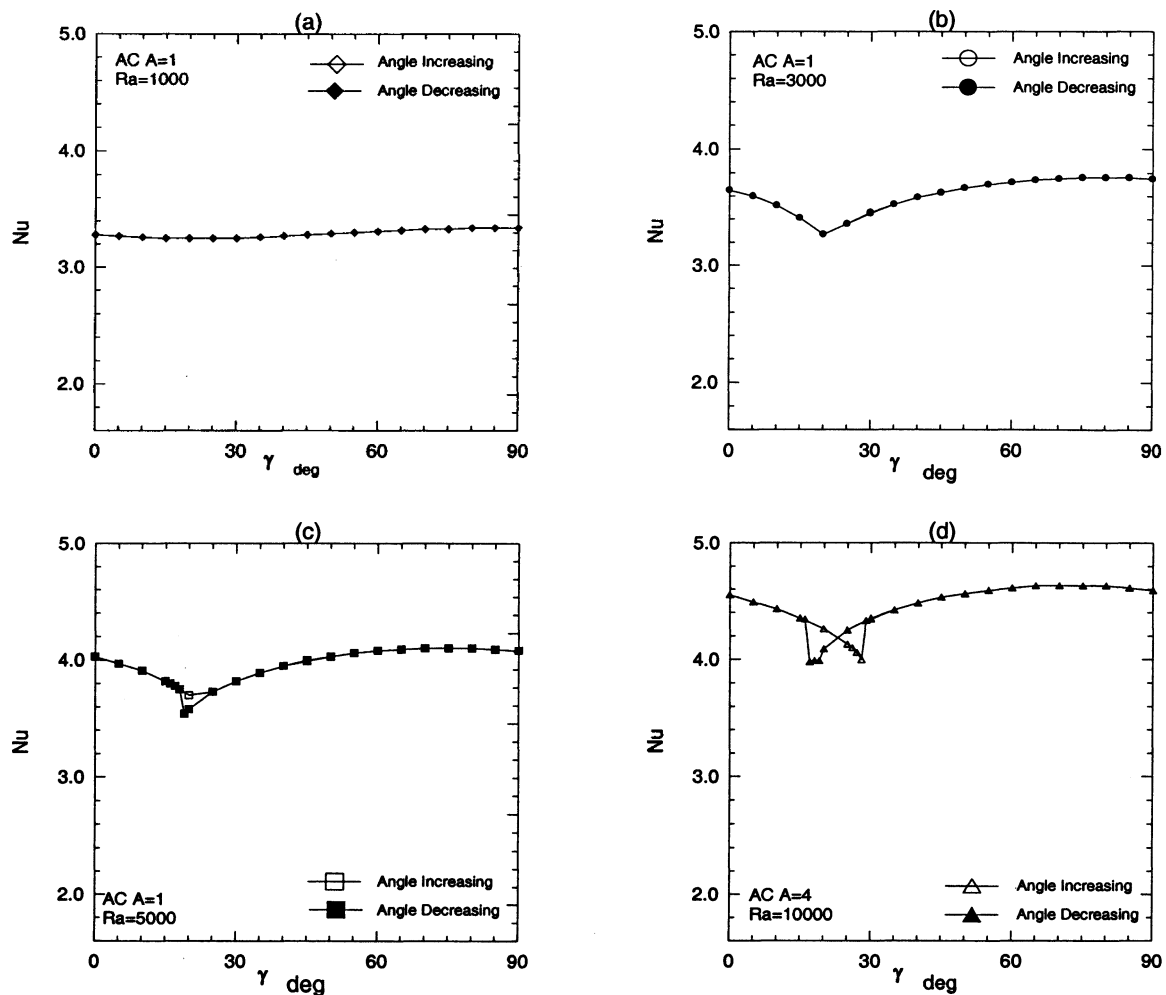


Fig. 3.13 Average Nu number (bottom wall) as a function of inclination angle γ for angle increasing and decreasing at various Ra numbers for AC configuration and A=1.

3.5 CA configuration

3.5.1 Case of increasing γ

All forces in the case of CA configuration impel convective cell rotating in the anticlockwise direction in both the horizontal and the inclined cavity cases. Anticlockwise cell is caused by the left cold wall even at a very low Ra number. For example, as Ra=1000, rotating cell is also formed, Fig. 3.14. During the process of increasing the angle of inclination from horizontal to vertical, this cell was always rotating in the same direction, so heat transfer rate did not experience any sudden changes.

As the left insulated wall was replaced with a cold wall, average Nu number at the top wall of the horizontal cavity increased continuously from 0.669 at $Ra=1000$ to 1.99 at $Ra=10^4$, as shown in Fig 3.15. Since cold area is doubled as compared with AA configuration, heat transfer rate of the hot bottom wall greatly increased. As shown in Figs. 3.15 and 3.2, Nu number at the bottom wall is at least 2.3 times of its value in the case of AA configuration at $\gamma = 0^\circ$, and at least 2.1 times at $\gamma = 90^\circ$.

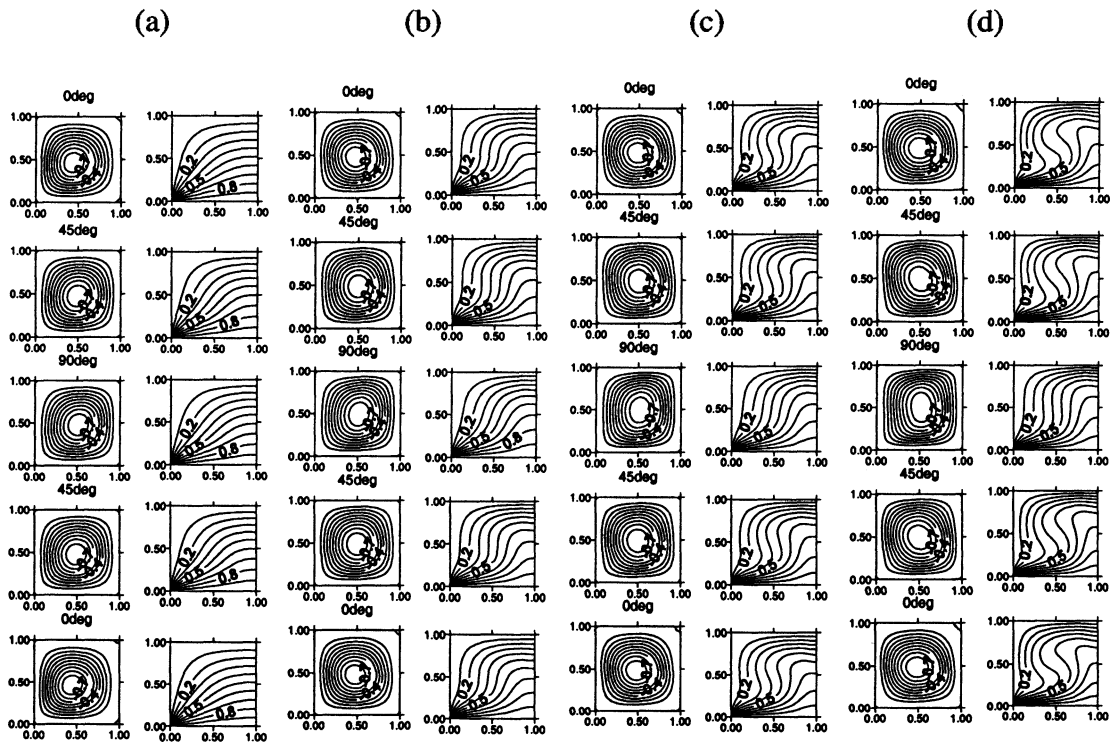


Fig. 3.14 Normalized streamlines and isothermal lines for CA configuration at various angles of inclination and four Ra numbers. (a) $Ra=1000$, (b) $Ra=3000$, (c) $Ra=5000$, (d) $Ra=10^4$. Positive values indicate rotation in clockwise direction.

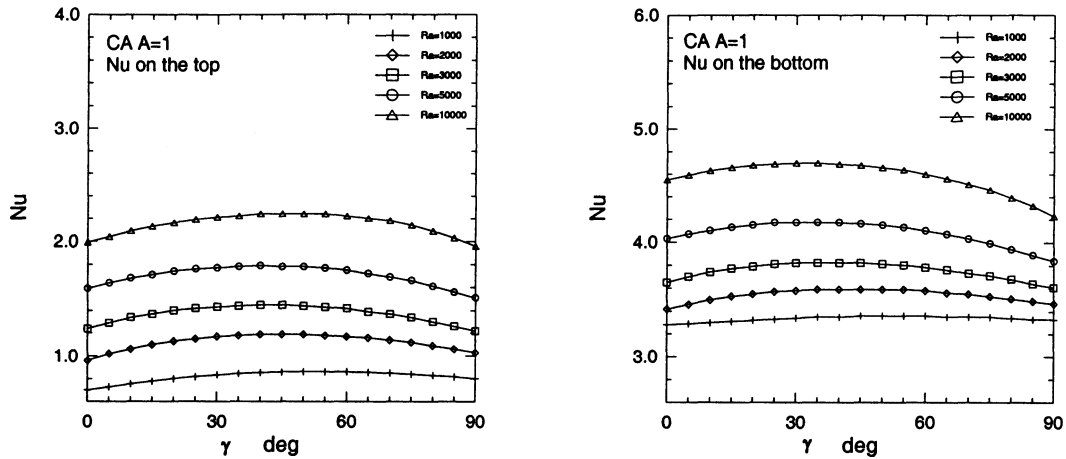


Fig. 3.15 Variation of average Nu number (both top and bottom walls) with inclination angle at various Ra numbers for CA configuration and A=1.

3.5.2 Case of decreasing γ

Since all forces cooperate with each other in keeping the convective cell rotating in the anticlockwise direction as cavity is inclining, flow fields produced for the case of angle decreasing were similar to those resulted in the case of angle increasing, as illustrated in Fig. 3.16, and therefore, no hysteresis phenomena could be observed.

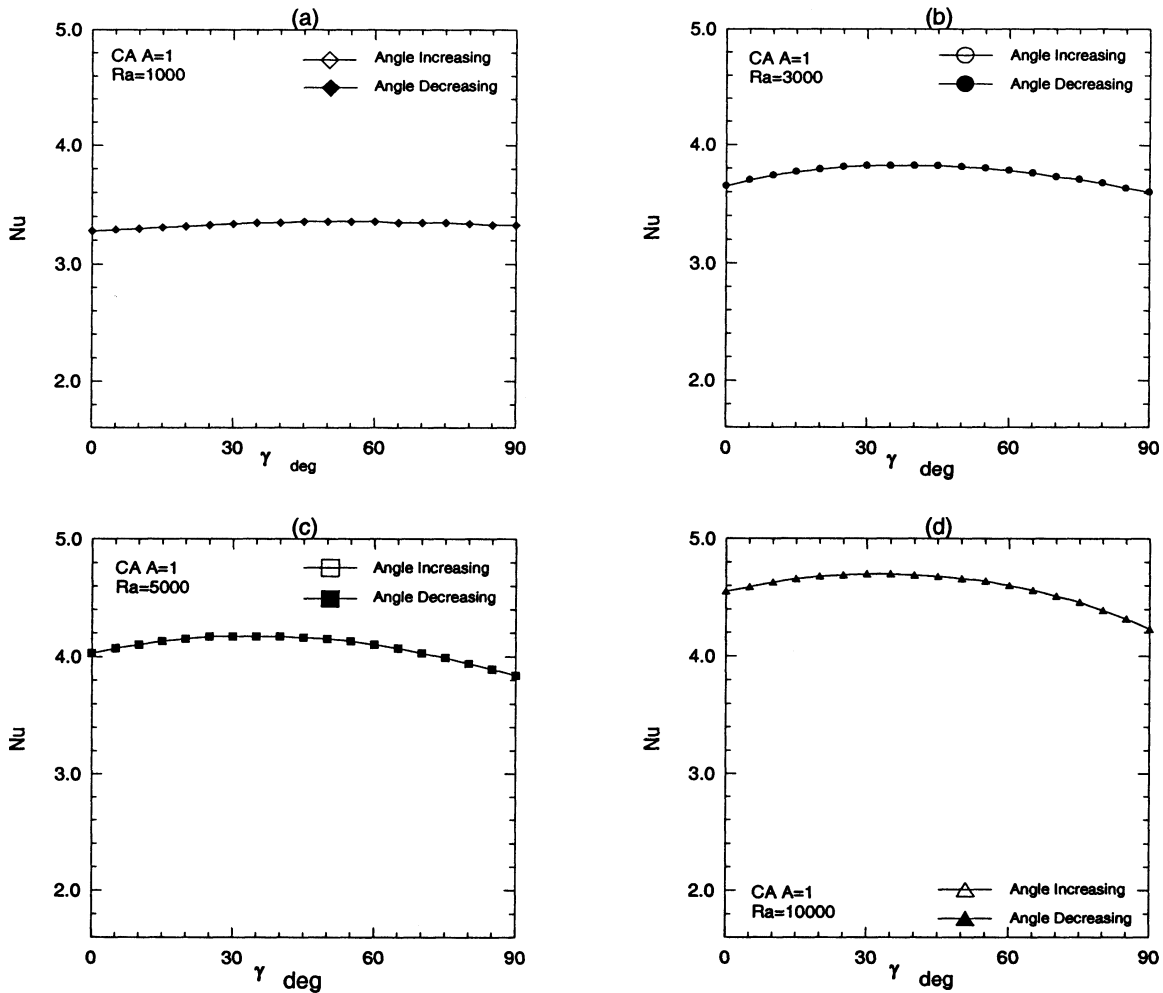


Fig. 3.16 Average Nu number (bottom wall) as a function of inclination angle γ for angle increasing and decreasing at various Ra numbers for CA configuration and A=1.

3.6 CC configuration

3.6.1 Case of increasing γ

At $\gamma = 0^\circ$, downward forces at the two cold end walls produced two cells for all Ra numbers, as shown in Fig. 3.17. As angle increased, the anticlockwise cell at the left side of the cavity was strengthened and the clockwise cell at the right side was decelerated by the upslope force at the heated bottom wall and the down slope force at the cold top wall. Eventually at $\gamma > 45^\circ$, mode transition from two cells pattern, observed at $\gamma = 0^\circ$, to one unicell flow structure was completed. It is worth noting here that, although there was

mode-transition, the process took place gradually, as evident from the gradual change in average Nu numbers of the top and bottom walls, see Fig. 3.18.

Compared with AA configuration, three walls are cold in the case of CC configuration, which is three times of the AA case. Heat transfer rate of the heated bottom wall, as was expected, greatly increased. At $Ra=10^4$ and $\gamma = 0^\circ$, Nu number is 2.88 times of the AA case. For Ra numbers 5000, 3000, 2000, 1000, Nu numbers are 3.19, 5.46, 5.42, 5.40 times that of the AA configuration, respectively. As for the top wall, although stronger convection is expected to enhance rate of heat transfer, the left and right end walls absorbed most of the energy from the bottom wall and the rate of heat transfer from the top wall was greatly reduced, see Figs. 3-18 and 3.2.



Fig. 3.17 Normalized streamlines and isothermal lines for CC configuration at various angles of inclination and four Ra numbers. (a) Ra=1000, (b) Ra=3000, (c) Ra=5000, (d) Ra=10⁴. Positive values indicate rotation in clockwise direction.

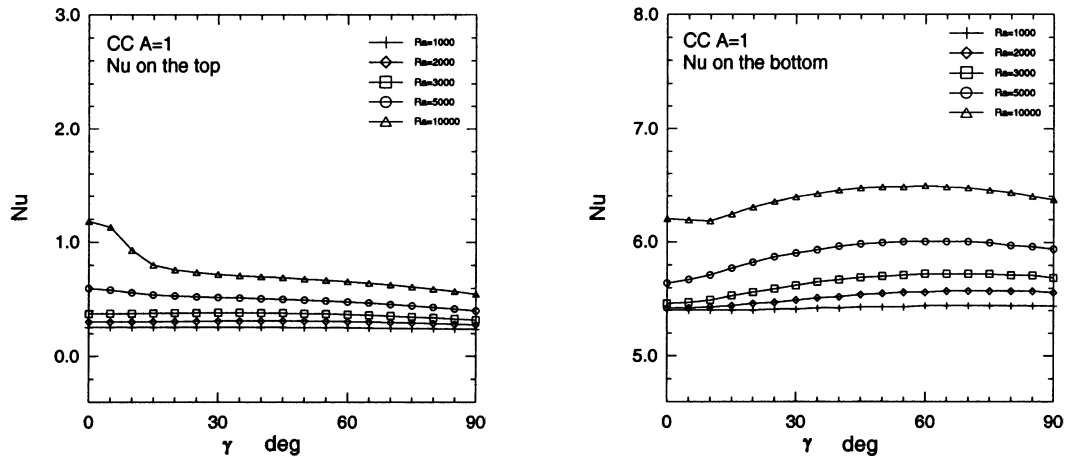


Fig. 3.18 Variation of average Nu number (both top and bottom walls) with inclination angle at various Ra numbers for CC configuration and A=1.

3.6.2 Case of decreasing γ

For angle decreasing, since the anticlockwise cell produced at $\gamma = 90^\circ$ was decelerated and became smaller, more space was available for a clockwise cell to appear at the right side that was produced by the buoyancy force at the right cold wall and the cross force at the heated bottom wall. Hysteresis phenomena could not be observed in this case as shown in Fig. 3.19.

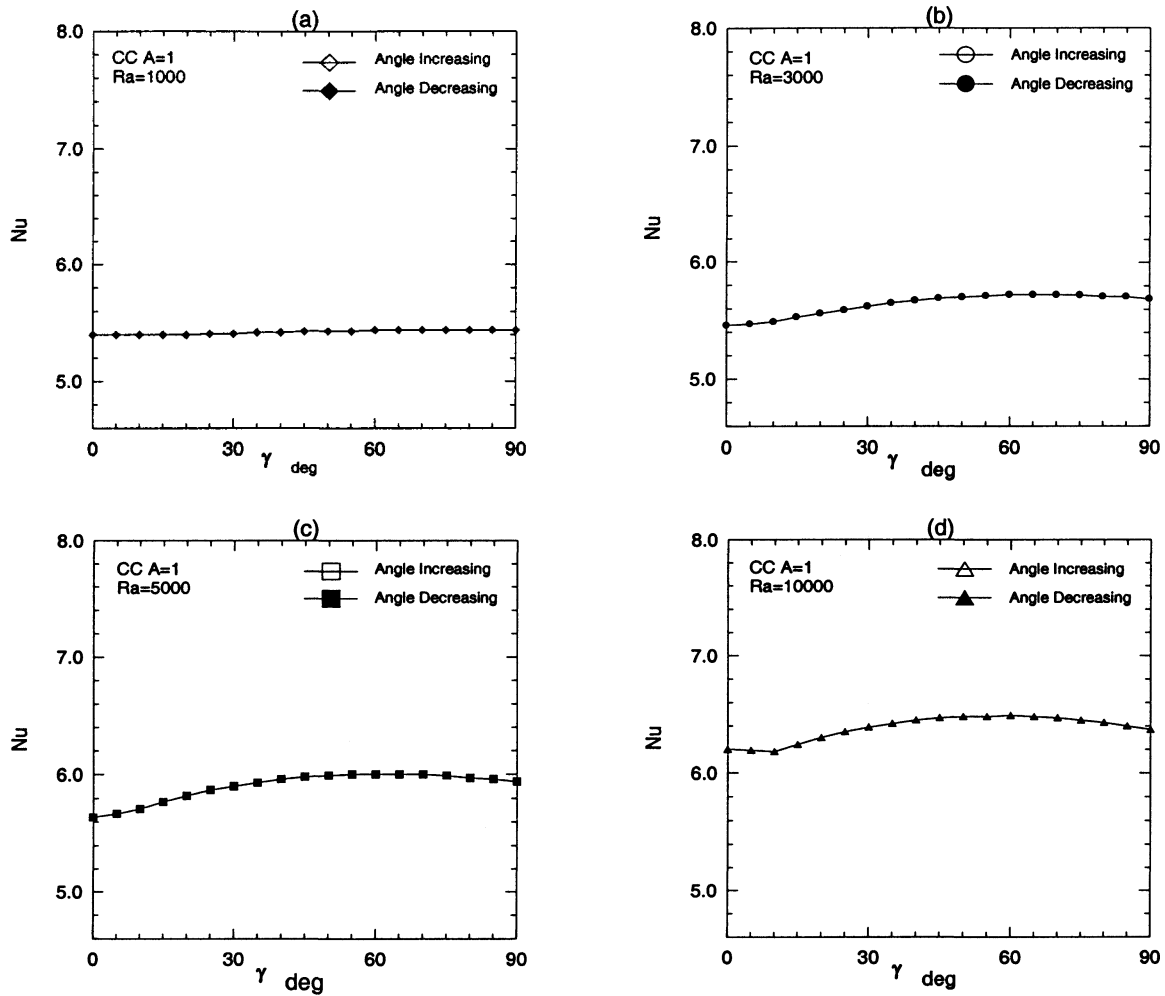


Fig. 3.19 Average Nu number (bottom wall) as a function of inclination angle γ for angle increasing and decreasing at various Ra numbers for CC configuration and A=1.

3.7 LL configuration

3.7.1 Case of increasing γ

With the two end walls having linear temperature distributions, convection took place at much higher Ra number. The critical value of Ra number for the LL configuration is more than 5000, see Fig. 3.20, which is much higher than that was observed in the case of AA configuration, Fig 3.1. For Ra number ≤ 5000 , Nu number is equal to 1.0. Normalized streamlines and isothermal lines as presented in Fig. 3.20. For Ra=10000, convective flow starts with a clockwise cell. Due to the symmetry of the

thermal conditions in LL configuration, another solution having an anticlockwise cell is also expected if sweeping direction in the numerical algorithm was reversed. For $Ra=1000$ and 3000 , flow field end up with the conduction limit when cavity come back to 0° from 90° . For $Ra=5000$, it ends up with an anticlockwise cell due to stronger velocities in the initial condition for $\gamma=0^\circ$ in the angle decreasing case. Heat transfer rate increased between $\gamma = 0^\circ$ to 40° and remained almost unchanged from $\gamma = 45^\circ$ to 90° , Fig. 3.21. Heat transfer rate in this case is lower than of the AA configuration because fluid is preheated for the bottom wall and pre-cooled for the top wall regardless of the rotating directions.

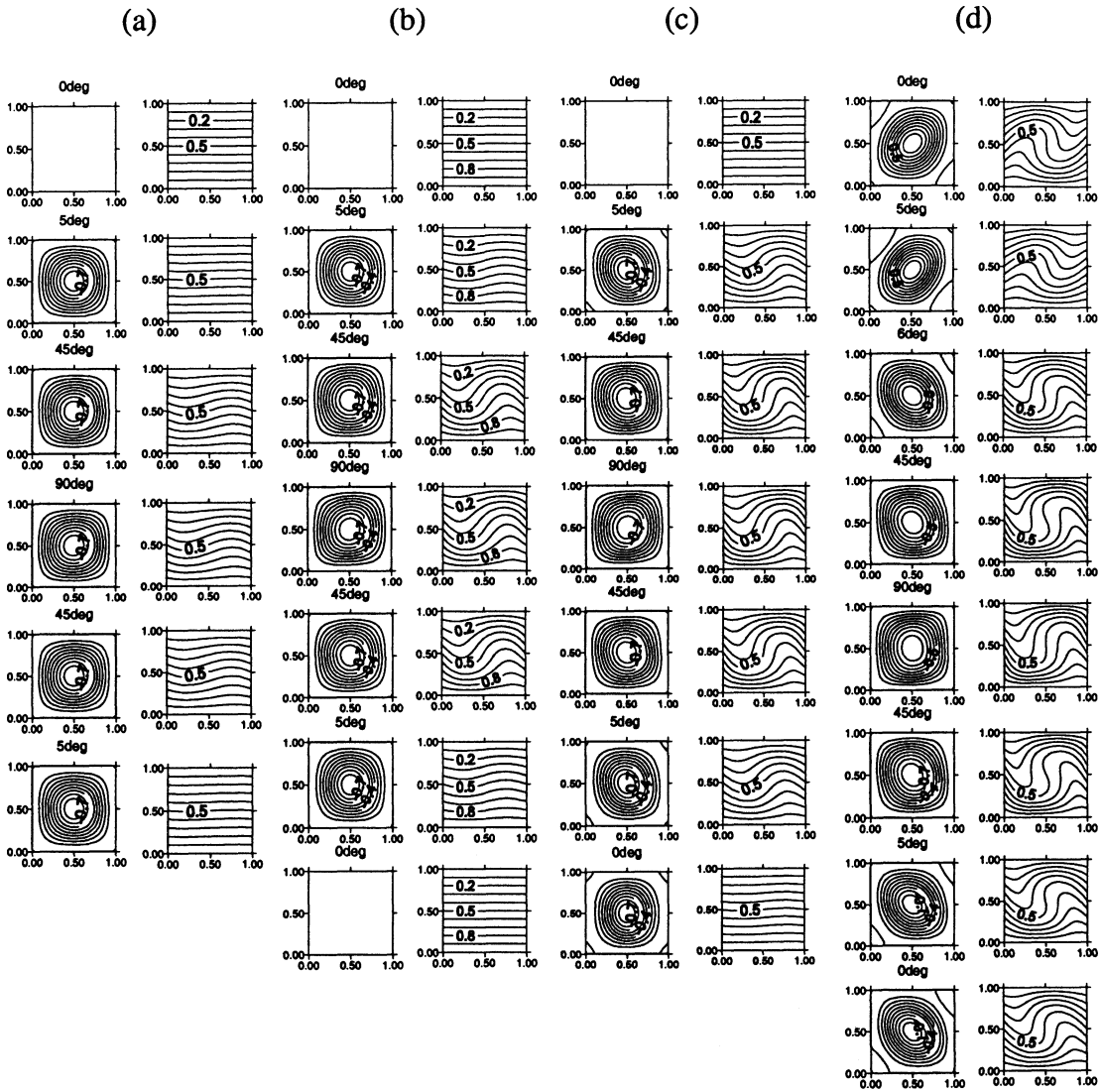


Fig. 3.20 Normalized streamlines and isothermal lines for LL configuration at various angles of inclination and four Ra numbers. (a) Ra=1000, (b) Ra=3000, (c) Ra=5000, (d) Ra=10⁴. Positive values indicate rotation in clockwise direction.

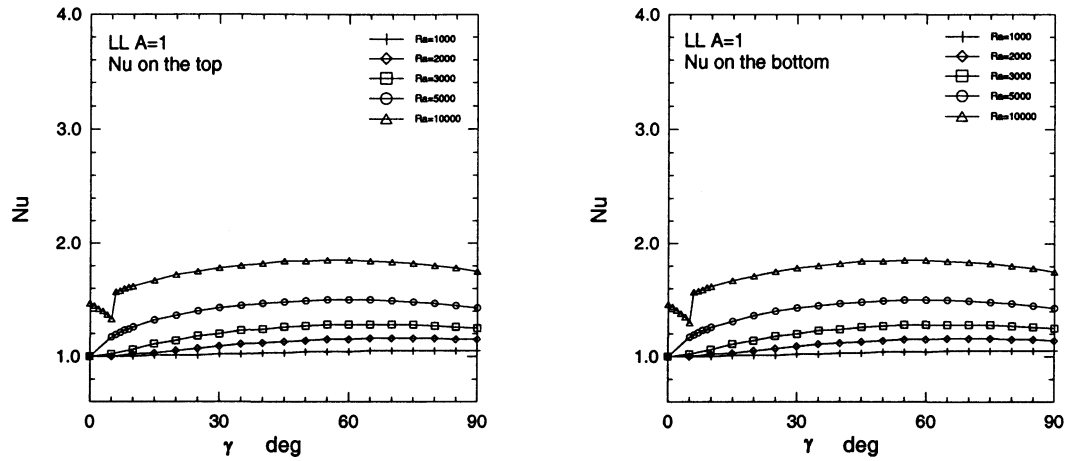


Fig. 3.21 Variation of average Nu number (both top and bottom walls) with inclination angle at various Ra numbers for LL configuration and A=1.

3.7.2 Case of decreasing γ

No hysteresis phenomena was observed for all Ra numbers except at $Ra = 10^4$ at $1^\circ \leq \gamma \leq 5^\circ$, in Fig. 3.22.

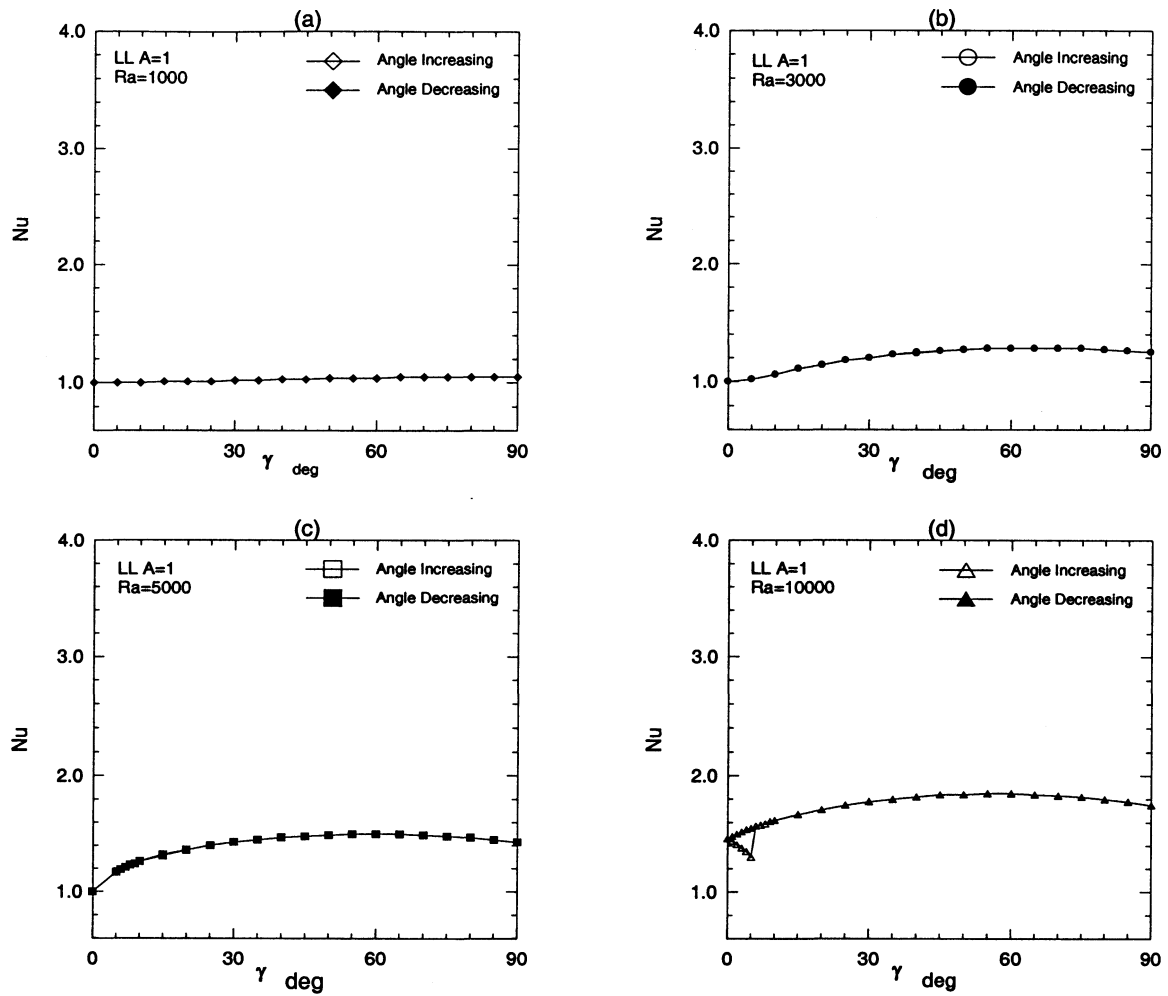


Fig. 3.22 Average Nu number (bottom wall) as a function of inclination angle γ for angle increasing and decreasing at various Ra numbers for LL configuration and A=1.

Chapter 4

Numerical Results - Case of Rectangular Cavity with Flat Bottom

In many of the practical applications mentioned in chapter 1, cavities are not necessarily square, but rather, rectangular. It has been confirmed through many studies that increasing cavity aspect ratio introduces much more complexity into the nature of thermally driven convection flows. In the present chapter, results obtained for the case of rectangular cavities with flat bottom are presented considering the seven configurations of end wall thermal conditions shown in Fig. 1.7, Ra number in the range between 10^3 and 10^4 , Pr number constant at 0.7. Two aspect ratios have been investigated, namely, $A = 2$ and 4. Starting with $\gamma=0^\circ$, similar to the routine employed in the case of square cavities, steady, two-dimensional natural convection flows have been investigated considering two cases of changing cavity angle of inclination: increasing from $\gamma = 0^\circ$ to 90° ; and decreasing from $\gamma = 90^\circ$ back to 0° . Results obtained for $A = 2$ will be presented and discussed first followed by those obtained for $A = 4$.

4.1 Rectangular cavity with $A=2$

As width/height aspect ratio increases from 1 to 2, end walls will have less effect on the entire natural convection flow inside the cavity. Higher aspect ratio means that viscous dissipation or friction at the two end walls will have less influence inside the cavity; and consequently, flow patterns with multi-cells are much easier to form, as compared with the case of aspect ratio =1, presented in chapter 3. Because flows with multi-cells co-exist inside the cavity, flow mode-transition is possible to occur. Flow

mode-transition means that a multi cells flow pattern merges into a unicell mode or unicell is divided into multi cells. Flow mode-transition in rectangular inclined cavities has been reported and investigated by Soong and Tzeng [21]. However, they considered only cavities with insulated end walls, which is equivalent to AA configuration and $A=4$ of the present study.

4.1.1 AA configuration

4.1.1.1 Case of increasing γ

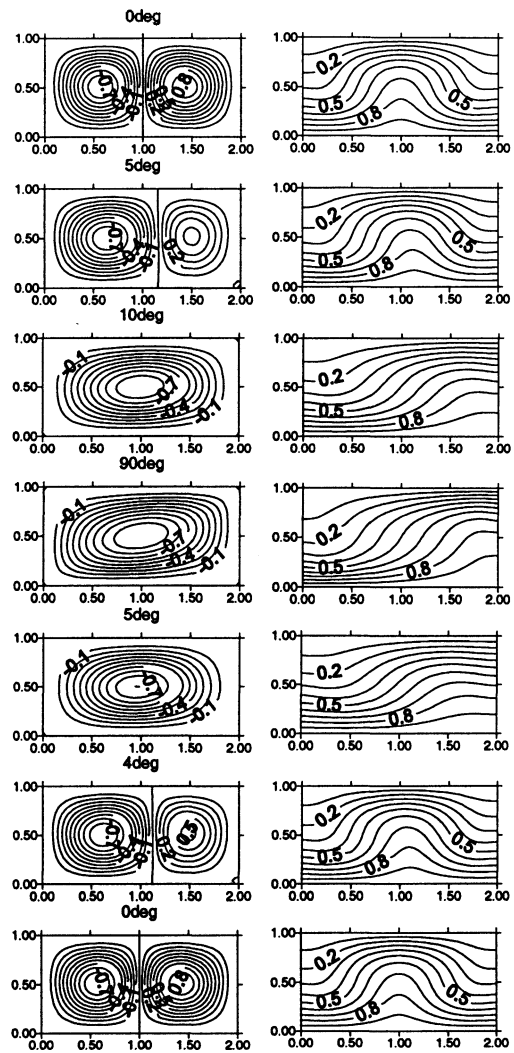
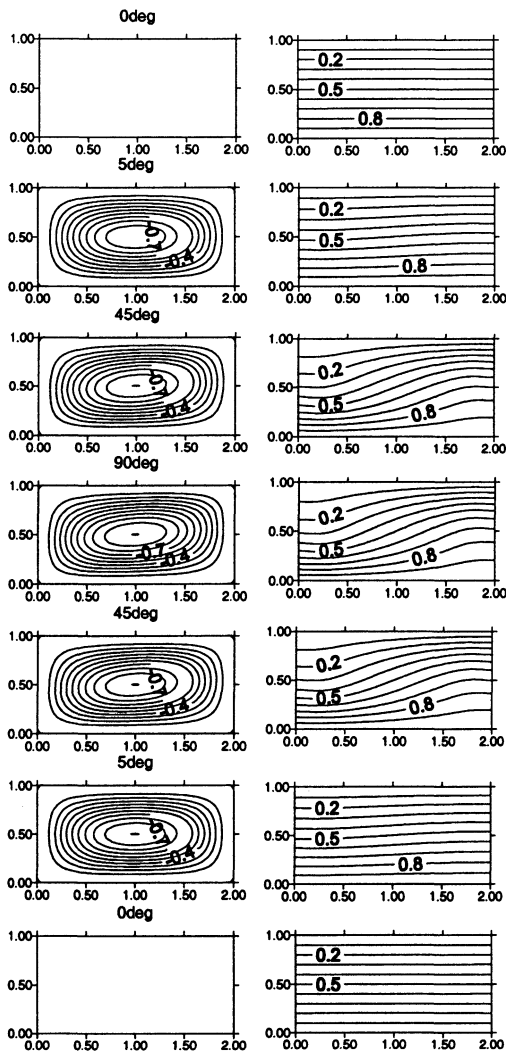
At $Ra = 1000$ and $\gamma = 0^\circ$, no convection flow is produced and heat transfer inside the cavity is dominated by conduction. As γ increased to 5° , upslope and down slope buoyancy forces at the hot bottom and cold top walls accelerated the flow and produced a unicell flow structure with convective cell rotating in the anticlockwise direction, as shown in Fig 4.1a. Nu number at both top and bottom walls is still equal to 1.0, Fig. 4.2, i.e., a conduction-dominated flow or what is called a “basic”-flow still controls heat transfer inside the cavity. The anticlockwise cell became stronger as γ further increased up to 90° . At $Ra = 3000$ and $\gamma = 0^\circ$, due to friction at the two end walls, fluid at the middle of the cavity rises at a higher velocity than that of the fluid at each end wall, resulting into a multi-cell flow structure having two cells. The right hand side cell (RHSC) rotates in the clockwise direction, while the one on the left hand side (LHSC) rotates in the anticlockwise direction. As γ increased to 5° , the upslope and down slope forces at the bottom and top walls increased, which strengthened and enlarged the LHSC and at the same time decelerated and decreased the size of the RHSC, Fig 4.1b. At $\gamma = 10^\circ$, the RHSC has completely vanished, the LHSC occupied the whole cavity, and

therefore, mode-transition completed. It is worth noting here that for $\gamma \leq 10^\circ$, although the cell at the left end is accelerated, the one at the right end is greatly decelerated, the overall rate of heat transfer of the top and bottom walls decreased, as shown in Fig 4.2. Flow patterns with more cells produced higher rates of heat transfer inside cavity. This conclusion has been arrived at in many instances, as will be discussed later.

At $\gamma \geq 10^\circ$ the unicell structure dominated all the way up to $\gamma = 90^\circ$. However, as shown in Fig 4.2, the rate of heat transfer of both walls increased as γ increased up to 60° then decreased as $\gamma > 60^\circ$, for Ra numbers between 1000 and 5000. For Ra = 10^4 , this value would be changed to $\gamma = 55^\circ$. This result is similar with what was observed in the experimental investigation in inclined cavities reported in [19]. The variation in rate of heat transfer rate of the unicell pattern during γ increasing can be explained by looking at velocity distributions inside the cavity, i.e. high velocity would result in better heat transfer rate if there is only one cell in the whole cavity. For example, at Ra = 5000, the maximum stream function ψ_{\max} is equal to 9.47, when unicell pattern is formed. It keeps increasing from 9.47 to 11.1 at $\gamma = 60^\circ$ and then decreases to 9.76 at $\gamma = 90^\circ$. The change tendency in Nu number is exactly the same as that of the stream function. The value of the stream function actually denotes the strength of the cell. At Ra = 3000 and 10^4 , similar trends between stream function and heat transfer rate can be obtained except that the value of γ at which mode transition took place is different.

(a)

(b)



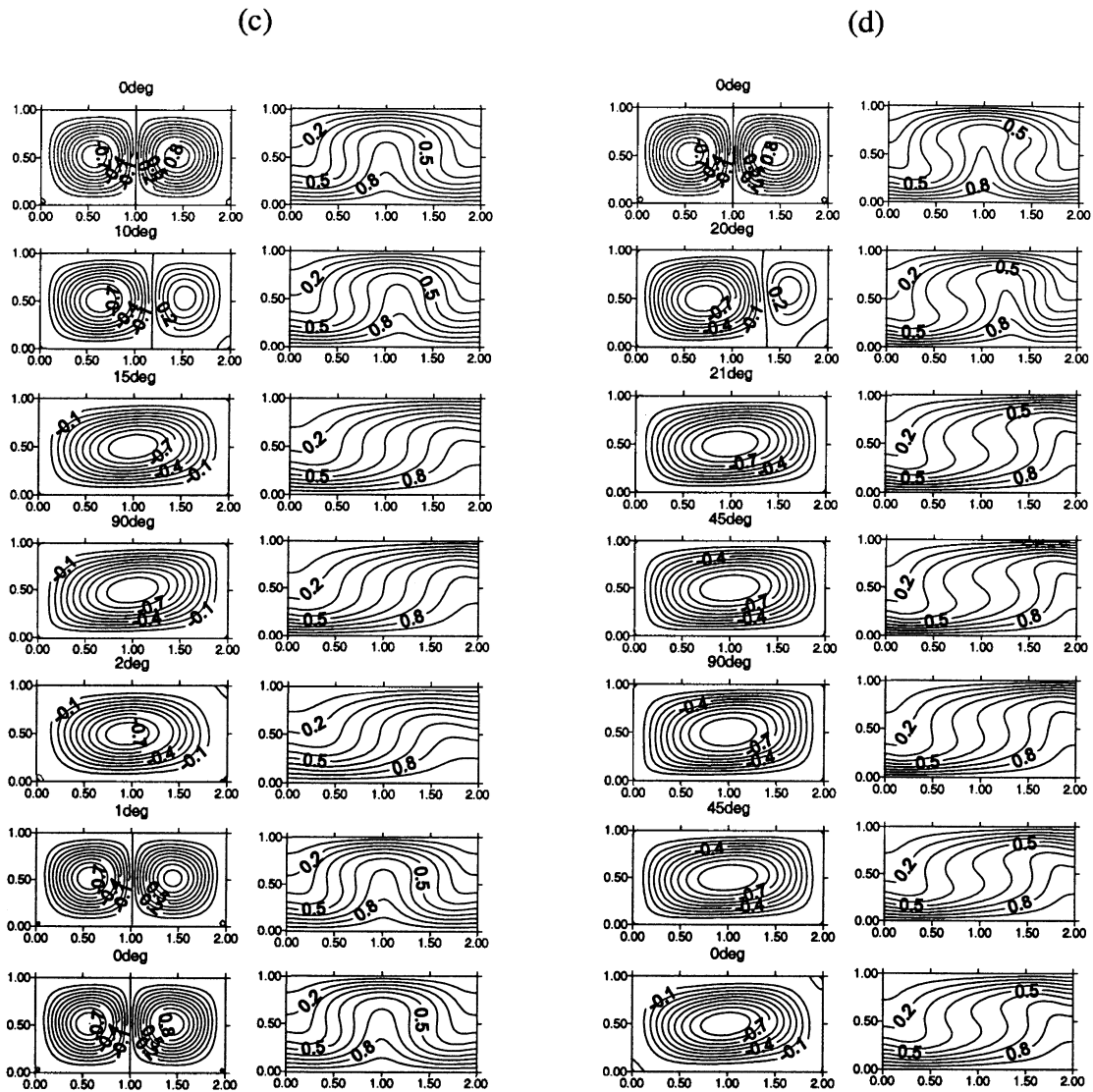


Fig. 4.1 Normalized streamlines and isothermal lines for AA configuration at various angles of inclination and four Ra numbers. (a) Ra=1000, (b) Ra=3000, (c) Ra=5000, (d) Ra=10⁴. Positive values indicate rotation in clockwise direction.

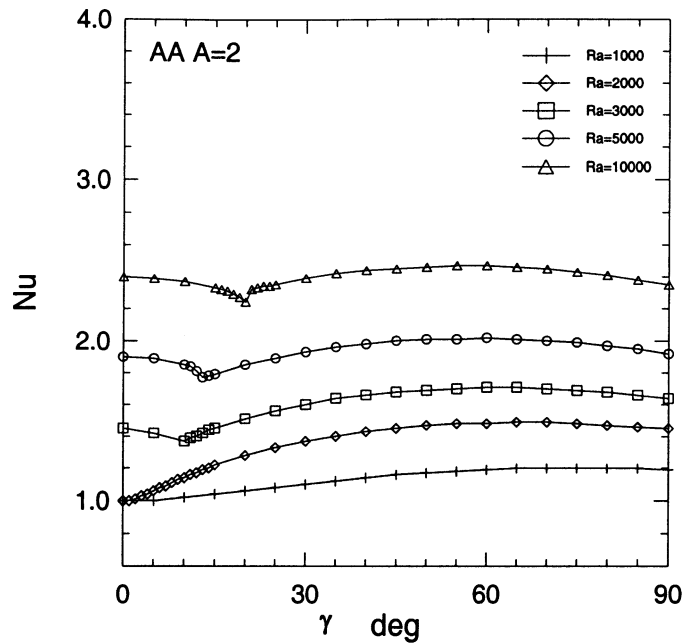


Fig. 4.2 Variation of average Nu number (both top and bottom walls) with inclination angle at various Ra numbers for AA configuration and A=2.

The variation in rate of heat transfer rate of the unicell pattern during increasing γ can also be explained by looking at the distribution of velocity component in x-direction, u , at a location close to the wall. Distributions of u for $Ra = 5000$ at $y = 0.05$ and $\gamma = 45^\circ$, 60° , and 75° are shown in Fig. 4.3. These three velocity distributions clearly indicate that u reaches its maximum value at $\gamma = 60^\circ$, where rate of heat transfer is at its maximum value. At $\gamma = 45^\circ$ and 75° , the two distributions are almost the same, so rates of heat transfer at these two angles are very close to each other.

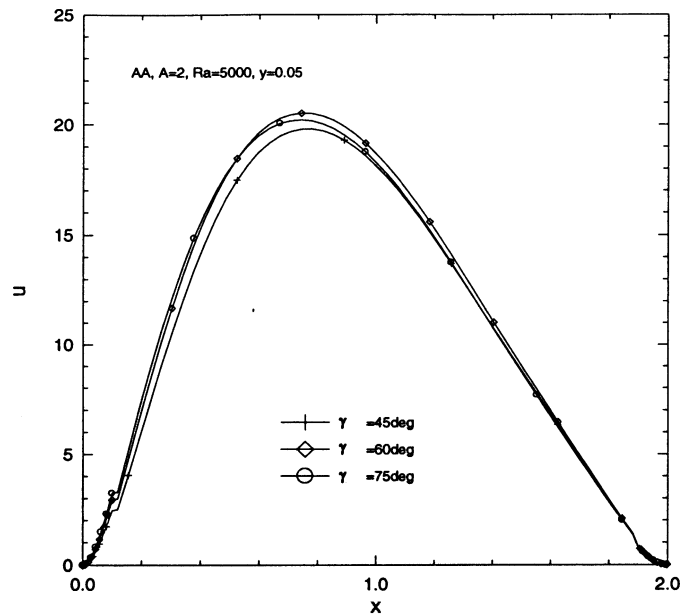


Fig. 4.3 Distribution of velocity component in x-direction at various angles of inclination, Ra = 5000, AA configuration.

Comparison between results of $A = 2$ and those of $A = 1$ shows that as A increased, value of critical Ra number decreased, i.e., convection takes place at lower Ra numbers. This observation is consistent with what has been reported in the literature. Viscous dissipation at the two end walls in the case of small A requires higher driving forces to initiate convection flows inside the cavity.

The other important observation is that at $A = 1$ unicell flow patterns dominated almost all cases of Ra and γ considered. At $A = 2$ both multi-cell and unicell flow structures appeared, and hence mode transformation took place, which resulted in sudden changes in rate of heat transfer shown in Fig 4.2.

4.1.1.2 Case of decreasing γ

At Ra = 1000, Fig 4.4a, no significant difference between results obtained in the two courses of changing γ was observed. However, at Ra = 3000, Fig 4.4b, two solutions

deviate in a small region of angle of inclination around $5^\circ < \gamma < 10^\circ$. In the case of γ decreasing, initial conditions with higher velocities resulted in a delay in mode-transition until $\gamma = 4^\circ$. However, at $\gamma < 5^\circ$, the same flow fields and rates of heat transfer have been restored, Fig 4.4b.

At $Ra = 5000$, hysteresis region extends to higher angles of inclination $\gamma \leq 15^\circ$, and, again, flow fields and heat transfer rates are exactly the same at $\gamma = 0^\circ$, Fig. 4.4c. At $Ra = 10^4$, hysteresis region extends to $\gamma \leq 20^\circ$ and heat transfer rates at $\gamma = 0^\circ$ is lower by 15.8% than that obtained at $\gamma = 0^\circ$ in the case of angle increasing, Fig 4.4d. Fig. 4.1 (d) indicates that flow field starts with two cells at the beginning of the inclination and ends up with one cell, this is the reason for the lower Nu number obtained for angle decreasing at $\gamma = 0^\circ$.

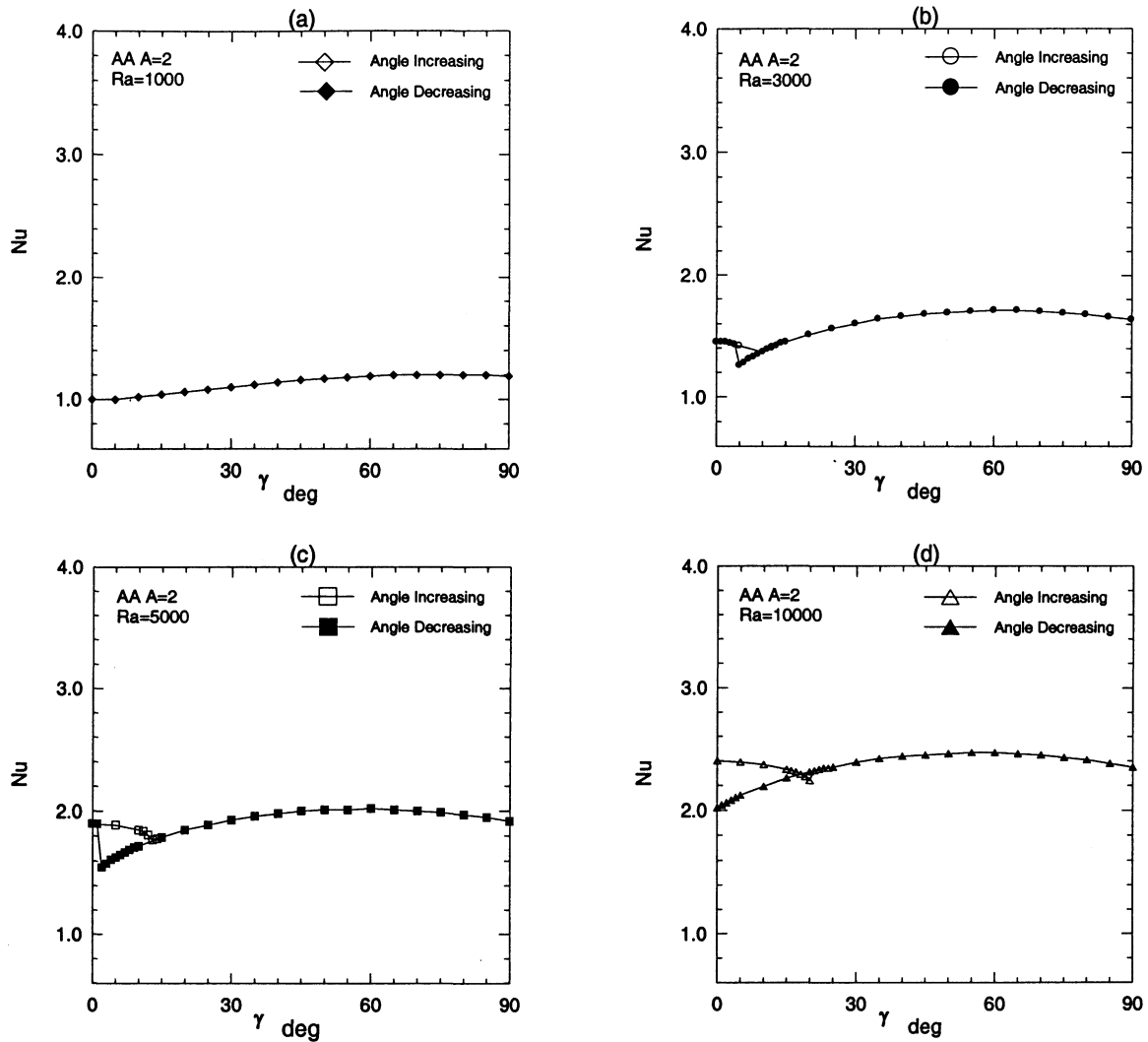


Fig. 4.4 Average Nu number (bottom wall) as a function of inclination angle γ for angle increasing and decreasing at various Ra numbers for AA configuration and A=2.

Hysteresis phenomenon discussed above for the case of A =2 is due to mode transition from two-cell to unicell flow patterns. For A = 1 case hysteresis observed was because of change in direction of rotation of the unicell flow pattern observed in that case. That change in direction of rotation, as discussed in chapter 3, depends on either a physical reason such as different thermal boundary conditions, or on a numerical reason such as sweeping direction used in the iterative procedure.

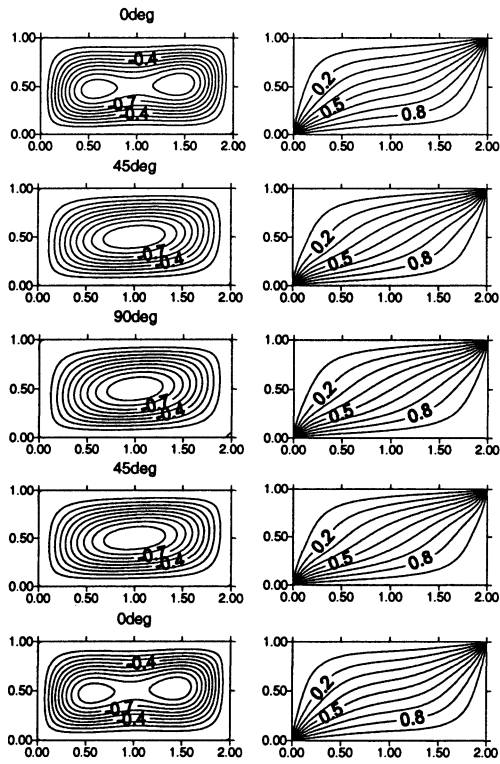
4.1.2 CH configuration

4.1.2.1 Case of increasing γ

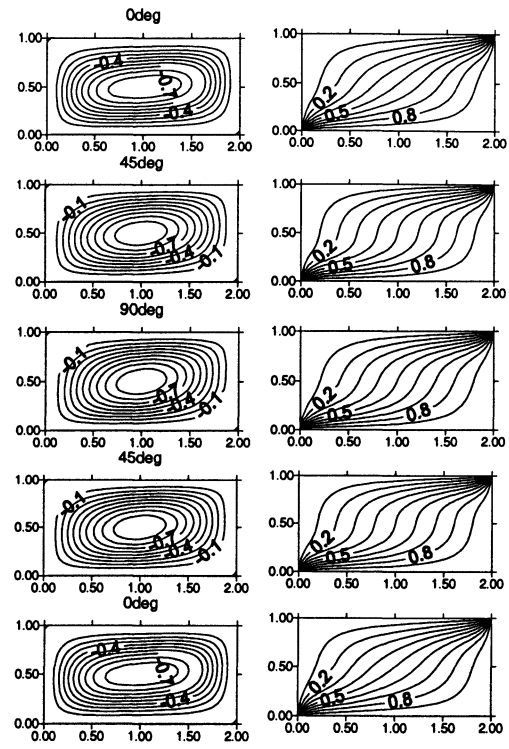
In CH configuration, because fluid is accelerated due to temperature gradients at both the left and right end walls, where ψ_{\max} is at least 22.0 % higher than that obtained in the case of AA configuration. For all Ra numbers, produced cells are strong enough to occupy the whole cavity and no mode-transition is observed. Therefore, for all values of Ra number, only unicell flow patterns are produced, as shown in Fig. 4.5. It is worth noting here that at Ra = 1000 and $\gamma = 0^\circ$, due to low velocities produced in this case, flow structure is in the form of what is called two-in-one unicell pattern, which is observed only for Ra = 1000 and $\gamma = 0^\circ$. Anticlockwise rotating cells remained all the way from $\gamma = 0^\circ$ up to $\gamma = 90^\circ$ and back to 0° , see Fig. 4.5. Heat transfer rate is greatly enhanced compared with AA configuration. At $\gamma = 0^\circ$, i.e., in the case of horizontal cavity, Nu number for CH configuration is 31%, 42%, 62.0%, 115%, 100% higher than the AA configuration, for Ra=10⁴, 5000, 3000, 2000, and 1000, respectively, as shown in Figs. 4.2 and 4.6. At $\gamma = 90^\circ$, i.e., in the case of vertical cavity, CH configuration also has significantly higher heat transfer rates than AA configuration.

CH configuration has better heat transfer rate than AA configuration due to the effect of the end wall. The area of the end walls for A=2 case is 33.3% of all the walls of the cavity. While for A=1 case, it is 50%. So the enhancement in rate of heat transfer for A=1 case should be greater than A = 2 case. Nu number for A = 2 case is, as expected, lower than that of the A = 1 case.

(a)



(b)



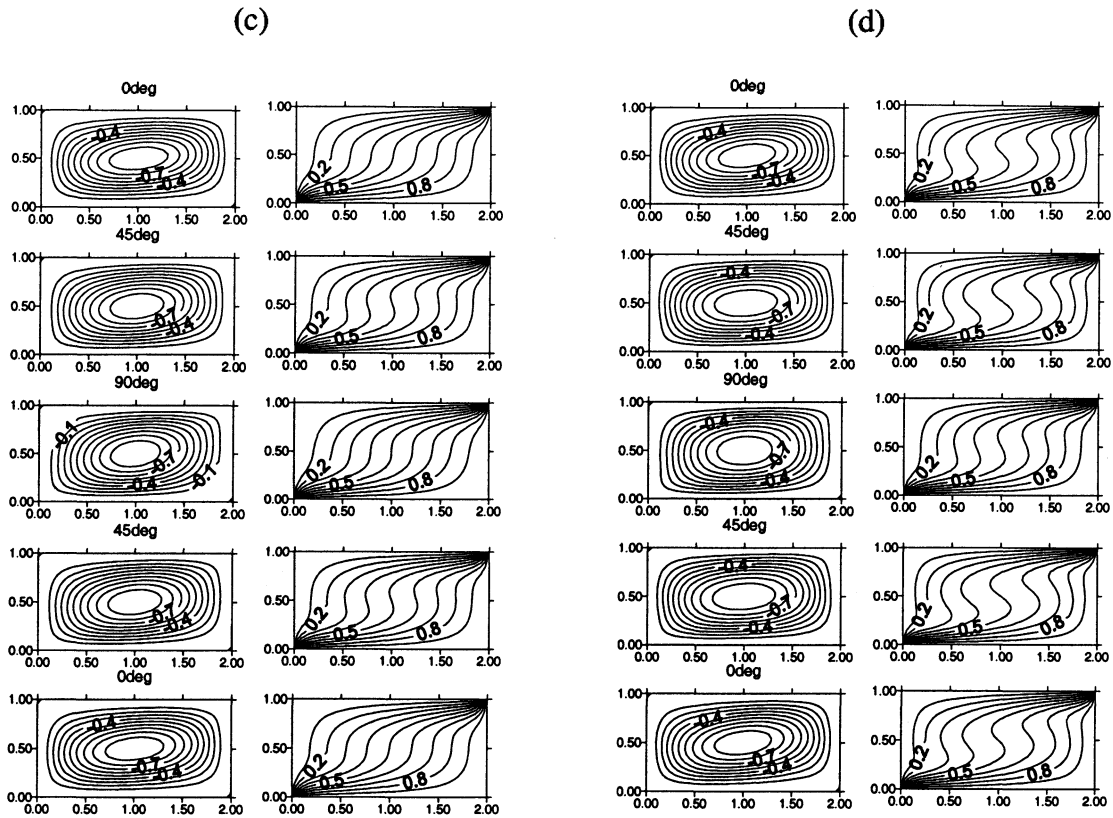


Fig. 4.5 Normalized streamlines and isothermal lines for CH configuration at various angles of inclination and four Ra numbers. (a) Ra=1000, (b) Ra=3000, (c) Ra=5000, (d) Ra=10⁴. Positive values indicate rotation in clockwise direction.

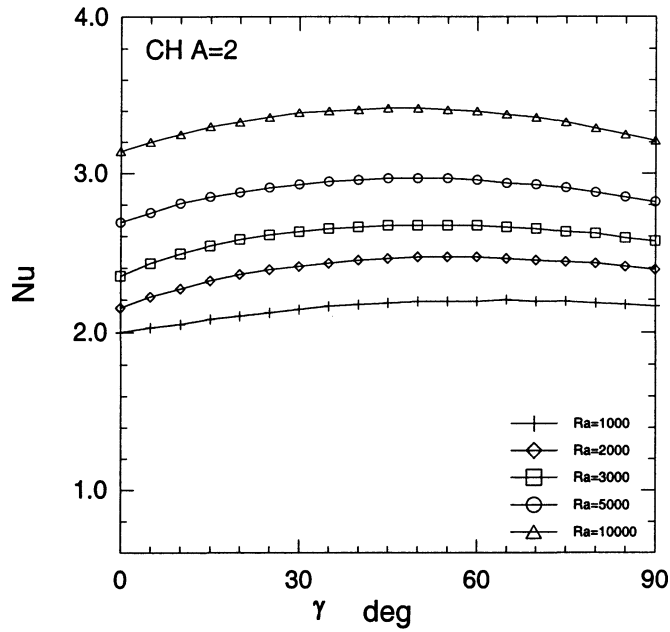


Fig. 4.6 Variation of average Nu number (both top and bottom walls) in the case of increasing angle of inclination at various Ra numbers for CH configuration and A=2.

4.1.2.2 Case of decreasing γ

No mode transition or hysteresis phenomenon can be observed in this case, as shown in Fig. 4.5 and 4.7, which is the same as A=1 case.

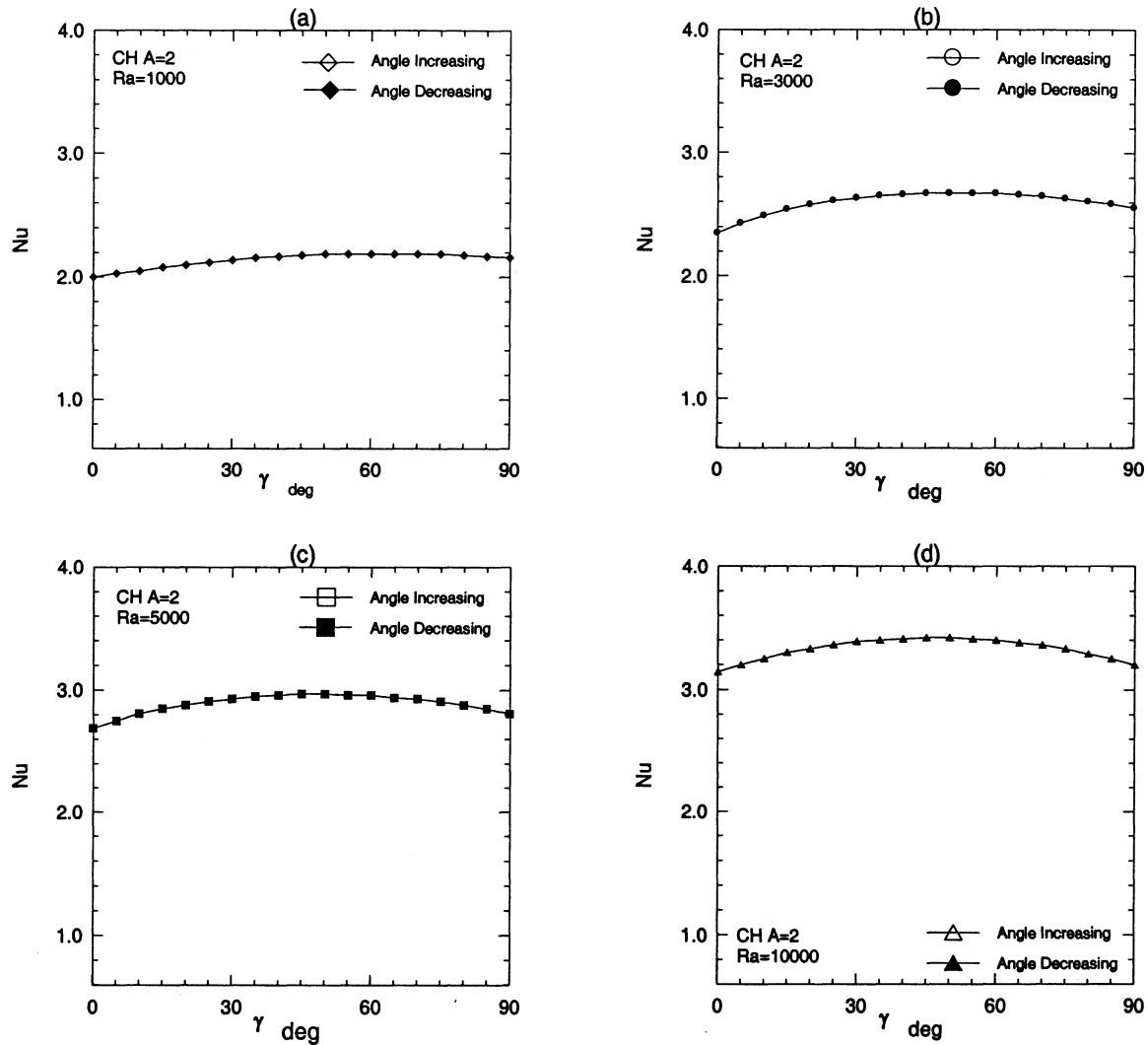


Fig. 4.7 Average Nu number (bottom wall) as a function of inclination angle γ for angle increasing and decreasing at various Ra numbers for CH configuration and A=2.

4.1.3 HC configuration

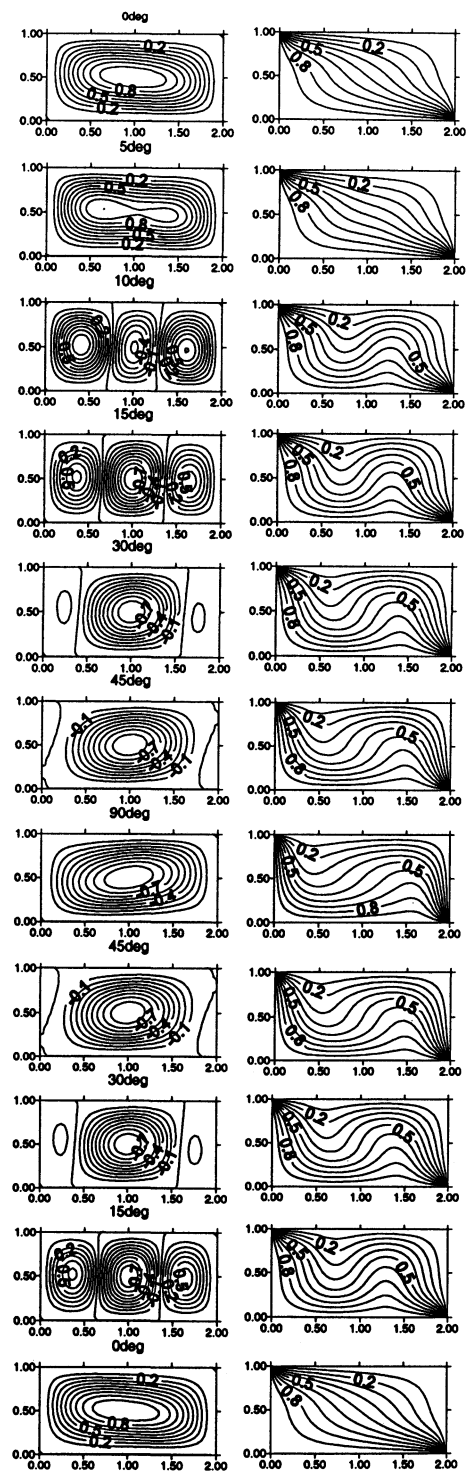
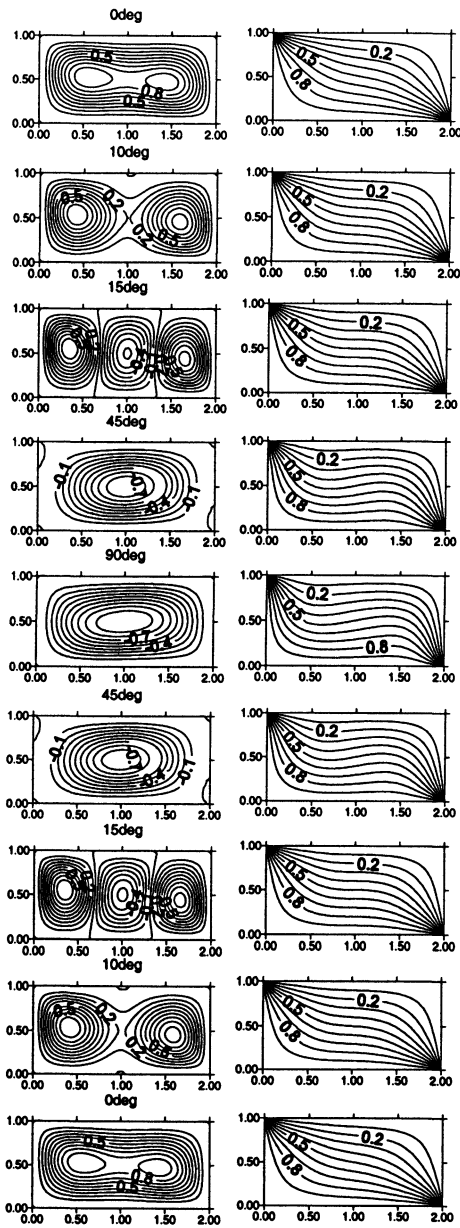
4.1.3.1 Case of increasing γ

Temperature gradients at the left hot end wall and at the right cold end wall compel fluid in clockwise direction, Fig. 4.8. Cell rotates in this direction is further heated by left end wall and further cooled by the right end wall, so heat transfer rate is greatly increased, as compared with AA configuration, by 100%, 115%, 62.1%, 41.6%, 30.8% for Ra=1000, 2000, 3000, 5000, and 10^4 , respectively, in the case of horizontal

cavity, as shown in Figs. 4.9 and 4.2. As cavity is inclined, velocities inside the cavity are reduced with the development of the upslope force from bottom wall, so the unicell flow mode can not occupy the whole cavity and is transformed into a three-cell pattern as shown in Fig. 4.8. As a result of that mode-transition from unicell to multi-cell, a drastic increasing in Nu number can be observed in Fig. 4.9. As cavity is further inclined, clockwise rotating cells on the left and right sides of the cavity can not resist the increasing upslope force and finally form a unicell flow pattern with one cell rotating in the anticlockwise direction for $Ra < 10^4$. For $Ra=10^4$, cross force plays more important role in the development of the flow field. As inclination angle increases, cross force from the bottom wall decreases, which decelerates the clockwise rotating cell at the right side of the cavity, so that cell disappears before the cell at the left part. While cavity is further inclined, unicell forms after $\gamma = 45^\circ$, Fig. 4.8.

(a)

(b)



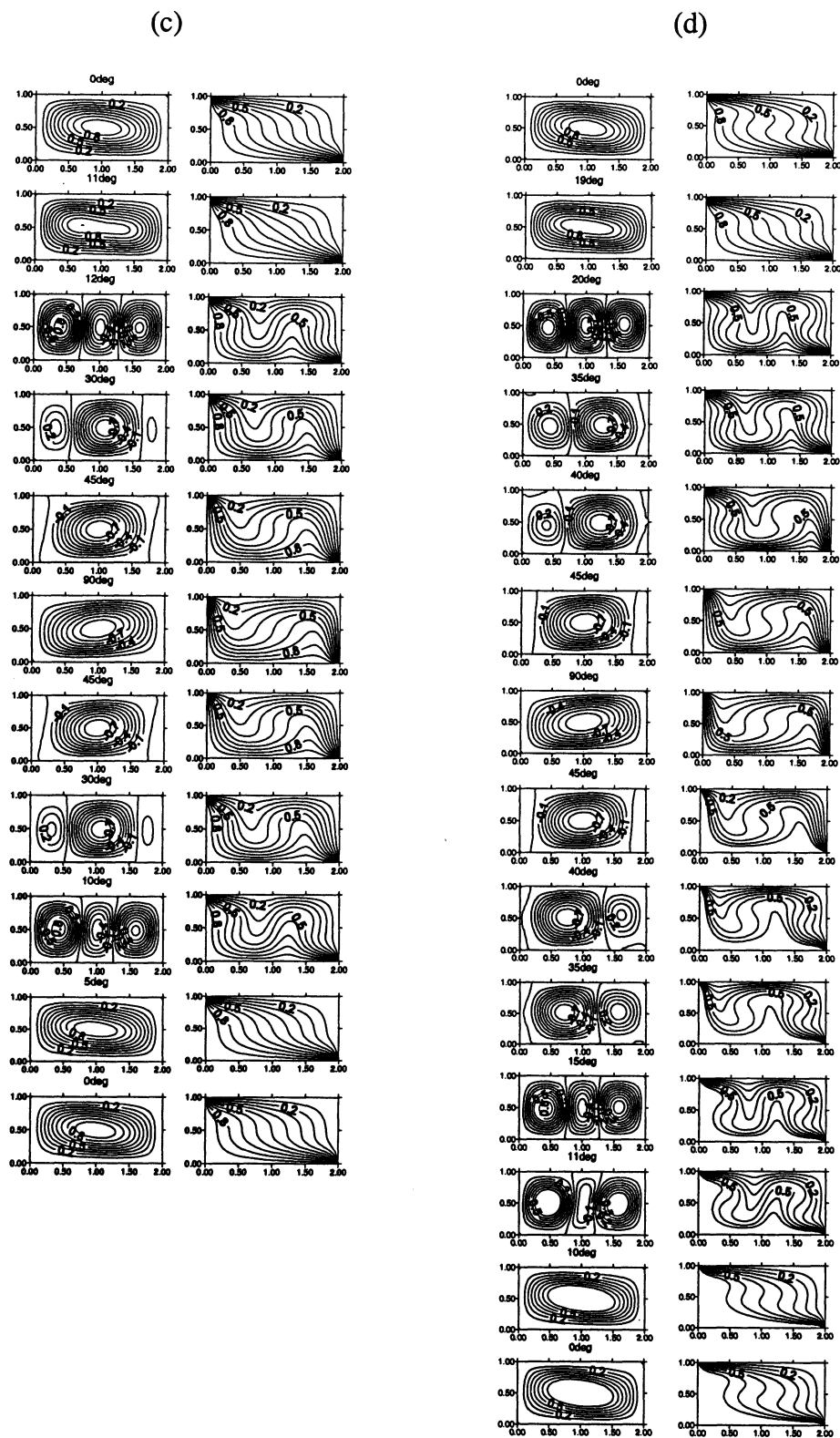


Fig. 4.8 Normalized streamlines and isothermal lines for HC configuration at various angles of inclination and four Ra numbers. (a) $Ra=1000$, (b) $Ra=3000$, (c) $Ra=5000$, (d) $Ra=10^4$. Positive values indicate rotation in clockwise direction.

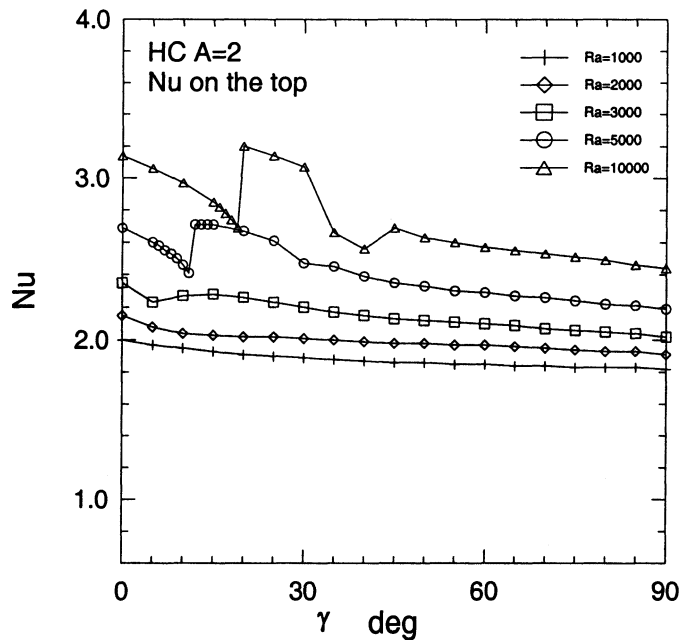


Fig. 4.9 Variation of average Nu number (both top and bottom walls) with inclination angle at various Ra numbers for HC configuration and A=2.

As mentioned before, the end wall area proportion in A=2 case is lower than A=1 case, heat transfer rate for A=2 is lower than A=1 in the horizontal cavity in angle increasing case. Upslope, down slope, upward, and downward forces in this case can not be exactly balanced even for Ra numbers lower than critical value due to the different operation area in A=2 case, flow patterns with four cell co-existing can not be observed in this case. Two units in x direction provide the opportunity for flow fields starting with one cell, then change to three cell, and finally go back to one cell, which can not be obtain in cavities with lower aspect ratios, such as A=1.

4.1.3.2 Case of decreasing γ

For $Ra = 1000$ and 3000 , no hysteresis phenomenon can be observed. As for $Ra=5000$, it occurs between 5° and 15° and no drastic change in Nu number can be observed, which is different from case of angle increasing. For angle decreasing from 90° to 0° at $Ra=10^4$, with the continuous increasing of the cross force from bottom wall, clockwise cell at right side is produced before the cell at the left side, which is different from case of angle increasing, as shown Fig. 4.8, so a difference in Nu number for angle increasing and decreasing from 25° to 45° can be observed in Fig. 4.10. Further decrease in inclination angle results in the reproduction of unicell structure due to the stronger upward and downward forces from left and right end walls, which accelerate the cell and cause sudden drop in Nu number at $Ra=10^4$, Fig. 4.10d.

As mentioned before, mode transition determines heat transfer difference for angle increasing and decreasing for $A=2$ case. As for $A=1$, the change of the rotating direction makes the effect of the end wall on the bottom wall heat transfer different for angle increasing and decreasing.

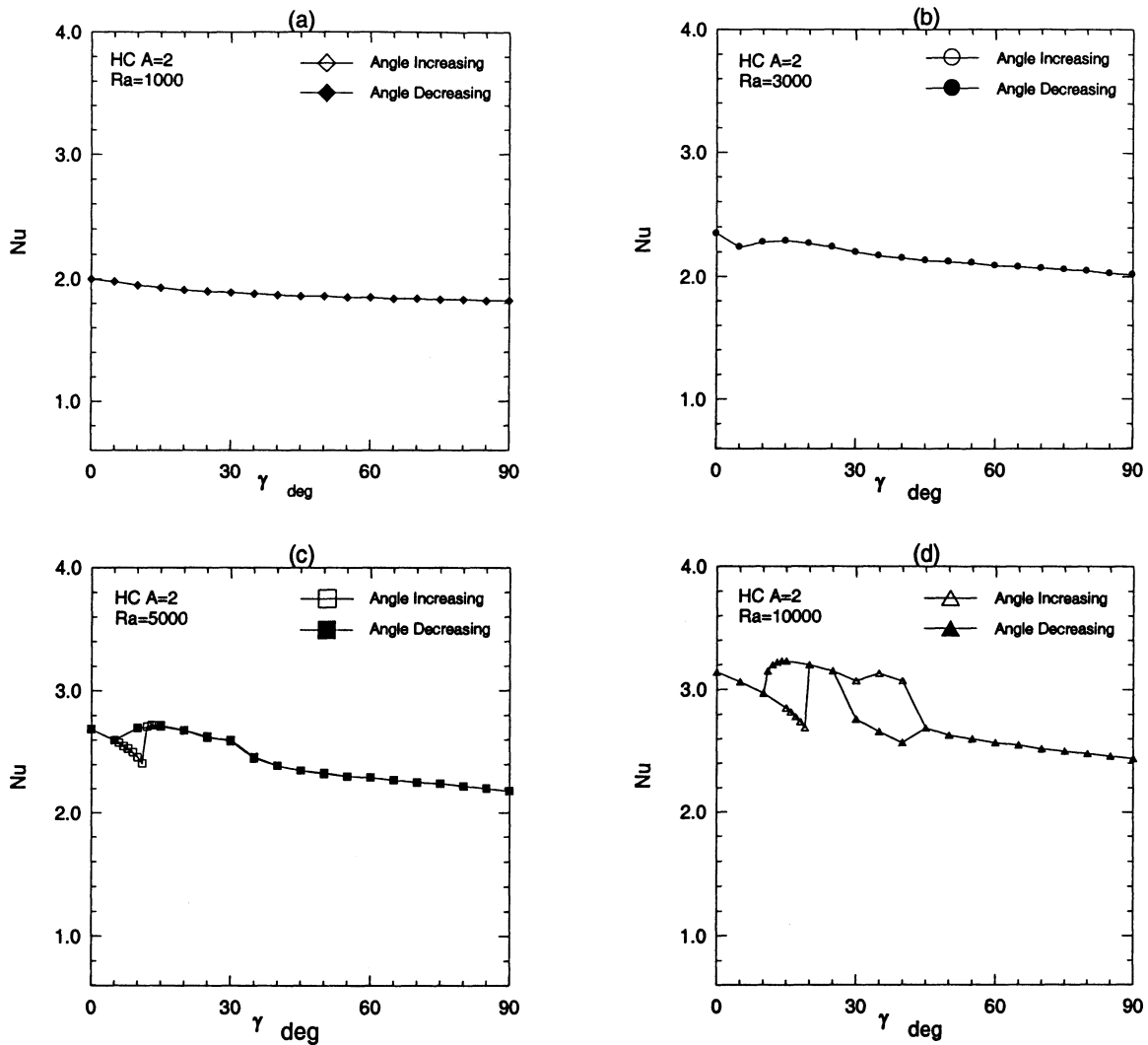


Fig. 4.10 Average Nu number (bottom wall) as a function of inclination angle γ for angle increasing and decreasing at various Ra numbers for HC configuration and $A=2$.

4.1.4 AC configuration

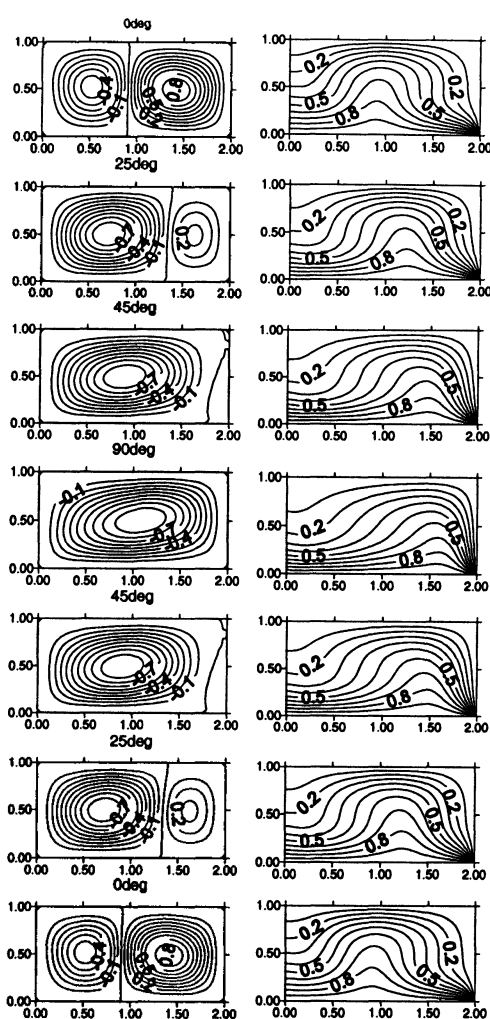
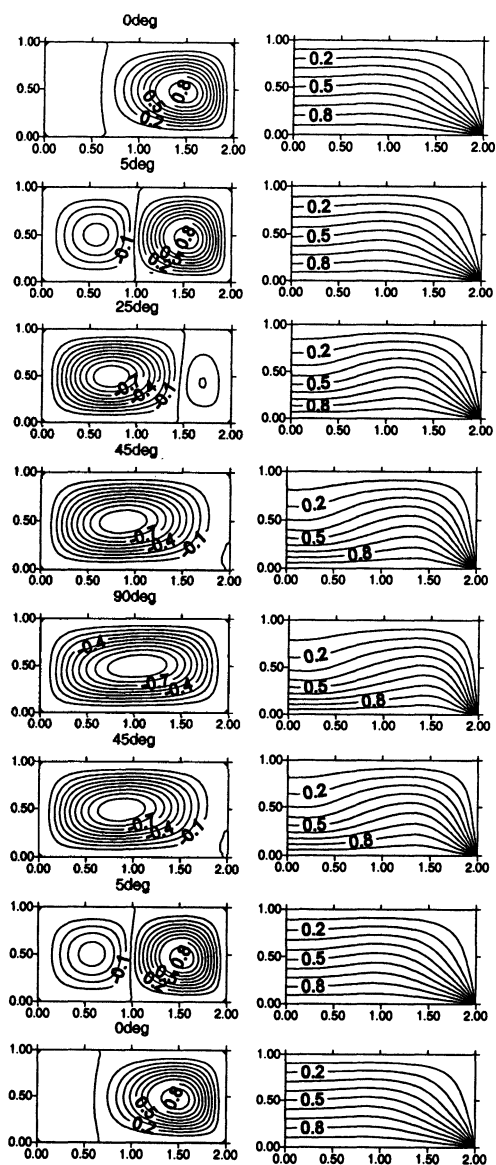
4.1.4.1 Case of increasing γ

At $Ra = 1000$, similar to the case of AA configuration shown in Fig. 4.1a, in this case the cross force is not strong enough to produce an anticlockwise cell because Ra number is lower than the critical value. Fig. 4.11 shows a cell on the right side of the cavity, which is generated by the downward force at the cooled right end wall. As γ increased, the anticlockwise cell grows in size, and eventually occupies the whole cavity.

At $Ra \geq 3000$, which is higher than the critical value and at $\gamma = 0^\circ$, a two-cell flow pattern is observed. The cell on the right hand side is stronger and bigger than the one on the left hand side due to the downward force produced at the cold right end wall. As γ increased, the left side cell becomes bigger due to the development of the upslope force, Fig. 4.11. Since the cell on the right side, which is bigger than left one at $\gamma = 0^\circ$ absorbs heat from both top and left walls, is decelerated, Nu number of the top wall decreases as γ increases, Fig. 4.12. For the bottom wall, the left cell grows gradually while right cell disappears, so heat transfer rate does not change significantly, Fig. 4.12. At $\gamma = 0^\circ$ and $Ra \geq 3000$, with the clockwise cell in the right part of the cavity, right end wall can further cool the fluid and greatly increases heat transfer rate of the bottom wall. But for the top wall, its effect is not significant, so at $\gamma = 0^\circ$, Nu number of the top wall is very close to that of the AA configuration shown in Figs. 4.2 and 4.12. At $\gamma = 90^\circ$, a unicell flow pattern occupies the whole cavity where the anticlockwise cell is pre-cooled by the left wall before it reaches the top wall, Fig. 4.11, so much lower heat transfer rates are obtained at the top wall, Fig. 4.12, as compared with those obtained in the case of AA configuration, Fig. 4.2. This phenomenon also occurs in the case of $A=1$.

(a)

(b)



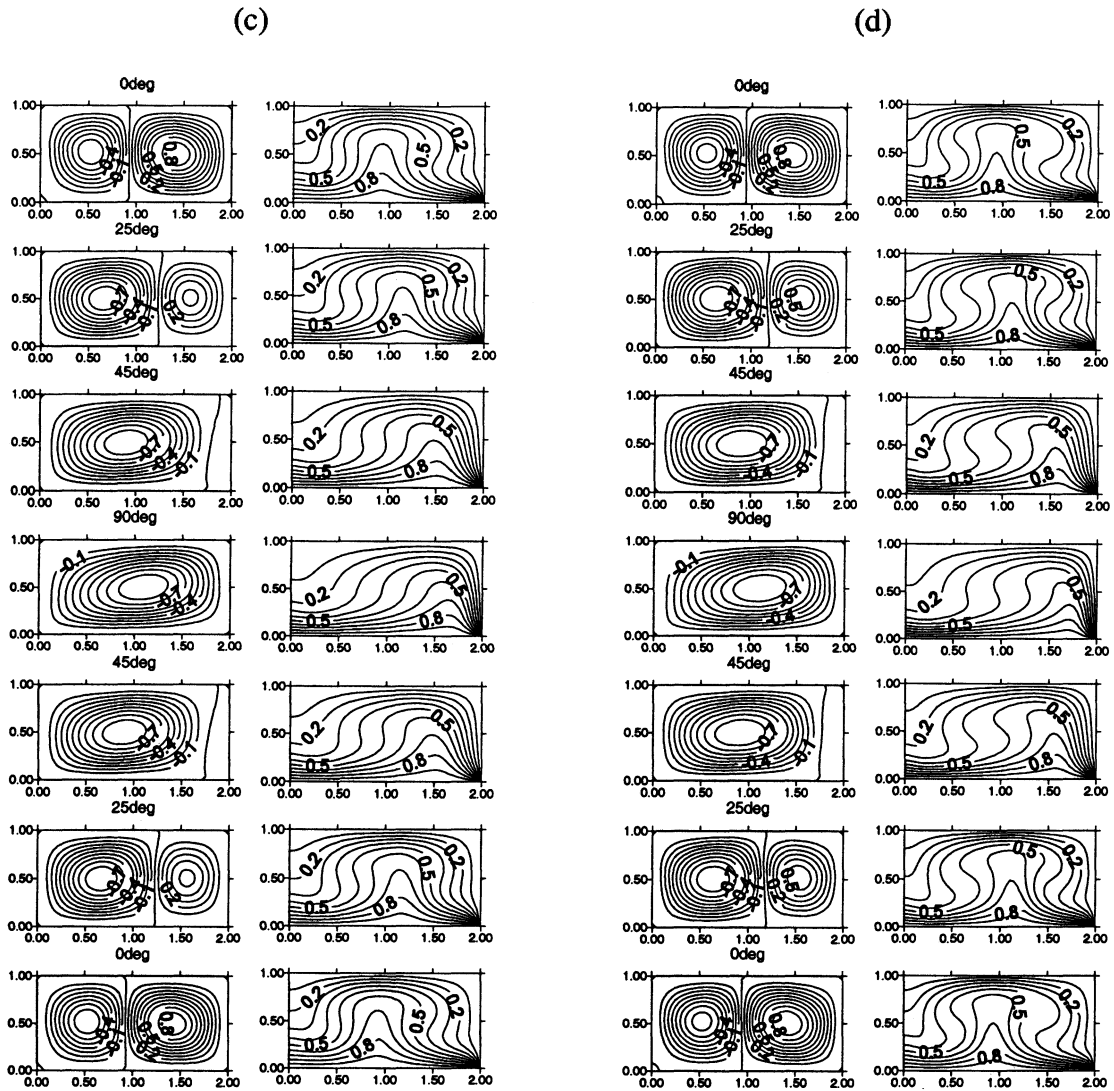


Fig. 4.11 Normalized streamlines and isothermal lines for AC configuration at various angles of inclination and four Ra numbers. (a) $Ra=1000$, (b) $Ra=3000$, (c) $Ra=5000$, (d) $Ra=10^4$. Positive values indicate rotation in clockwise direction.

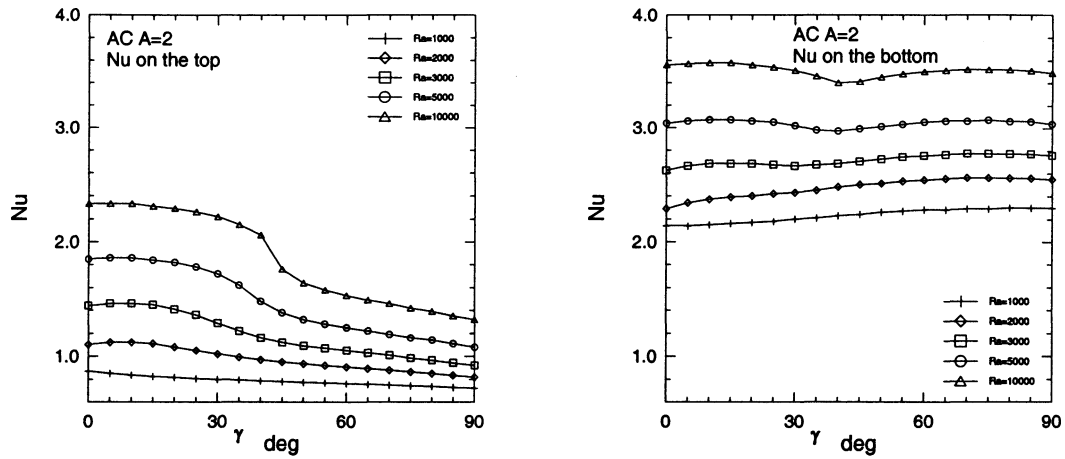


Fig. 4.12 Variation of average Nu number (both top and bottom walls) with inclination angle at various Ra numbers for AC configuration and A=2.

4.1.4.2 Case of decreasing γ

Heat transfer rates for angle decreasing is the same as those obtained for angle increasing, Fig. 4.13. No hysteresis phenomenon can be observed, which is different from the case of A=1.

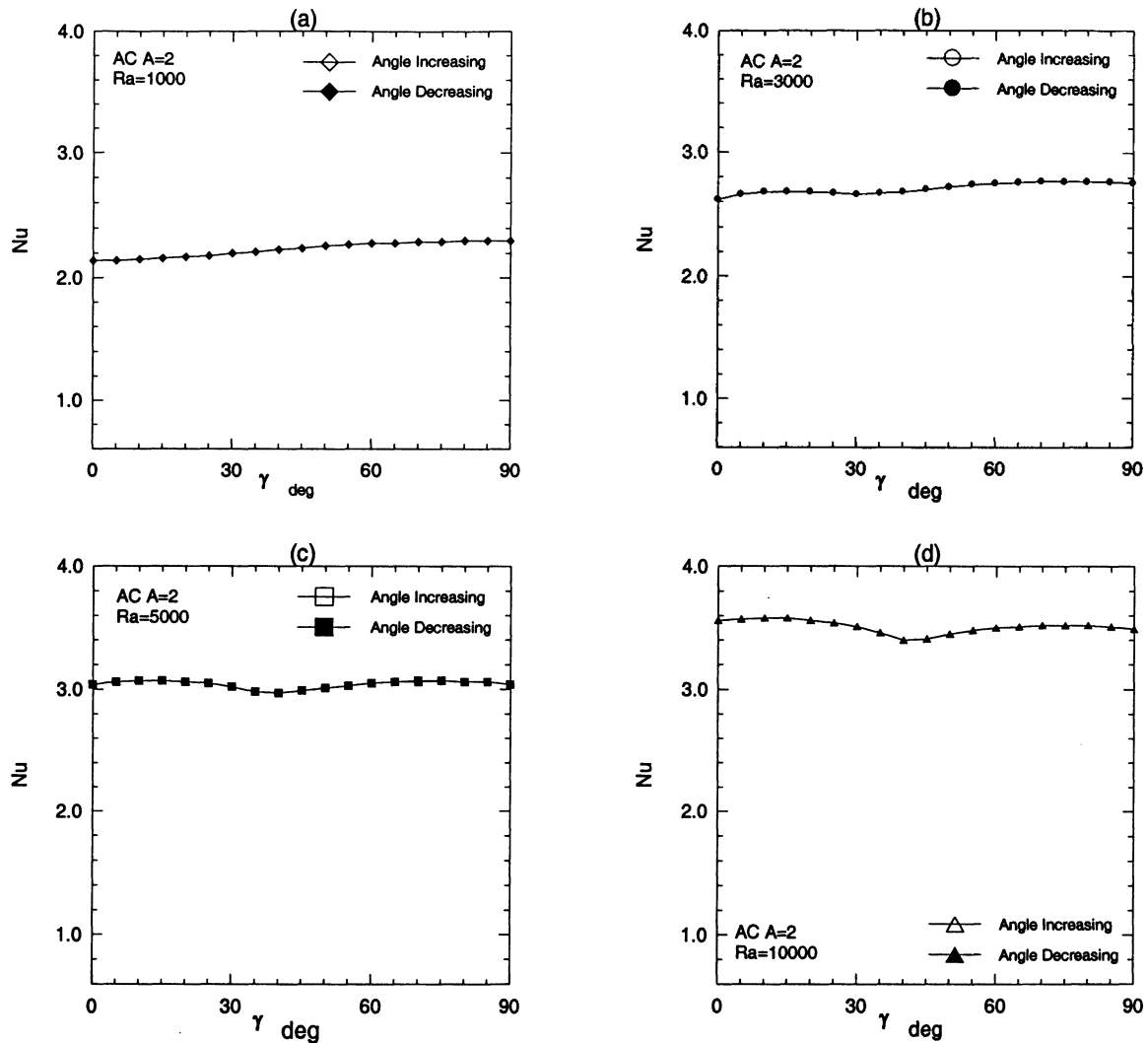


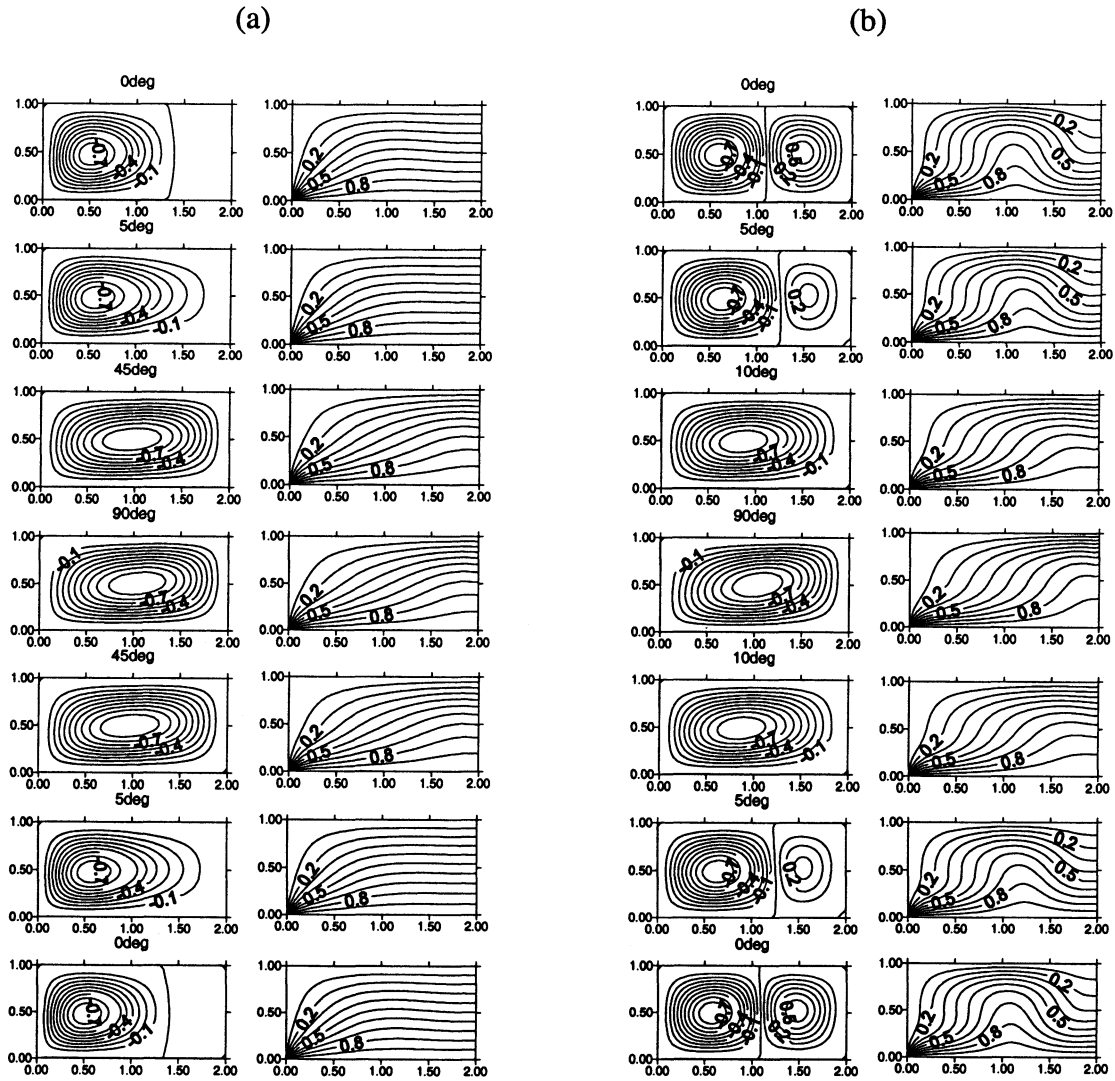
Fig. 4.13 Average Nu number (bottom wall) as a function of inclination angle γ for angle increasing and decreasing at various Ra numbers for AC configuration and A=2.

4.1.5 CA configuration

4.1.5.1 Case of increasing γ

At the beginning of the inclination for $Ra = 1000$, anticlockwise cell appears in horizontal cavity, which is stronger and stronger during increase of γ , as shown in Fig. 4.14. Due to the critical Ra number limit, except at $\gamma < 5^\circ$, where cross force dominates heat transfer in the cavity, Nu numbers of top wall are very close to those obtained in the

AA configuration. Nu number of the bottom wall is higher than the AA configuration due to higher heated/cooled proportion, see Figs 4.2 and 4.15.



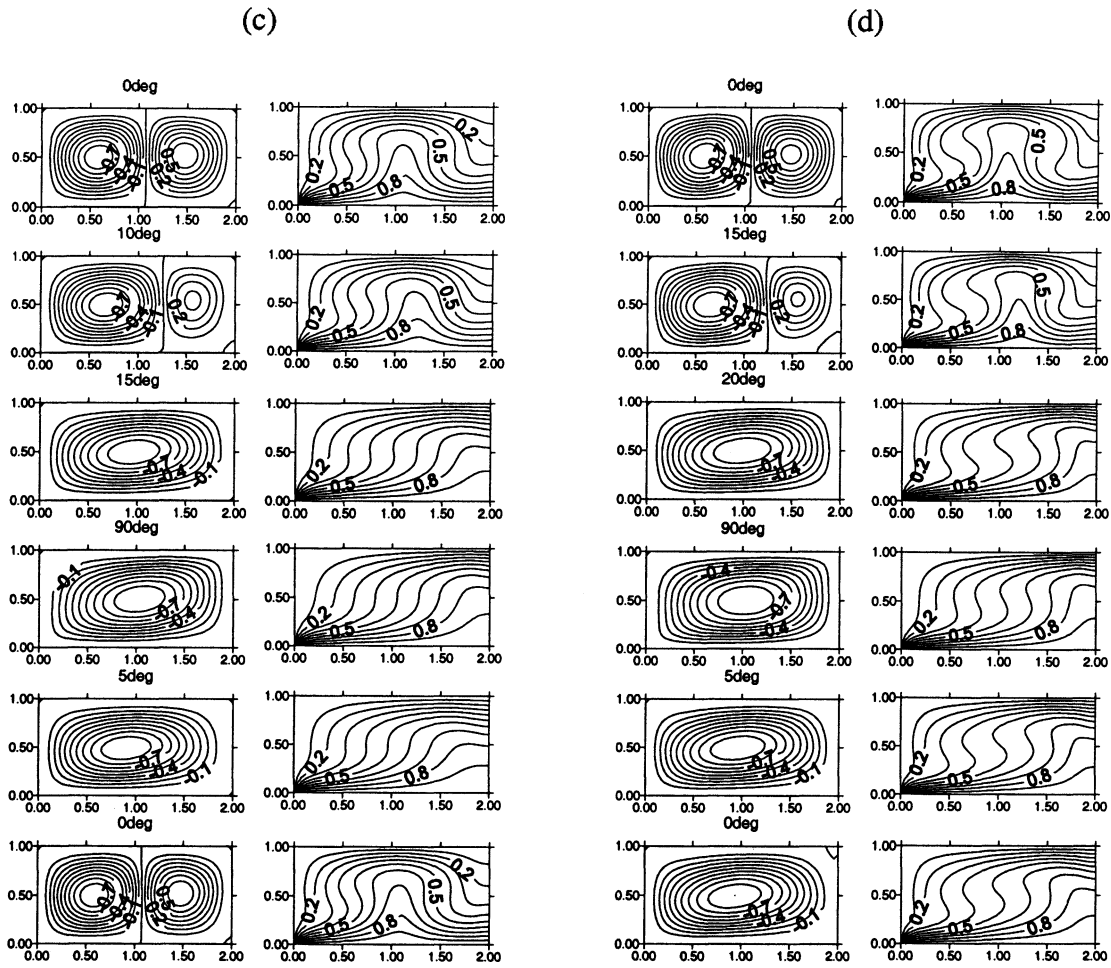


Fig. 4.14 Normalized streamlines and isothermal lines for CA configuration at various angles of inclination and four Ra numbers. (a) $Ra=1000$, (b) $Ra=3000$, (c) $Ra=5000$, (d) $Ra=10^4$. Positive values indicate rotation in clockwise direction.

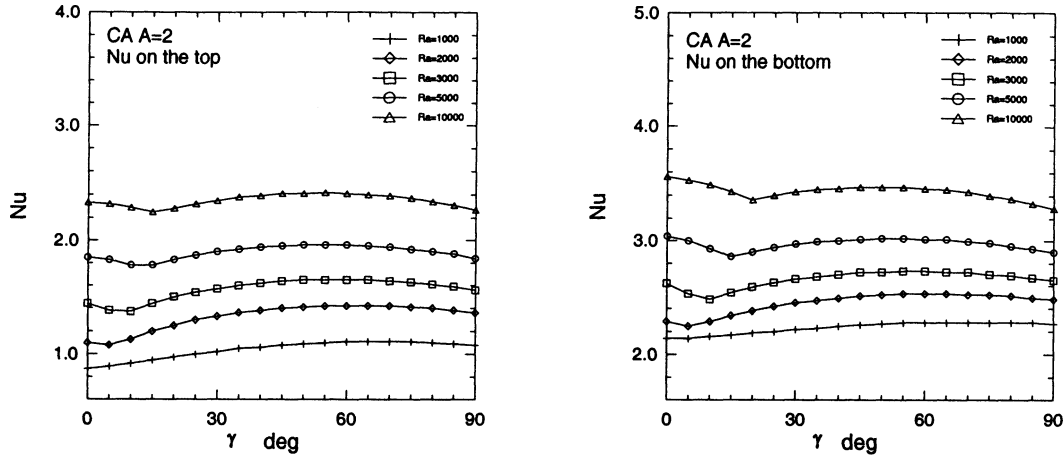


Fig. 4.15 Variation of average Nu number (both top and bottom walls) with inclination angle at various Ra numbers for CA configuration and A=2.

For $Ra \geq 3000$, due to the left cold end wall, asymmetric cells can be observed at $\gamma = 0^\circ$, as shown in Fig. 4.14. Anticlockwise cell at left side is obviously accelerated by the left wall and is stronger than the one on the right side. As γ increased, the left cell occupies the whole cavity after certain inclination angle. Heat transfer does not change significantly during γ increasing, Fig. 4.15, due to the gradual mode transition as shown in Fig.4.14. The cold end wall increases the cooling-heating ratio, which enhances the heat transfer rate of the hot bottom wall as compared with AA configuration, Figs. 4.2 and 4.15. For the top wall, unlike AC configuration (Fig. 4.11), the cold left wall never had a chance to pre-cool fluid before it arrives at the top wall, so heat transfer rate is very similar to the AA configuration for $Ra \geq 3000$, as shown in Figs. 4.2 and 4.15.

For $Ra > 3000$, similar mode transition can be observed during the case of γ increasing, except that mode transition from two cells to one cell occurs between $\gamma=10^\circ$ and 15° for $Ra = 5000$ and between 15° and 20° for $Ra=10^4$, Fig. 4.14. Similar to AA configuration, heat transfer rate increases at a certain angle after unicell pattern is formed

and then decrease. For example, for $Ra=10^4$, $\psi_{\max}=15.7$ at $\gamma=20^\circ$, at which case a unicell flow pattern is formed and keeps increasing until both Nu number and ψ_{\max} reach their maximum values at $\gamma=45^\circ$, where $\psi_{\max}=16.2$. Finally, at $\gamma=90^\circ$, ψ_{\max} decreases to 13.1, and Nu number also decreases.

During γ increasing, similar trends in Nu number are observed after unicell flow patterns are formed as compared with $A=1$ case. Whereas, in $A=1$ case, cooled/heated ratio is equal to 2. While for $A=2$ case it is equal to 1.5. So Nu number of the heated bottom wall is lower in $A=2$ case, Figs. 3.15 and 4.15.

4.1.5.2 Case of decreasing γ

Fig. 4.16 indicates no hysteresis phenomenon for $Ra < 5000$. At $Ra = 5000$ mode transition for angle increasing took place at γ between 10° and 15° , and between 5° and 0° for angle decreasing case. A two-cell flow pattern is obtained at $\gamma = 0^\circ$ for angle decreasing, which is the same as in the case of angle increasing. However, for $Ra = 10^4$, a unicell pattern is obtained at $\gamma = 0^\circ$ due to higher initial velocities, $\psi_{\max}=14.3$ at $\gamma=5^\circ$, compared with $\psi_{\max}=8.55$ at $\gamma = 5^\circ$ for $Ra=5000$. Rates of heat transfer resulted from unicell flow patterns are lower than those resulted from multi-cell structures observed in the case of angle increasing, i.e., more cells produce higher rates of heat transfer. For $Ra = 5000$, at $\gamma = 3^\circ$, Fig. 4.16c, the unicell flow mode produced a rate of heat transfer 12.6% lower than that in the case of angle increasing, Fig 4.15c. For $Ra=10^4$ and $\gamma = 0^\circ$ rate of heat transfer lower by 16.7%, Fig. 4.16d, is the result of the unicell structure produced in that case, Fig. 4.14d.

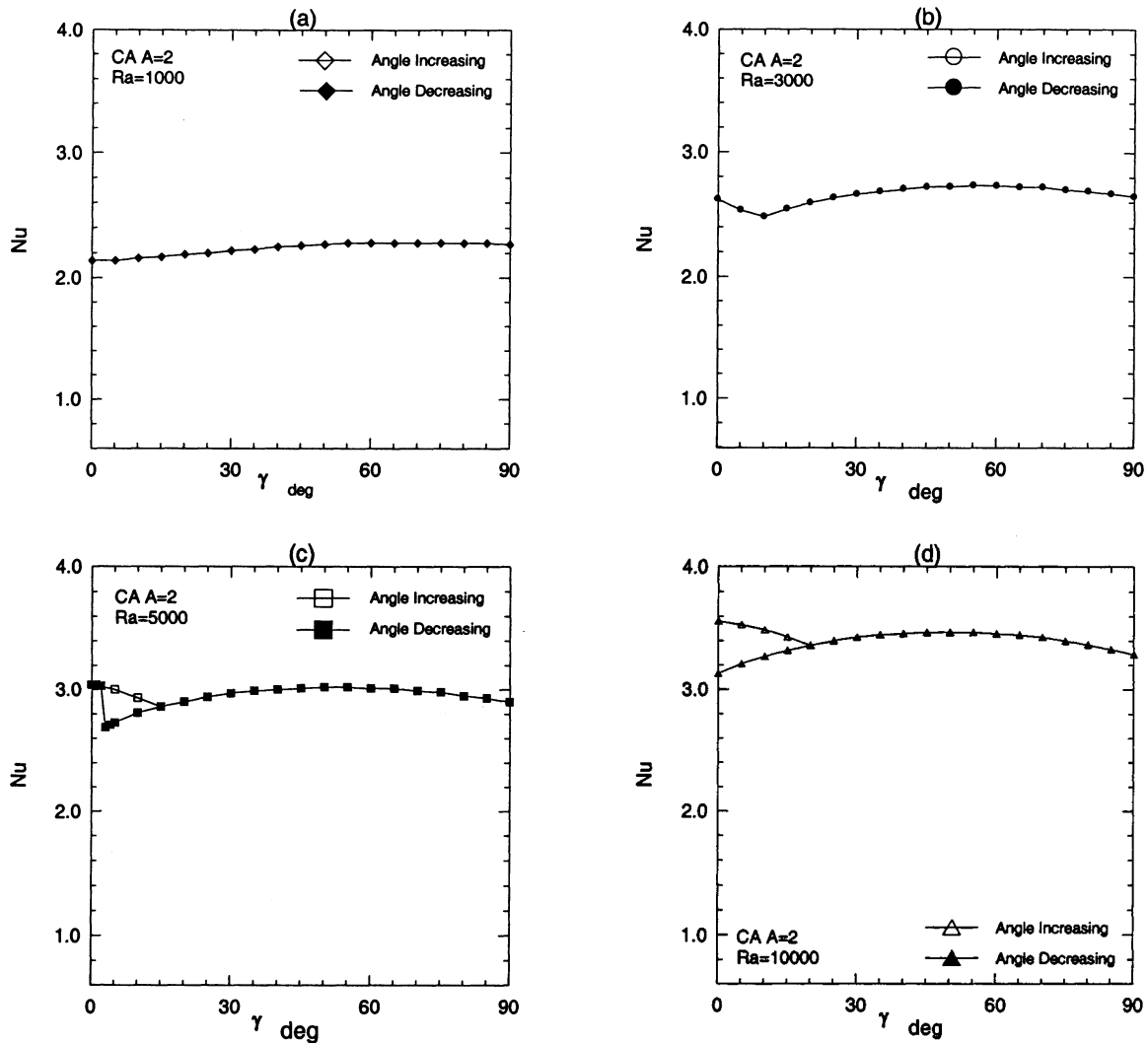


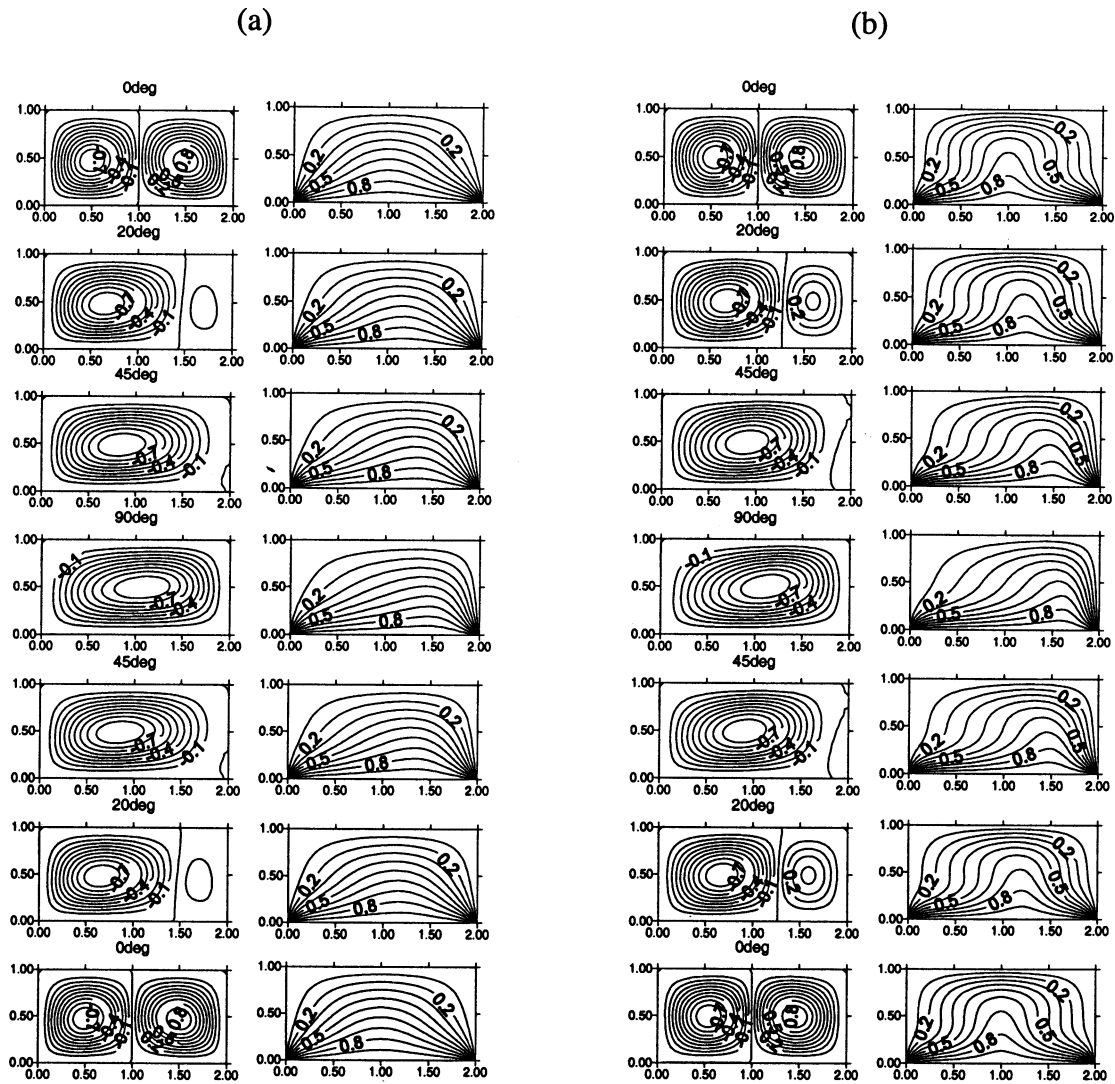
Fig. 4.16 Average Nu number (bottom wall) as a function of inclination angle γ for angle increasing and decreasing at various Ra numbers for CA configuration and A=2.

4.1.6 CC configuration

4.1.6.1 Case of increasing γ

At $\gamma = 0^\circ$, downward forces at left and right end walls generate a two-cell flow pattern for all Ra numbers, Fig. 4.17. Clockwise cell on left side shrinks during γ increasing and finally can not resist stronger upslope force from bottom wall when γ exceeds 45° , which is similar to A=1 case. Transition of the two-cell mode to a unicell mode results in a gradual decrease in Nu number, for γ from 0° to 45° . Furthermore, since

in the case of unicell mode, right end wall pre-cools fluid before it goes to top wall, so heat transfer rate of the top wall keeps decreasing the way until $\gamma = 90^\circ$, Fig. 4.18.



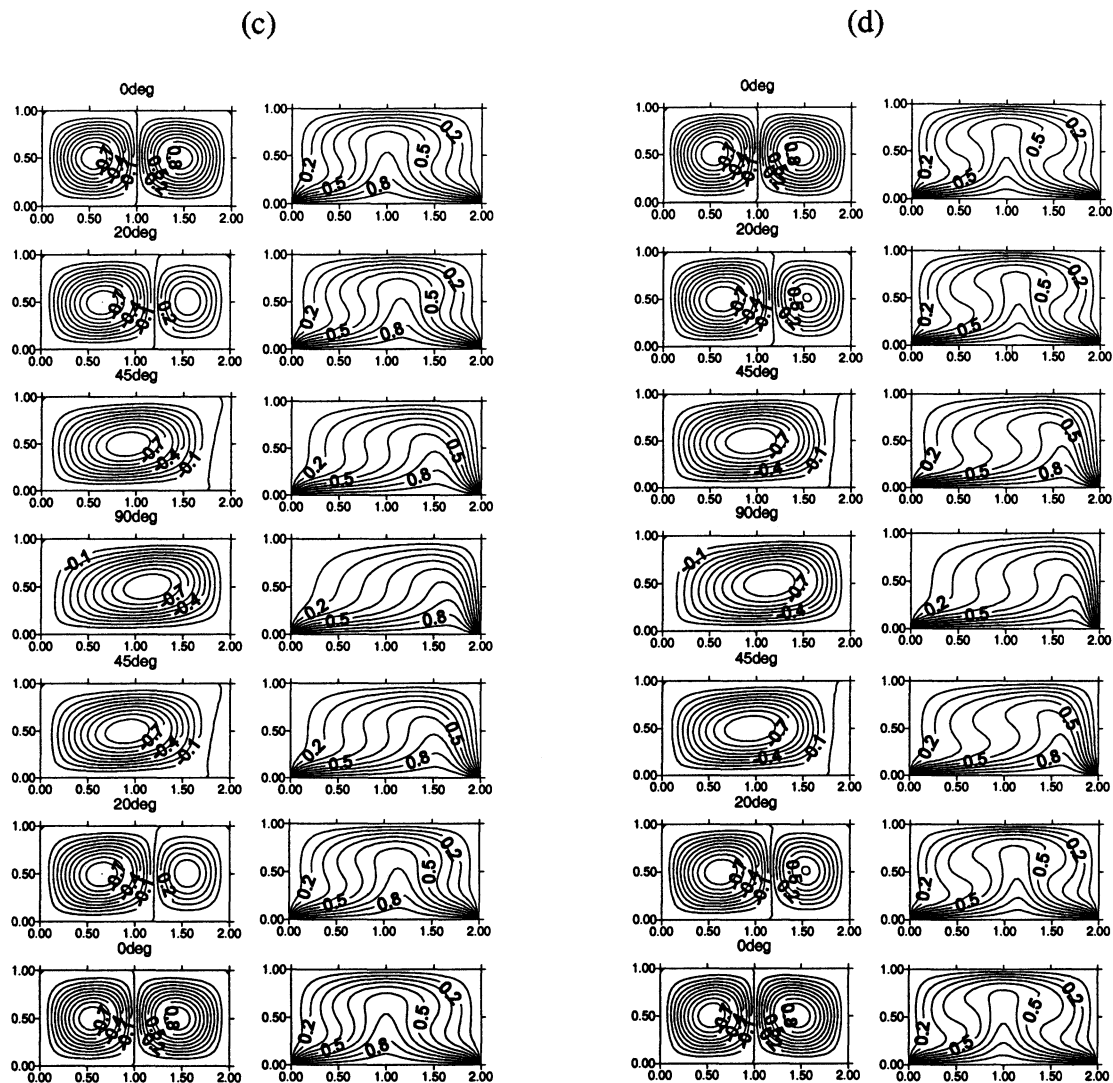


Fig. 4.17 Normalized streamlines and isothermal lines for CC configuration at various angles of inclination and four Ra numbers. (a) Ra=1000, (b) Ra=3000, (c) Ra=5000, (d) Ra=10⁴. Positive values indicate rotation in clockwise direction.

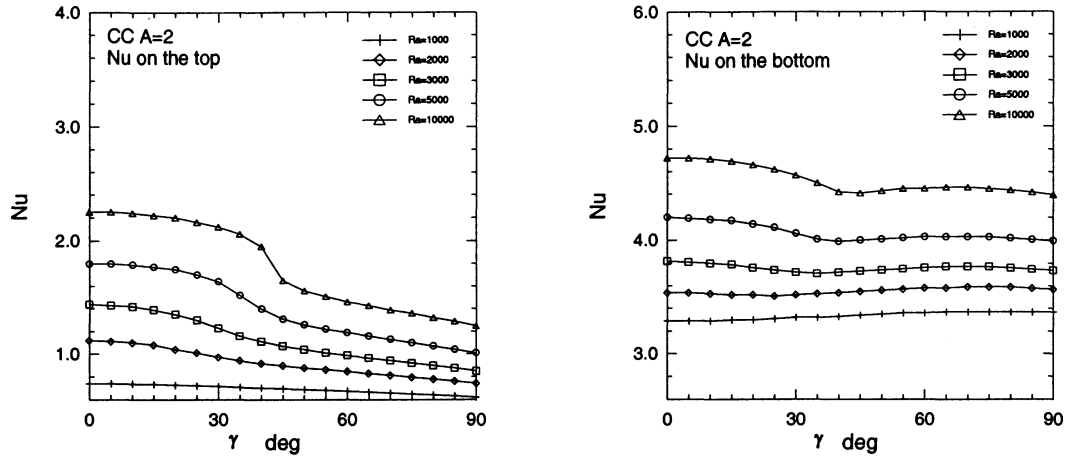


Fig. 4.18 Variation of average Nu number (both top and bottom walls) with inclination angle at various Ra numbers for CC configuration and A=2.

Rate of heat transfer of the bottom wall decreases when number of cells decreases from two to one, and remains almost constant after the unicell pattern is formed, Fig. 4.18, because no pre-heating occurs as γ increases. Almost the same trend can be observed for all Ra numbers, except that higher Ra numbers have more significant changes in Nu numbers of the bottom wall during γ increasing.

Due to the same reason mentioned in the case of CA configuration, heat transfer rate of the bottom wall in A=2 case is lower than A=1 case.

4.1.6.2 Case of decreasing γ

As γ decreases, flow fields return to two-cell structures for all Ra numbers, which is different from AA configuration, see Figs. 4.1 and 4.17. Hysteresis phenomenon can not be observed in this case, Fig. 4.19, which is the same as A=1 case. It is worth noting here that in this case that the downward forces at the two end walls seemed to help in the re-establishment of the two-cell flow patterns as γ decreased, which means that hysteresis

phenomenon is not necessarily caused by mode-transition. Although, occurrence of mode transition is a required condition, it is not sufficient for hysteresis to occur.

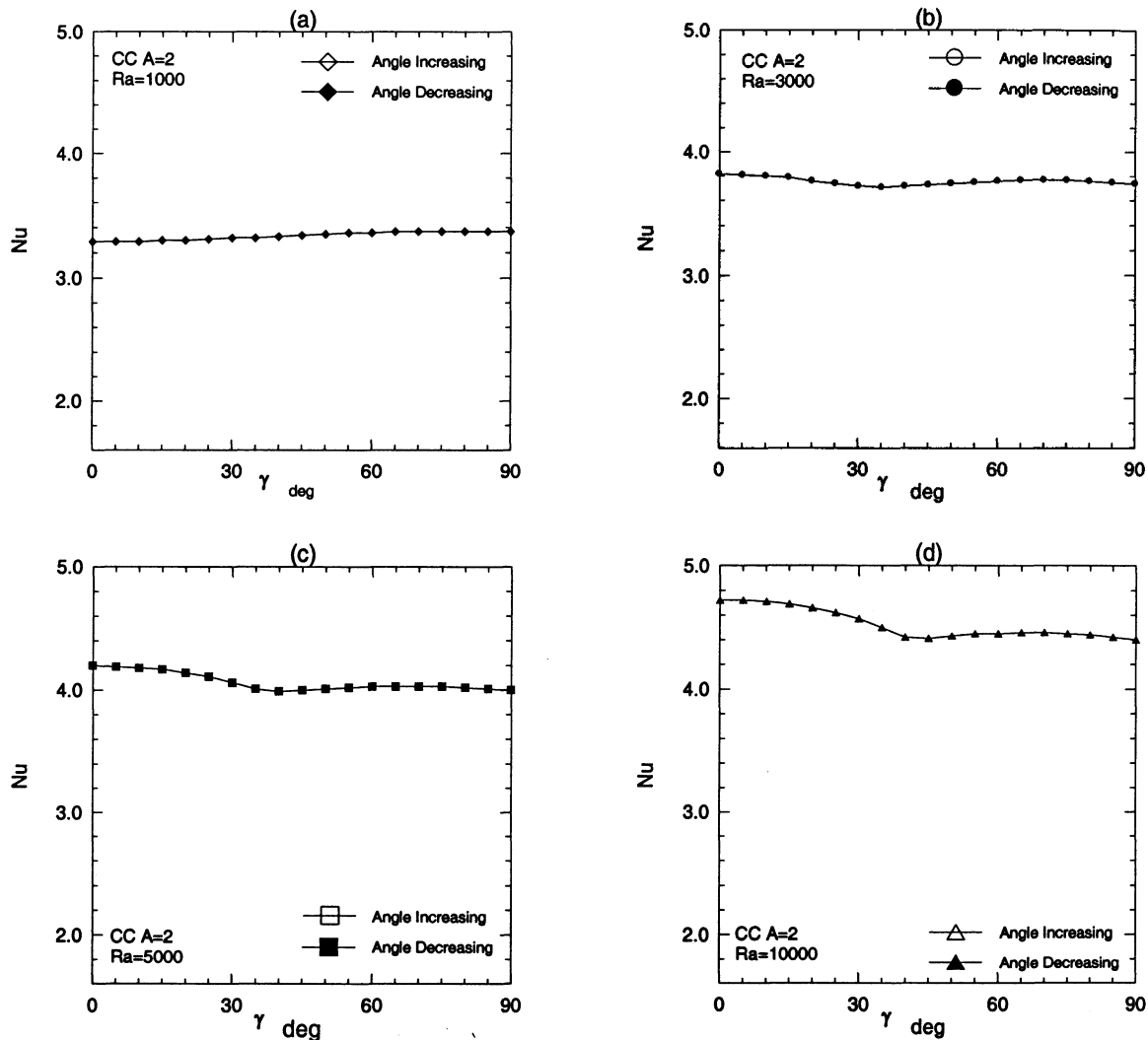


Fig. 4.19 Average Nu number (bottom wall) as a function of inclination angle γ for angle increasing and decreasing at various Ra numbers for CC configuration and A=2.

4.1.7 LL configuration

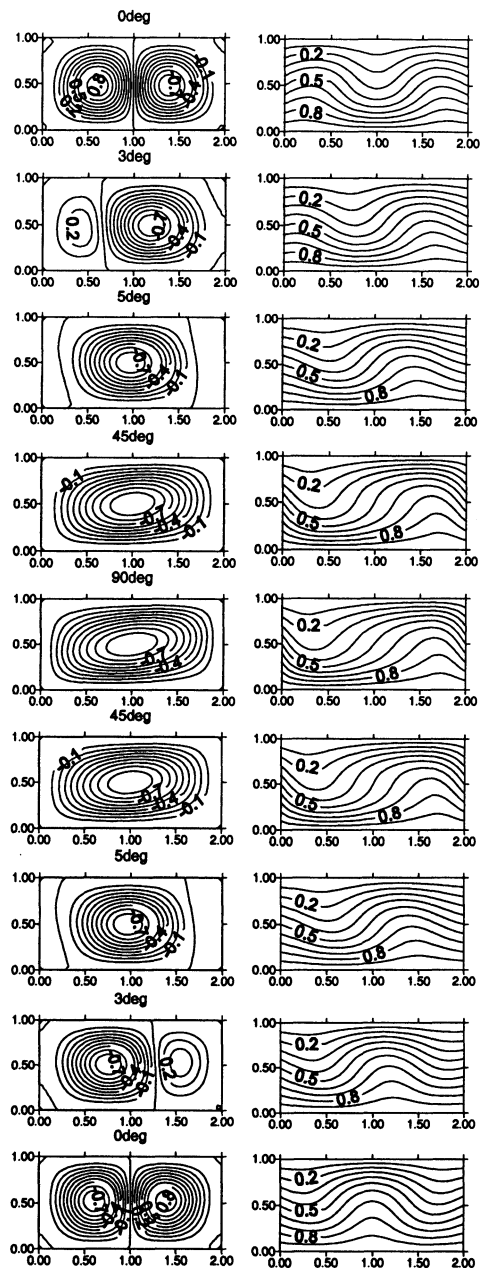
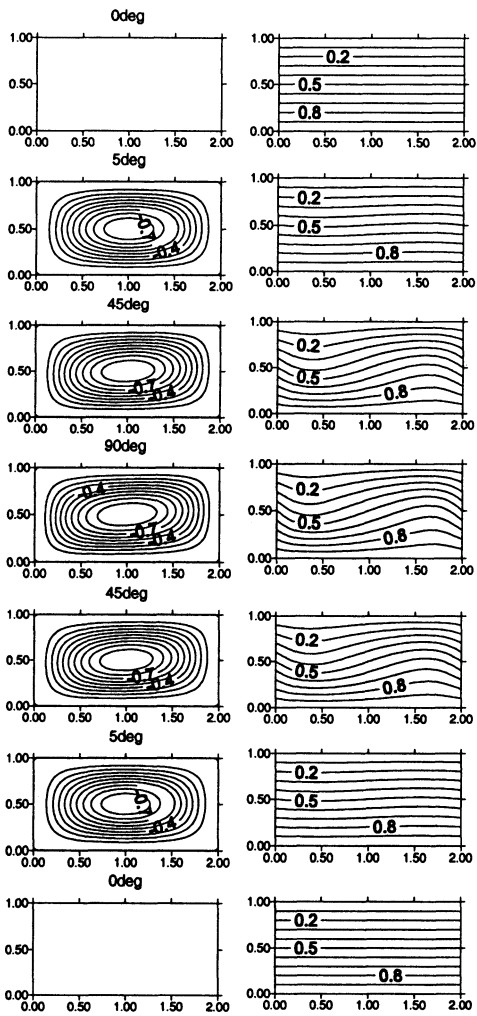
4.1.7.1 Case of increasing γ

When initially cold fluid exchanges heat with left and right end walls having linear temperature distributions (from hot on the bottom to cold on the top), fluid is compelled by the upward buoyancy force from both end walls and convection flow take

place, when Ra number is higher than the critical value. A clockwise cell and an anticlockwise cell are formed at the left and right sides of the cavity, respectively, Fig. 4.20. Fluid is pre-cooled at both end walls before it arrives at the top wall, so heat transfer rate of the top wall is greatly reduced for Ra numbers beyond the critical value, when compared with the AA configuration, Figs. 4.2 and 4.21. For example, at $\gamma = 0^\circ$, Nu number of the top wall is 26.9% less for Ra = 3000, 28.9% less for Ra=5000 and 29.2% less for Ra= 10^4 . At $\gamma = 90^\circ$, due to pre-cooling of the unicell structure at the right end wall, Nu number is about 10% less than AA configuration, Figs. 4.2 and 4.21.

(a)

(b)



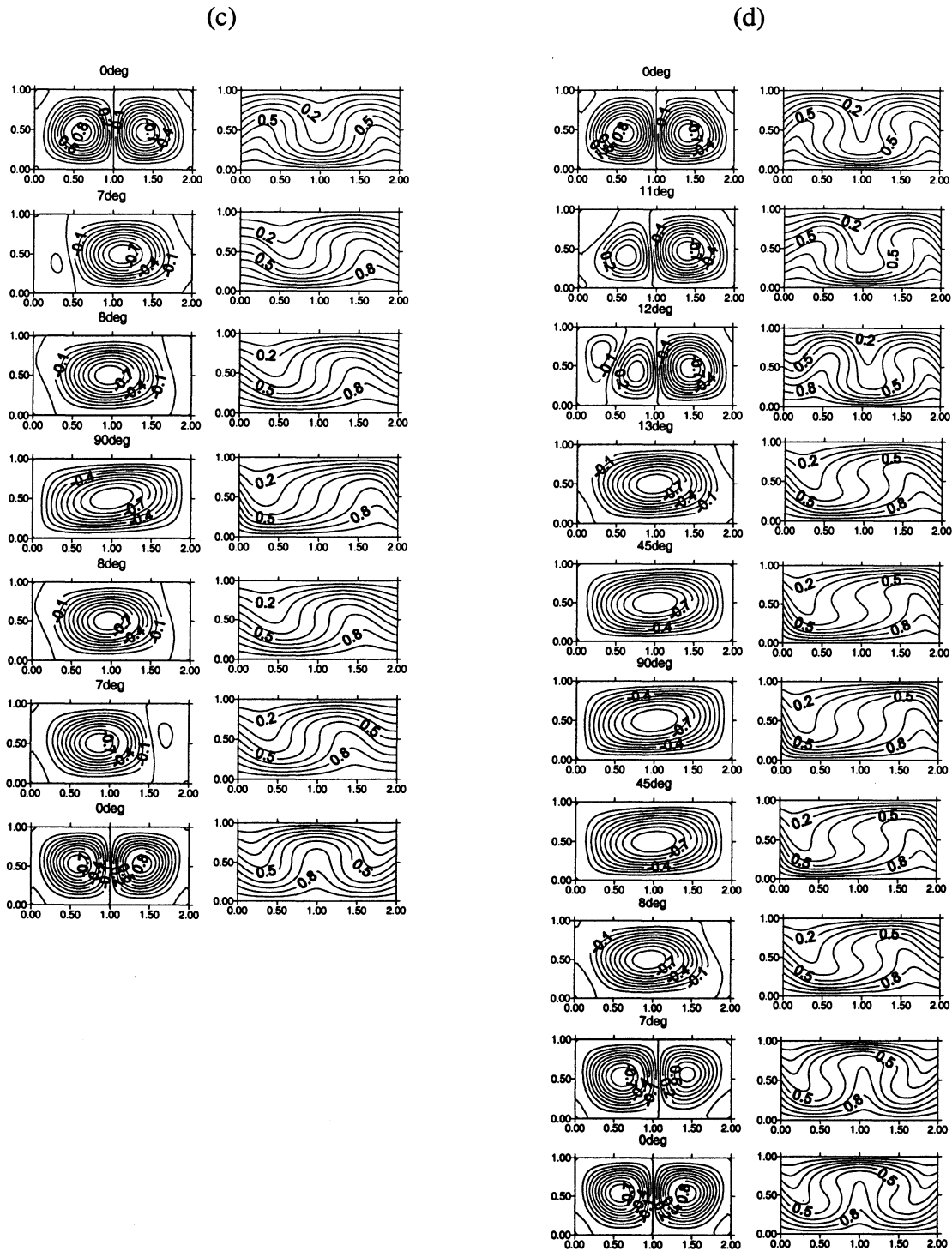


Fig. 4.20 Normalized streamlines and isothermal lines for LL configuration at various angles of inclination and four Ra numbers. (a) Ra=1000, (b) Ra=3000, (c) Ra=5000, (d) Ra=10⁴. Positive values indicate rotation in clockwise direction.

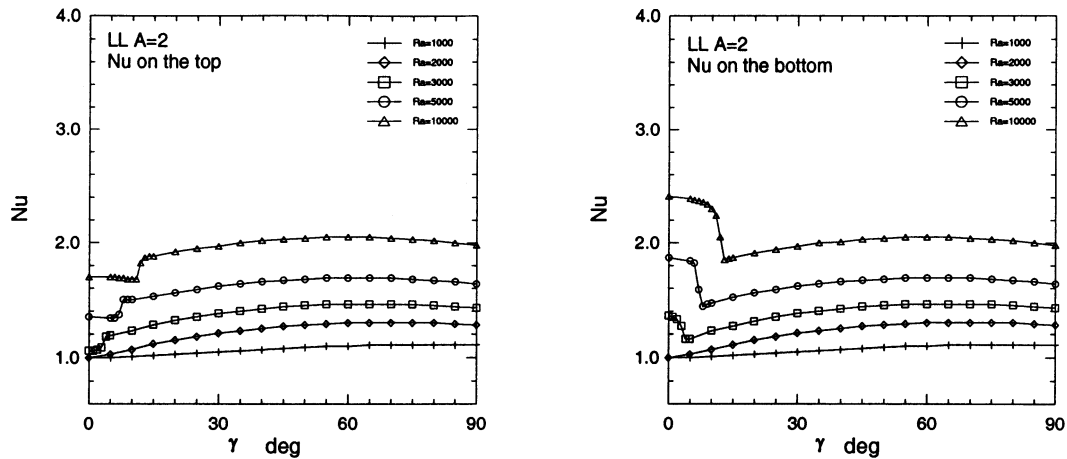


Fig. 4.21 Variation of average Nu number (both top and bottom walls) with inclination angle at various Ra numbers for LL configuration and A=2.

Almost the same rate of heat transfer can be obtained from the bottom wall compared with AA configuration at $\gamma = 0^\circ$. It seems that the effect of the two end walls with linear temperature distributions on rate of heat transfer from bottom wall is equivalent to that of insulated end walls at $\gamma = 0^\circ$. When the angle of inclination increases, clockwise cell shrinks and the anticlockwise cell grows due to the increasing upslope force. Finally, a unicell flow structure occupies the whole cavity.

Two cells rotating in opposite direction are pre-cooled by both of end walls, so heat transfer rate of bottom wall is higher than that of top wall when $\gamma = 0$, Fig. 4.21. However, in the case of A=1, only one cell is obtained in the cavity at $\gamma = 0^\circ$, so fluid is pre-cooled by left wall before it reaches top wall, and pre-heated by right wall before it reaches bottom wall, so heat transfer rate is almost the same from top and bottom walls, see Fig. 3.21.

4.1.7.2 Case of decreasing γ

As γ decreases, no hysteresis phenomenon can be observed at $Ra=1000$. For $Ra > 1000$, since fluid in the cavity is initially heated, it is very hard to decide whether the upward or downward forces from left and right end walls are accelerating or decelerating the cells. Cross force plays more important role in mode transition in this case. At a range of γ between 8° and 3° for different Ra numbers, cross force produces a clockwise cell in the right side of the cavity, Fig. 4.20 (b, c, d). Although flow field ends up with two cells, it has a different rotation direction as compared with flow field obtained at $\gamma = 0^\circ$ for angle increasing. Both of these two cells are preheated by the left and right end walls before they reach bottom wall in angle decreasing case, so heat transfer rate on the bottom wall is greatly lower compared with the angle increasing, Fig. 4.22. At $\gamma = 0^\circ$, the maximum difference in Nu number between the two cases of angle increasing and decreasing is 21.3% for $Ra = 3000$, 27.3% for $Ra=5000$, and 29% for $Ra=10^4$, respectively, in horizontal cavity, Fig. 4.22.

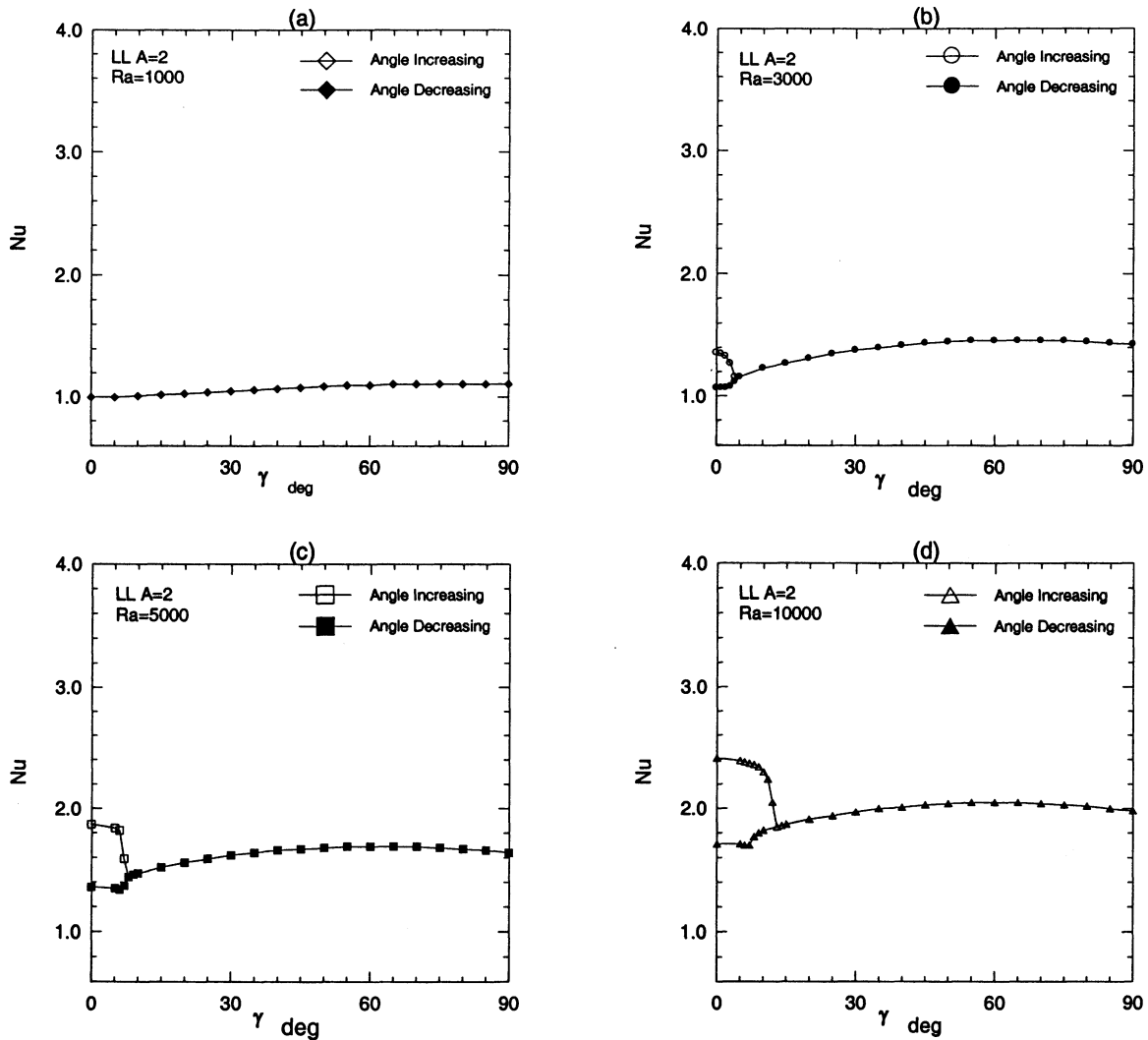


Fig. 4.22 Average Nu number (bottom wall) as a function of inclination angle γ for angle increasing and decreasing at various Ra numbers for LL configuration and $A=2$.

4.2 Rectangular cavity with higher aspect ratios

In case of cavities with higher aspect ratios, more space is available, so it is expected that more cells will be produced and the opportunity of mode transition is greatly increased, in both cases of angle increasing and decreasing. Difference in mode transition at angle increasing and decreasing may be more significant than that discussed in chapter 3 for $A=1$ and in section 4.1 for $A=2$. Since more than two cells might co-exist in the cavity in the case of higher aspect ratios, it is possible that mode transition might

occur from a multi-cell flow pattern to another multi-cell pattern, but with fewer cells. When mode transition takes place in this way, more than one drastic change in rates of heat transfer (i.e., in values of Nu number) is expected to take place. Most practical applications involve cavities with higher aspect ratios and most of the time these drastic changes in rates of heat transfer are not desirable. This warrants the study of mode-transition of natural convection in cavities with higher aspect ratios. Cavities with $A = 4$ have been chosen in the present study as a representative for this category. The choice of $A = 4$ was mainly due to the availability of results in the literature to be compared with those of the present study, as discussed in chapter 2.

4.2.1 AA configuration

4.2.1.1 Cases of increasing γ

For $Ra=1000$, which is below critical Ra number, no motion can be observed when cavity is in the horizontal position, i.e., at $\gamma = 0^\circ$, Fig. 4.23. “Basic flow” dominates up to $\gamma = 5^\circ$, in which case heat transfer depends only on heat conduction as shown in Figs. 4.23 and 4.27. A unicell pattern remains all the way as γ increases to 90° and decreases back to 5° . Maximum difference in rate of heat transfer at $\gamma = 0^\circ$ and 90° is about 11.0%, Fig. 4.27.

For $Ra=3000$ and $\gamma = 0^\circ$, a multi-cell flow pattern with four cells is produced by the cross force as shown in Fig. 4.24. Clockwise cell on the right side of the cavity disappears as γ approaches 24° due to the increasing upslope force from the bottom wall and down slope force from the top wall. Mode transition from four-cell to three-cell takes place at γ between 0° and 10° resulting in a small drop in Nu number, Fig 4.26. Another

mode transition from three cells to two-in-one cell (3T2) occurs between $\gamma = 24^\circ$ and 25° , which causes a more noticeable drop, 8.0%, in Nu number, Fig. 4.27. As γ increases, Nu number increases until $\gamma = 70^\circ$ then decreases as γ goes to 90° .

For $Ra=5000$, mode transition occurs before $\gamma = 15^\circ$, where four cells merge into three cells with the cell in the right side of the cavity disappearing, Fig. 4.25. This mode transition did not cause a drastic change in Nu number. Only 1.5% difference between Nu number at $\gamma = 15^\circ$ and 0° . Another mode transition (3T1) occurs between 31° and 32° , which causes 22.3% drop in Nu number, Fig. 4.27. Similar trend is observed for $Ra=10^4$ in which case the 3T1 mode transition causes 21.2% drop in Nu number at $\gamma = 35^\circ$, as shown in Fig. 4.27. It is worth noting here that the angles at which both mode transitions occur, increase as Ra number increases, i.e., mode transition is delayed at higher Ra numbers. A higher Ra number results in stronger cells of the initial multi-cell structure produced at $\gamma = 0^\circ$. As γ increases, mode transition occurs when the clockwise rotating cell at the right hand side of the cavity disappears, which is caused by the increasing upslope force as γ increases. A stronger right cell requires much higher upslope force to cause it to decelerate and eventually disappear, which needs a higher angle of inclination.

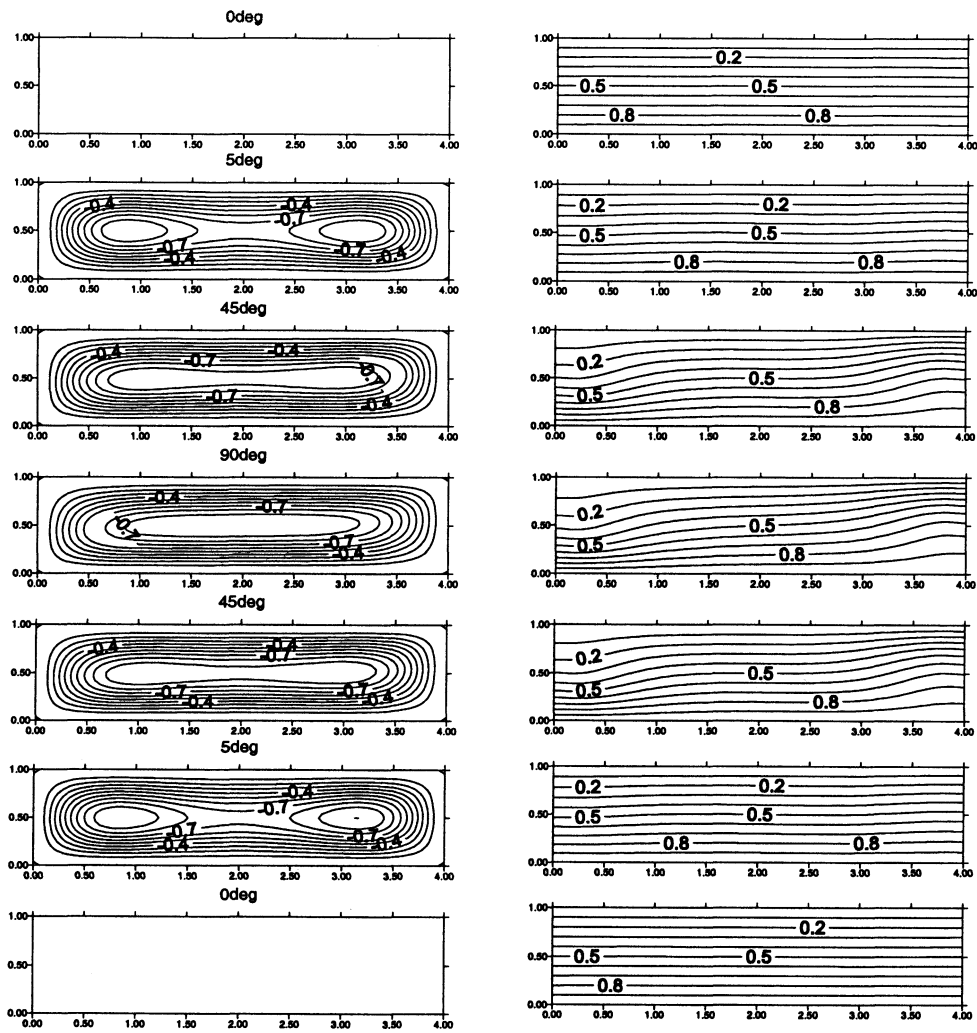


Fig. 4.23 Normalized streamlines and isothermal lines for AA configuration at various angles of inclination for $Ra=1000$ and $A=4$. Positive values indicate rotation in clockwise direction.

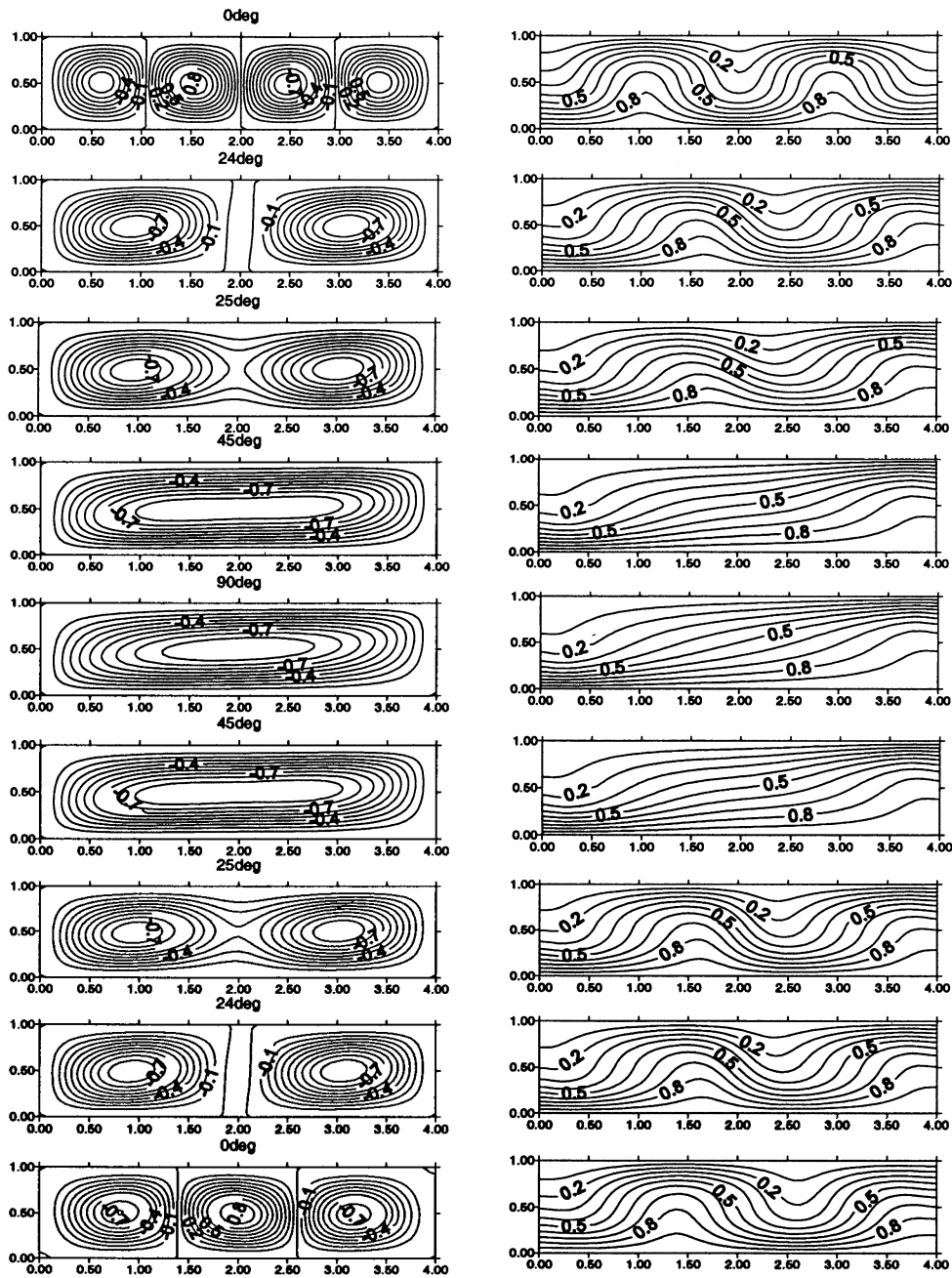


Fig. 4.24 Normalized streamlines and isothermal lines for AA configuration at various angles of inclination for $Ra=3000$ and $A=4$. Positive values indicate rotation in clockwise direction.

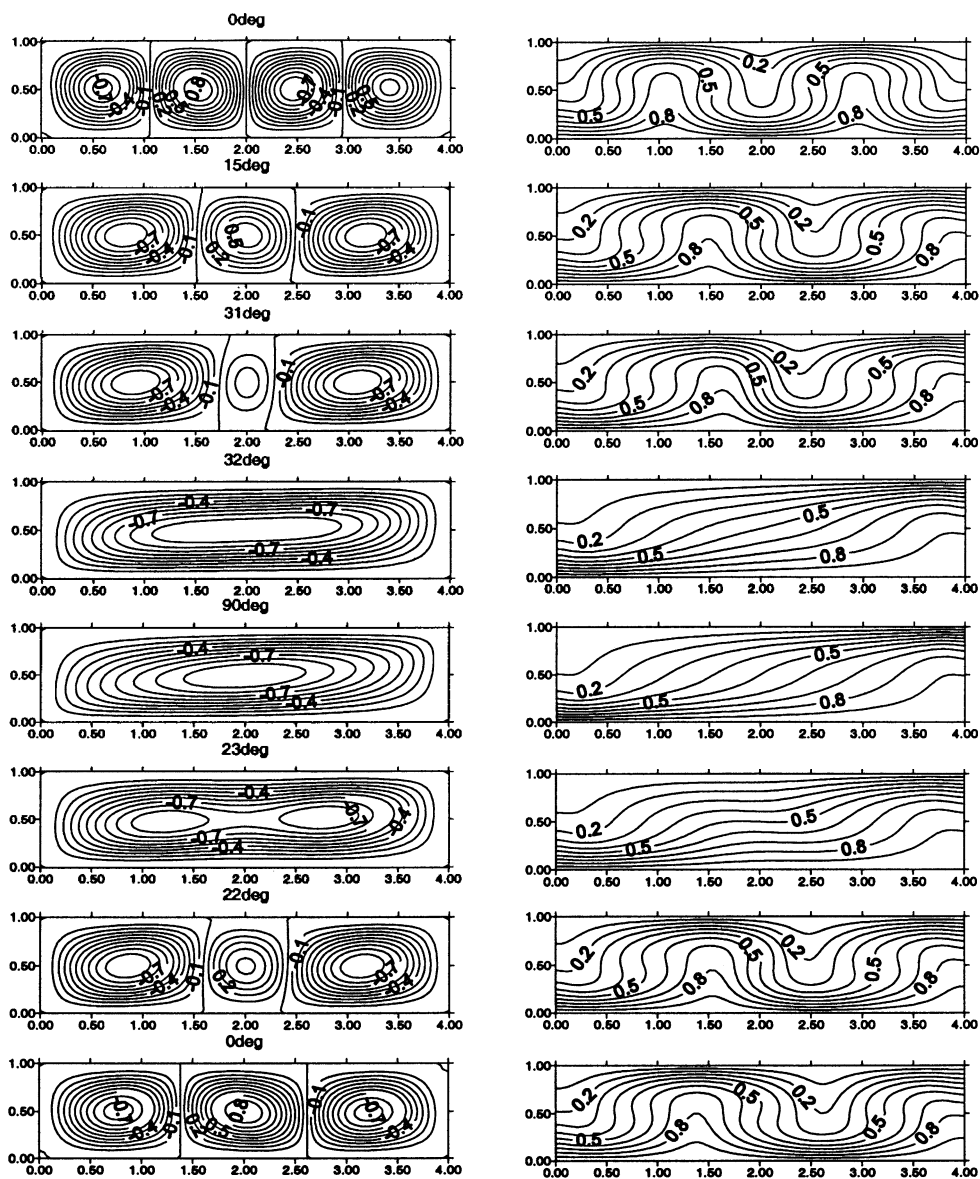


Fig. 4.25 Normalized streamlines and isothermal lines for AA configuration at various angles of inclination for $Ra=5000$ and $A=4$. Positive values indicate rotation in clockwise direction.

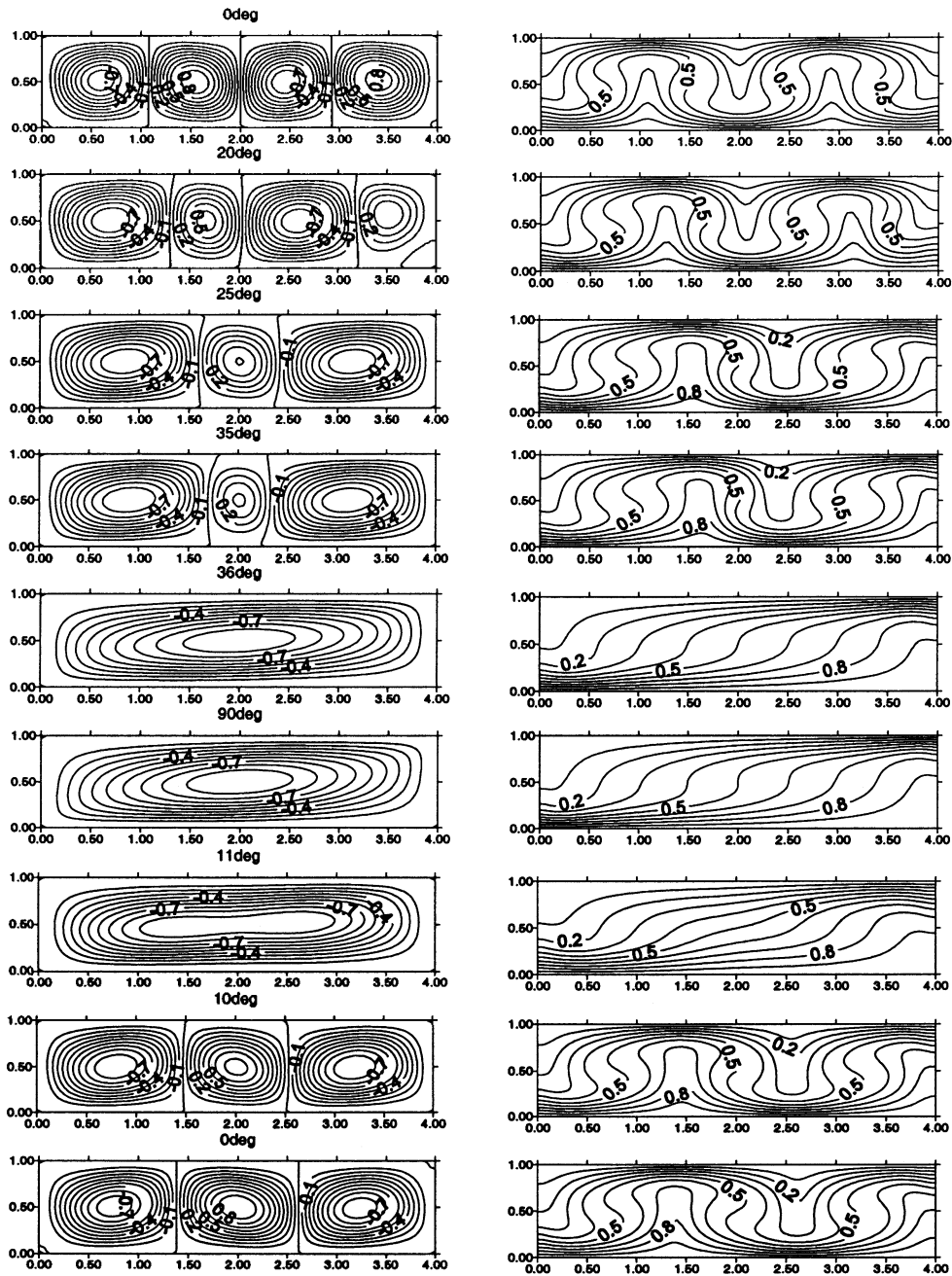


Fig. 4.26 Normalized streamlines and isothermal lines for AA configuration at various angles of inclination for $Ra=10^4$ and $A=4$. Positive values indicate rotation in clockwise direction.

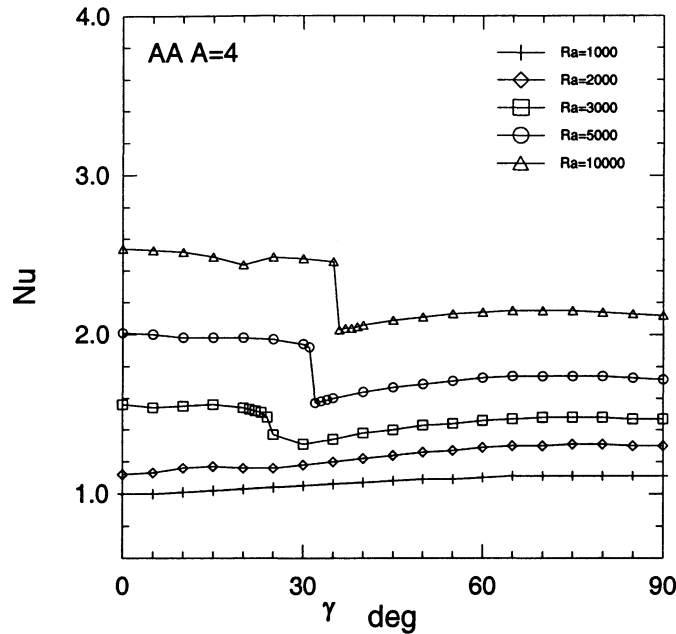


Fig. 4.27 Variation of average Nu number (both top and bottom walls) with inclination angle at various Ra numbers for AA configuration and A=4.

4.2.1.2 Cases of decreasing γ

At Ra = 1000, no significant difference can be observed between the two cases of angle increasing and decreasing, Fig. 4.28. At Ra = 3000, as angle decrease from 90° to 0°, the location of mode transition and the resulted change of Nu number are the same as in the case of angle increasing. A small hysteresis region is observed at $\gamma < 5^\circ$. Because of the initially stronger velocities in the case of angle decreasing for $\gamma = 0^\circ$, where $\psi_{max} = 5.13$ for angle decreasing. Stronger and larger cells are produced and therefore, the resulted flow field is a three-cell structure instead of four as in the case of γ increasing. Because less cells means lower rate of heat transfer, at $\gamma = 0^\circ$ there is a 6% difference in Nu numbers of angle decreasing and increasing, Fig. 4.28.

For Ra=5000, hysteresis region extends over a wider region of γ between 35° and 0°. In the case of γ decreasing, only one mode transition from 1 to 3 took place at $\gamma = 23^\circ$

resulting in a 25.3% increase in Nu number, Fig. 4.28. At $\gamma = 0^\circ$, because flow field ends up with three cells instead of four, Nu number is 5% lower than that obtained in the case of increasing γ .

For $Ra = 10^4$, mode transition from 1 to 3 is further delayed until $\gamma = 11^\circ$, resulting in about 32% increase in Nu number. At $\gamma = 0^\circ$, a difference of 4.7% between Nu number of γ decreasing and increasing can be observed.

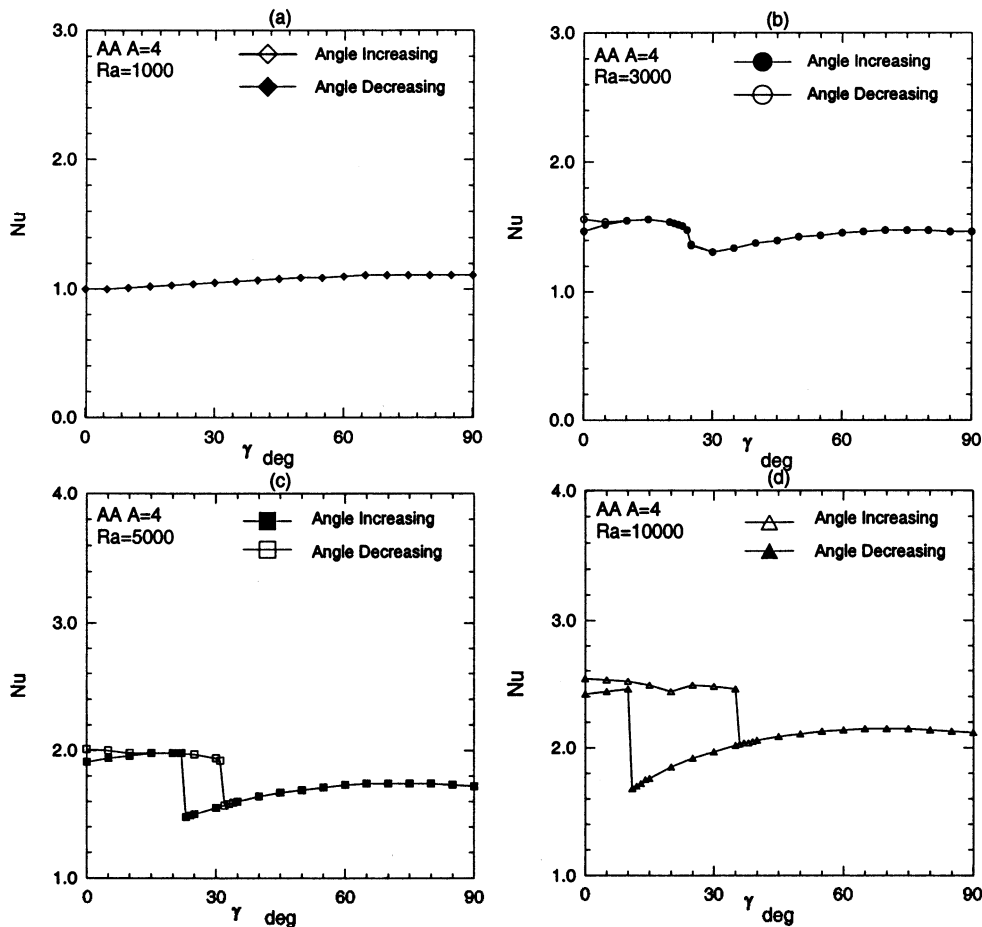


Fig. 4.28 Average Nu number (bottom wall) as a function of inclination angle γ for angle increasing and decreasing at various Ra numbers for AA configuration and A=4.

4.2.2 CH configuration

4.2.2.1 Cases of increasing γ

Due to temperature gradients at the two end walls, convection contributes immediately even at Ra below the critical limit, such as $Ra=1000$. These temperature gradients are also responsible for the development of a three-cell flow pattern, see Figs. 4.29 to 4.32. At $\gamma = 0^\circ$, Nu number is increased compared with AA configuration by 51%, 74%, 33%, 23% and 17% for $Ra = 1000, 2000, 3000, 5000, \text{ and } 10^4$, respectively, as shown in Figs. 4.27 and 4.33.

For $Ra = 1000$, i.e., below critical value, convection cell in the middle of the cavity is produced by the two cells at the two end walls, Fig. 4.29. As γ increases three cells merge producing a unicell flow structure at $\gamma = 5^\circ$.

For $Ra \geq 3000$, Figs. 4.30, 4.31 and 4.32, the middle cell is accelerated by the cross force, which makes it much stronger as compared with $Ra=1000$. This can be evident by $\psi_{\max} = 1.15$ in $Ra = 1000$. However, $\psi_{\max} = 5.43, 8.57, 13.9$ in $Ra = 3000, 5000, 10^4$, respectively. At $Ra=3000$, mode transition (3T1) occurs at the same location as AA configuration between $\gamma = 24^\circ$ and 25° , resulting in a 6 % drop in Nu number, Fig. 4.33. As Ra number increases to 5000, and 10^4 , the angle at which that mode transition (3T1) took place is almost the same as in the case of AA configuration. Nu number drop due to mode transition is 18.0% at $Ra=5000$ and 17.7% at $Ra=10^4$.

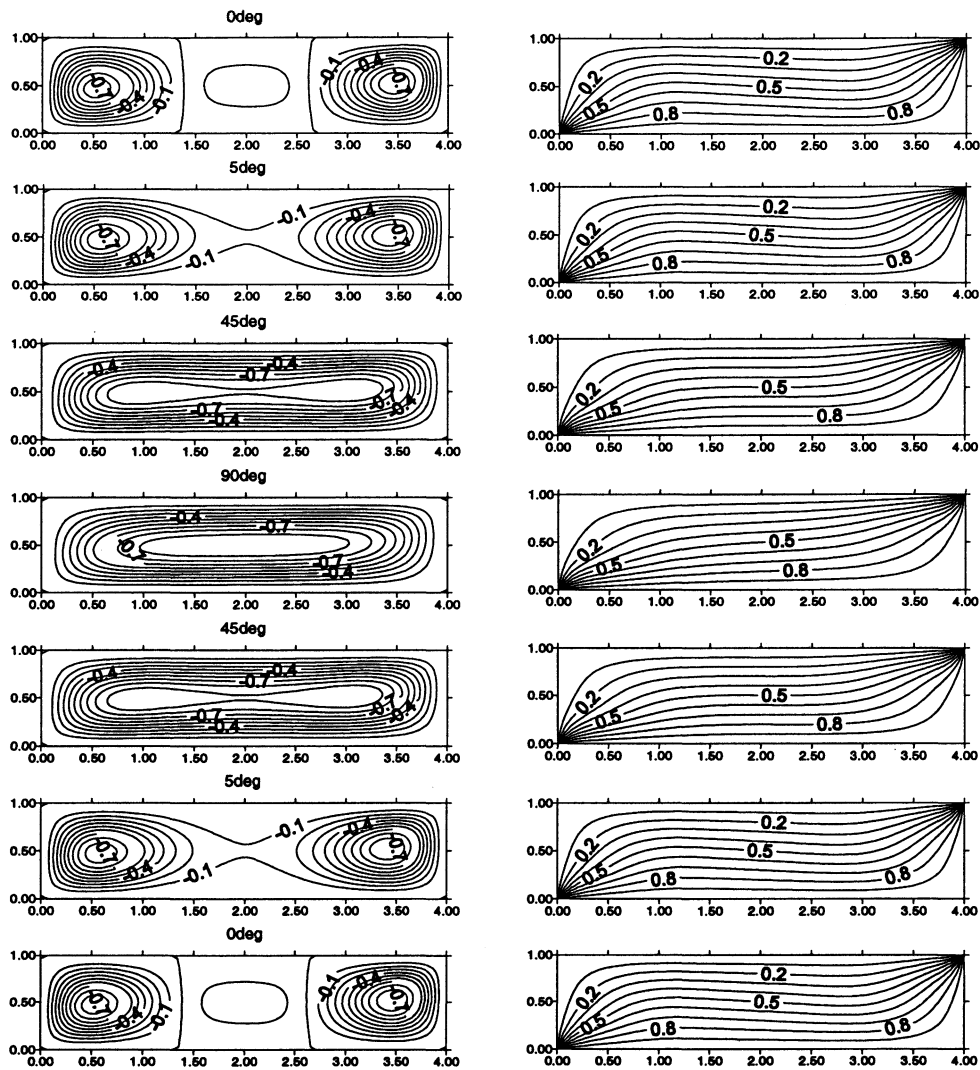


Fig. 4.29 Normalized streamlines and isothermal lines for CH configuration at various angles of inclination for $Ra=1000$ and $A=4$. Positive values indicate rotation in clockwise direction.

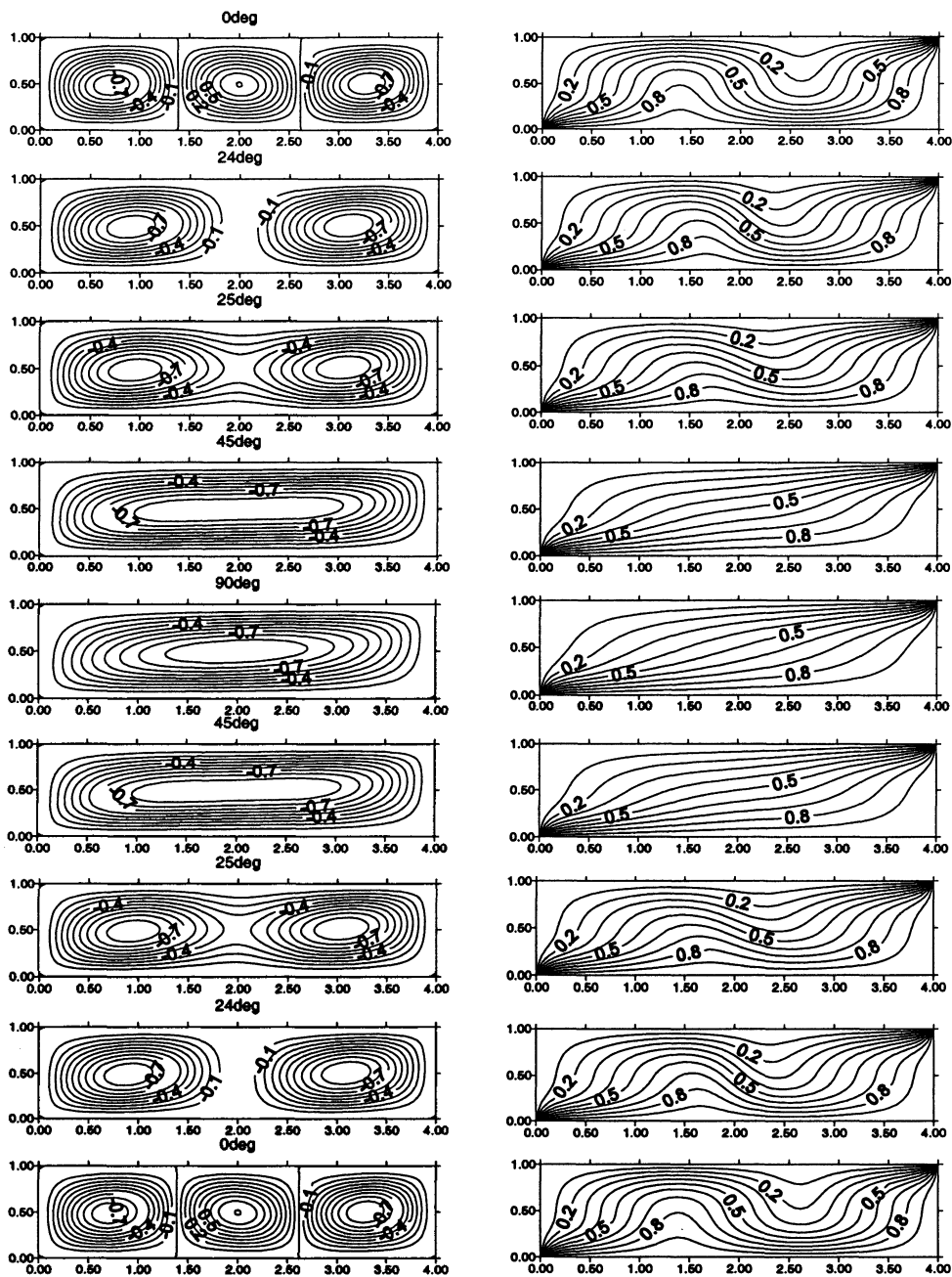


Fig. 4.30 Normalized streamlines and isothermal lines for CH configuration at various angles of inclination for $Ra=3000$ and $A=4$. Positive values indicate rotation in clockwise direction.

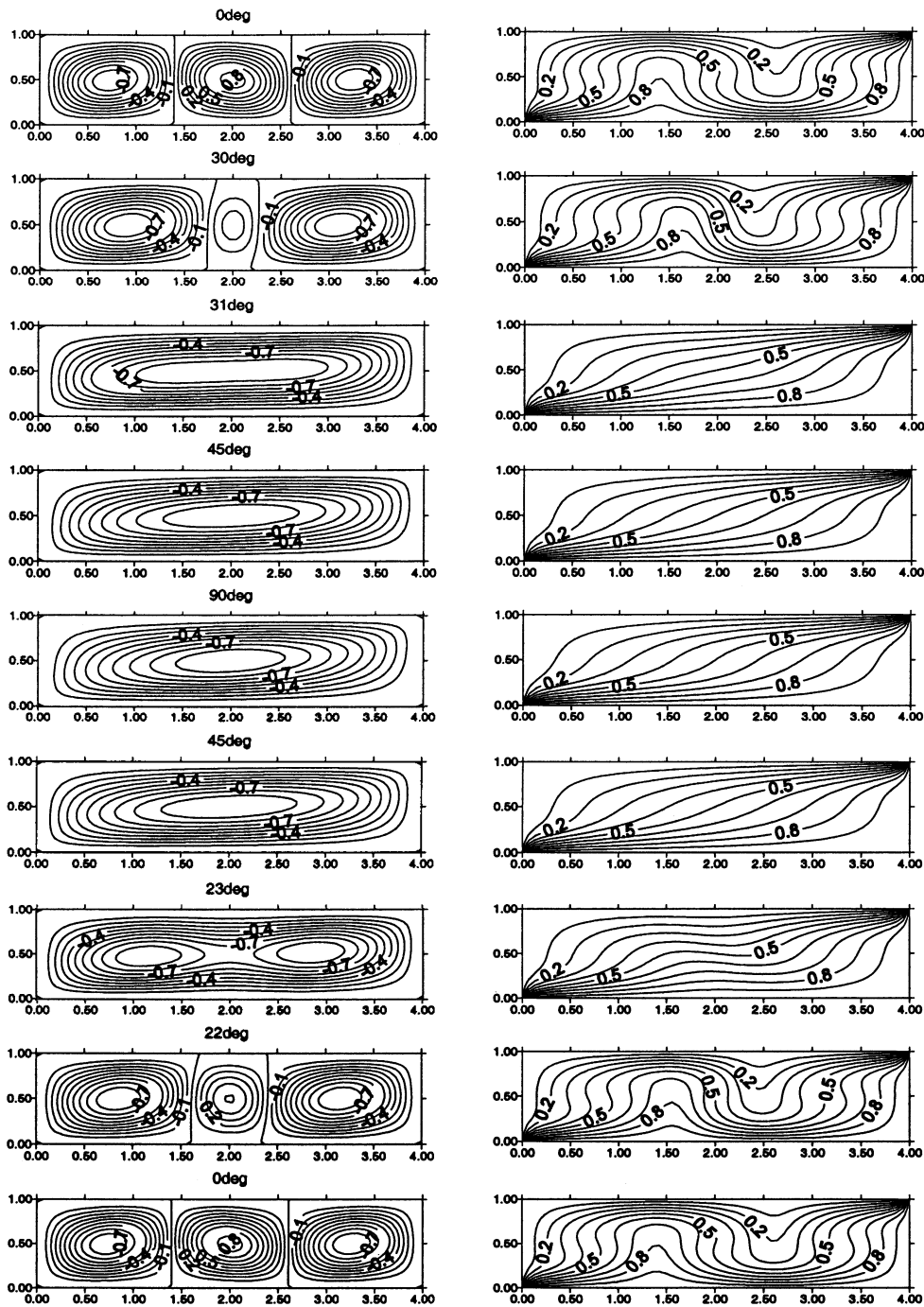


Fig. 4.31 Normalized streamlines and isothermal lines for CH configuration at various angles of inclination for $Ra=5000$ and $A=4$. Positive values indicate rotation in clockwise direction.

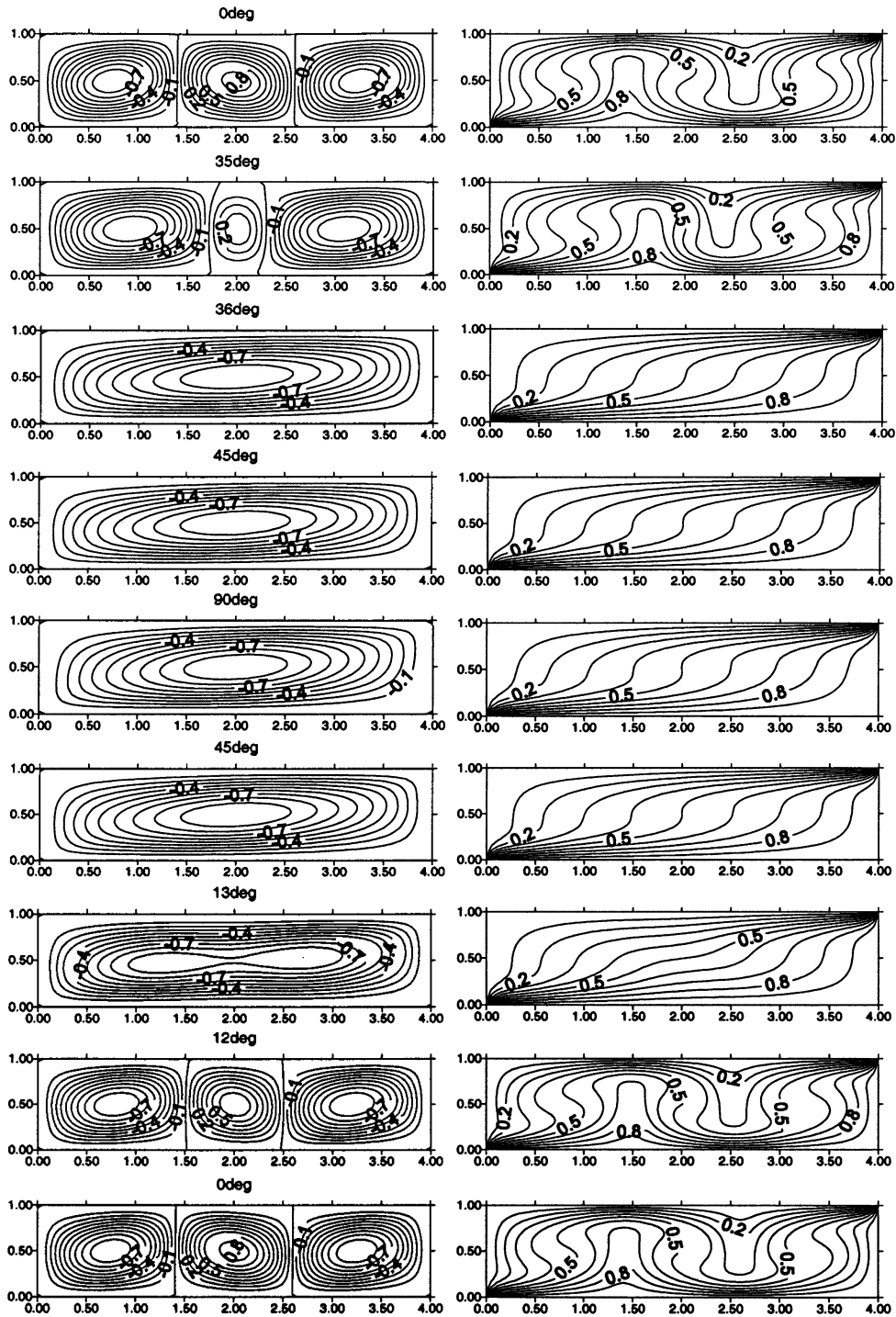


Fig. 4.32 Normalized streamlines and isothermal lines for CH configuration at various angles of inclination for $Ra=10^4$ and $A=4$. Positive values indicate rotation in clockwise direction.

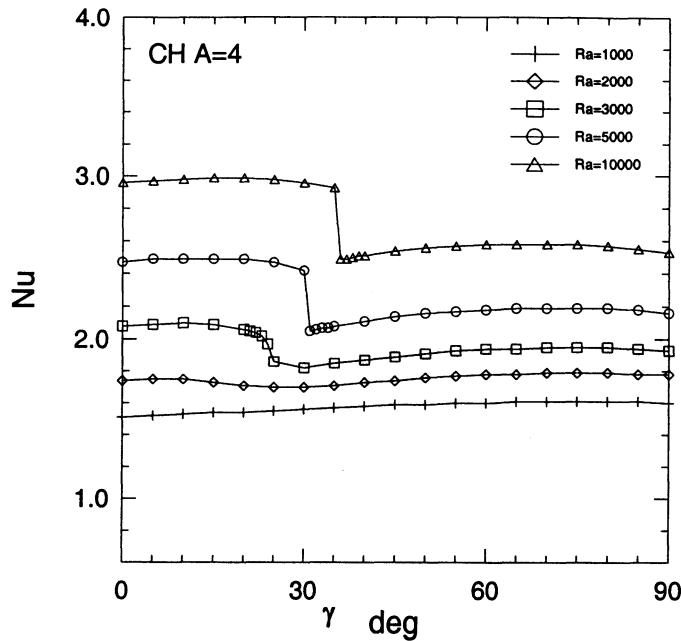


Fig. 4.33 Variation of average Nu number (both top and bottom walls) with inclination angle at various Ra numbers for CH configuration and A=4.

4.2.2.2 Cases of decreasing γ

Fig. 4.34 shows the calculated average Nu number for the two cases of increasing and decreasing γ for CH configuration. At $Ra \leq 3000$, no significant difference between the results obtained in the two courses of changing γ was observed. At $Ra = 5000$, two solutions deviate in a small region of inclination around γ between 20 and 30°. For $Ra = 10^4$, the range of γ , at which the hysteresis region exists, extends to higher angles between 10° and 35°. As illustrated in Fig. 4.32 for the case of increasing γ , at $\gamma = 0^\circ$, thermal conditions of the two end walls resulted in higher flow velocities, as evident from the value of $|\psi|_{\max} = 13.9$, which is about 13% higher than that obtained for AA configuration. Flow fields with higher velocities always result in fewer cells. Mode transition took place at $\gamma = 35^\circ$ where $|\psi|_{\max} = 15.9$ in angle increasing. In the case of

decreasing γ , a unicell flow pattern dominated until $\gamma = 13^\circ$. Here, it is worth noting that $|\psi|_{\max}$ at $\gamma = 35^\circ$ was 19.6, which is about 40% higher than that obtained in the case of increasing γ , and is equal to what was obtained in the case of AA configuration. Also, mode transition in the case of decreasing γ for CH configuration takes place earlier than that in the case of AA configuration, where it took place at $\gamma = 11^\circ$. This early mode transition is attributed to the effect of the imposed temperature gradients at the end walls. These temperature gradients resulted in a decrease in buoyancy force in the upslope-stream direction (x-direction). This effect speeded up the break-up of the unicell flow pattern, which is sustained by the upslope force, into a multi-cell structure which is, on the other hand, sustained by the cross-stream buoyancy force.

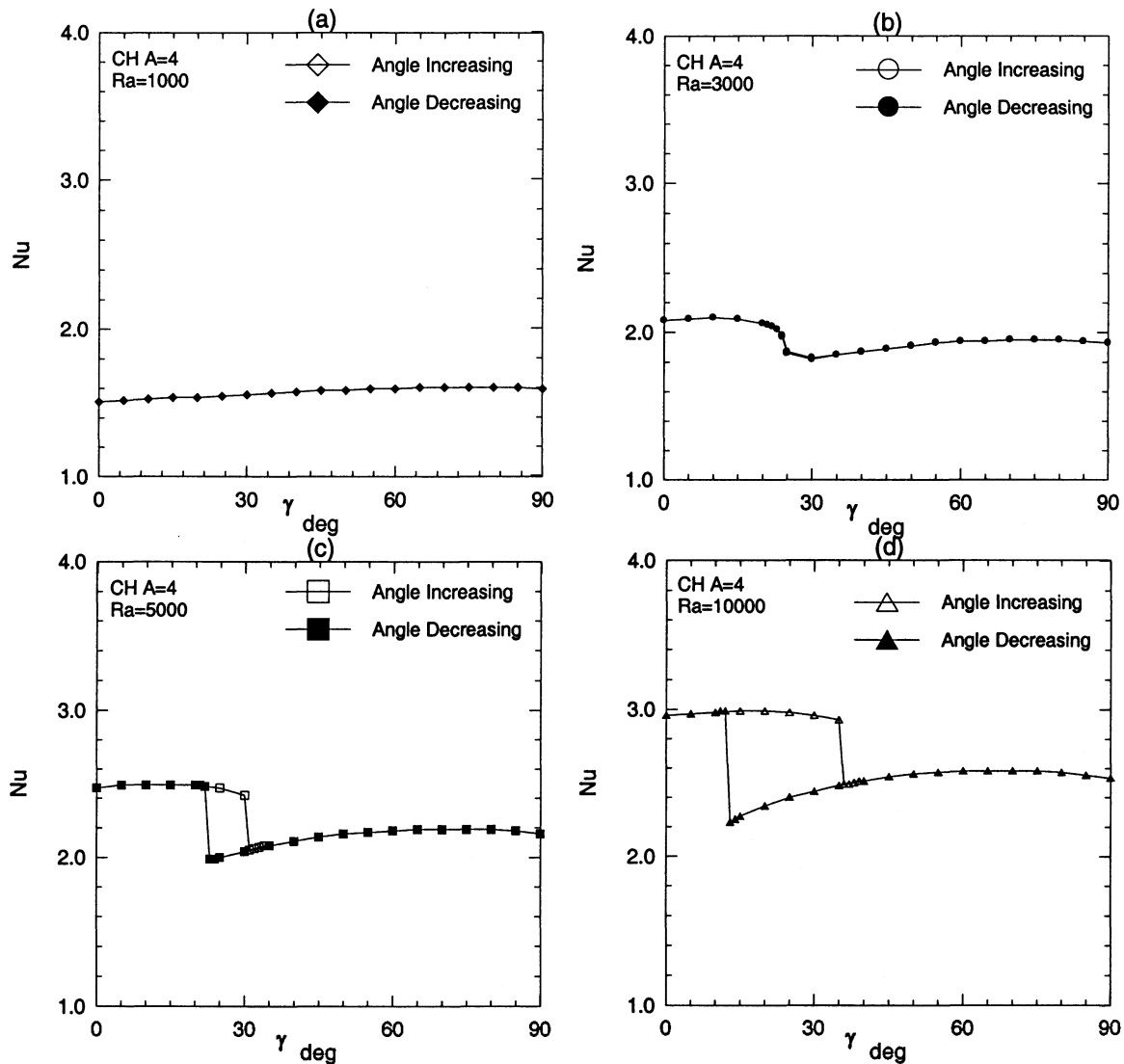


Fig. 4.34 Average Nu number (bottom wall) as a function of inclination angle γ for angle increasing and decreasing at various Ra numbers for CH configuration and $A=4$.

4.2.3 HC configuration:

4.2.3.1 Cases of increasing γ

At $\gamma = 0^\circ$, upward force from heated left wall and downward force from cooled right wall generate two cells at each side of the cavity. For $Ra = 1000$, i.e., less than the critical value, cell in the middle of the cavity is generated by these two cells, Fig. 4.35. As γ increases, the cell in the middle, which is in anticlockwise direction, is accelerated

by the upslope force and overtaken the cells beside it, which is different from the CH configuration. Finally, this middle cell occupies the whole cavity resulting in a unicell flow structure at $\gamma \geq 45^\circ$ for all Ra numbers, see Figs. 4.35 to 4.38. After the unicell flow pattern is formed, Nu number keeps decreasing all the way until $\gamma = 90^\circ$. The corresponding maximum stream function also decreases. For example, at $Ra=10^4$, ψ_{\max} is equal to 21.9 at $\gamma = 65^\circ$ and keeps decreasing to $\gamma = 90^\circ$, where it equals to 21.0. It is worth noting here that because the direction of rotation of the main cell, the one at the middle that took over the other two, is in the same direction of cavity rotation as γ increases, no sudden changes occur and as a result of that all mode transitions occur gradually, and no drastic changes in Nu number can be obtained.

Due to the additional heating from the heated left end wall and additional cooling from the right end wall, rate of heat transfer for both of top and bottom walls are increased by 51%, 55.4%, 33.3%, 22.9%, 16.5% at $\gamma = 0^\circ$ for $Ra=1000, 2000, 3000, 5000, 10^4$, respectively, as shown in Fig. 4.39. Similar to the case of $A = 2$, at $A = 4$, rate of heat transfer of bottom wall is lower than that in the case of $A=1$.

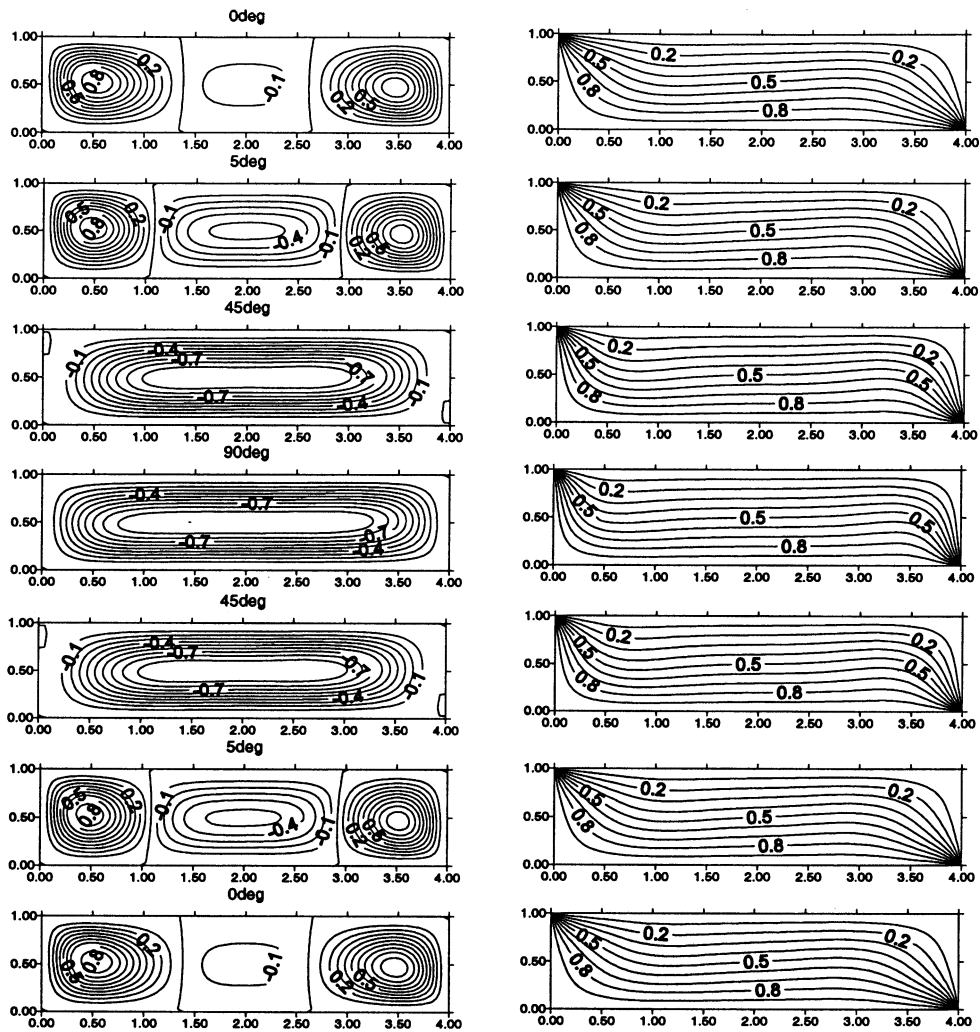


Fig. 4.35 Normalized streamlines and isothermal lines for HC configuration at various angles of inclination for $Ra=1000$ and $A=4$. Positive values indicate rotation in clockwise direction.

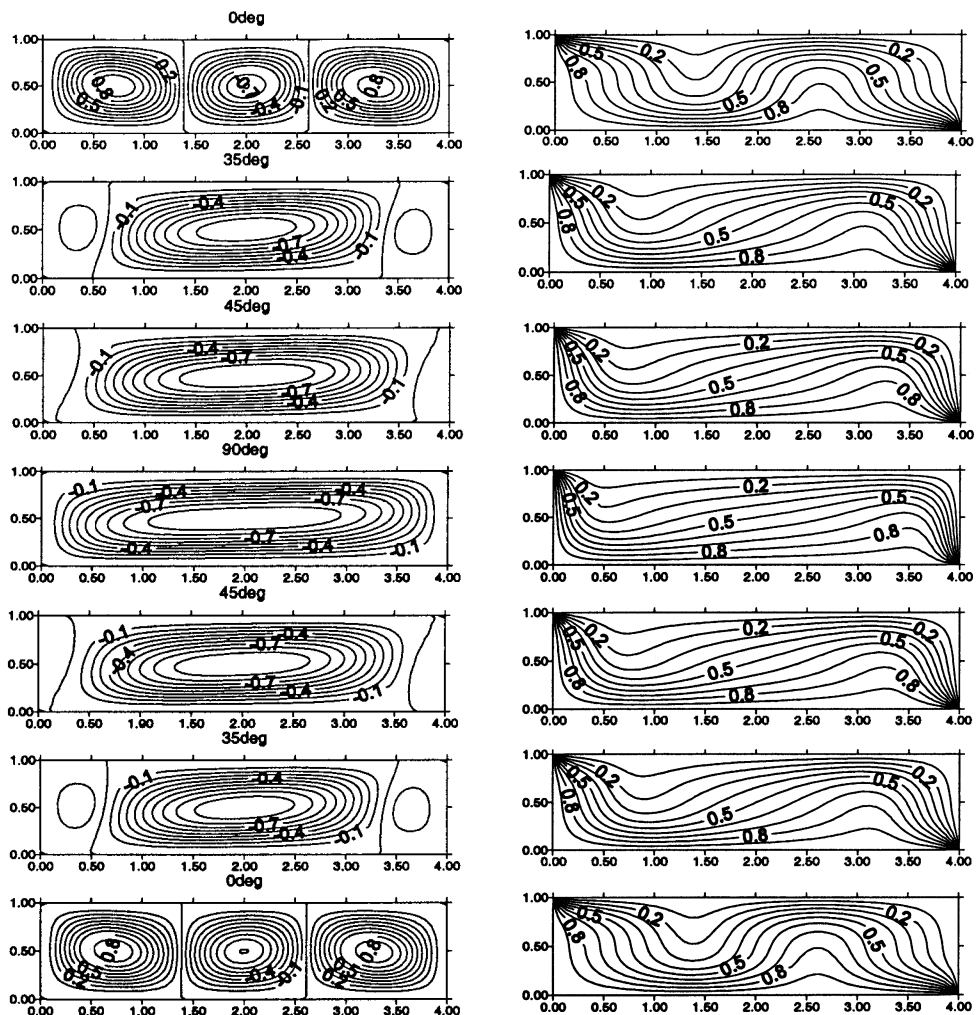


Fig. 4.36 Normalized streamlines and isothermal lines for HC configuration at various angles of inclination for $Ra=3000$ and $A=4$. Positive values indicate rotation in clockwise direction.

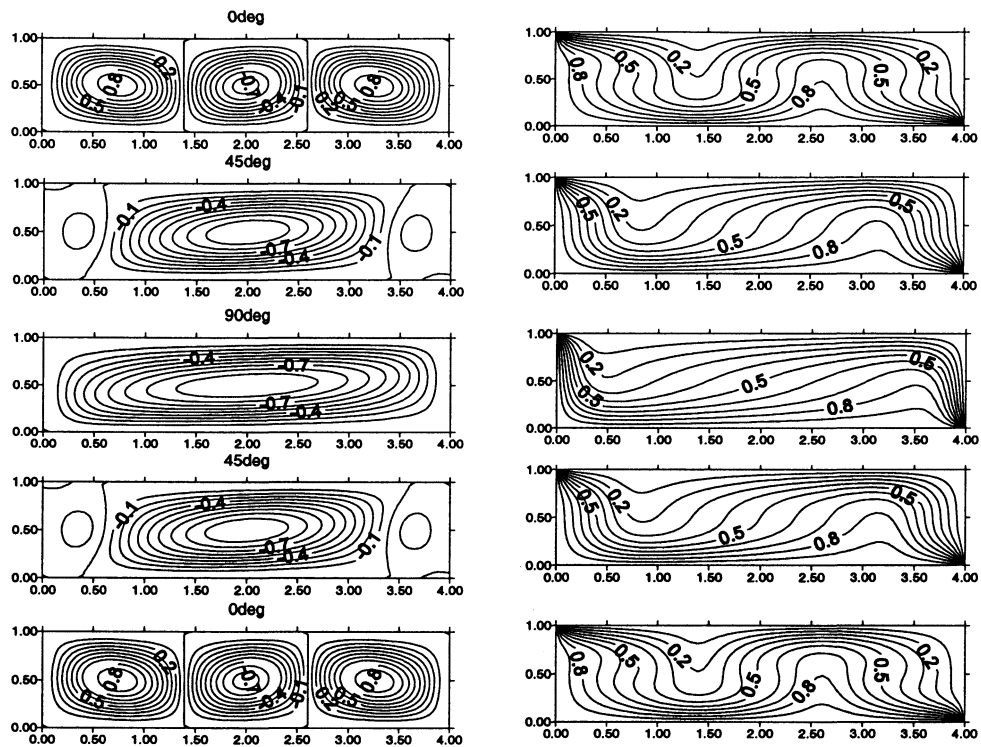


Fig. 4.37 Normalized streamlines and isothermal lines for HC configuration at various angles of inclination for $Ra=5000$ and $A=4$. Positive values indicate rotation in clockwise direction.

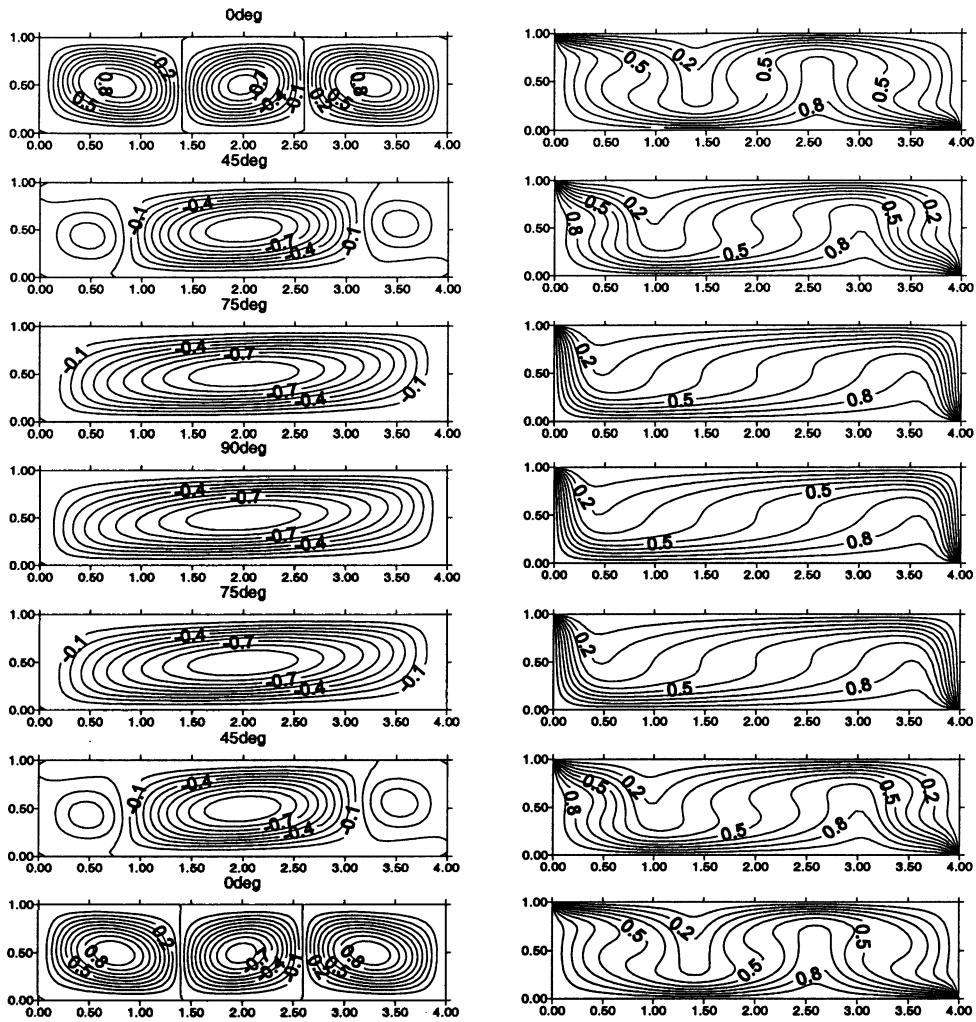


Fig. 4.38 Normalized streamlines and isothermal lines for HC configuration at various angles of inclination for $Ra=10^4$ and $A=4$. Positive values indicate rotation in clockwise direction.

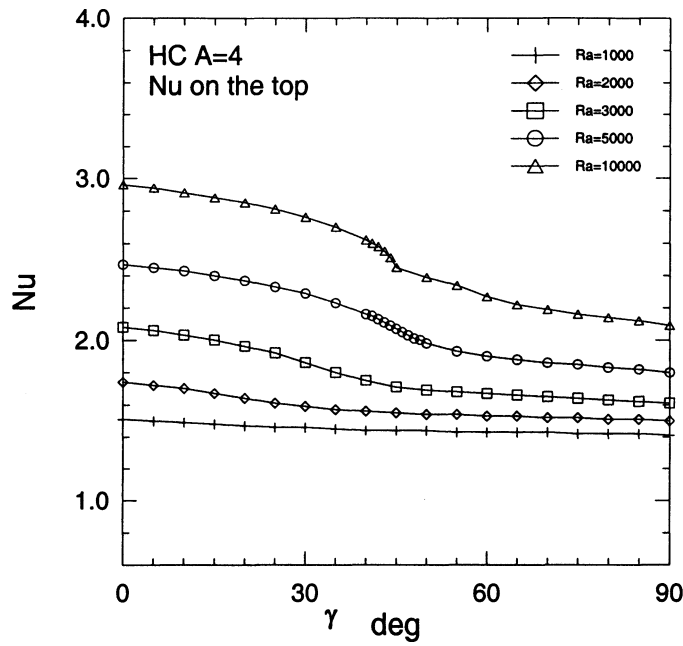


Fig. 4.39 Variation of average Nu number (both top and bottom walls) with inclination angle at various Ra numbers for HC configuration and A=4.

4.2.3.2 Cases of decreasing γ

In the case of angle decreasing, mode transition follows the same pattern as in the angle increasing case. Almost no hysteresis phenomenon can be observed as shown in Fig. 4.40, which is the same as A=2 and A=1 case. Only a little difference for Ra=10⁴ at γ between 45° and 60° can be observed.

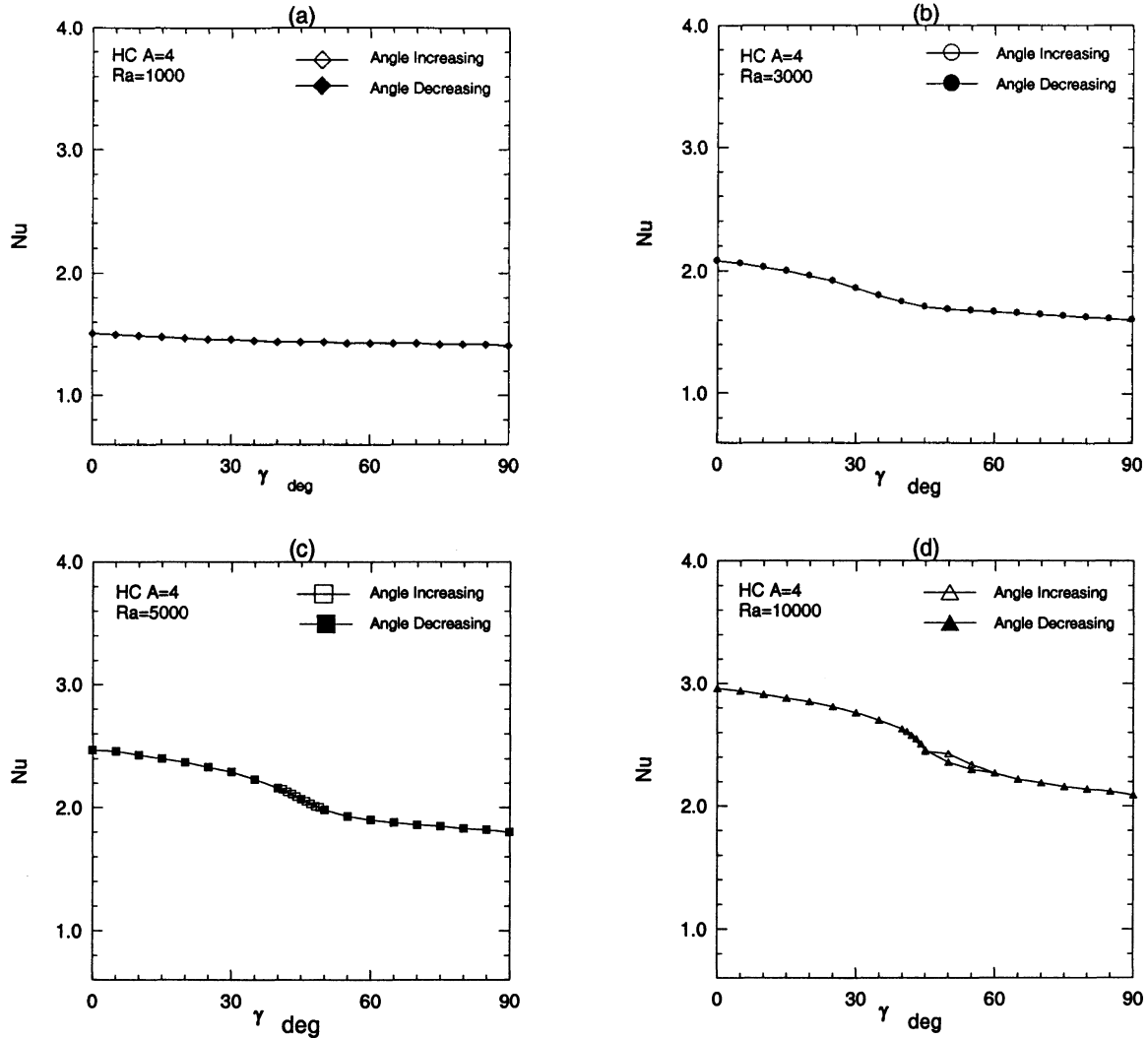


Fig. 4.40 Average Nu number (bottom wall) as a function of inclination angle γ for angle increasing and decreasing at various Ra numbers for HC configuration and A=4.

4.2.4 AC configuration

4.2.4.1 Cases of increasing γ

Downward force from right end wall generates a clockwise cell in horizontal cavity even for $Ra=1000$, Fig. 4.41. Conduction dominates heat transfer at the left part of the cavity. At $Ra = 1000$ and $\gamma = 0^\circ$, heat transfer rate of bottom wall increased by 57% as compared with AA configuration due to convection produced by the cold left end wall, Figs.4.27 and 4.45. As for the top wall, Nu number should increase due to convection as

well. However, because there is no heat transfer at an area at the right/top corner of the cavity surrounded by walls at same temperatures, that effect overcome the effect of convection, and Nu number eventually decreases by 6.4% as compared with AA configuration, Fig. 4.45. As γ increases, with the development of the upslope force, unicell formed at left part of the cavity and finally dominates the whole cavity when $\gamma \geq 45^\circ$ for all Ra numbers, Figs. from 4.41 to 4.44.

For Ra = 3000 and $\gamma = 0^\circ$, a multi-cell flow pattern with four cells is obtained, similar to the case of AA configuration, Figs. 4.24 and 4.42. As compared with AA configuration, heat transfer rate of the bottom wall increases by 38% and that of the top wall remains the same, Figs. 4.27 and 4.45, at $\gamma = 0^\circ$. Mode transition took place at γ between 19° and 20° , causing a 12% and 10% drop in Nu number of the top and bottom walls, respectively.

For Ra = 5000, mode transition takes place between 24° and 25° , which is different from the AA configuration, Figs. 4.25 and 4.43. Heat transfer rate of bottom and top walls decreases by 11.2% and 14%, respectively, Fig. 4.45.

For Ra=10⁴, four cells produced at $\gamma = 0^\circ$, Fig. 4.44. Mode transition takes place at γ between 19° and 20° , resulting in 10% and 12% drops in Nu number of top and bottom walls, respectively, Fig. 4.45. After mode transition, flow pattern having two cells is produced. Left one is supported by the upslope force, while right one is developed by the downward force from right wall. As $\gamma \geq 45^\circ$, developing upslope force dominates and flow mode changes into a unicell structure.

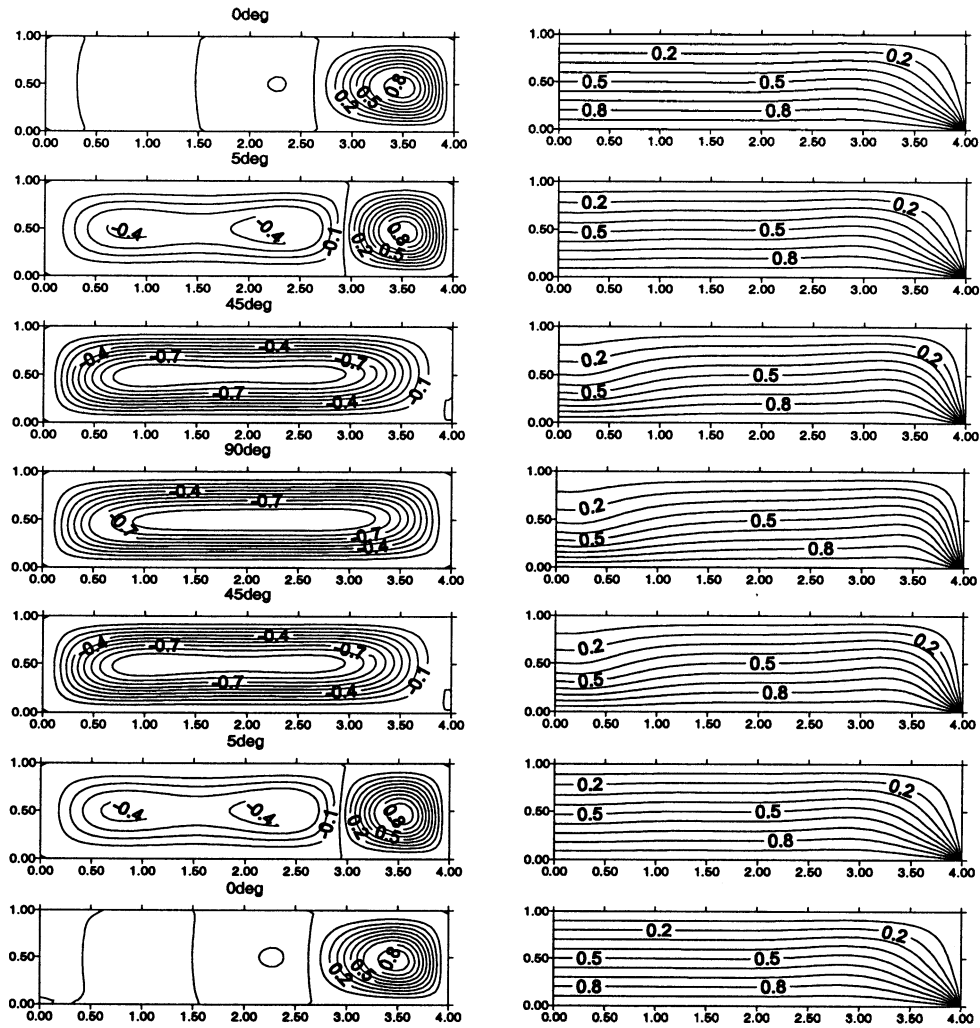


Fig. 4.41 Normalized streamlines and isothermal lines for AC configuration at various angles of inclination for $Ra=1000$ and $A=4$. Positive values indicate rotation in clockwise direction.

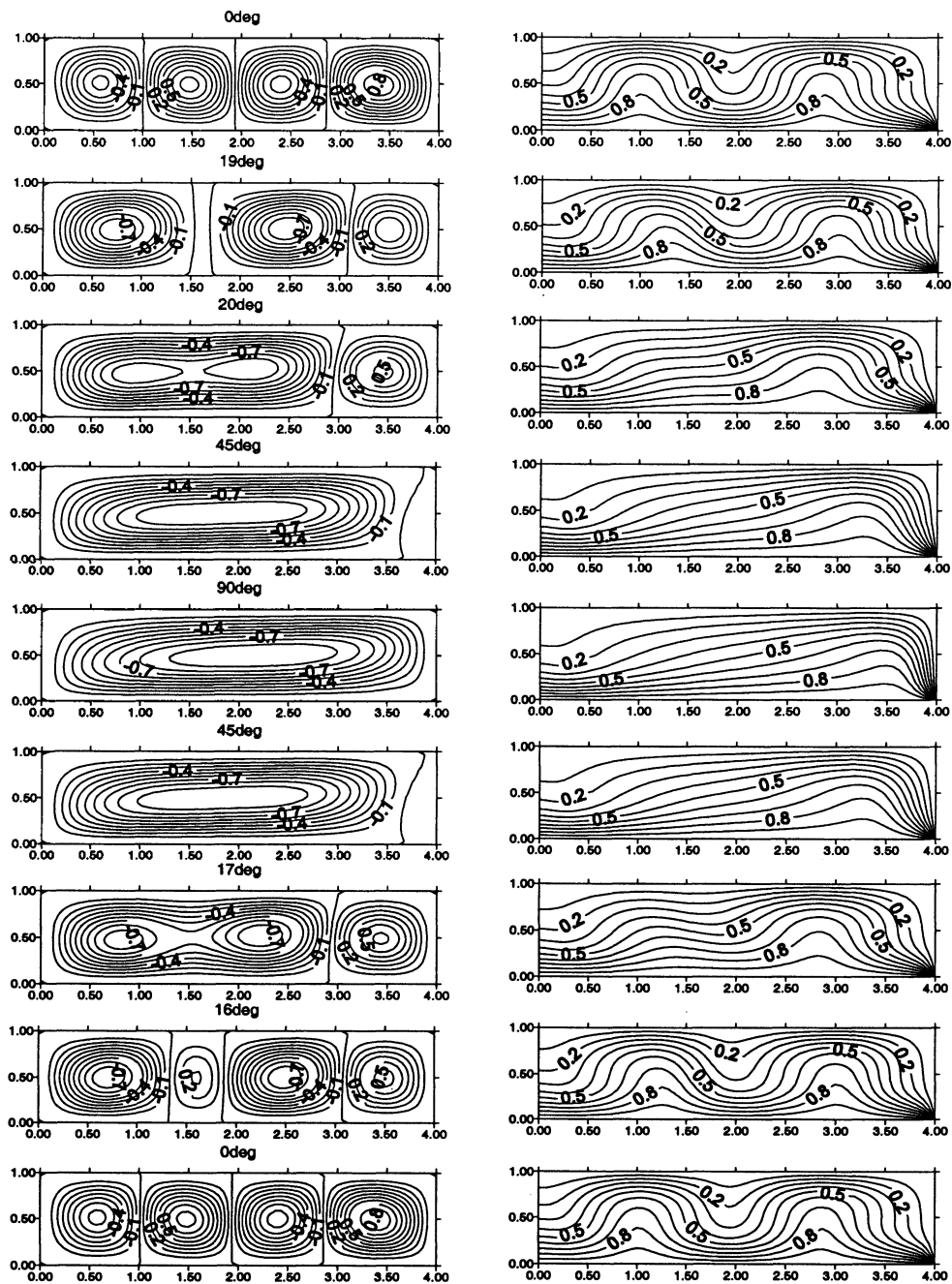


Fig. 4.42 Normalized streamlines and isothermal lines for AC configuration at various angles of inclination for $Ra=3000$ and $A=4$. Positive values indicate rotation in clockwise direction.

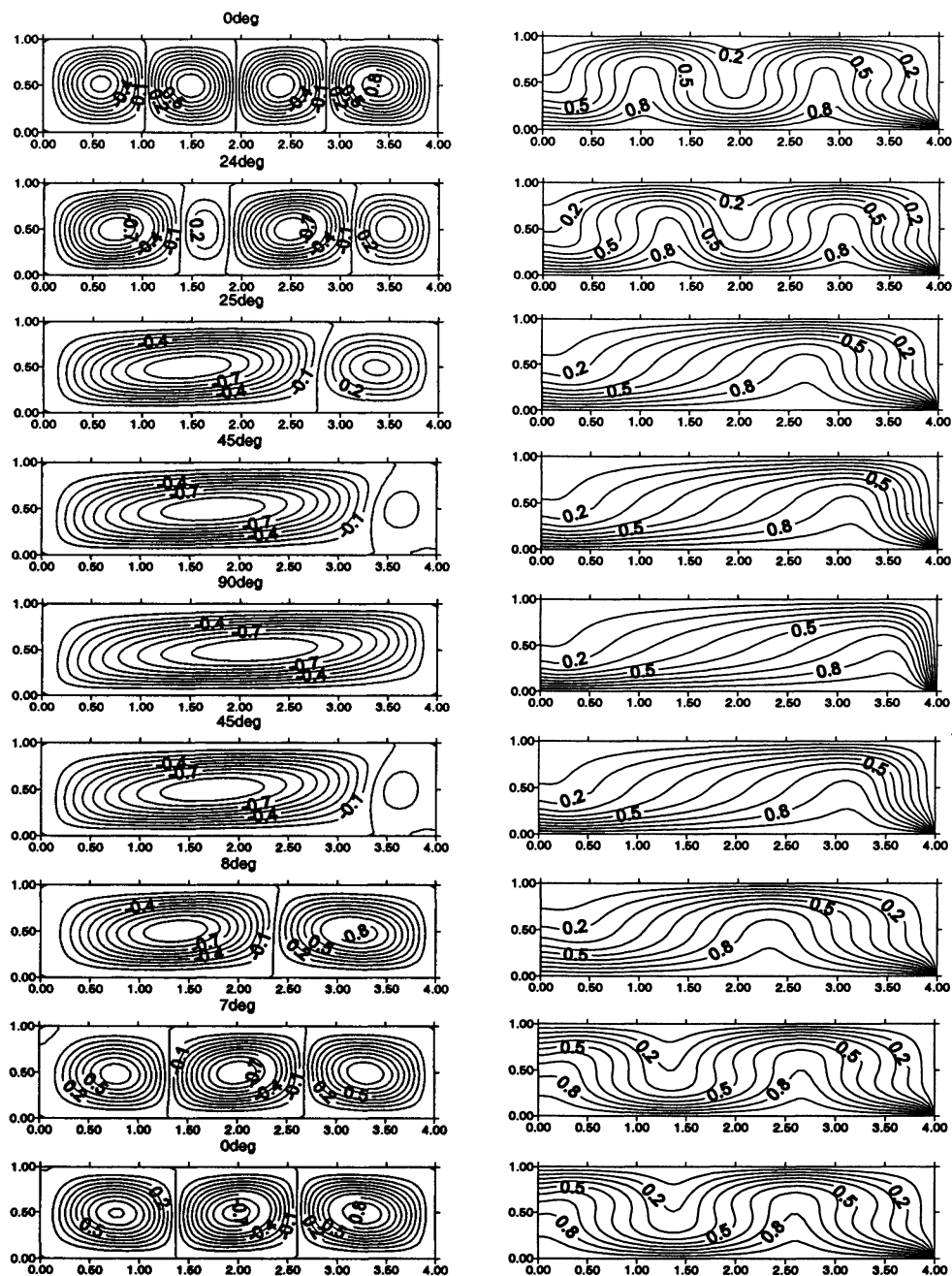


Fig. 4.43 Normalized streamlines and isothermal lines for AC configuration at various angles of inclination for $Ra=5000$ and $A=4$. Positive values indicate rotation in clockwise direction.

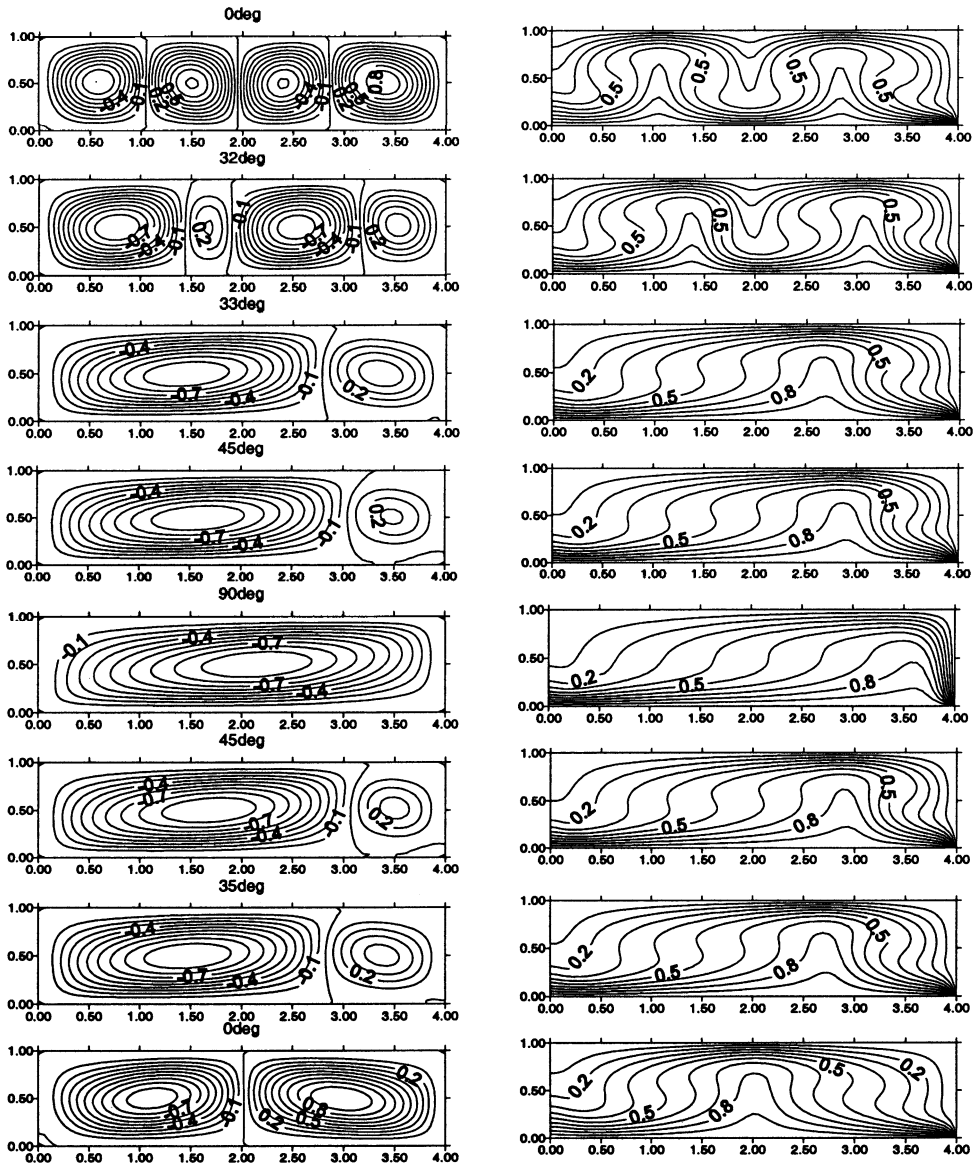


Fig. 4.44 Normalized streamlines and isothermal lines for AC configuration at various angles of inclination for $Ra=10^4$ and $A=4$. Positive values indicate rotation in clockwise direction.

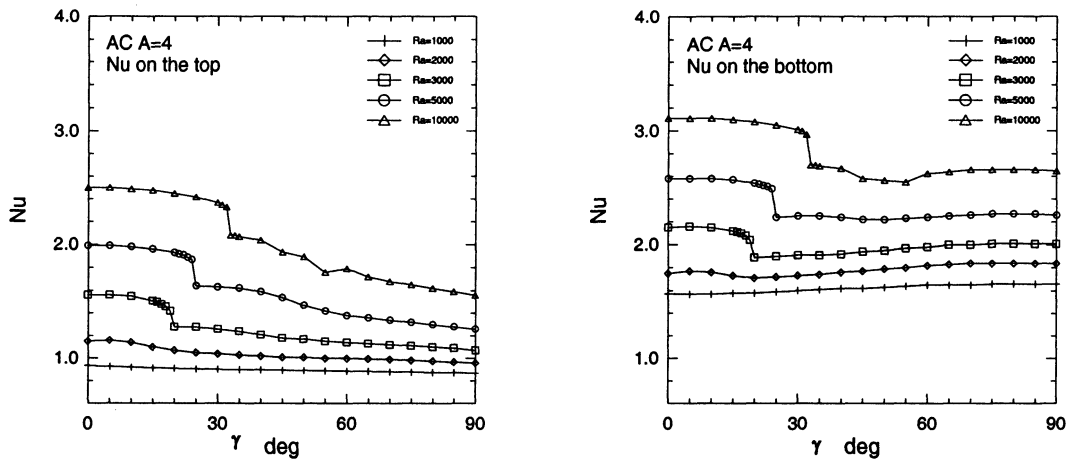


Fig. 4.45 Variation of average Nu number (both top and bottom walls) with inclination angle at various Ra numbers for AC configuration and A=4.

4.2.4.2 Cases of decreasing γ

No hysteresis phenomenon can be observed at $Ra = 1000$, Fig. 4.46. For $Ra=3000$, hysteresis phenomenon is more obvious than in the case of AA configuration, Figs 4.28 and 4.46. Mode transition for angle decreasing took place at γ between 17° and 16° , which is different than the case of angle increasing where it took place at γ between 19° and 20° , Fig. 4.46. Due to temperature gradient at the cold right end wall, a four-cell flow pattern forms as cavity returns back to horizontal position, Fig. 4.42. Mode transition occurred between 8° and 7° for angle decreasing for $Ra=5000$. Nu number of the top and bottom walls increases by 11% and 13.4%, respectively, Fig. 4.46. No mode transition occurs for $Ra=10^4$. On the way returning back to horizontal position, downward force produces a clockwise cell at $\gamma > 45^\circ$ for all Ra numbers, as shown in Figs. 4.42 - 4.44. Comparing $Ra=3000, 5000$ with 10^4 , $Ra=3000$ has lowest velocities, so left cell is broken into three cells as angle decreases, Fig. 4.42. Since magnitude of velocities in the case of $Ra=5000$ is between that of $Ra = 3000$ and 10^4 , left cell is broken into two cells, Fig. 4.43. Due to

the strongest velocities in the case of $Ra=10^4$, the space at the left part of the cavity is not enough for left cell to be broken, so no sudden changes in Nu number can be observed for angle decreasing, Fig. 4.46.

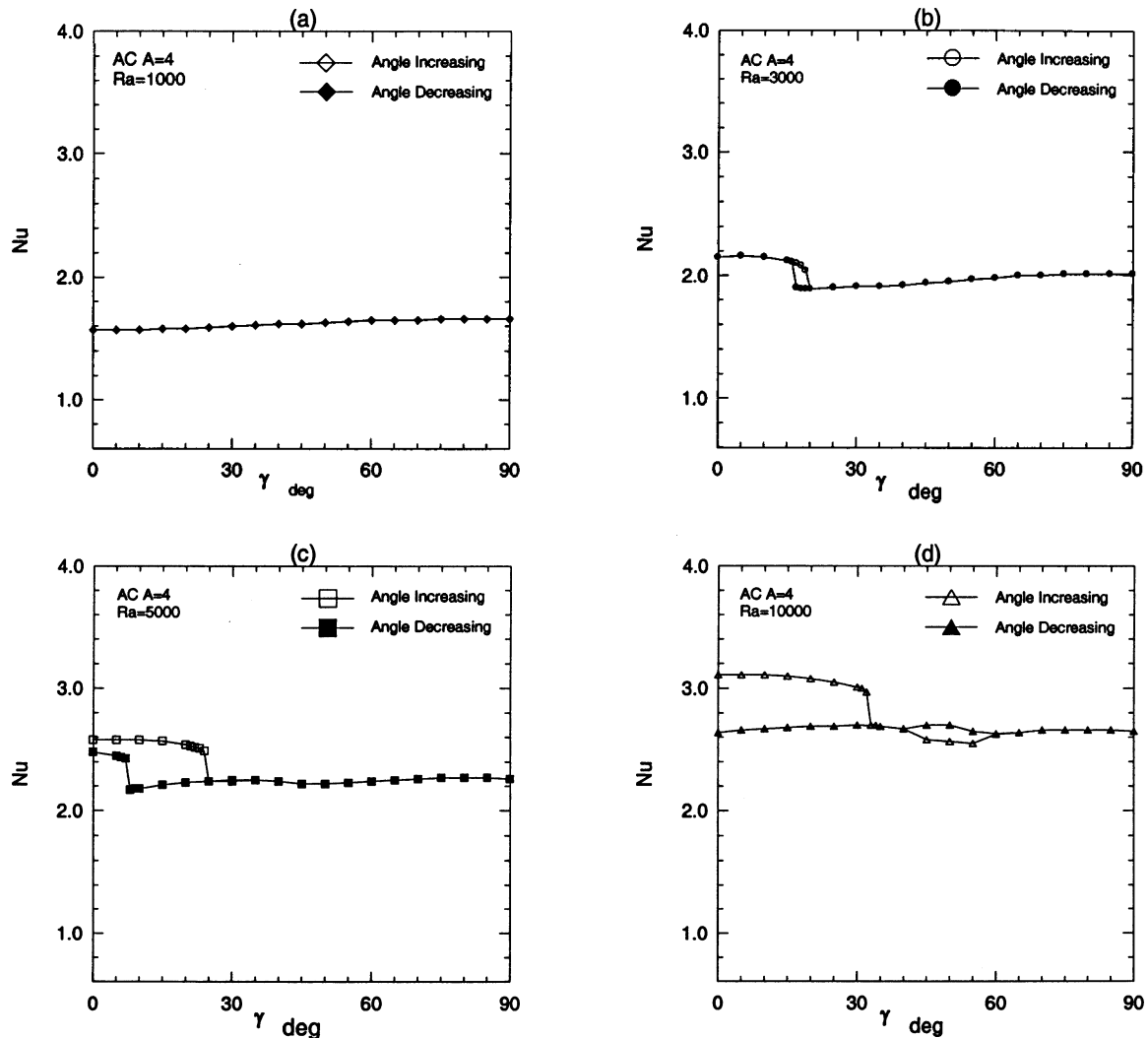


Fig. 4.46 Average Nu number (bottom wall) as a function of inclination angle γ for angle increasing and decreasing at various Ra numbers for AC configuration and $A=4$.

4.2.5 CA configuration:

4.2.5.1 Cases of increasing γ

At $\gamma = 0^\circ$, CA configuration has the same heat transfer rate as AC configuration, as shown in Figs. 4.45 and 4.51. As compared with AA configuration, as left end wall is

replaced with a cold wall, a downward force is generated. Anticlockwise cell is compelled next to the left wall, which has the same effect on the cell as the upslope force from the bottom when γ increases. Due to further cooling of the cell from left end wall, heat transfer rate of bottom wall is increased, as compared with AA configuration, Figs. 4.27 and 4.51. As γ increases, cell rotating in the anticlockwise direction is accelerated by the growing upslope force and eventually occupies the whole cavity as γ increased further. This process is observed for all Ra numbers as shown in Figs. 4.47 - 4.50.

For Ra=1000 and $\gamma=0^\circ$, right side of the cavity is dominated by conduction, Fig. 4.47. For Ra = 3000, cross force produces multi-cells, Fig. 4.48. Mode transition (3T1) takes place at γ between 24° and 25° , which is the same as AA configuration, Fig. 4.24. Nu number of the bottom and top walls decreases by 6.4% and 8.2%, respectively, Fig. 4.51.

For Ra = 5000 and 10° , location of mode transition for angle increasing is almost the same as AA configuration, as shown in Figs. 4.27 and 4.51. The relevant changes in Nu numbers of the top wall of the cavity are also very similar to the case of AA configuration, which means that the cold left end wall does not effect too much mode transition and the heat transfer rate of the top wall.

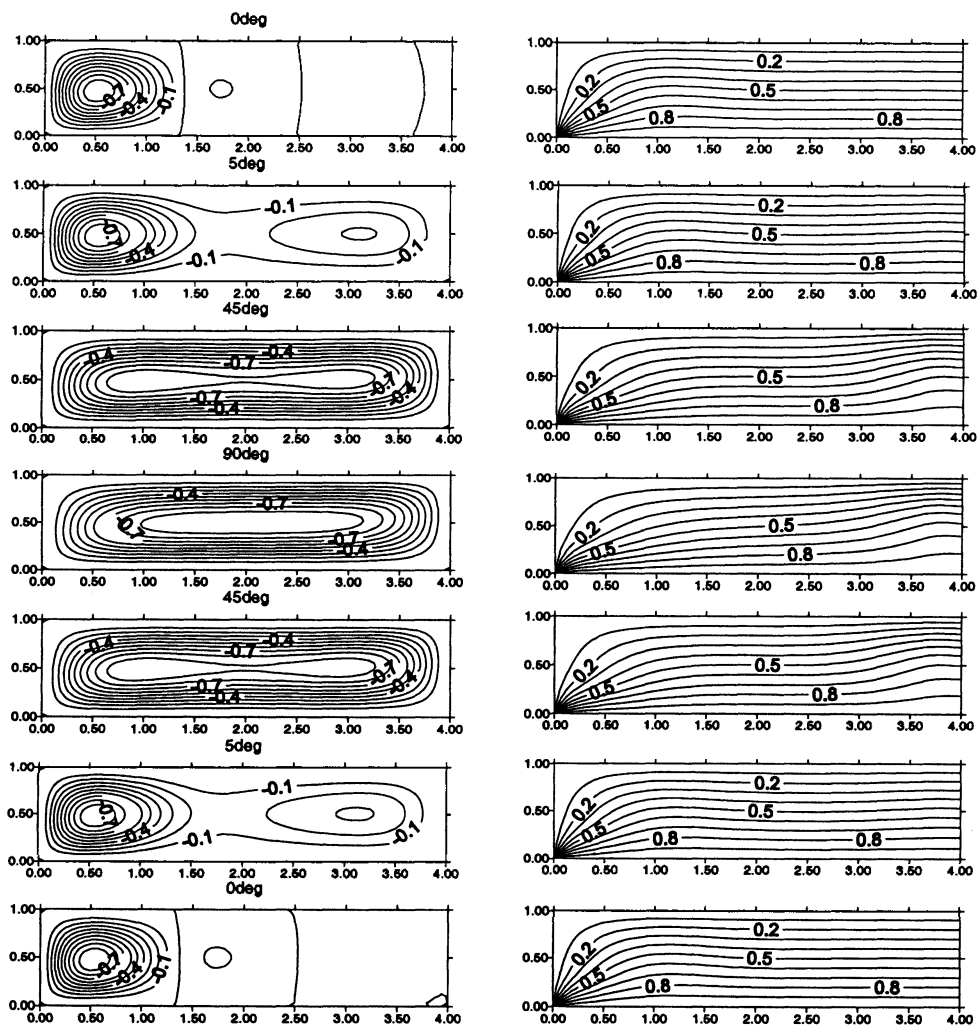


Fig. 4.47 Normalized streamlines and isothermal lines for CA configuration at various angles of inclination for $Ra=1000$ and $A=4$. Positive values indicate rotation in clockwise direction.

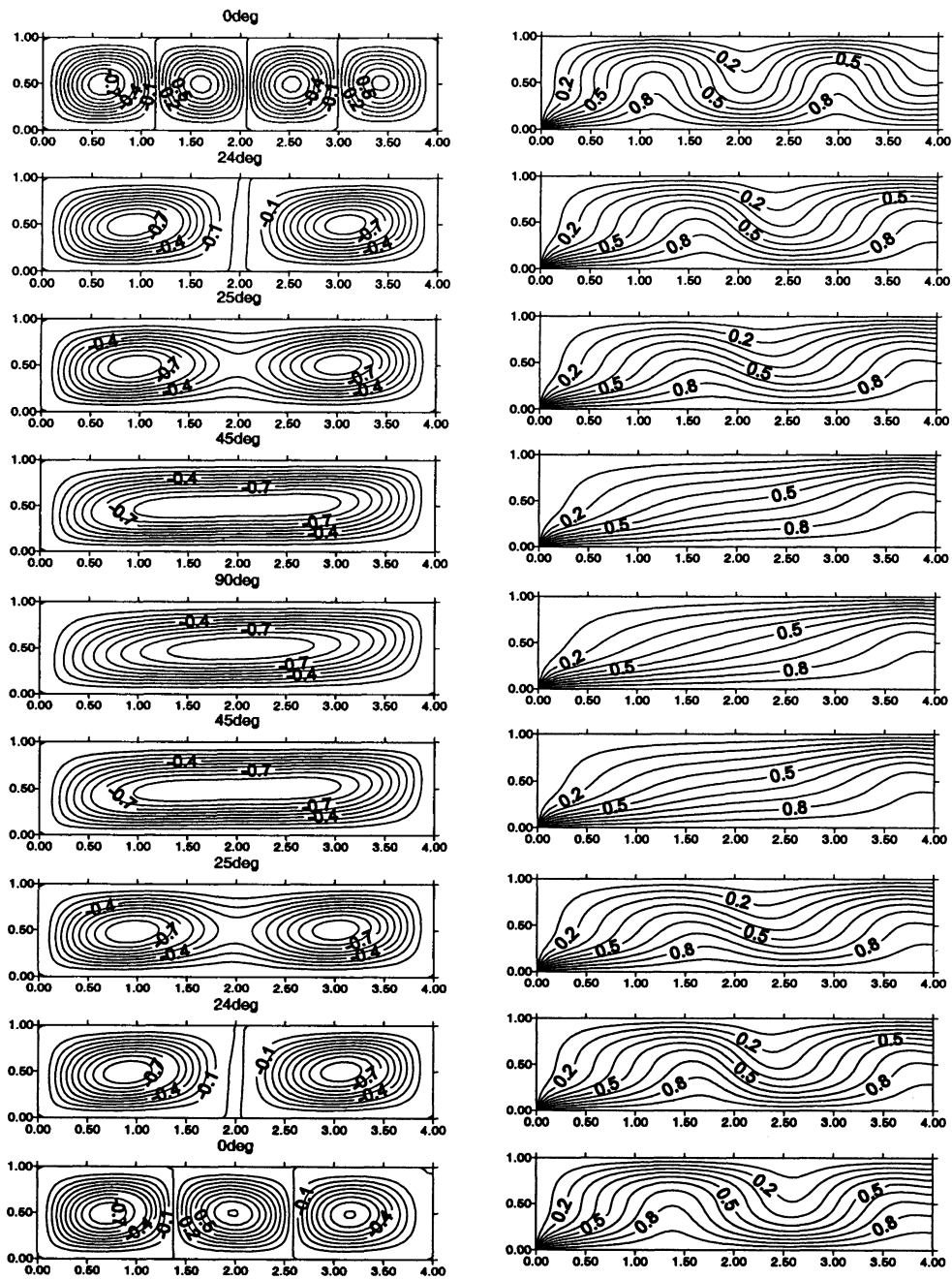


Fig. 4.48 Normalized streamlines and isothermal lines for CA configuration at various angles of inclination for $Ra=3000$ and $A=4$. Positive values indicate rotation in clockwise direction.

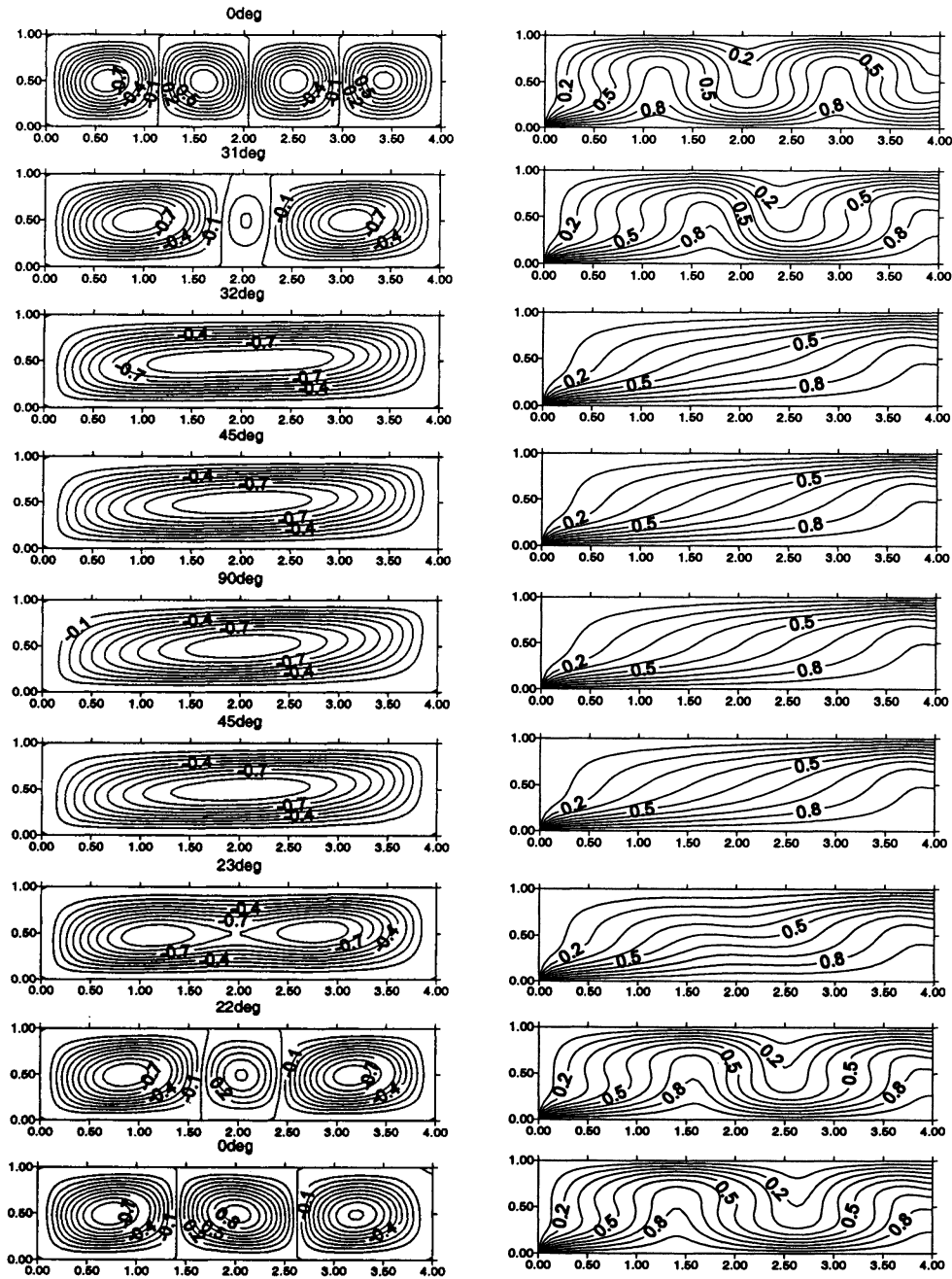


Fig. 4.49 Normalized streamlines and isothermal lines for CA configuration at various angles of inclination for $Ra=5000$ and $A=4$. Positive values indicate rotation in clockwise direction.

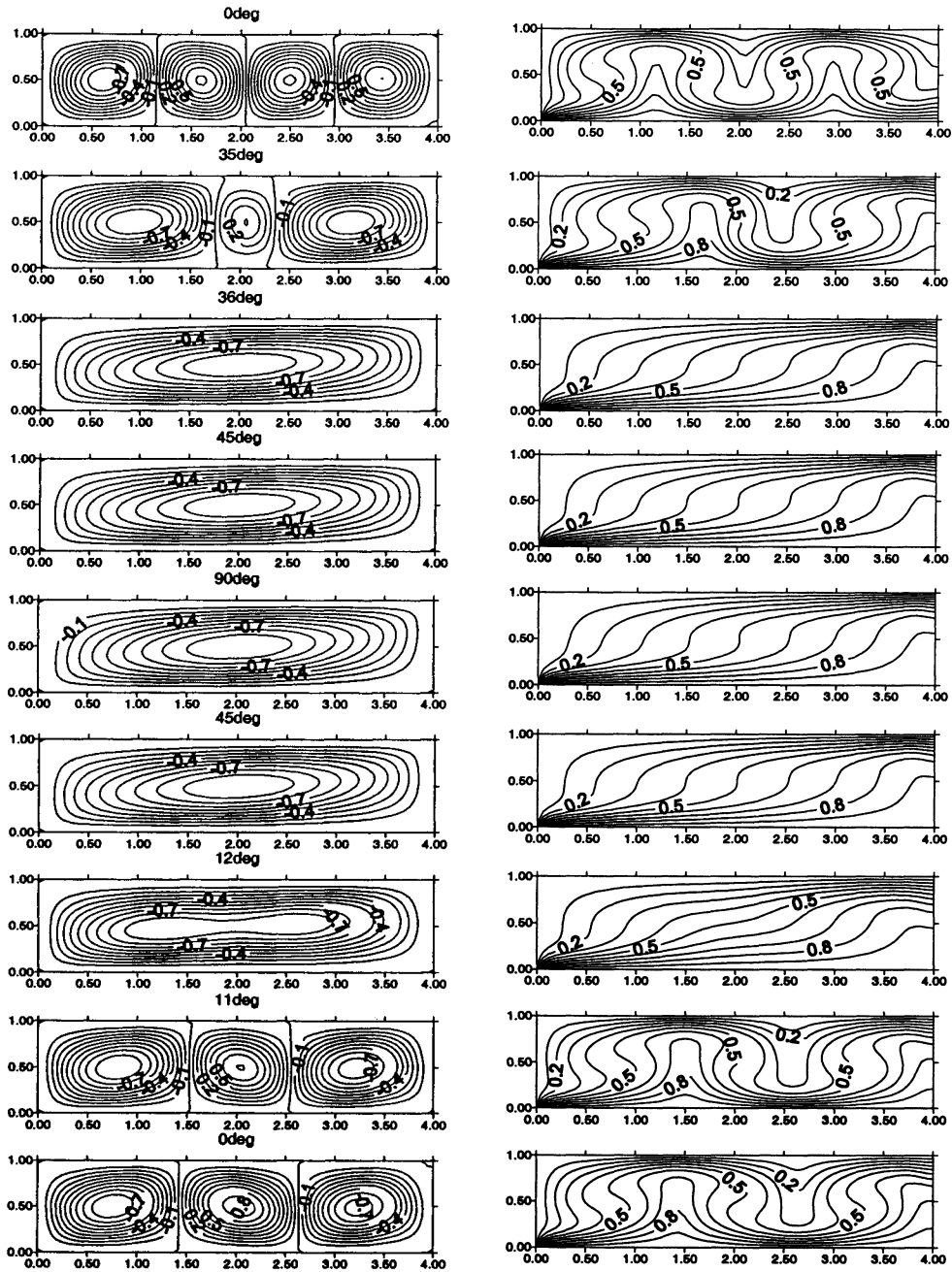


Fig. 4.50 Normalized streamlines and isothermal lines for CA configuration at various angles of inclination for $Ra=10^4$ and $A=4$. Positive values indicate rotation in clockwise direction.

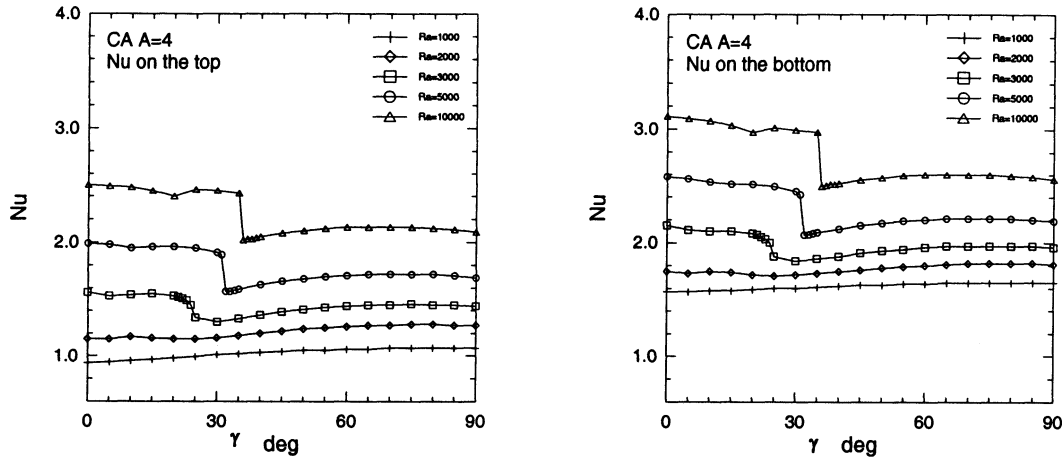


Fig. 4.51 Variation of average Nu number (both top and bottom walls) with inclination angle at various Ra numbers for CA configuration and A=4.

4.2.5.2 Cases of decreasing γ

No hysteresis phenomenon can be observed at $Ra=1000$. Hysteresis region for $Ra = 3000$ is located between 10° and 0° , which is very similar to AA configuration. Flow field finally ends up with three cells instead of four cells at $\gamma = 0^\circ$, which results in 7.7% and 8.8% difference in Nu number of the top and bottom walls, respectively. For $Ra > 3000$, mode transition takes place at the same angle as in the case of AA configuration and ends up with three cells at $\gamma = 0^\circ$. Furthermore, Nu number changes following the same trend as in AA configuration, as shown in Fig. 4.52.

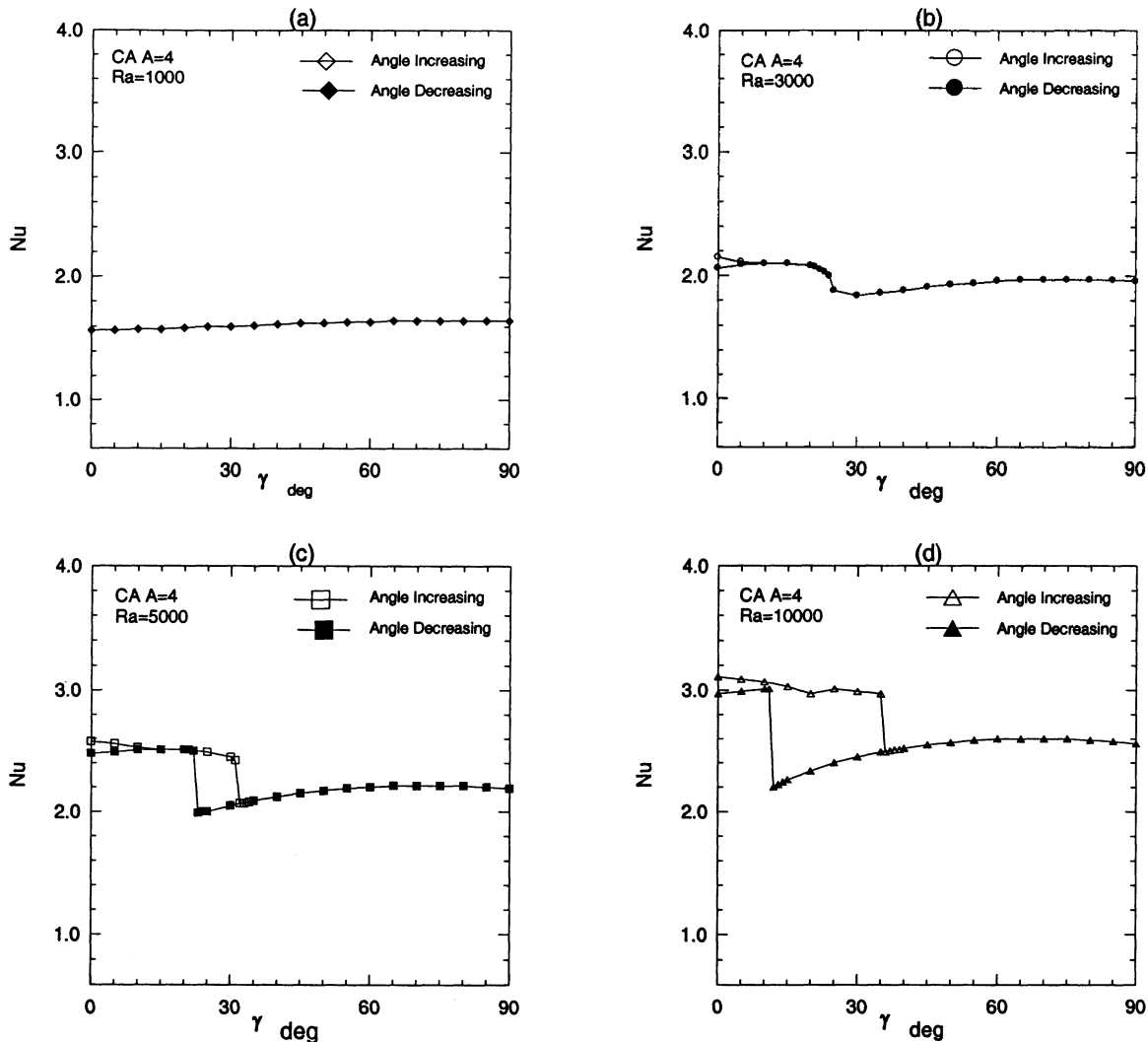


Fig. 4.52 Average Nu number (bottom wall) as a function of inclination angle γ for angle increasing and decreasing at various Ra numbers for CA configuration and A=4.

4.2.6 CC configuration:

4.2.6.1 Cases of increasing γ

With the replacement of the left and right adiabatic end walls with cold walls, cooling area is greatly increased, so heat transfer rate of the bottom wall is significantly increased by 114%, 112.5%, 75%, 56.2%, 44.9% for Ra=1000, 2000, 3000, 5000, 10^4 , respectively, at $\gamma = 0^\circ$, see Figs. 4.27 and 4.57. Increasing γ results into an early mode-transition from multi-cells to unicell, where the pre-cooling effect of the two cold walls

caused a significant decrease in the heat transfer effectiveness of the top wall. That decrease reached its maximum limit at $\gamma = 90^\circ$ as shown in Fig. 4.57.

For $Ra=1000$, which is lower than the critical value, convection is produced by and concentrated at the two cold end walls; heat transfer is dominated by heat conduction in the middle of the cavity, as shown in Fig. 4.53. Cell rotating in anticlockwise direction at left side of the cavity develops with the assistance of the upslope force at bottom wall; and finally occupies the whole cavity. Mode transition (3T1) for $Ra = 3000$ takes place at $\gamma = 18^\circ$, Fig. 4.54, resulting in a drop in Nu number of the top and bottom walls by 11% and 7.0%, respectively.

Mode transition (3T1) for $Ra = 5000$ is delayed until $\gamma = 23^\circ$, Fig. 4.55, resulting in a drop in Nu number of the top and bottom walls by 12.2% and 10.0%, respectively. It is worth noting here that the number of cells in case of CC (HH) configurations is always an even number due to the downwards at the two end walls. Although it seems that odd number of cell appears in $Ra = 3000$, there is actually a weak cell in the 'motionless' area at $\gamma = 18^\circ$. The value of this weak cell is less than 0.1, so it is not shown in the Figs. 4.54.

At $Ra=10^4$ and $\gamma = 0^\circ$, a four-cell flow pattern is observed, which is the same as those observed for $Ra = 3000$ and 5000. As the cavity is inclined, i.e., γ is increased, the temperature gradient at the right end wall produces a downward force that results into a clockwise rotating cell. At $\gamma = 30^\circ$, a transition in the flow pattern takes place, which reduces the number of cells to only 2. This transition causes a sudden drop in average Nu number of the top and bottom walls of the cavity, as shown in Fig. 4.57. The whole cavity is then occupied by one cell except at the right corner where the downward force

caused by the thermal condition of the right wall sustains a clockwise rotating cell. The two opposing forces, the one caused by the upward temperature gradient and the downward force caused by the cold right wall co-exist until $\gamma = 45^\circ$ at which time the clockwise rotating cell can not resist the upward flow coming from the hot wall and, then, is smeared out, at which time the whole cavity is occupied by a unicell flow. At $\gamma = 0^\circ$, heat transfer effectiveness of the top wall for Ra numbers ≥ 3000 has slightly decreased compared with AA configuration, Figs. 4.27 and 4.57. For Ra= 2000, it is increased by about 10%, while decreased by about 40% at Ra=1000. These results warrant a closer look at the effect of the two cold walls on flow pattern, and hence on the effectiveness of the heat transfer of the top wall.

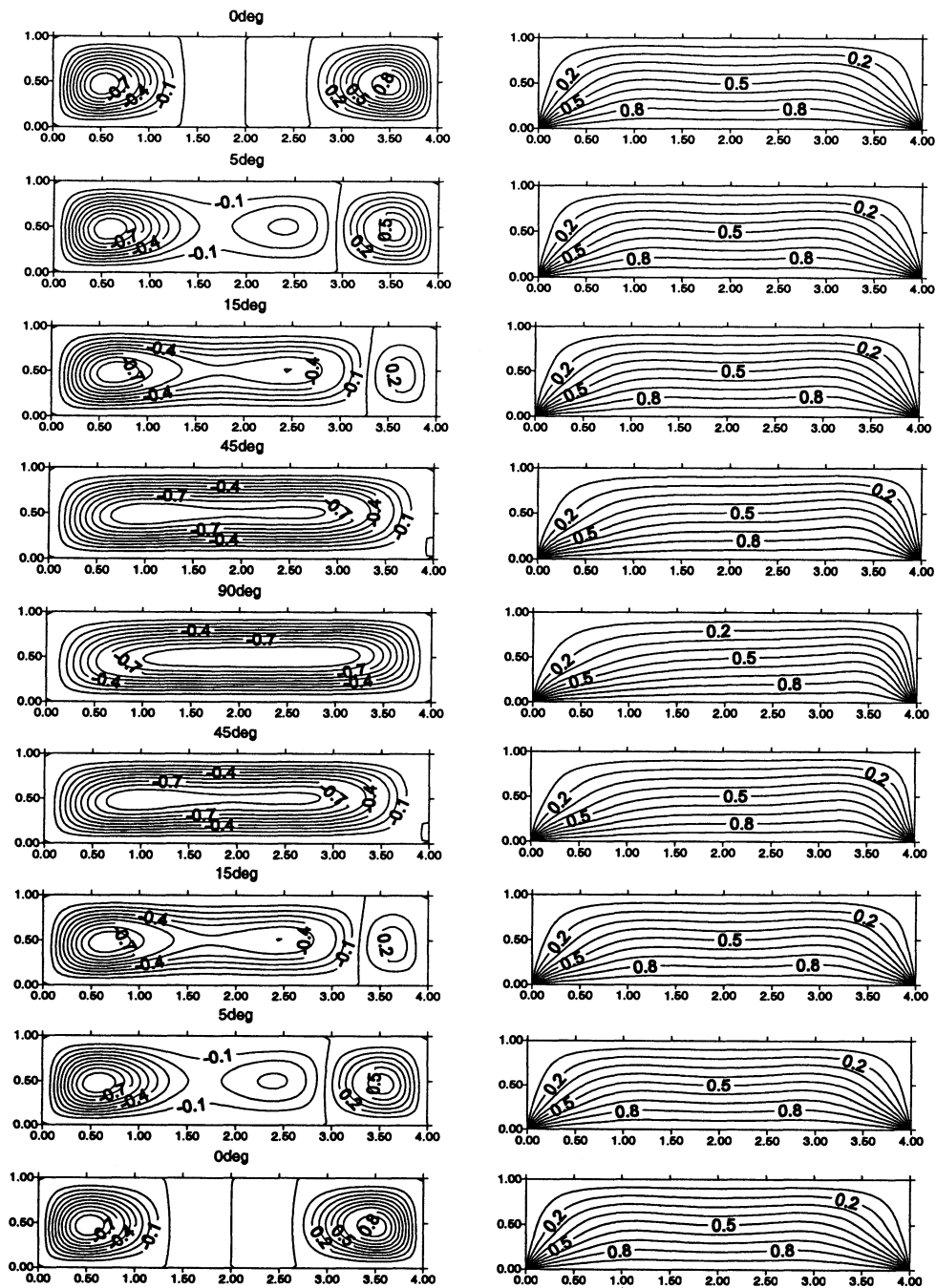


Fig. 4.53 Normalized streamlines and isothermal lines for CC configuration at various angles of inclination for $Ra=1000$ and $A=4$. Positive values indicate rotation in clockwise direction.

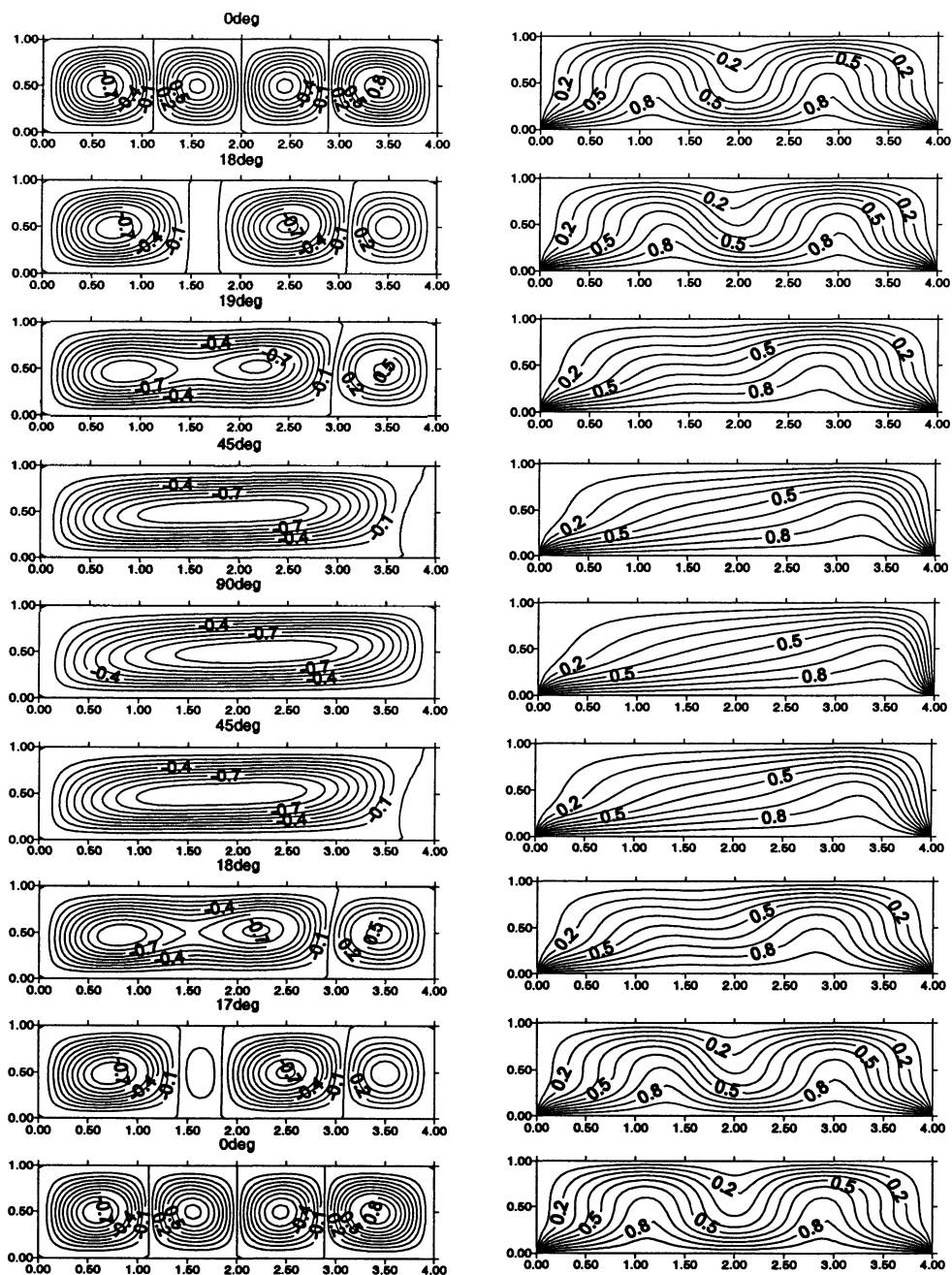


Fig. 4.54 Normalized streamlines and isothermal lines for CC configuration at various angles of inclination for $Ra=3000$ and $A=4$. Positive values indicate rotation in clockwise direction.

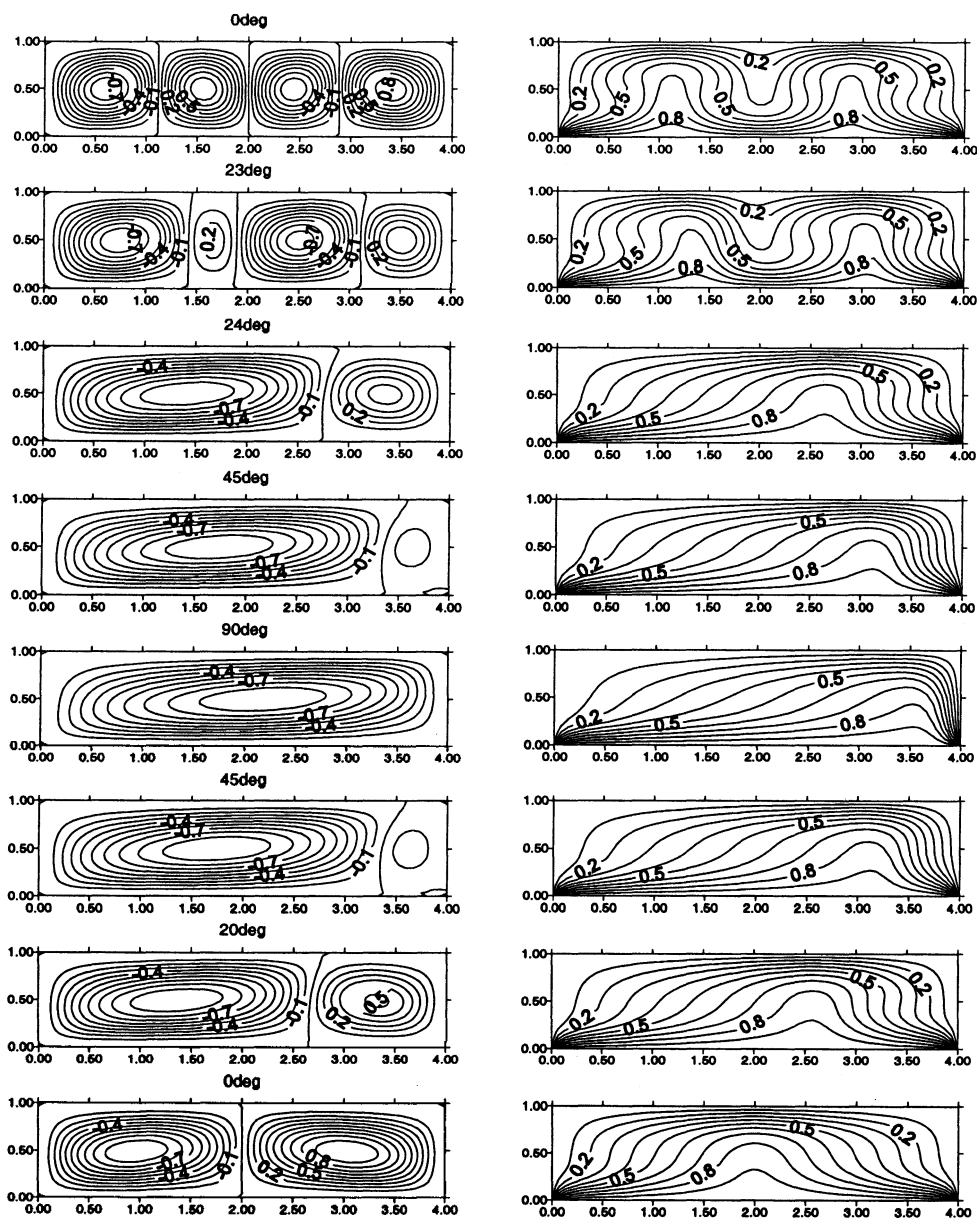


Fig. 4.55 Normalized streamlines and isothermal lines for CC configuration at various angles of inclination for $Ra=5000$ and $A=4$. Positive values indicate rotation in clockwise direction.

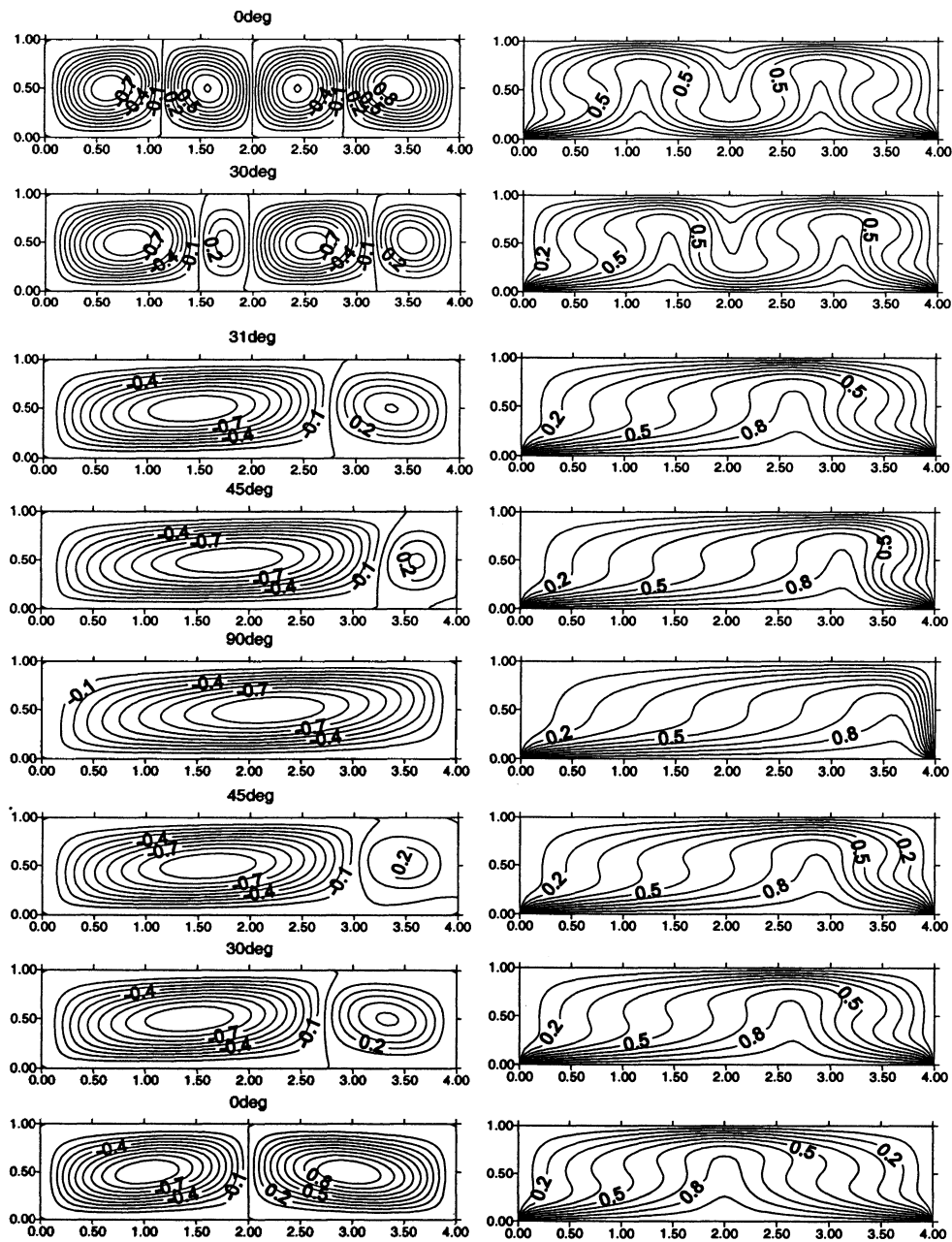


Fig. 4.56 Normalized streamlines and isothermal lines for CC configuration at various angles of inclination for $Ra=10^4$ and $A=4$. Positive values indicate rotation in clockwise direction.

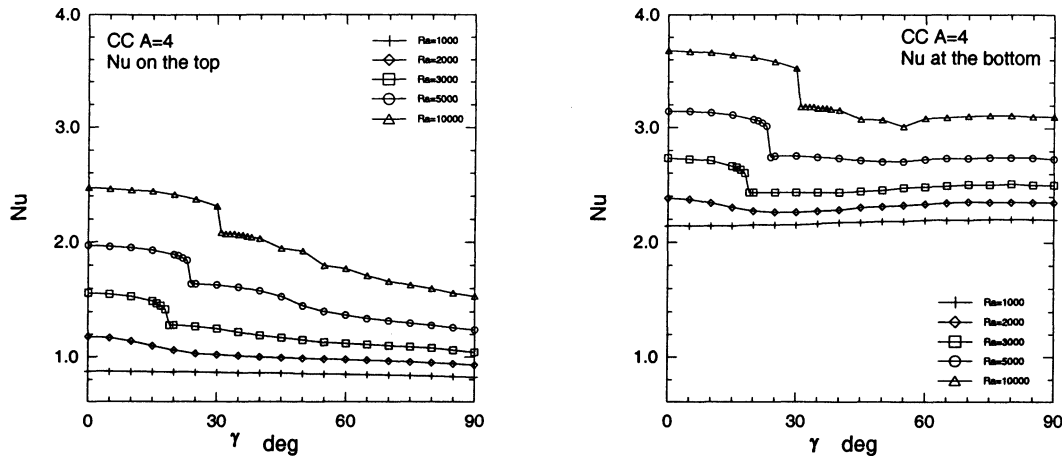


Fig. 4.57 Variation of average Nu number (both top and bottom walls) with inclination angle at various Ra numbers for CC configuration and A=4.

Fig. 4.58 shows average Nu number of the top wall at $\gamma = 0^\circ$ for Ra between 1000 and 5000. At Ra below critical value, the two cold walls promote convection at the two sides of the cavity, while there is no heat transfer at two corners on the top, which causes a decrease in the amount of heat transfer from the top wall. At Ra= 1600, convection flow produced by the two cold walls is strengthened by the cross temperature gradient producing a multi-cell flow at the middle of the cavity, which enhances the effectiveness of the heat transfer at the top wall. This effect is observed until Ra =3000, at which time the cross temperature gradient and the resulted multi-cells flow becomes strong enough for heat to be transferred from the bottom to the top wall. As Ra increases further, the pre-cooling caused by the two cold end walls results into a slight decrease in the effectiveness of heat transfer of the top wall. Fig 4.59 and 4.60 show the distribution of the vertical velocity, v at $y = 1/2$ and the local Nu number of the top wall for Ra = 1000, 2000, and 5000, and $\gamma = 0^\circ$. A noticeable increase in v can be observed for Ra equal to

1000 and 2000 as comparing CC with AA configuration. As for Ra further increased from 2000 to 5000, ν does not noticeably change.

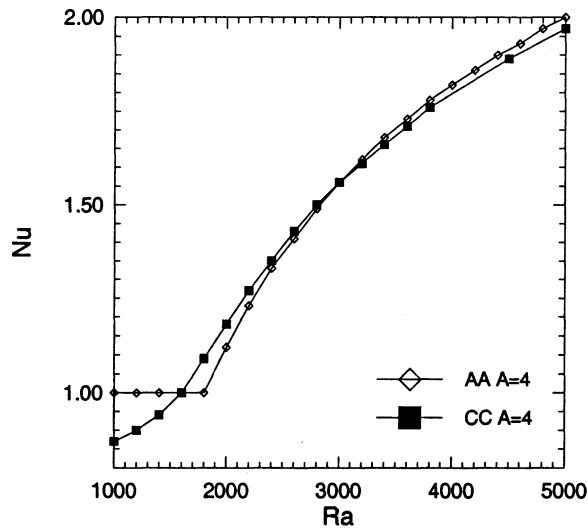


Fig. 4.58 Average Nu on the top of the horizontal cavity for AA and CC configurations for Ra ranged between 1000 and 5000 with $A=4$, $Pr=0.7$.

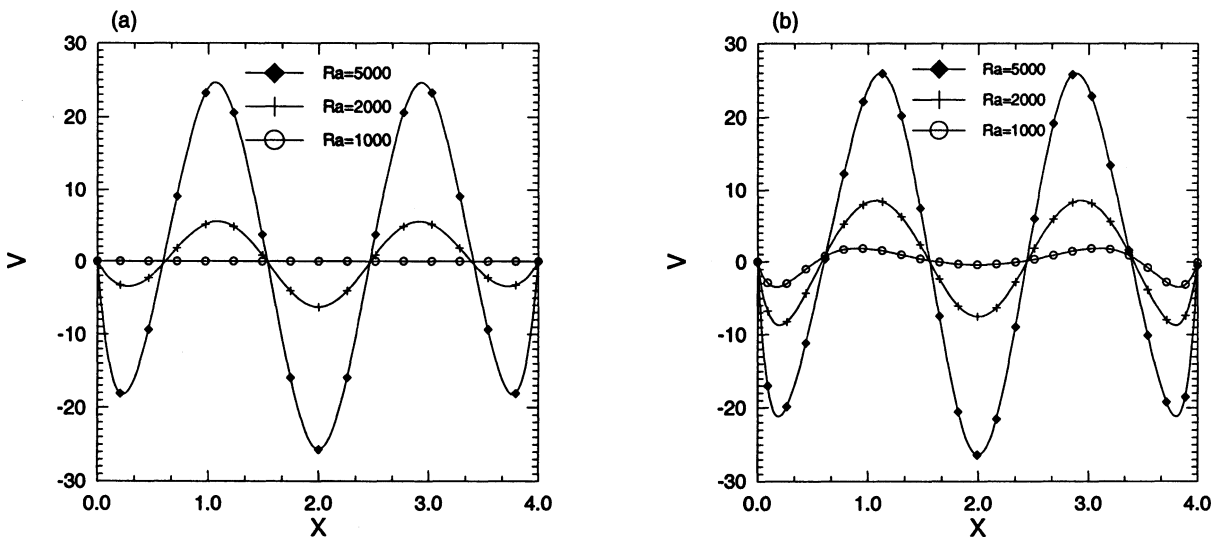


Fig. 4.59 Velocity distribution in the horizontal cavity for AA, CC configurations in $y=0.5$ for $A=4$ and $Pr=0.7$ with $Ra=1000, 2000, 5000$, (a) AA case, (b) CC case.

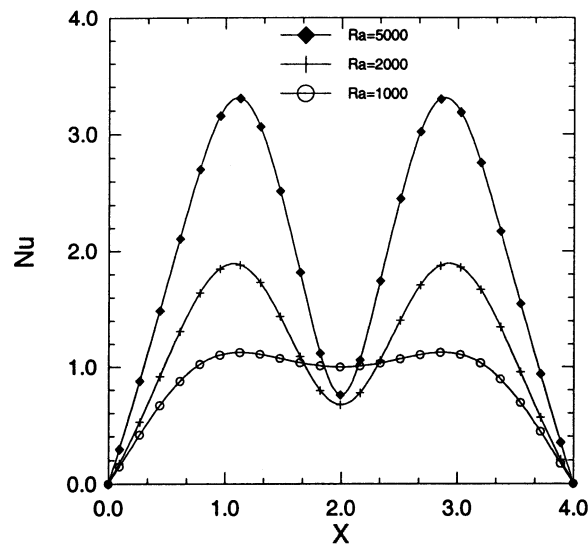


Fig. 4.60 Local Nu distribution on the top wall of the horizontal cavity for CC configuration for $A=4$, $Pr=0.7$ with $Ra=1000, 2000, 5000$.

4.2.6.2 Cases of decreasing γ

As angle of inclination decreases from 90° to 0° , for $Ra=1000$, no hysteresis phenomenon can be observed as shown in Fig. 4.61. At $Ra=3000$, location of mode transition is very close to that in the case of angle increasing, within 1° difference. Nu number of the top and bottom walls changes due to mode transition by about 11% and 6%, respectively, Fig. 4-57. Four cells co-exist when cavity returns back to 0° , which is different from AA configuration.

At $Ra = 5000$, Fig 4.56, two solutions deviate in a hysteresis region extending between $\gamma = 0^\circ$ and about 25° . For $Ra = 10^4$, a hysteresis region similar to that observed for $Ra = 5000$ extends between $\gamma = 0^\circ$ and about 30° . A second region of two solutions exists in the range of γ around 40° and 60° , Fig 4.57.

Upon decreasing γ , for $Ra=10^4$, the effect of initial conditions on the resulted flow velocities was significant. At $\gamma = 30^\circ$, $|\psi|_{\max}$ was 17.6, which is about 17% higher than its

value of 15.0 obtained at the same angle of inclination during the case of increasing γ .

Higher velocities always result in fewer cells. As γ was decreased back to 0° , a two-cell flow field was observed instead of four for angle increasing, see Fig. 4.56.

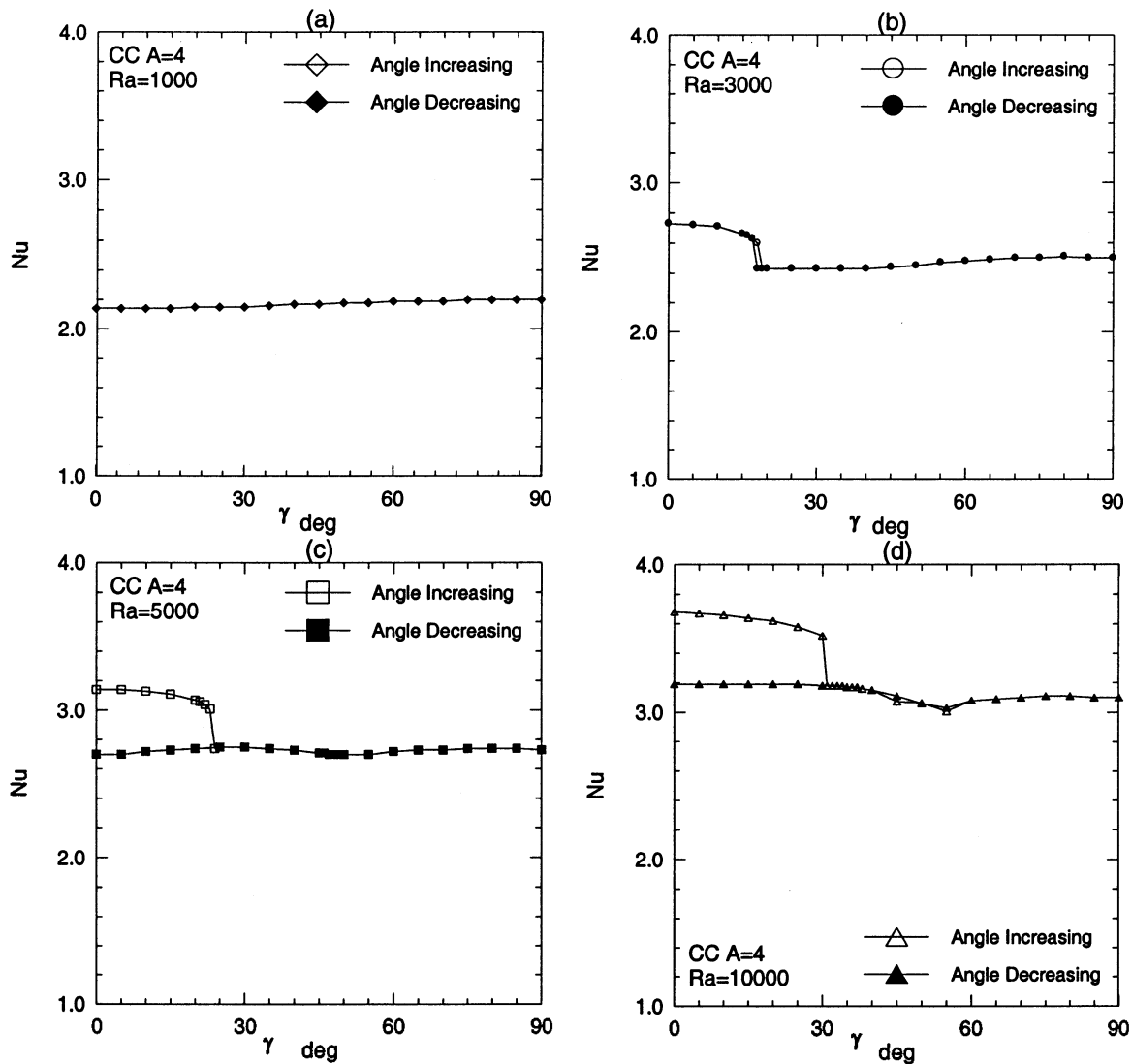


Fig. 4.61 Average Nu number (bottom wall) as a function of inclination angle γ for angle increasing and decreasing at various Ra numbers for CC configuration and $A=4$.

4.2.7 LL configuration

4.2.7.1 Cases of increasing γ

Two end walls with linear temperature distribution produce slower cells next to the two sides of the cavity, as compared with AA configuration, which is evident by two smaller cells can be observed at the left and right parts of the horizontal cavity, as shown in Figs. 4.62 - 4.65, for all Ra numbers. At $\gamma = 0^\circ$, both end walls pre-cools fluid before reaching top wall, so heat transfer rate of the top wall is reduced, for all Ra numbers beyond critical value, as compared with AA configuration, Figs. 4.27 and 4.66.

For Ra = 1000, no convection can be observed; and conduction dominates heat transfer in the cavity, similar to the case of AA configuration. As γ increased, a unicell flow pattern developed and remained all the way from $\gamma = 5^\circ$ to 90° . Nu number did not change that much, Fig. 4.66. For $Ra_c \leq Ra \leq 5000$, as γ increases, the cell at the left side disappears and two anticlockwise cells develop, see Figs. 4.63 and 4.64. This phenomenon occurs between $\gamma = 0^\circ$ and 5° for Ra = 3000 and between 5° and 10° for Ra=5000. Heat transfer rate decrease due to mode transitions by 5.3% and 8.1% for Ra =3000 and 5000, respectively. At Ra =10⁴, at γ between 5° and 10° , upslope force produces a new cell at the left side, rotating in anticlockwise direction, Fig. 4.65. This cell is pre-heated by left end wall and reduces heat transfer rate of the bottom wall by 5.4% for γ .changes from 5° to 10° . However, an increase in number of cells enhances heat transfer rate of top wall by 8.8%.

For Ra=3000, mode transition (3T1) occurs at $\gamma = 24^\circ$, Fig. 4.63, which is very close to AA configuration, Fig. 4.24. Nu number due to this mode transition drops by 13.5%.

For $Ra=5000$, mode transition (3T1) is delayed until $\gamma = 32^\circ$, causing a drop in Nu number by 22.2%, Fig. 4.66. A similar 20.7% drop in Nu number for $Ra=10^4$ occurs at $\gamma = 41^\circ$.

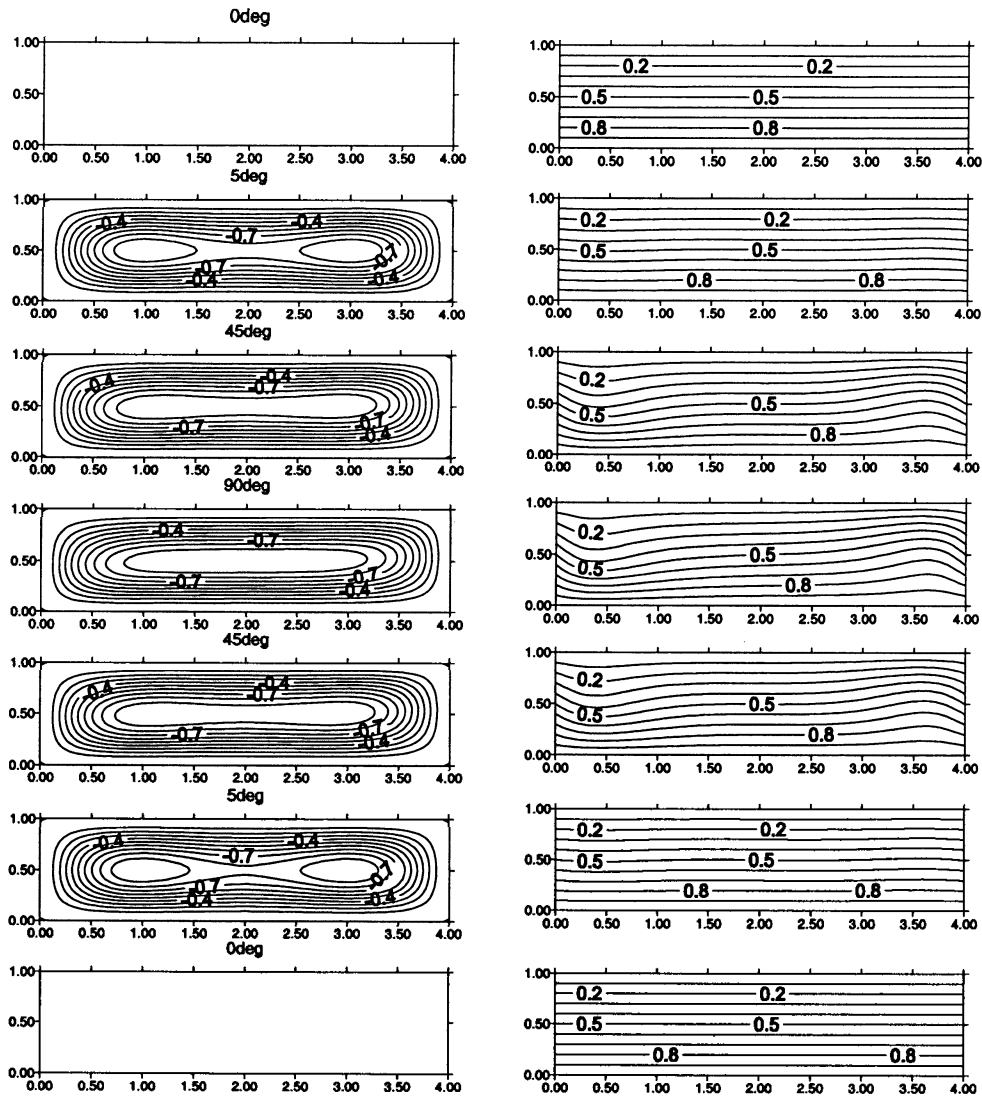


Fig. 4.62 Normalized streamlines and isothermal lines for LL configuration at various angles of inclination for $Ra=1000$ and $A=4$. Positive values indicate rotation in clockwise direction.

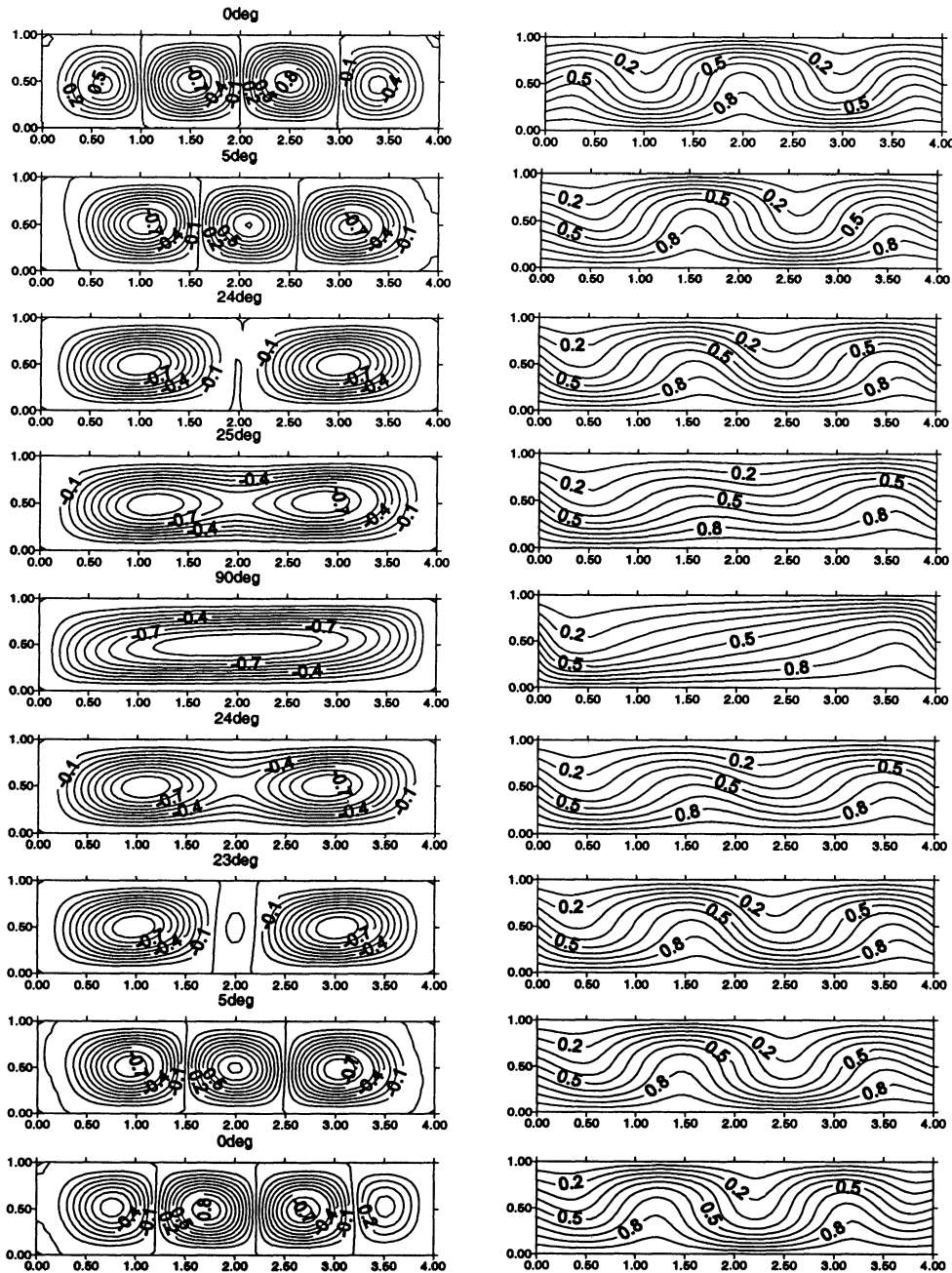


Fig. 4.63 Normalized streamlines and isothermal lines for LL configuration at various angles of inclination for $Ra=3000$ and $A=4$. Positive values indicate rotation in clockwise direction.

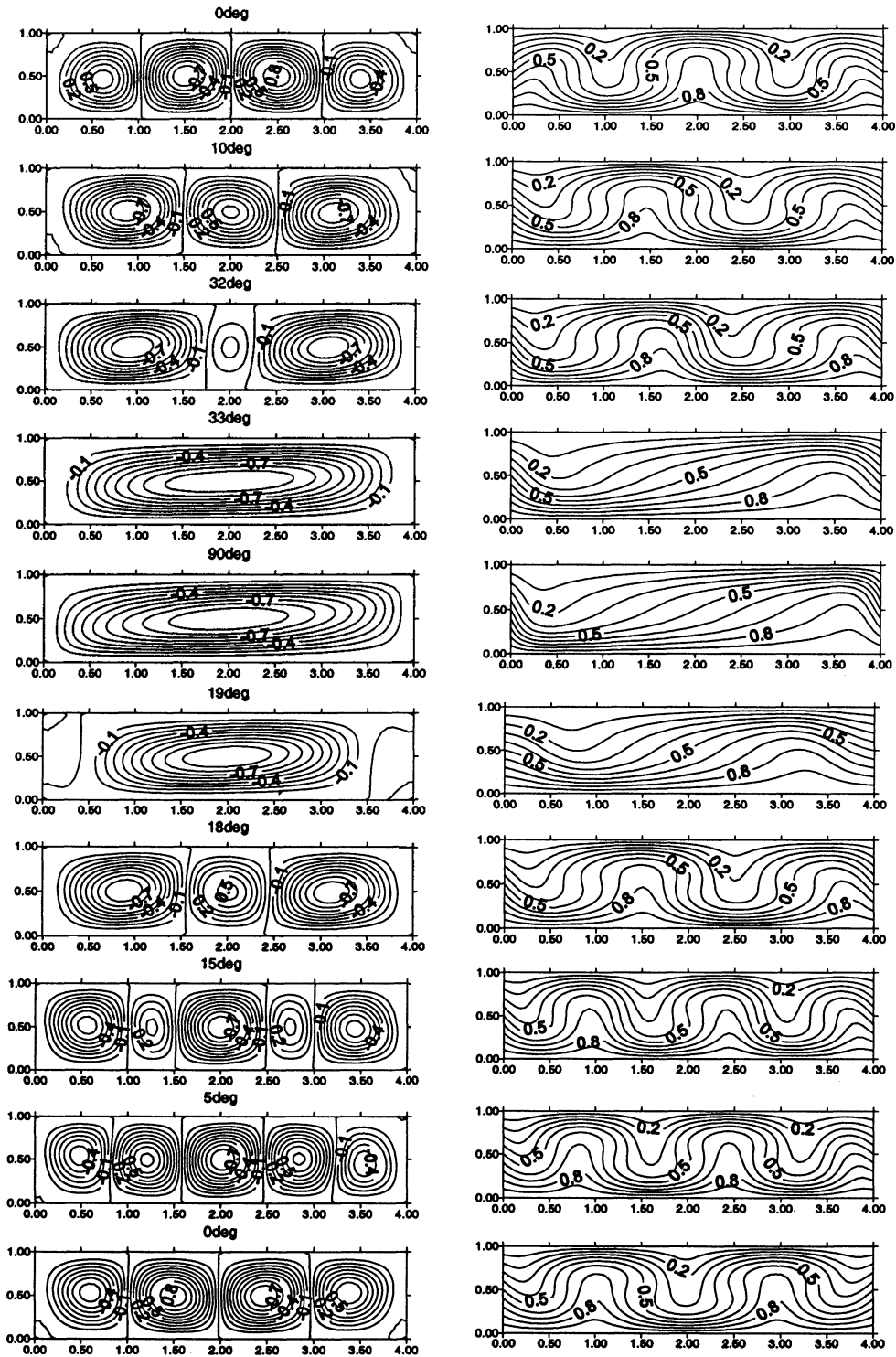


Fig. 4.64 Normalized streamlines and isothermal lines for LL configuration at various angles of inclination for $Ra=5000$ and $A=4$. Positive values indicate rotation in clockwise direction.

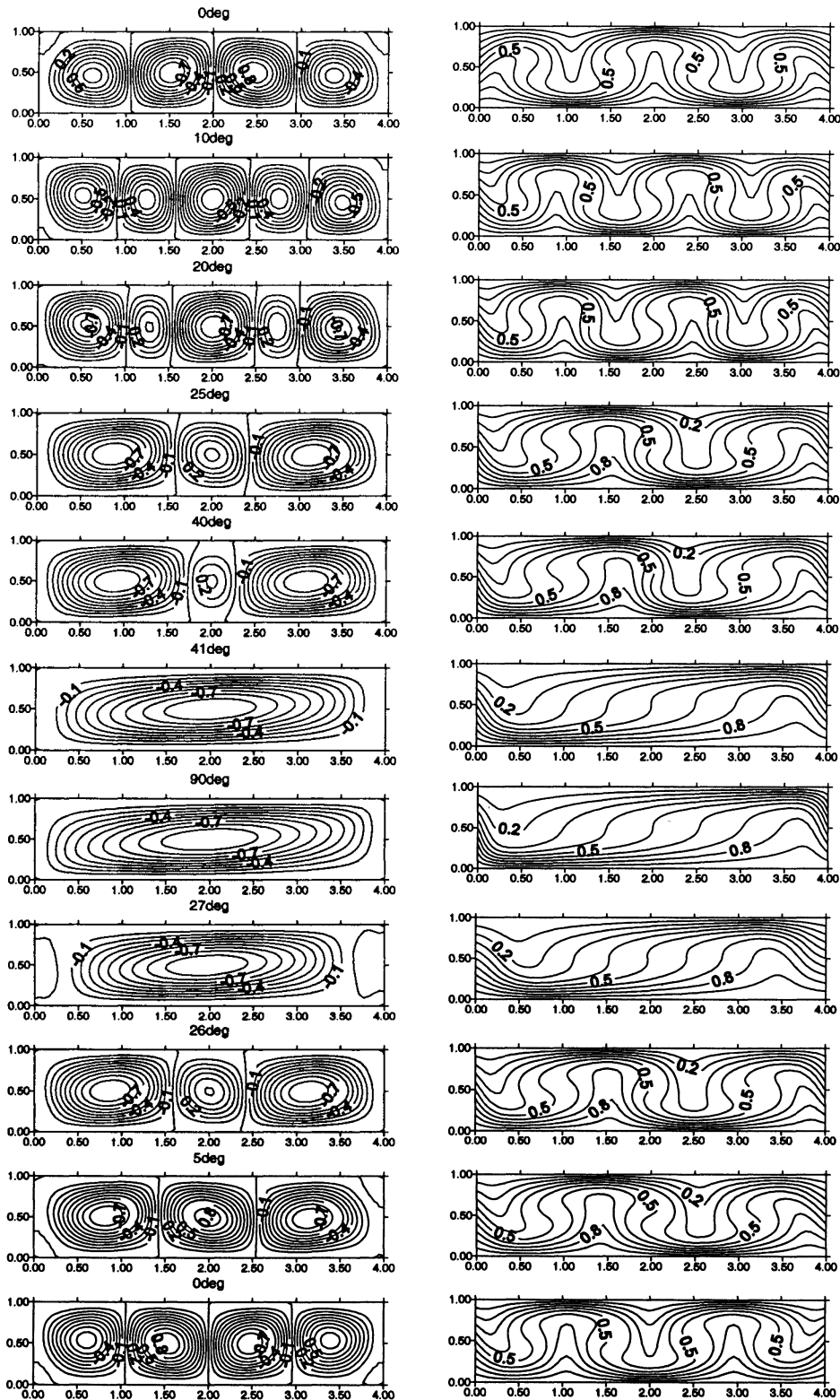


Fig. 4.65 Normalized streamlines and isothermal lines for LL configuration at various angles of inclination for $Ra=10^4$ and $A=4$. Positive values indicate rotation in clockwise direction.

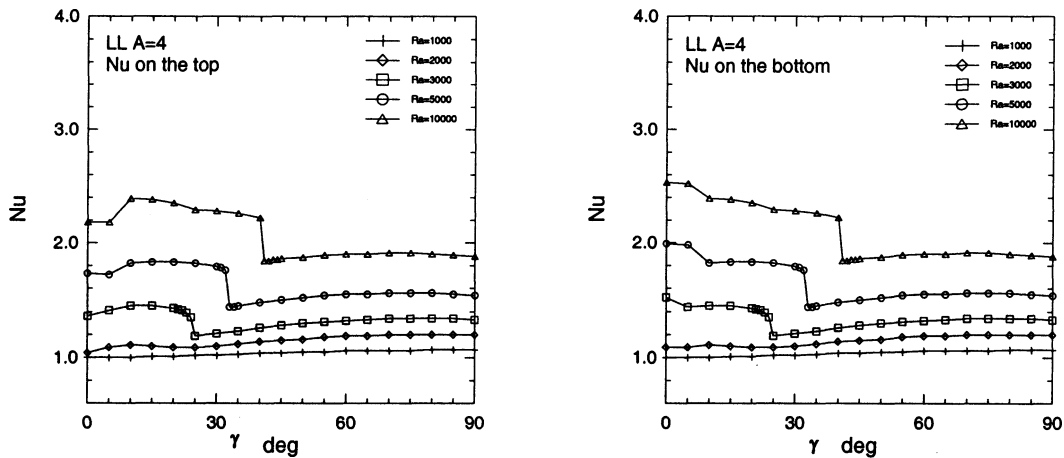


Fig. 4.66 Variation of average Nu number (both top and bottom walls) with inclination angle at various Ra numbers for LL configuration and A=4.

4.2.7.2 Cases of decreasing γ

Hysteresis phenomenon can not be observed at Ra=1000, Figs 4.62 and 4.67. Fig. 4.67 shows hysteresis region for LL case similar to AA configuration. However, a closer look at flow fields reveals the difference in hysteresis phenomenon at $\gamma = 0^\circ$ of these two cases.

For Ra > 1000, in AA configuration, the observed difference in Nu number at $\gamma = 0^\circ$ is due to the difference in number of cells produced in the two cases of angle increasing and decreasing. However, for LL configuration, difference in rate of heat transfer rate for angle increasing and decreasing is because of different rotating directions, as shown in Figs. 4.63 -4.65.

For Ra=3000, hysteresis can be observed in two regions. Drastic increase in Nu number, by 12.2%, occurs at $\gamma = 24^\circ$, which is 1° different from case of angle increasing.

For $Ra = 5000$, Nu number increases by 25% due to mode transition at $\gamma = 19^\circ$, Fig. 4.67. After mode transition, due to the developing cross force, cell at the right side is broken into three cells. As cross force is developed further, anticlockwise cell at the right side finally disappears and four cells occupy the whole cavity. The directions of rotation of these four cells are exactly opposite to that at $\gamma = 0^\circ$ in the case of angle increasing. In this case, fluid is pre-heated at the left and right end walls; and so rate of heat transfer of the bottom wall is 13.1% lower than in the case of angle increasing, as shown in Fig. 4.67.

For $Ra = 10^4$, Nu number of the bottom wall, due to the same reason, is reduced by 26%. Since flow velocities in the case of $Ra=10^4$ are stronger than $Ra=5000$, as γ decreases, the cell at the left side is too strong to be broken. Finally, cross force forms a clockwise cell in the right part of the cavity, as shown in Fig. 4.65.

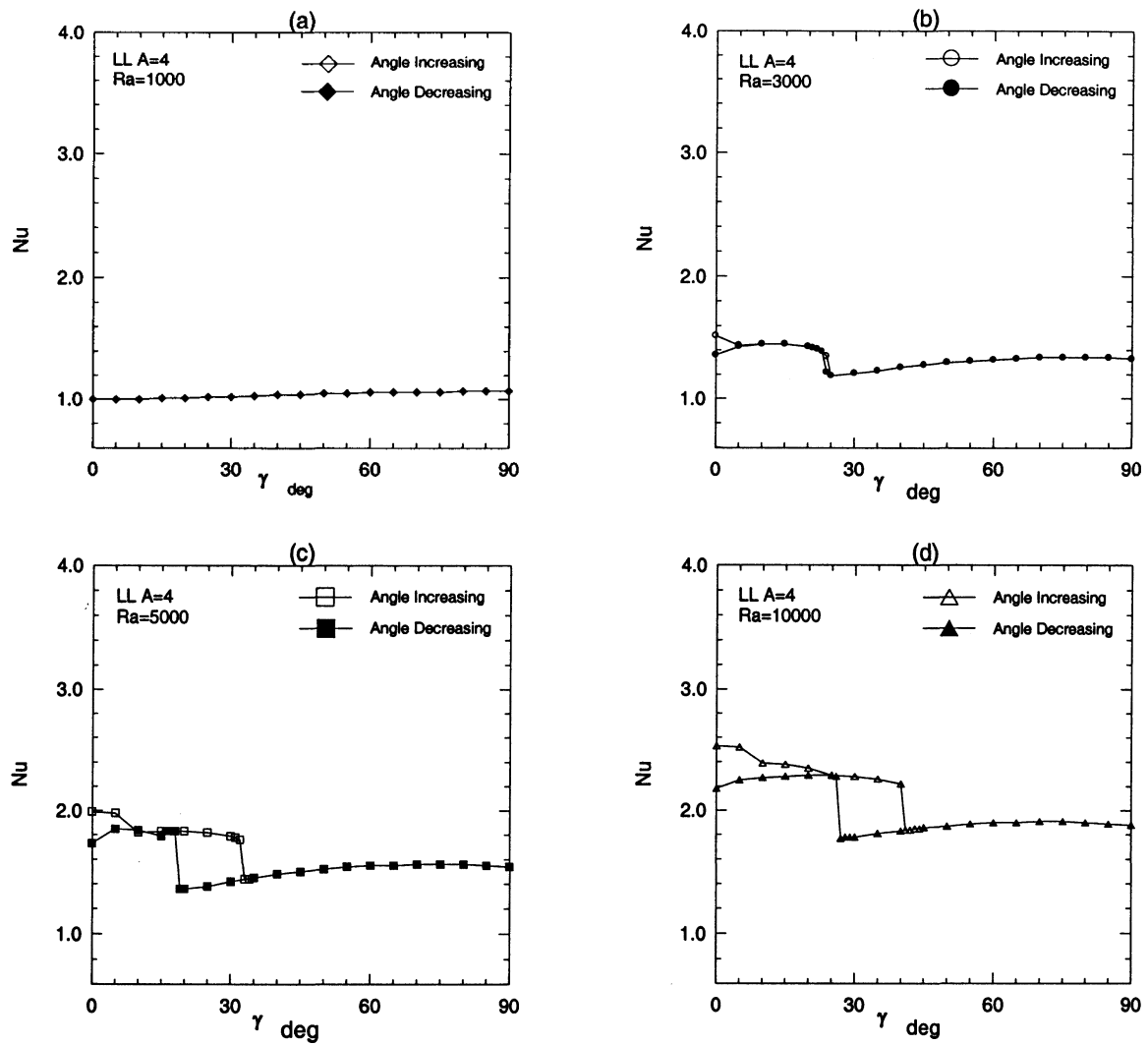


Fig. 4.67 Average Nu number (bottom wall) as a function of inclination angle γ for angle increasing and decreasing at various Ra numbers for LL configuration and $A=4$.

Chapter 5

Numerical Results - Case of Rectangular Cavity with Curved Bottom

In many of the engineering applications where natural convection plays an important role, not all cavities are exactly regular in shape, i.e., with flat walls. Irregular geometries are very common in many applications. Results presented in chapters 3 and 4 have demonstrated the fact that heat transfer rates inside inclined enclosures might encounter sudden changes due to flow mode-transitions. Although, thermal conditions of end walls have significant effects on these mode-transitions, and hence, could be used to alter or device certain rates of heat transfer inside the cavity, as was demonstrated by results presented in these two chapters, those conditions might be defined by the nature of the engineering application, and not controlled by the system designer. It might still be desirable to alter or device a certain pattern of heat transfer inside the cavity. One of the possible parameters that might be useful in achieving that is by altering cavity geometry. One of the main objectives of the present study is to investigate the effect of changing the shape of the cavity bottom wall, from flat to curved, while keeping all other walls flat, on mode-transition in inclined cavities.

The geometry of the cavity curved bottom wall used in the present study is defined by the following quadratic equation:

$$y = (-|x - 2|^2 + 2^2) \times (SH / 2^2) \quad 5.1$$

x and y are the two coordinates and SH is the maximum height of the curved wall located at $X = L/2$, as shown in Fig. 1.7. Investigations are carried out considering various values

of SH and studying its effect on mode transition and rates of heat transfer inside the cavity. Values of SH used in the present study are: 0.05, 0.25, 0.45, 0.65, and 0.85. In order to compare results with those obtained for the base case of AA configuration, only insulated end walls were considered in the case of curved bottom cavities, denoted hereafter as AAC. Ra number was kept in the same range used in the case of regular cavities, i.e., between 10^3 and 10^4 . Pr number and width/height aspect ratio were kept unchanged at 0.7 and 4, respectively. Effect of cavity angle of inclination was investigated considering the same two cases of changing cavity angle of inclination: increasing from $\gamma = 0^\circ$ to 90° ; and decreasing from $\gamma = 90^\circ$ back to 0° .

In the case of curved bottom wall, buoyancy force at the bottom wall can be resolved into two components: one in the tangential-direction (F_t) and the other in the normal-direction (F_n). Relative magnitudes of these two components are expected to have a significant effect on mode-transition, and hence, on rates of heat transfer rate inside the cavity, as will be discussed below. Figs 5.1 and 5.2 present variation of average Nu number of bottom and top with change of γ in the case of angle increasing at various Ra numbers for AA and AAC configurations, considering different SH values in the case of AAC configuration.

5.1 AAC configuration with SH=0.05

5.1.1 Case of increasing γ

With such a low maximum height of curvature, F_n is much higher than F_t . At $\gamma = 0^\circ$, rate of heat transfer did not change that much as compared with the case of AA

configuration, except for $Ra < Ra_c$. In the case of AAC configuration at $\gamma = 0^\circ$, the component of buoyancy force F_t compels two cells at $Ra = 1000$, as shown in Fig. 5.3, resulting in an increase in Nu number ($Nu > 1$), as shown in Figs. 5.1a, 5.1b, 5.2a, and 5.2b. It is worth noting here that the cell on the right side and the one on the left side rotate in the clockwise and anticlockwise directions, respectively. As γ increased, a two-in-one flow structure developed at $\gamma = 5^\circ$ similar to AA configuration (see Figs. 5.3 and 4.23), which eventually merged into a unicell structure at $\gamma = 90^\circ$.

At $Ra = 3000$, a multi-cell flow pattern with four cells is produced at $\gamma = 0^\circ$, Fig. 5.4. Mode transition for $Ra=3000$ is more gradual than in the case of AA configuration. First mode transition from 4 to 3 cells, associated with a slight drop in Nu number, took place at $\gamma = 10^\circ$, instead of $\gamma = 5^\circ$ in AA configuration. The second mode transition (3T1), associated with a bigger drop in Nu number, took place at $\gamma = 25^\circ$, same as AA case. However, Nu number dropped only by about 2%, which is substantially lower than the 8% drop in the case of AA configuration.

Mode transitions (3T1) for $Ra = 5000$ took place at $\gamma = 30^\circ$ for angle, Fig. 5.5. Change in Nu number of bottom wall is about 22% for angle increasing, Fig. 5.1.

For $Ra=10^4$, mode transitions occurs at $\gamma = 39^\circ$ for angle increasing, which indicates that the curved bottom delays mode transition in this case. Mode transition causes 18.9% drop in Nu number on the bottom wall.

It is worth noting here that the case of $SH = 0.05$ resulted in an increase in the rate of heat transfer of both top and bottom walls for $Ra < Ra_c$ due to the contribution of convection. However, it decreased slightly for higher Rayleigh numbers. Another

important observation is that all flow fields developed at $\gamma = 0^\circ$, in both cases of γ increasing and decreasing, are characterized by multi-cell flow structures.

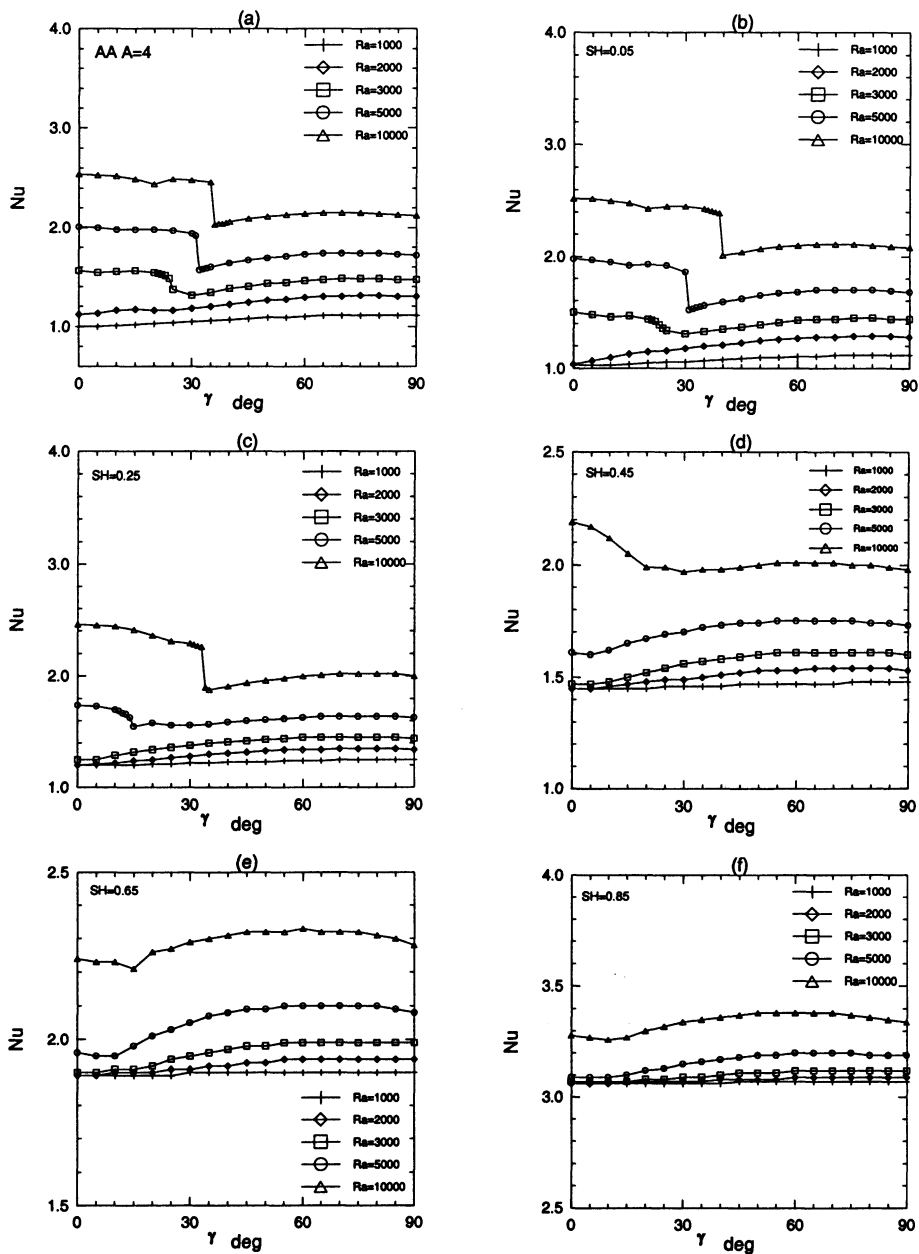


Fig. 5.1 Variation of average Nu number of bottom wall with inclination angle at five Ra numbers for AA and AAC configurations at different values of SH. (a) AA configuration, SH =0, (b) SH=0.05, (c) SH=0.25, (d) SH=0.45, (e) SH=0.65, (f) SH=0.85

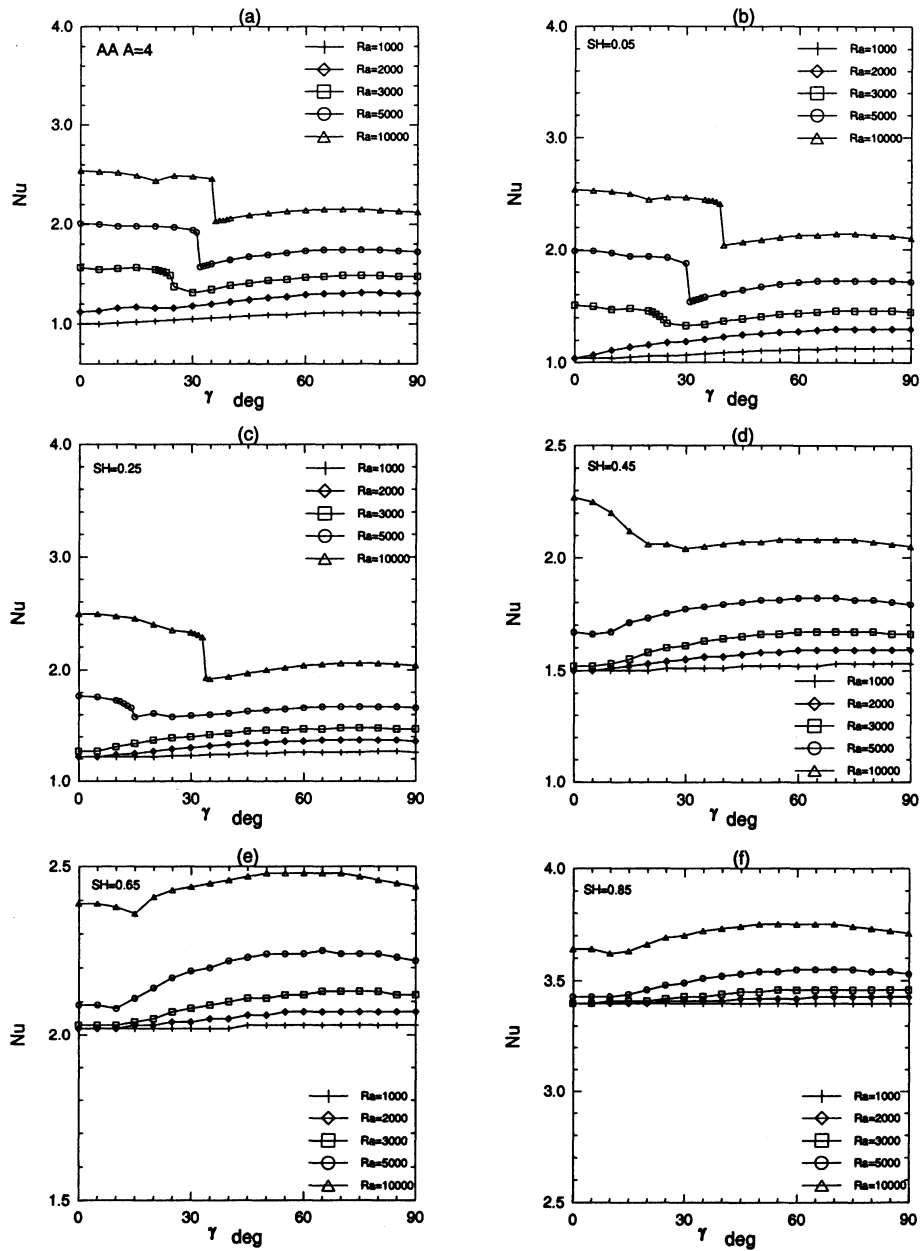


Fig. 5.2 Variation of average Nu number of top wall with inclination angle at five Ra numbers for AA and AAC configurations at different values of SH. (a) AA configuration, SH = 0, (b) SH=0.05, (c) SH=0.25, (d) SH=0.45, (e) SH=0.65, (f) SH=0.85

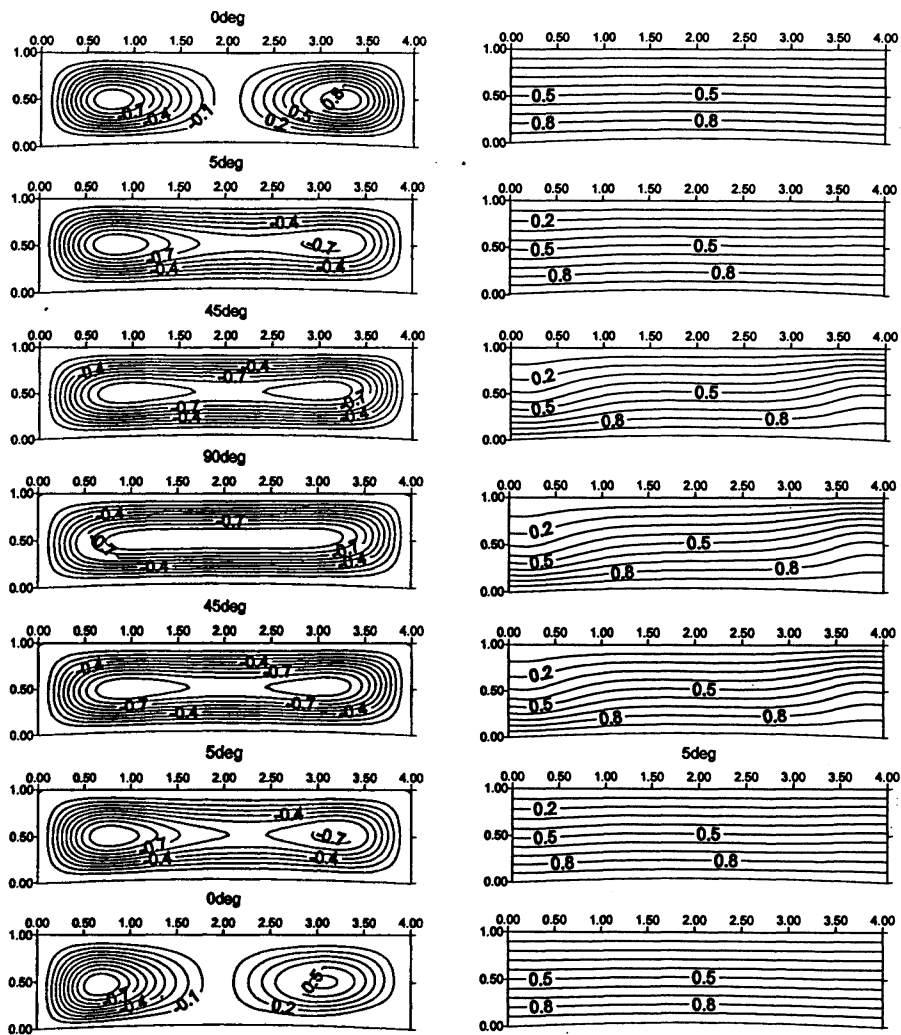


Fig. 5.3 Normalized streamlines and isothermal lines for AAC configuration at various angles of inclination for $Ra=1000$ and $SH=0.05$. Positive values indicate rotation in clockwise direction.

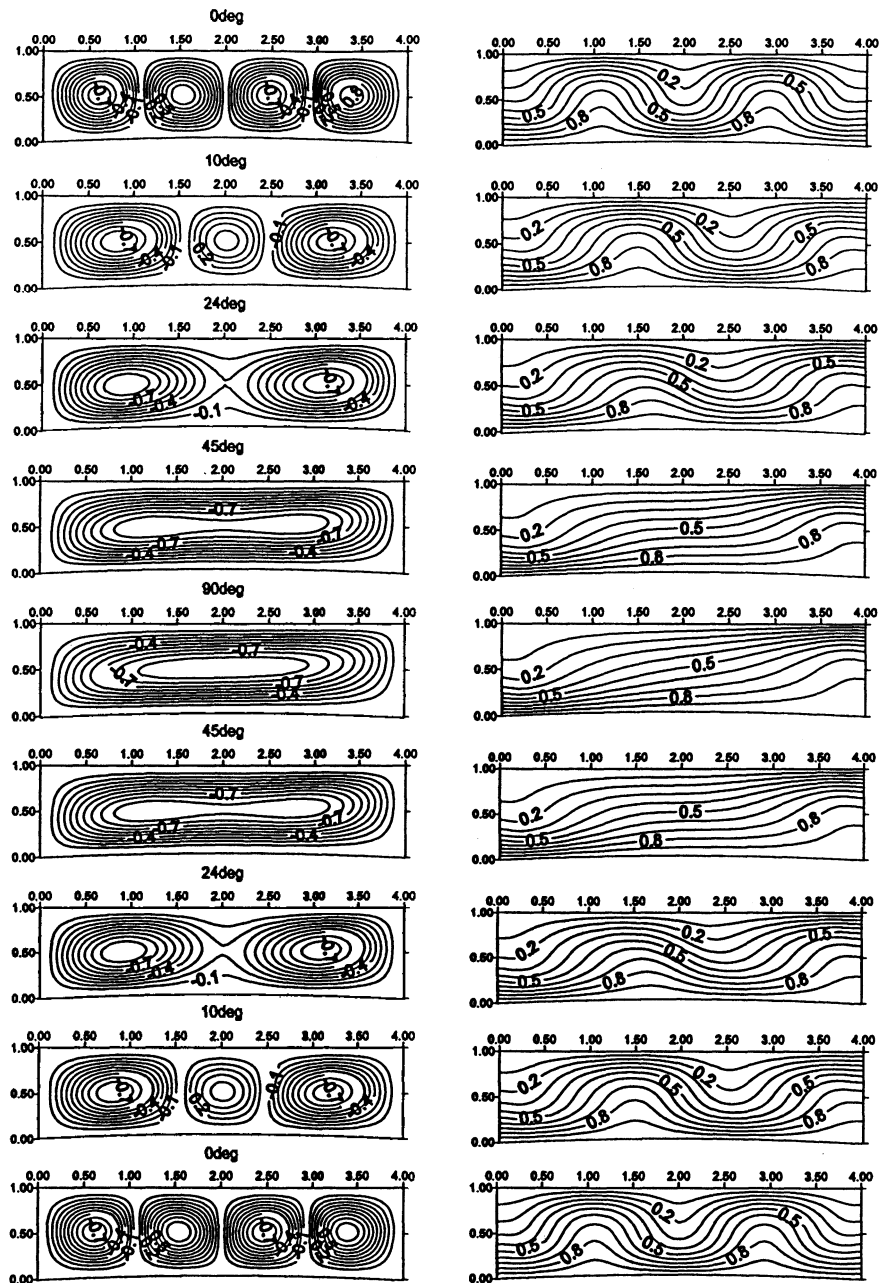


Fig. 5.4 Normalized streamlines and isothermal lines for AAC configuration at various angles of inclination for $Ra=3000$ and $SH=0.05$. Positive values indicate rotation in clockwise direction.

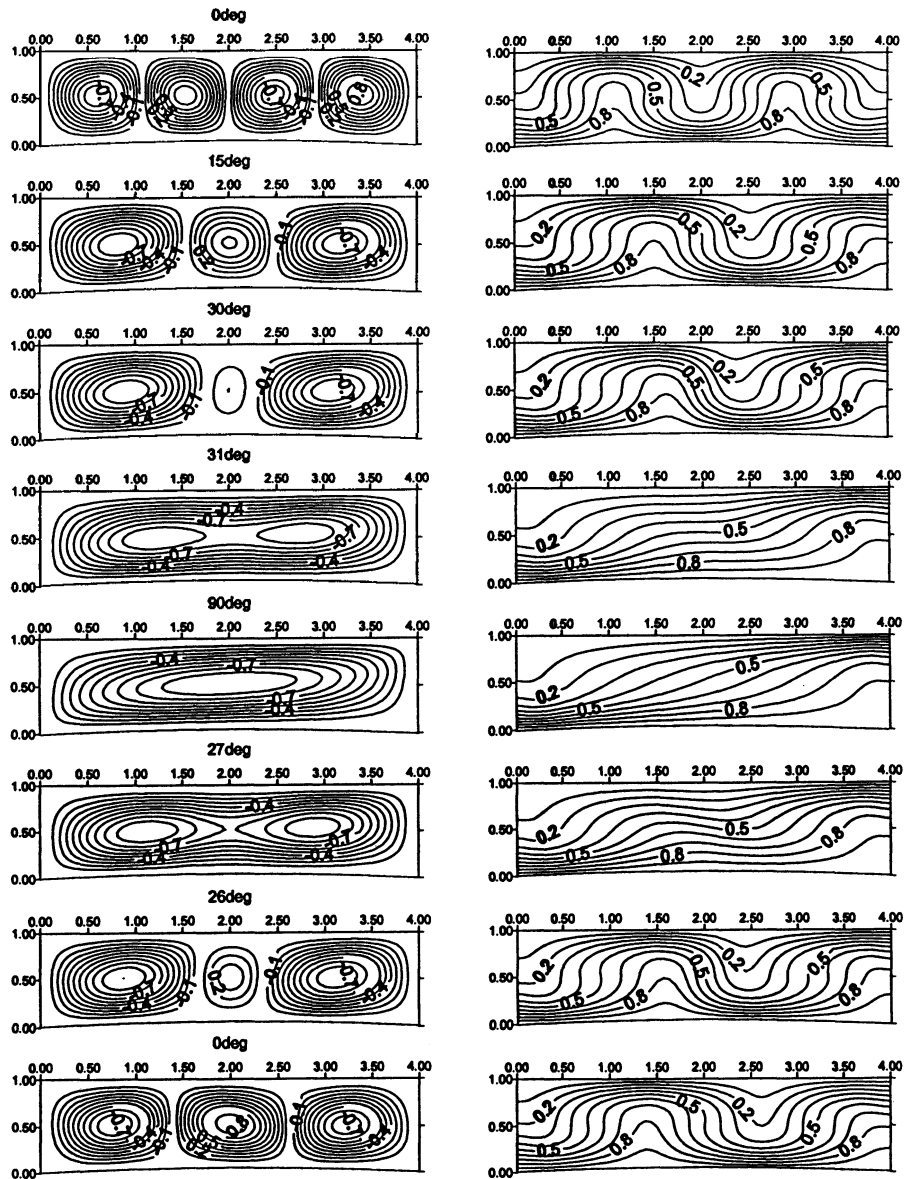


Fig. 5.5 Normalized streamlines and isothermal lines for AAC configuration at various angles of inclination for $Ra=5000$ and $SH=0.05$. Positive values indicate rotation in clockwise direction.

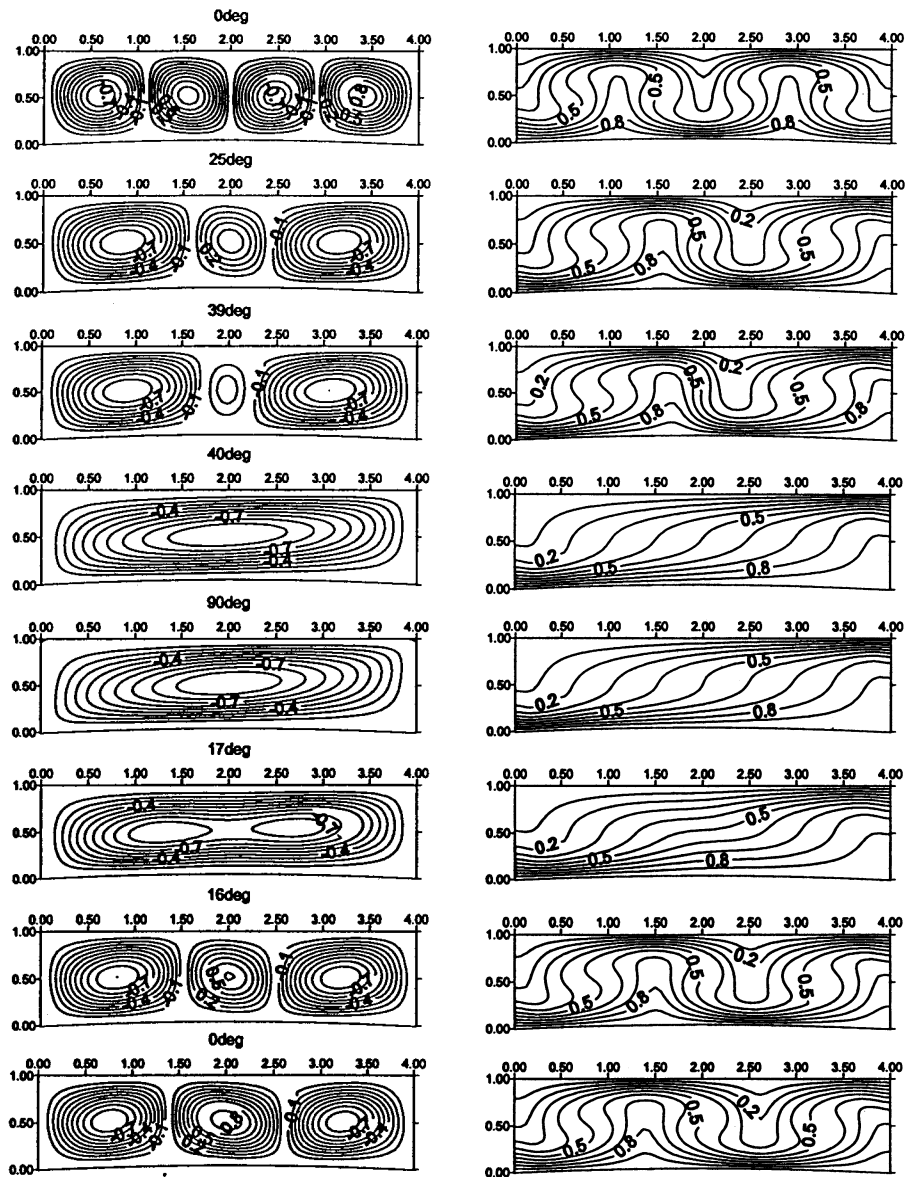


Fig. 5.6 Normalized streamlines and isothermal lines for AAC configuration at various angles of inclination for $Ra=10^4$ and $SH=0.05$. Positive values indicate rotation in clockwise direction.

5.1.2 Case of decreasing γ

For $Ra=1000$, similar trend to that of AA configuration is observed as γ decreased back to 0° , except that velocity distribution shifted towards the lower side of the cavity (the left side at $\gamma = 0^\circ$) as evident by the streamlines shown in Fig 5.3 and the local velocity (u) distribution in x direction at $y=0.9$ and $\gamma = 0^\circ$ in the case of γ decreasing, Fig. 5.7.

For $Ra=3000$, flow field ended up with four cells at $\gamma = 0^\circ$ in the case of angle decreasing (Fig. 5.4), which is different from the three cells developed in the case of AA configuration (Fig. 4.24), consistent with the maximum value of stream function in the initial conditions of $\gamma = 0^\circ$ in the case of angle decreasing.. For AAC, $\psi_{\max} = 4.54$ at $\gamma = 5^\circ$, which is lower than its value in the AA case, where $\psi_{\max} = 5.13$ at $\gamma = 5^\circ$, so it would result in more cells.

As for $Ra=5000$, mode transition (1T3) occurs at $\gamma = 27^\circ$ for angle decreasing, Nu number of bottom wall is about 21% for angle decreasing. A multi-cell flow pattern with three cells is finally obtained at $\gamma=0^\circ$ in the case of angle decreasing, which is the same as AA configuration, Figs. 4.25, 5.5. The difference in number of cells at $\gamma=0^\circ$ for angle increasing and decreasing causes a 10% difference in Nu number.

For $Ra=10^4$, mode transition (1T3) occurs at $\gamma = 17^\circ$ for angle decreasing, which indicates that the curved bottom speeds mode transition up for angle decreasing in this case as compared with AA configuration. At $\gamma=0^\circ$, just as in the flat bottom case, i.e., in

AA configuration, flow field ends up with three cells, as shown in Fig. 5.6, and Nu number is about 5% less than that of the angle increasing case.

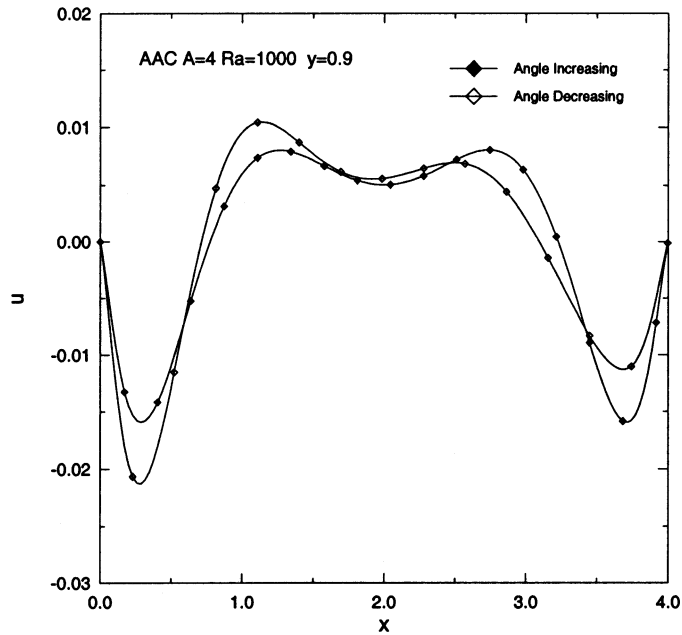


Fig. 5.7 Distribution of velocity component in x-direction for angle increasing and angle decreasing at $y=0.9$, $A=4$ and $Ra = 1000$, AAC configuration.

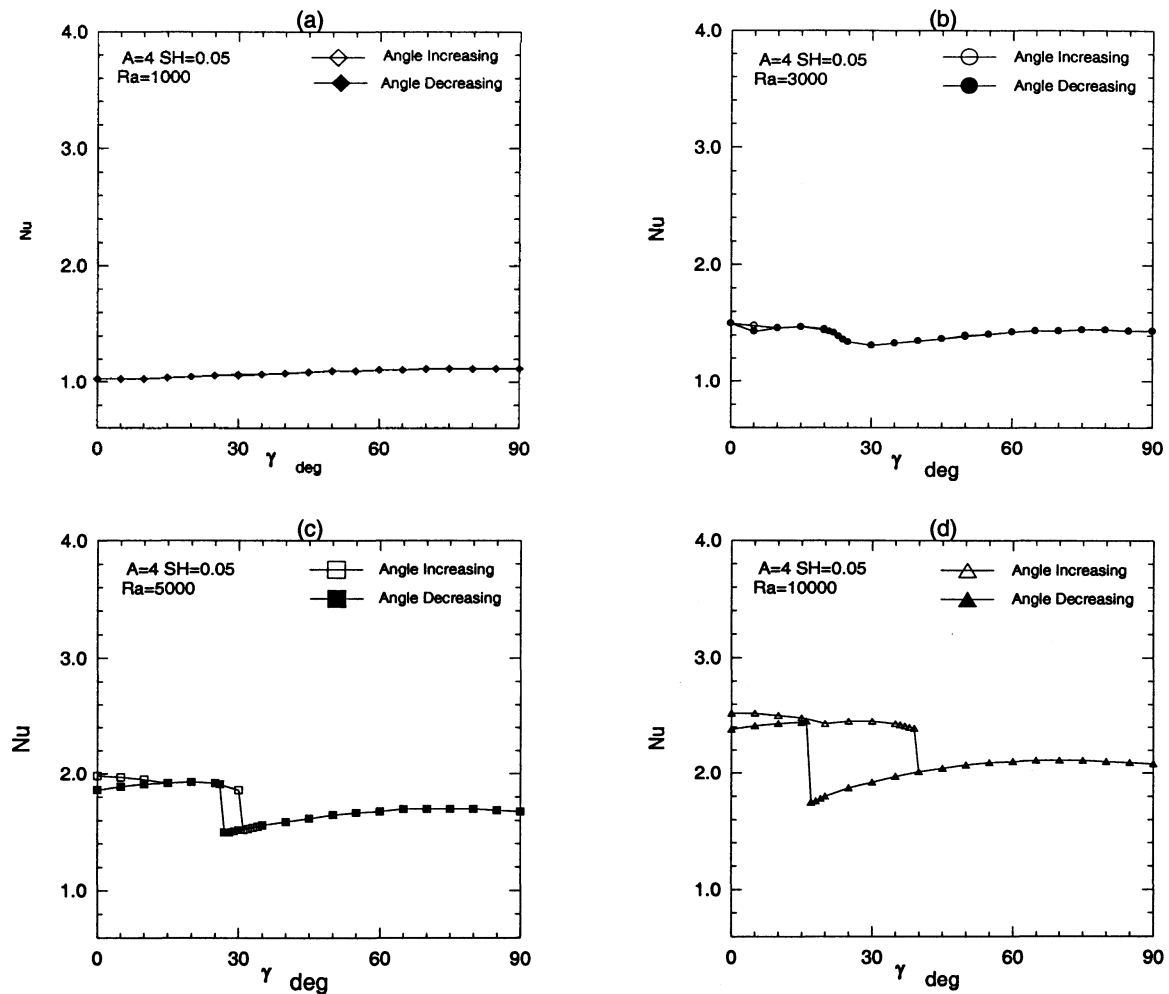


Fig. 5.8 Average Nu number (bottom wall) as a function of inclination angle γ for angle increasing and decreasing at various Ra numbers for AAC configuration and SH=0.05.

5.2 AAC configuration with SH=0.25

5.2.1 Case of increasing γ

With SH = 0.25, the component of buoyancy force F_t is greater than in the case of SH=0.05, so heat transfer at $Ra < Ra_c$ has been enhanced due to a stronger convective contribution. At $\gamma = 0^\circ$ for $Ra \leq 2000$, rate of heat transfer of both walls increased, due to convection, by 22% for $Ra = 1000$ and 2% for $Ra = 2000$, as compared with AA

configuration in horizontal cavity, see Figs. 5.1a and 5.1c. At $Ra=3000$, the stronger component in the tangential-direction resulted in two stronger cells at the cavity far left and right sides. The relatively (relative to $Ra = 1000$) stronger F_n resulted in the development of two weak cells in the middle of the cavity. Adding these two effects together, a multi-cell flow pattern with four cells is developed, as shown in Fig. 5.10. Due to the development of such localized convection flow, rate of heat transfer of both bottom and top walls decreased by 19.9% and 18.6% at $\gamma = 0^\circ$, respectively, as compared with AA configuration, Figs. 5.1a and 5.1c.

At $Ra=5000$ and $\gamma = 0^\circ$, Nu number of the bottom wall is reduced by 13.4% for the same reason. However, at $Ra=10^4$ and $\gamma = 0^\circ$, heat transfer rate of the bottom wall is only 3.1% lower than AA configuration.

No sudden changes in Nu number are observed for $Ra=3000$ and can hardly be seen for $Ra = 5000$, Figs. 5.1c and 5.2c. Mode transition (3T1) took place for $Ra=10^4$ at $\gamma = 33^\circ$ for angle increasing. Nu number change on the bottom wall corresponding to mode transition is 19.0%, Fig. 5.1, which is not as significant as in the case of flat bottom, Fig. 4.27.

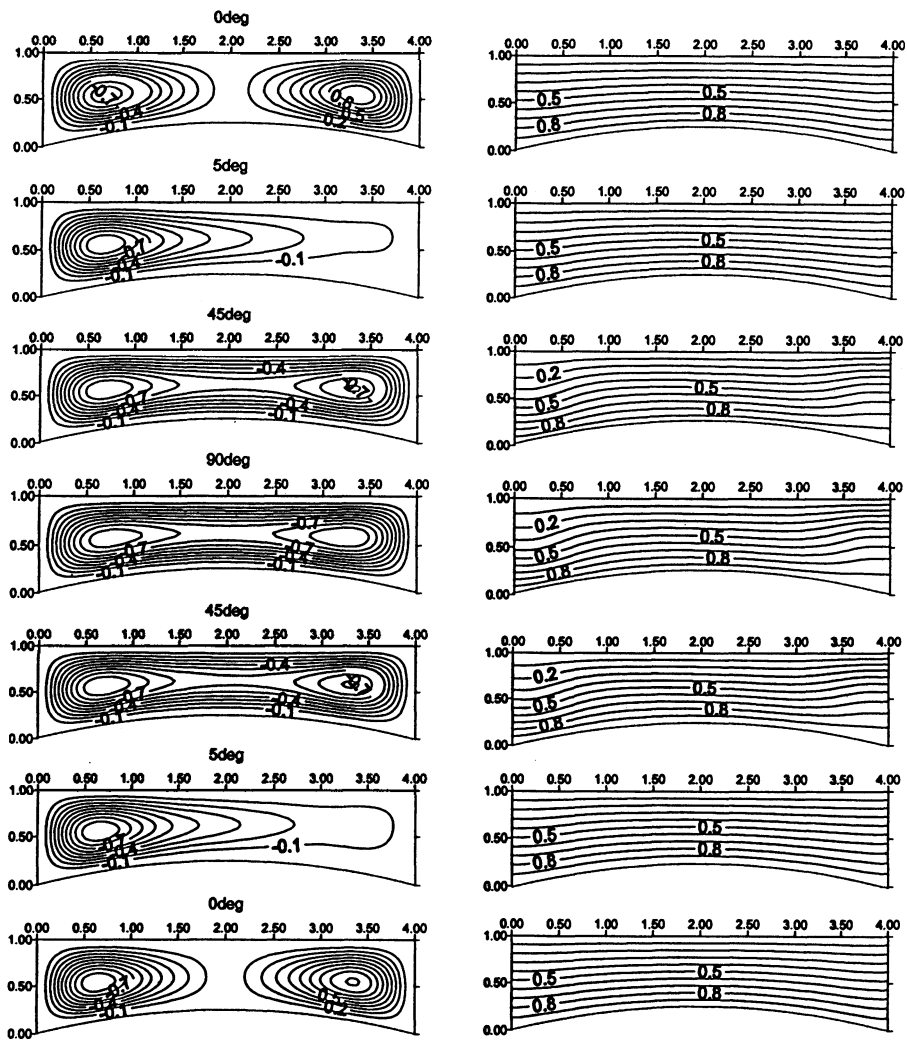


Fig. 5.9 Normalized streamlines and isothermal lines for AAC configuration at various angles of inclination for $Ra=1000$ and $SH=0.25$. Positive values indicate rotation in clockwise direction.

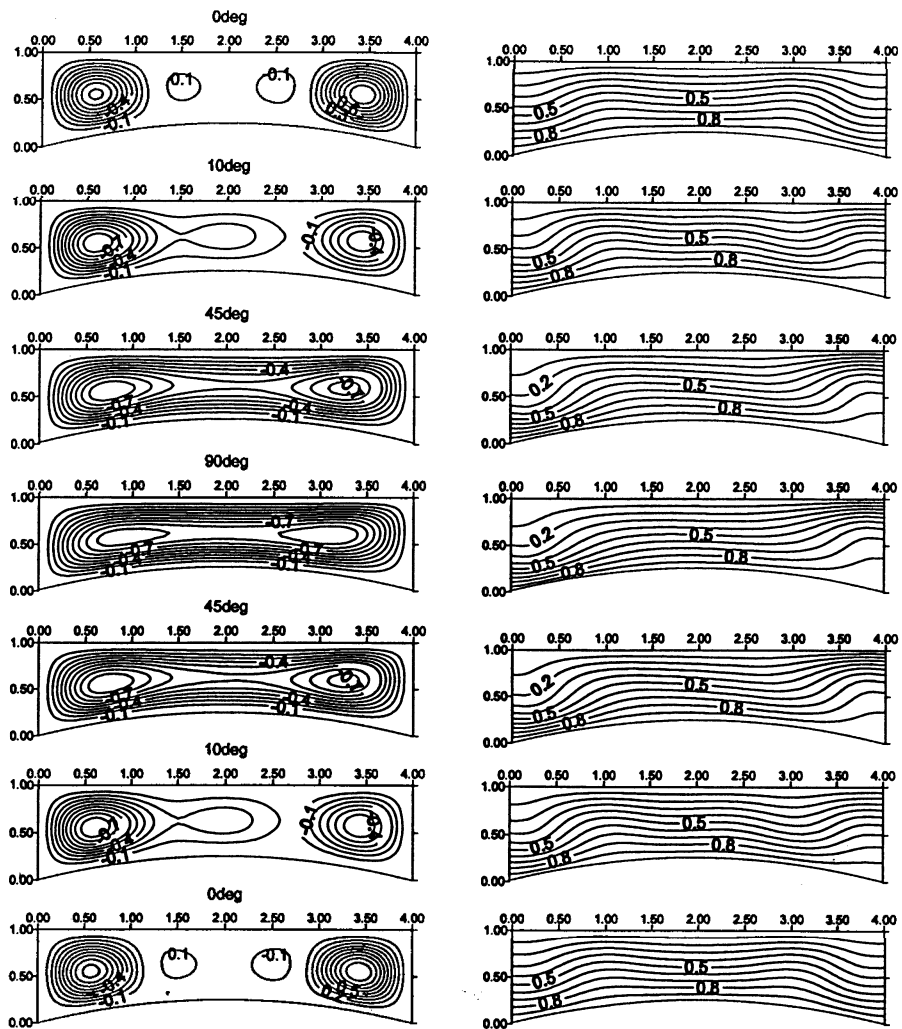


Fig. 5.10 Normalized streamlines and isothermal lines for AAC configuration at various angles of inclination for $Ra=3000$ and $SH=0.25$. Positive values indicate rotation in clockwise direction.

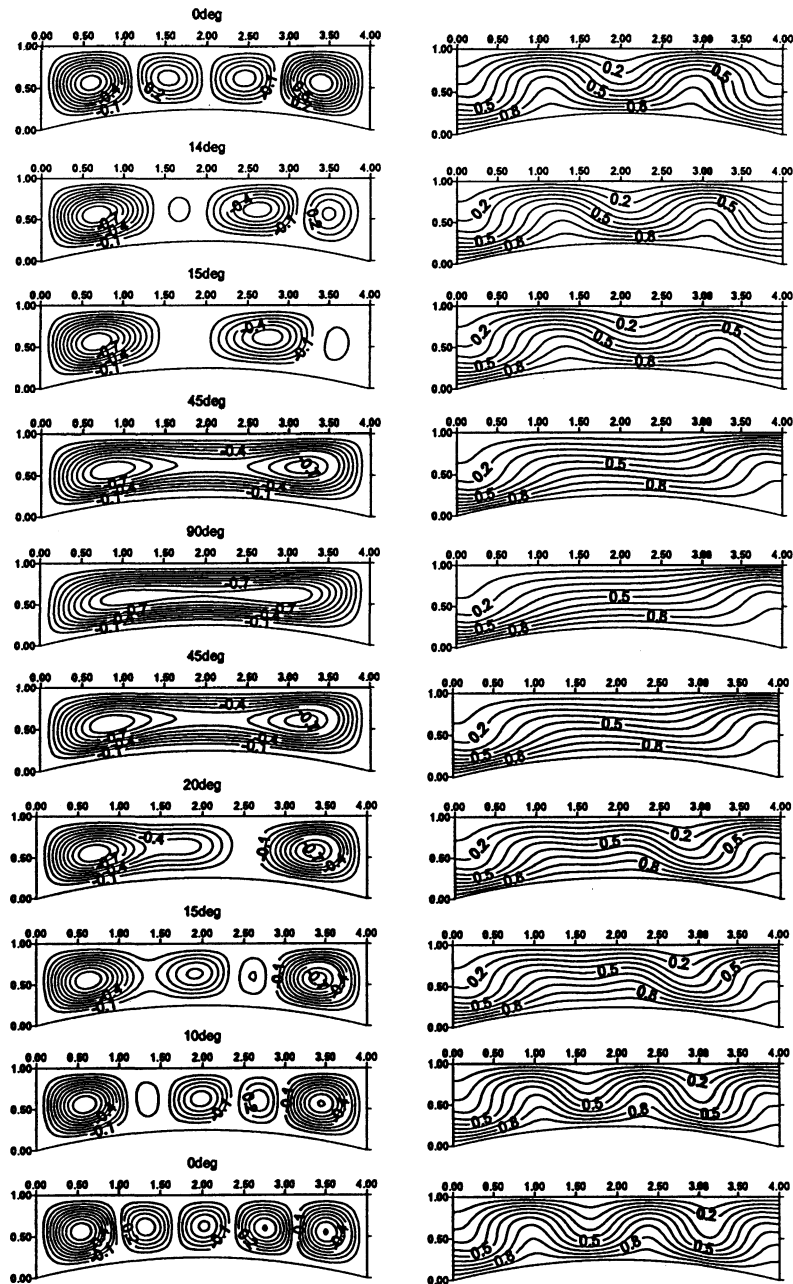


Fig. 5.11 Normalized streamlines and isothermal lines for AAC configuration at various angles of inclination for $Ra=5000$ and $SH=0.25$. Positive values indicate rotation in clockwise direction.

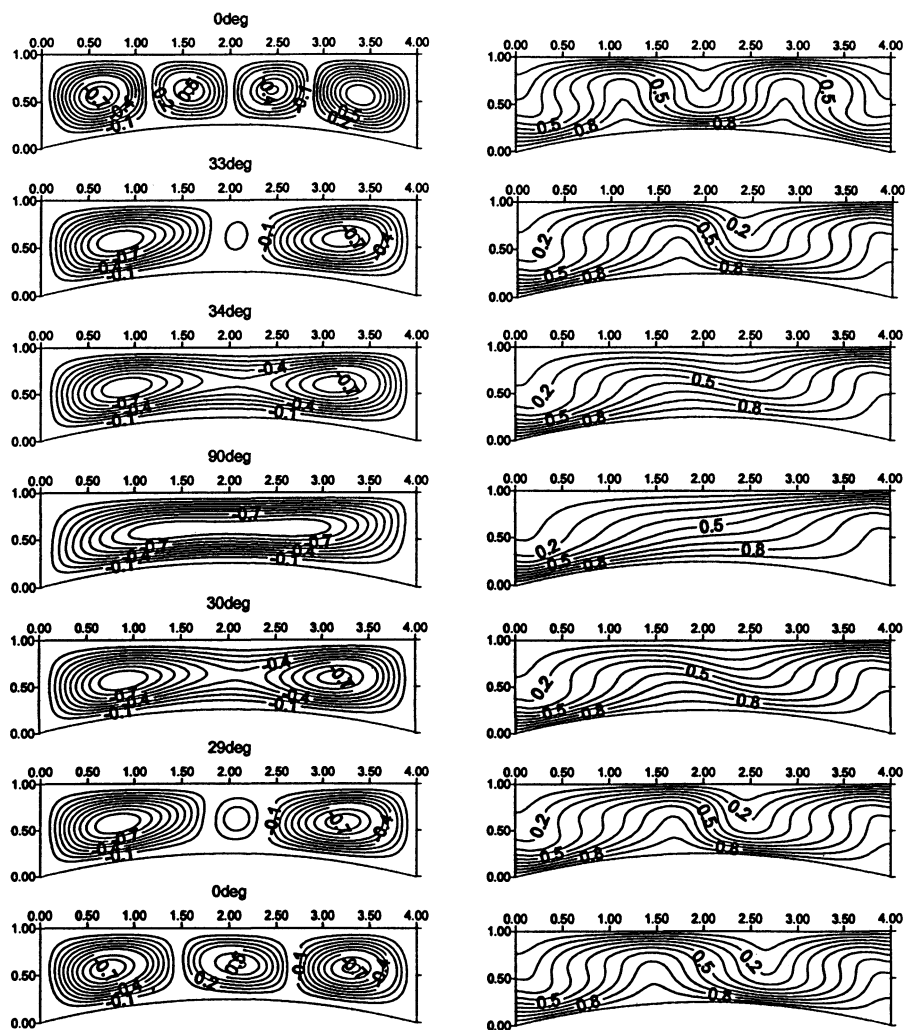


Fig. 5.12 Normalized streamlines and isothermal lines for AAC configuration at various angles of inclination for $Ra=10^4$ and $SH=0.25$. Positive values indicate rotation in clockwise direction.

5.2.2 Case of decreasing γ

For $Ra=1000$ and 3000 , no hysteresis phenomenon can be observed. For $Ra=5000$, hysteresis region occur from $\gamma = 20^\circ$ to 0° . Due to the competition of normal and tangential force, mode transition is very complicated in angle decreasing. Finally, fluid field ends up with five cells instead of four in the angle increasing at $\gamma = 0^\circ$. Heat transfer rate is a little bit increased at 1.1% on the bottom wall at $\gamma = 0^\circ$, Fig. 5.13.

For $Ra = 10^4$, mode transition (1T3) took place at $\gamma = 30^\circ$ for angle decreasing. It is greatly brought forward from $\gamma= 11^\circ$ to 30° , as compared with AA configuration, see Figs. 5.13 and 4.28. Nu number changes corresponding to mode transition is 17.8% for angle decreasing.

Similar to the case of $SH = 0.05$, all flow fields developed at $\gamma = 0^\circ$, in both cases of γ increasing and decreasing, are characterized by multi-cell flow structures for $Ra \geq 3000$.

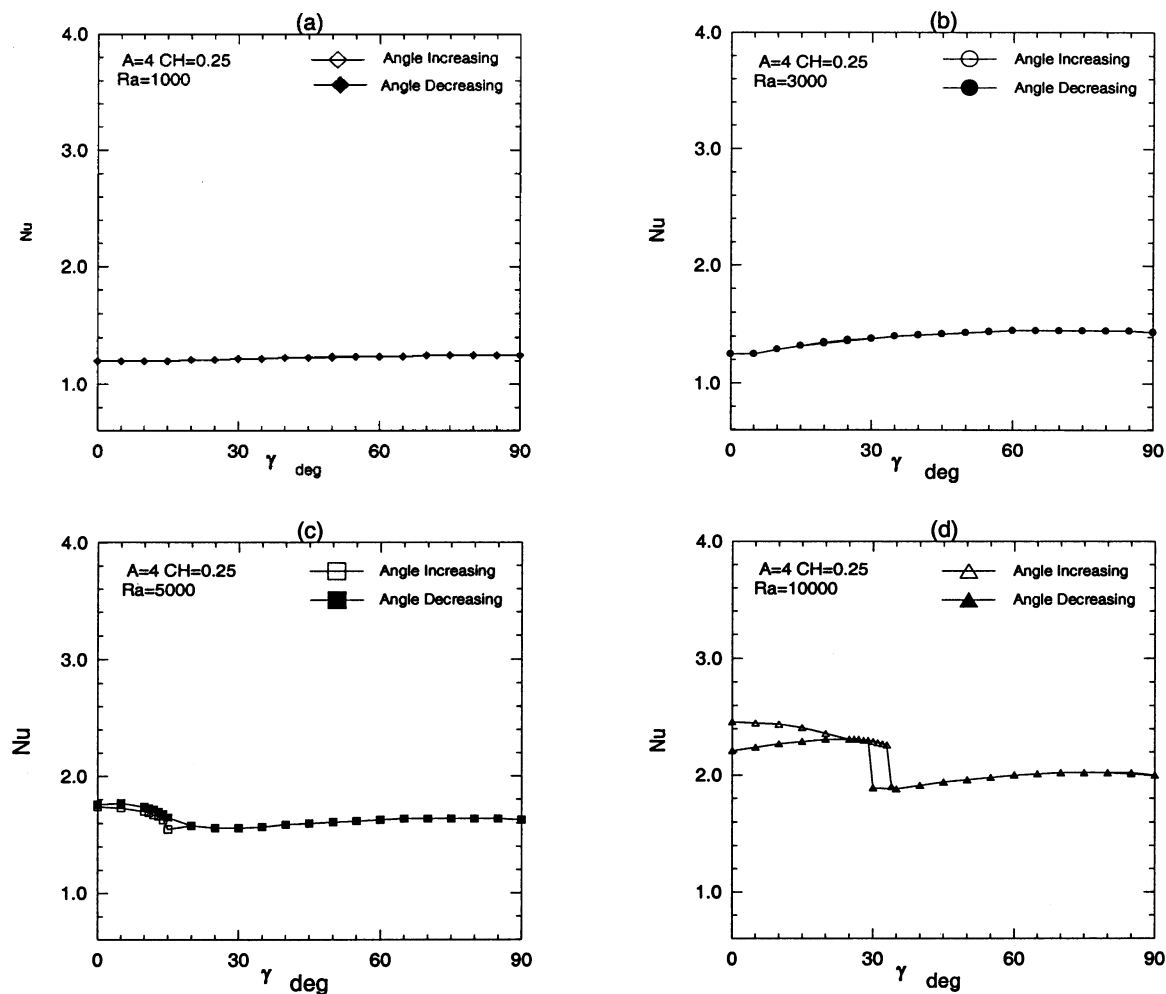


Fig. 5.13 Average Nu number of bottom wall as a function of inclination angle γ for angle increasing and decreasing at various Ra numbers for AAC configuration and SH=0.25.

5.3 AAC configuration with SH=0.45

5.3.1 Case of increasing γ

As height of the curvature is increased to 0.45, buoyancy force in tangential-direction become further stronger. That stronger forced caused more localized natural convection at the low sides of the cavity. Stronger cells rotating in the clockwise and anticlockwise directions are developed at the right and left sides, respectively. For all Ra

$< 10^4$, all flow fields developed at $\gamma = 0^\circ$, in both cases of γ increasing and decreasing, are characterized by these two strong cells at the two far sides of the cavity, Figs. 5.14-5.16. Heat transfer is dominated by conduction at the middle of the cavity. A multi-cell flow pattern is observed at $Ra = 10^4$, Fig 5.16.

As γ increases, the cell rotating in the anticlockwise direction at the left side of the cavity develops and finally occupies the whole cavity. The other cell in the right part of the cavity decelerates and eventually disappears as shown in Figs. 5.14 - 5.17.

At $\gamma = 0^\circ$ and $Ra \leq 2000$, rate of heat transfer rate of bottom wall increased by 45% and 29.5% at, respectively. For $Ra = 3000$ and 5000, rate of heat transfer of the bottom wall is 5.8% and 19.9% lower than flat bottom case, respectively. For $Ra=10^4$, Nu number of the bottom wall is 13.8% lower than flat bottom.

Due to the absence of multi-cell flow structures in the case of $SH = 0.45$, except at $Ra = 10^4$, no mode-transitions took place, and hence, no sudden drops in Nu number are observed. In the case of $Ra = 10^4$, although a multi-cell structure was developed at $\gamma = 0^\circ$, the middle cells were very weak, and as a result of that, they were very easily one by one overtaken by the strong cell on the left side of the cavity, resulting in a gradual drop in Nusselt number of both bottom and top walls, Figs. 5.1d and 5.2d.

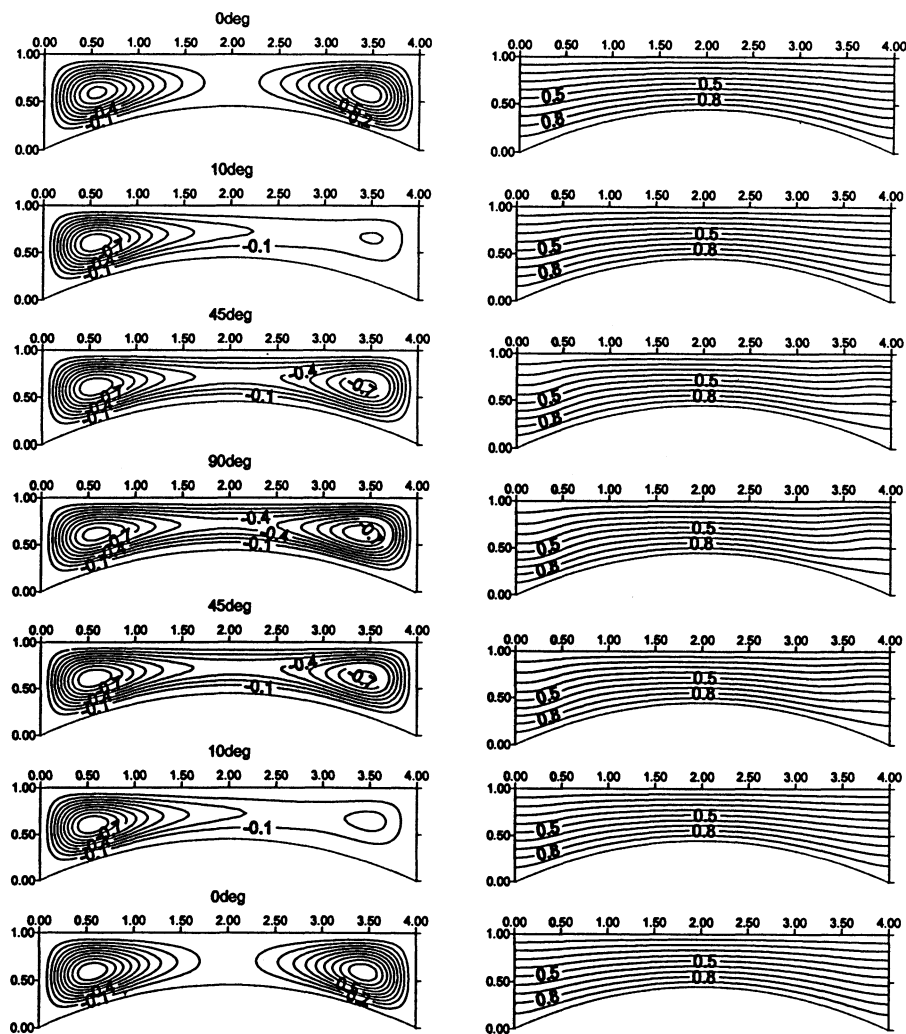


Fig. 5.14 Normalized streamlines and isothermal lines for AAC configuration at various angles of inclination for $Ra=1000$ and $SH=0.45$. Positive values indicate rotation in clockwise direction.

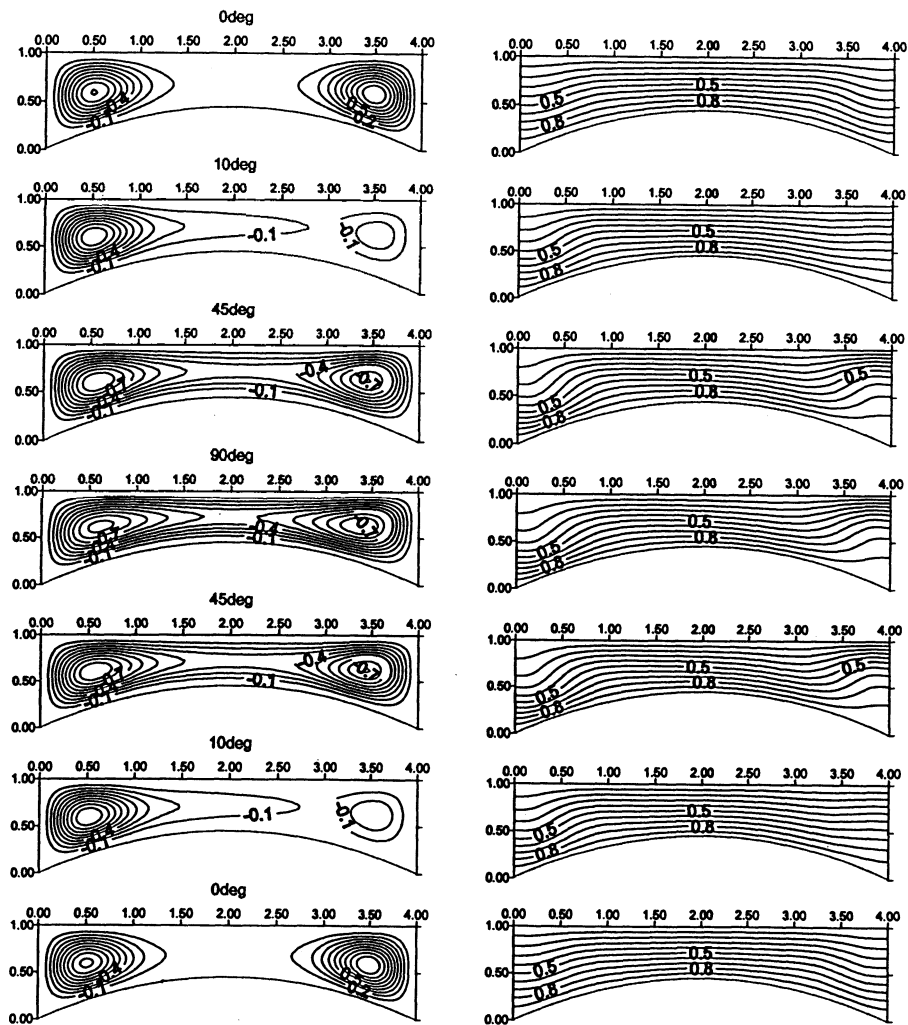


Fig. 5.15 Normalized streamlines and isothermal lines for AAC configuration at various angles of inclination for $Ra=3000$ and $SH=0.45$. Positive values indicate rotation in clockwise direction.

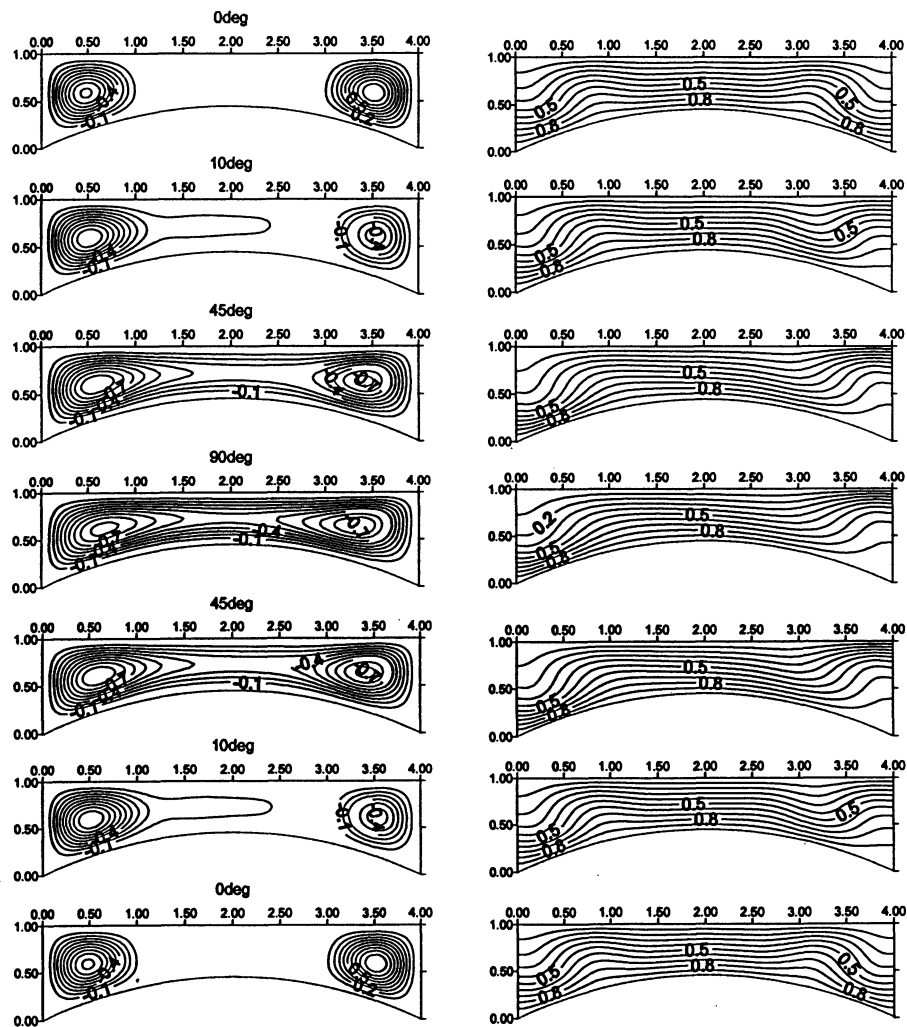


Fig. 5.16 Normalized streamlines and isothermal lines for AAC configuration at various angles of inclination for $Ra=5000$ and $SH=0.45$. Positive values indicate rotation in clockwise direction.

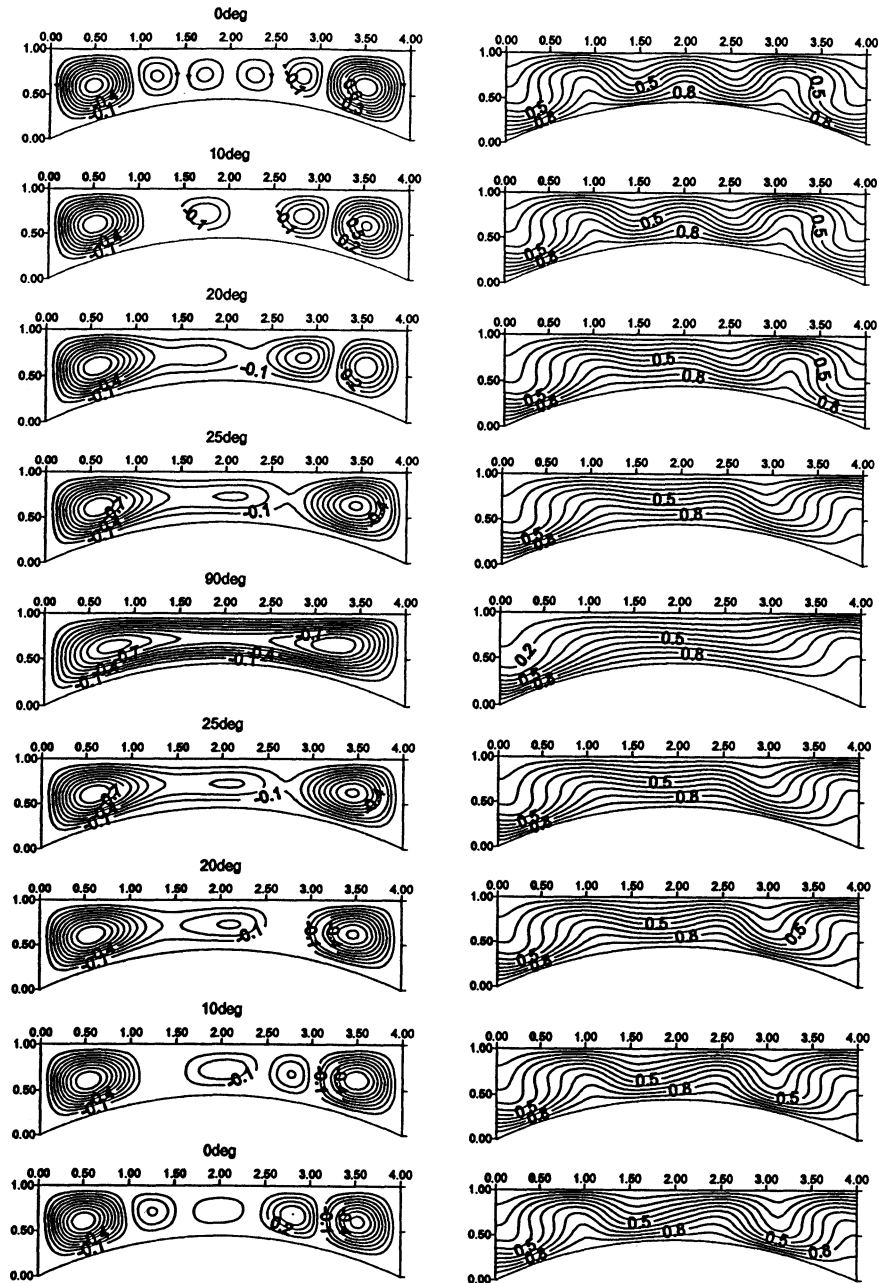


Fig. 5.17 Normalized streamlines and isothermal lines for AAC configuration at various angles of inclination for $Ra=10^4$ and $SH=0.45$. Positive values indicate rotation in clockwise direction.

5.3.2 Case of decreasing γ

No hysteresis is observed for $Ra < 10^4$. The multi-cell flow pattern that was observed in the case of $Ra = 10^4$, encountered few mode transition as γ increased and decreased, Fig. 5.17. A slight variation between the solutions obtained for the two cases of angle increasing and decreasing is observed at $\gamma < 25^\circ$, as shown in Fig. 5.18d.

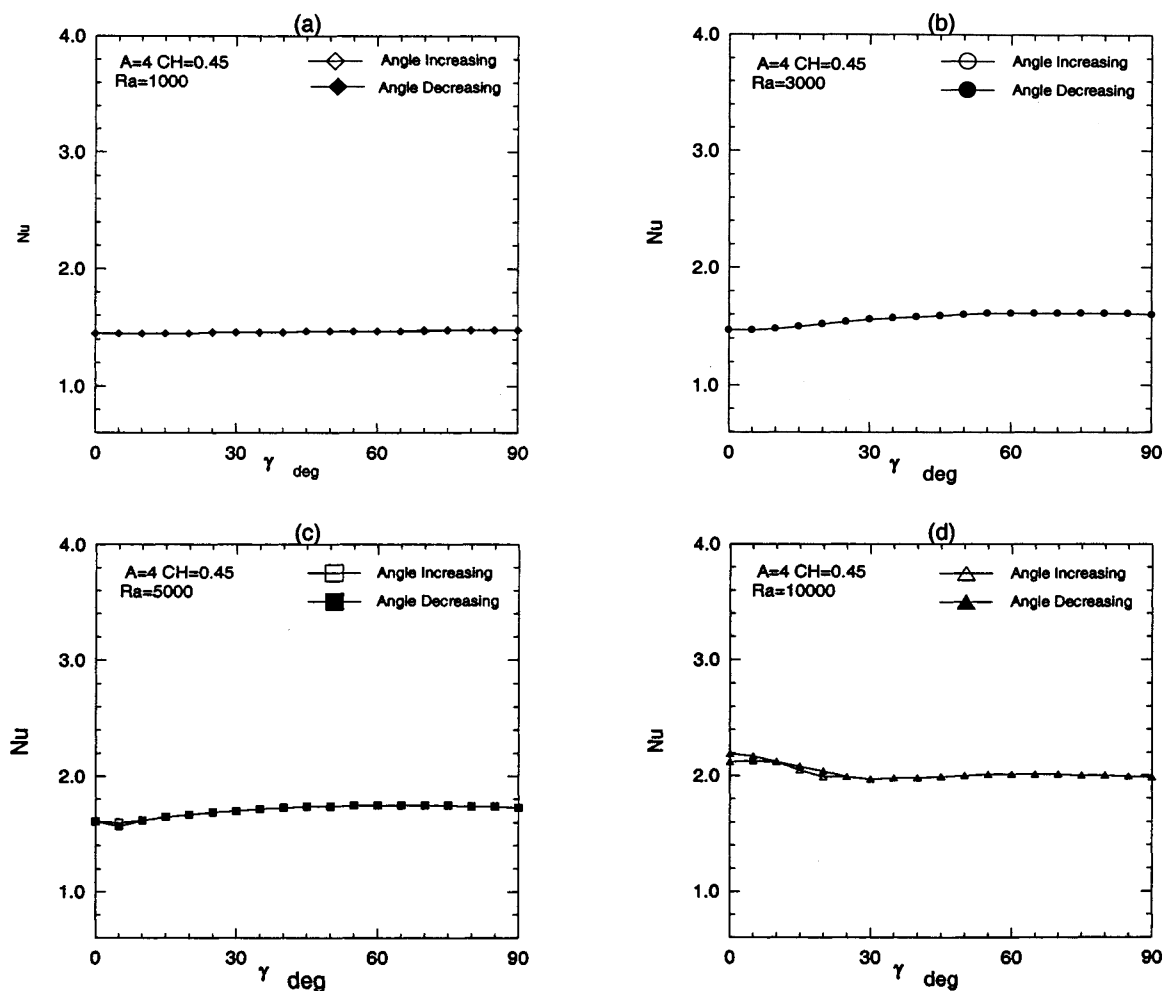


Fig. 5.18 Average Nu number of bottom wall as a function of inclination angle γ for angle increasing and decreasing at various Ra numbers for AAC configuration and SH=0.45.

5.4 AAC configuration with SH=0.65

5.4.1 Case of increasing γ

As SH is increased to 0.65, F_t is higher than F_n . At $Ra \leq 3000$, convection produced by F_t dominates a bigger portion of the cavity. At $Ra \leq 3000$ and $\gamma = 0^\circ$, with the increased height of curvature, convection enhanced rate of heat transfer of bottom wall by about 30% as compared with the case of SH = 0.45, Figs. 5.1d and 5.1e, and by 89%, 70, 22% at $Ra = 1000, 2000, \text{ and } 3000$, respectively, as compared with AA configuration.

As for $Ra=10^4$, at $\gamma = 0^\circ$, F_n still produces a weak cell, Fig. 5.22. The rate of heat transfer of the bottom wall decreased by 12%, as compared with AA case, Figs. 5.1a and 5.1e.

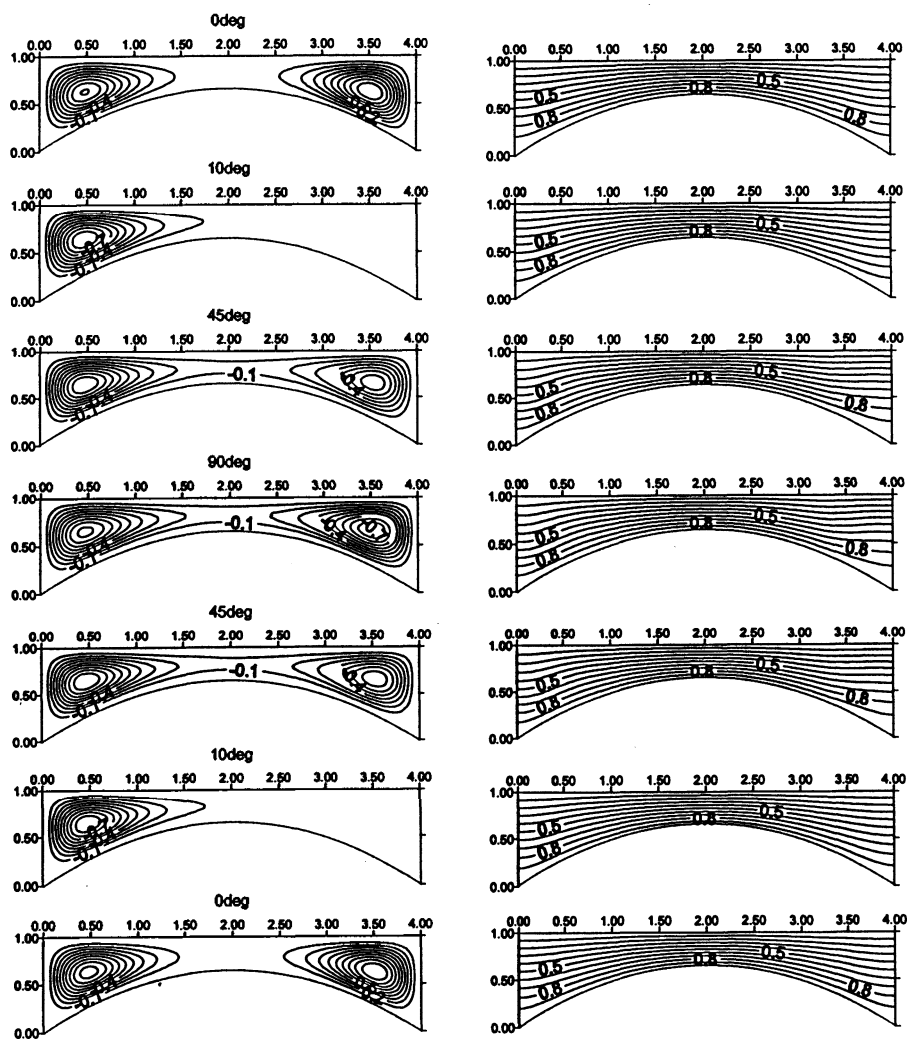


Fig. 5.19 Normalized streamlines and isothermal lines for AAC configuration at various angles of inclination for $Ra=1000$ and $SH=0.65$. Positive values indicate rotation in clockwise direction.

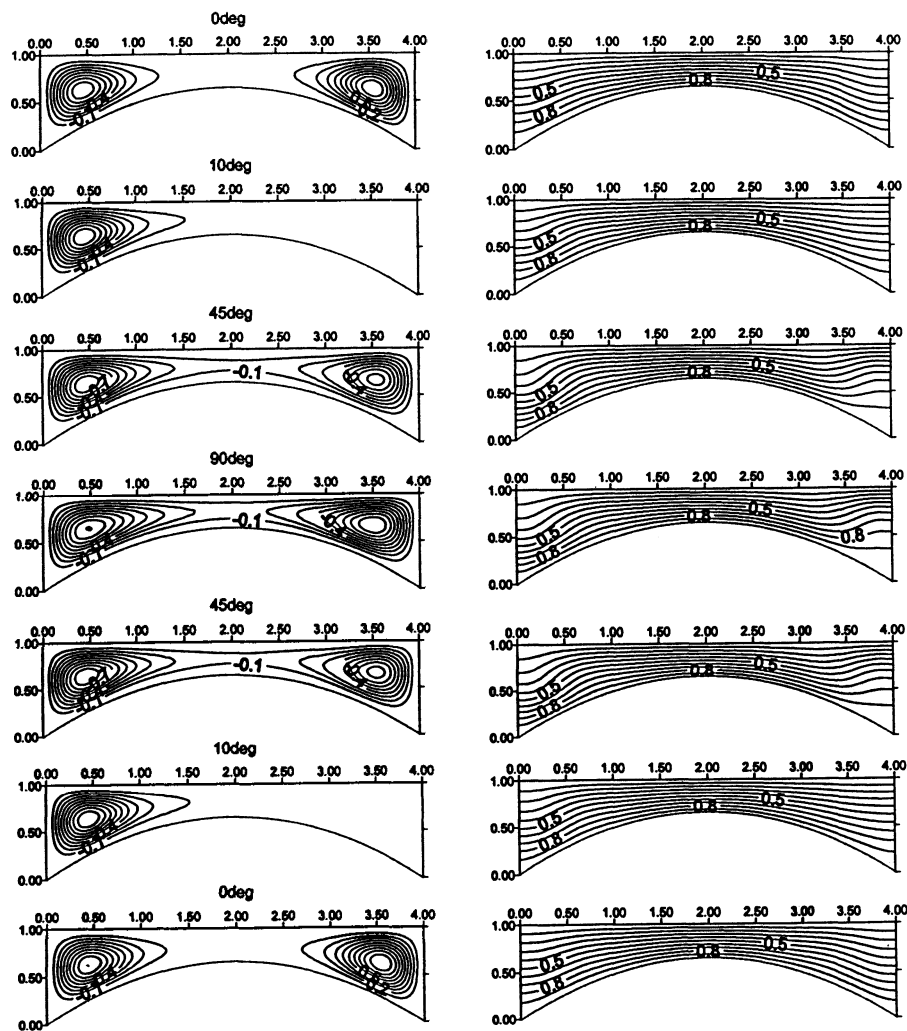


Fig. 5.20 Normalized streamlines and isothermal lines for AAC configuration at various angles of inclination for $Ra=3000$ and $SH=0.65$. Positive values indicate rotation in clockwise direction.

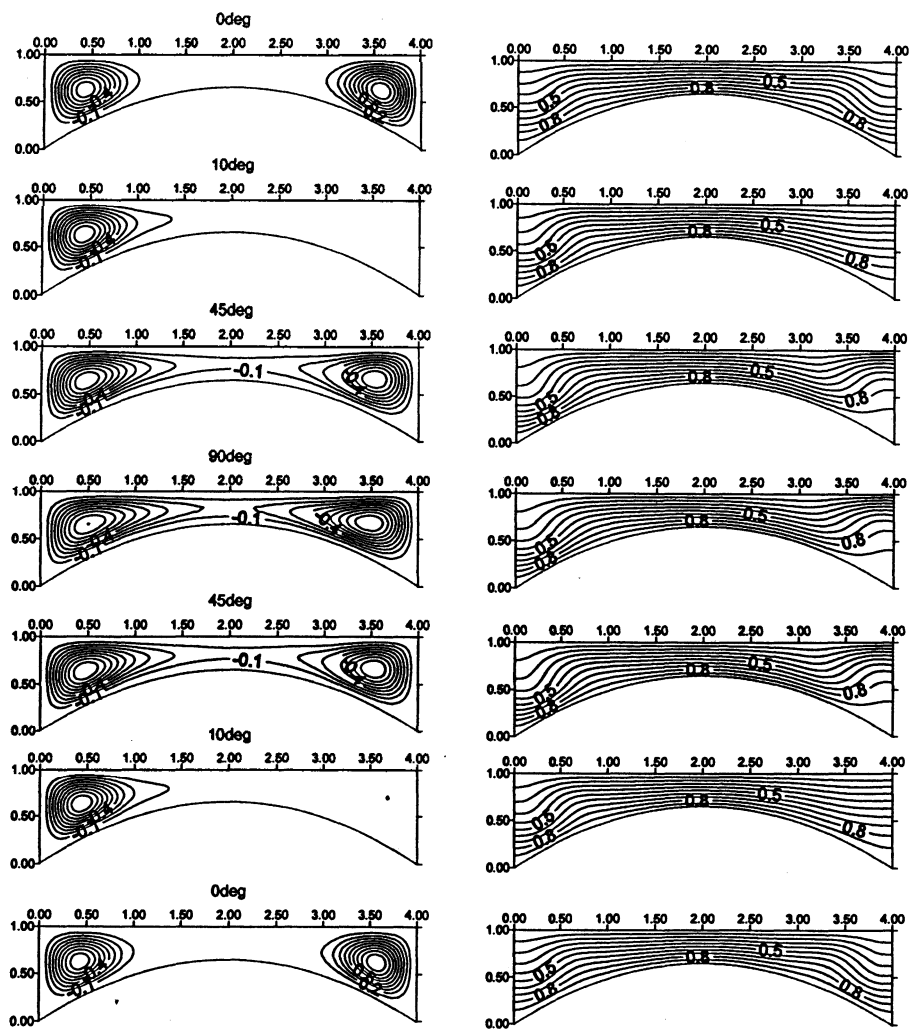


Fig. 5.21 Normalized streamlines and isothermal lines for AAC configuration at various angles of inclination for $Ra=5000$ and $SH=0.65$. Positive values indicate rotation in clockwise direction.

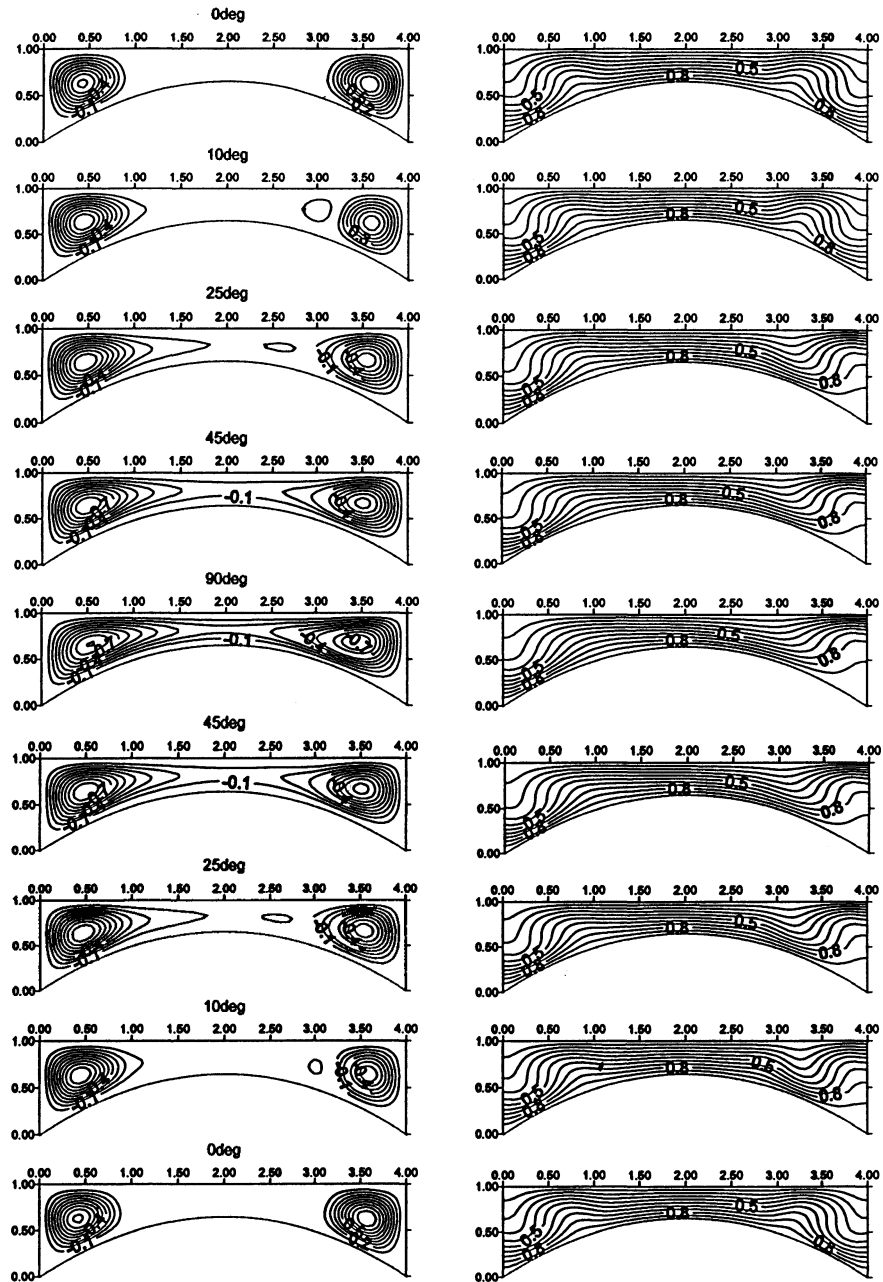


Fig. 5.22 Normalized streamlines and isothermal lines for AAC configuration at various angles of inclination for $Ra=10^4$ and $SH=0.65$. Positive values indicate rotation in clockwise direction.

5.4.2 Case of decreasing γ

Because F_t dominates the motion, no hysteresis phenomena can be observed at $Ra \leq 5000$, (Figs. 5.23a, b, and c), and rate of heat transfer at bottom wall for angle decreasing is exactly the same as for angle increasing. Without any drastic changes in Nu number generated by mode transition, rate heat transfer rate remains in a very close value during angle inclination Figs. 5.1 and 5.2. At $Ra = 10^4$, still a small difference in Nu number of the bottom wall is observed between γ increasing and decreasing at $\gamma < 20^\circ$, Fig. 5.23d.

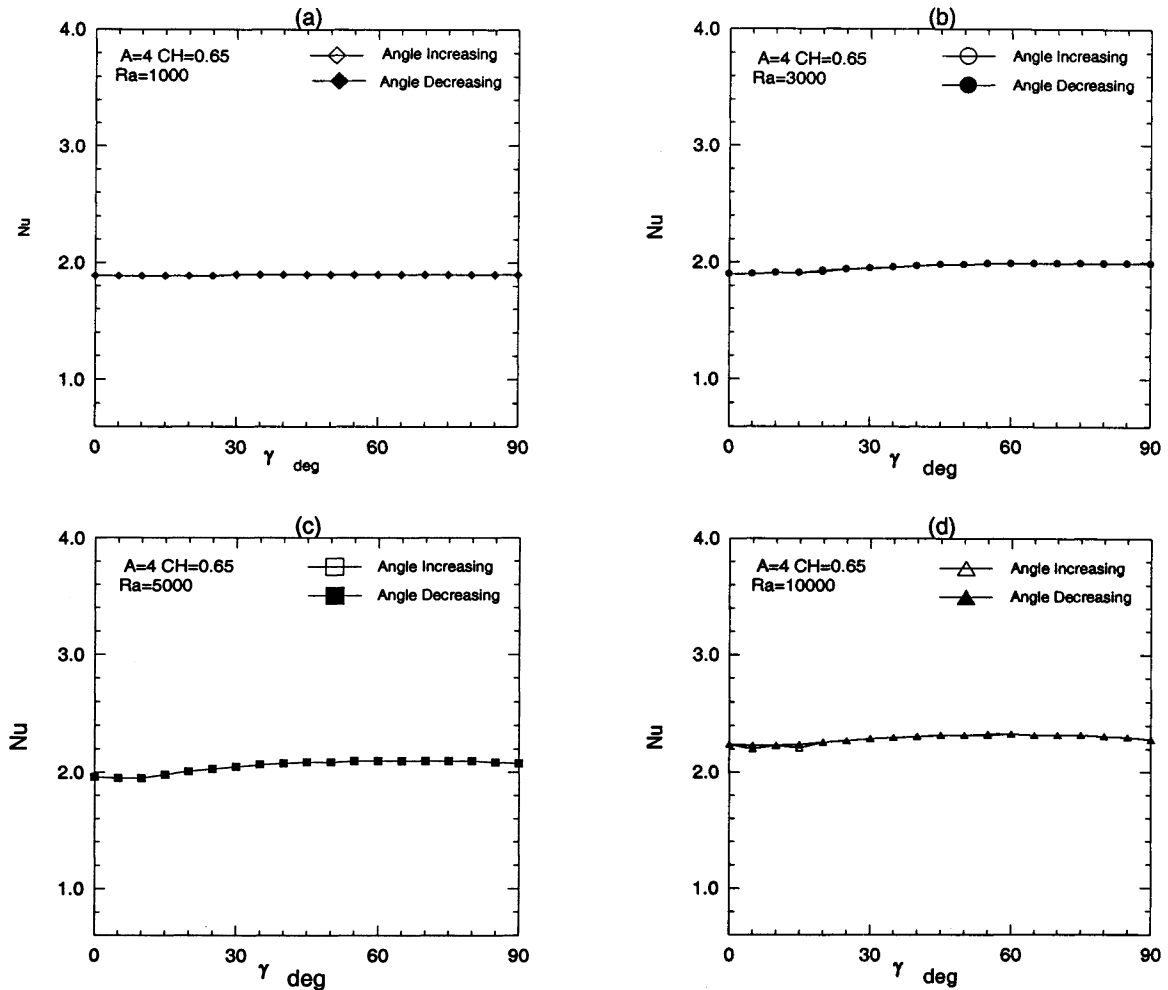


Fig. 5.23 Average Nu number (bottom wall) as a function of inclination angle γ for angle increasing and decreasing at various Ra numbers for AAC configuration and SH=0.65.

5.5 AAC configuration with SH=0.85

5.5.1 Case increasing γ

As curve height is equal to 0.85, F_t now is dominating the flow field for all Ra numbers. For all Ra numbers, all flow fields developed at $\gamma = 0^\circ$, in both cases of γ increasing and decreasing, are characterized by two strong cells at the two far sides of the

cavity, covering a much bigger portion of the cavity, Figs. 5.24-5.27. Heat transfer is dominated by conduction in a narrower region at the middle of the cavity.

Rate of heat transfer of bottom wall at $\gamma = 0^\circ$ increased significantly, as compared with AA case, by 206%, 173%, 96.2%, 53.7%, 29.1% for $Ra = 1000, 2000, 3000, 5000,$ and 10^4 , respectively, as shown in Figs. 5.1a and 5.1f.

Since only two cells appear at $\gamma = 0^\circ$ for all Ra numbers, no mode transitions (3T1) took place, Figs. 5.24 - 5.27. No drastic changes in Nu number can be observed, Fig. 5.1f. Rate of heat transfer for all Ra numbers remained almost at the same value during the two courses of change of inclination angle. These heat transfer characteristics are very important for engineering application. For example, according to these results, a curved bottom solar collector with $SH > 0.65$ can be used to enhance rate of heat transfer, and avoid having sudden changes in rate of heat transfer as its angle on inclination changes.

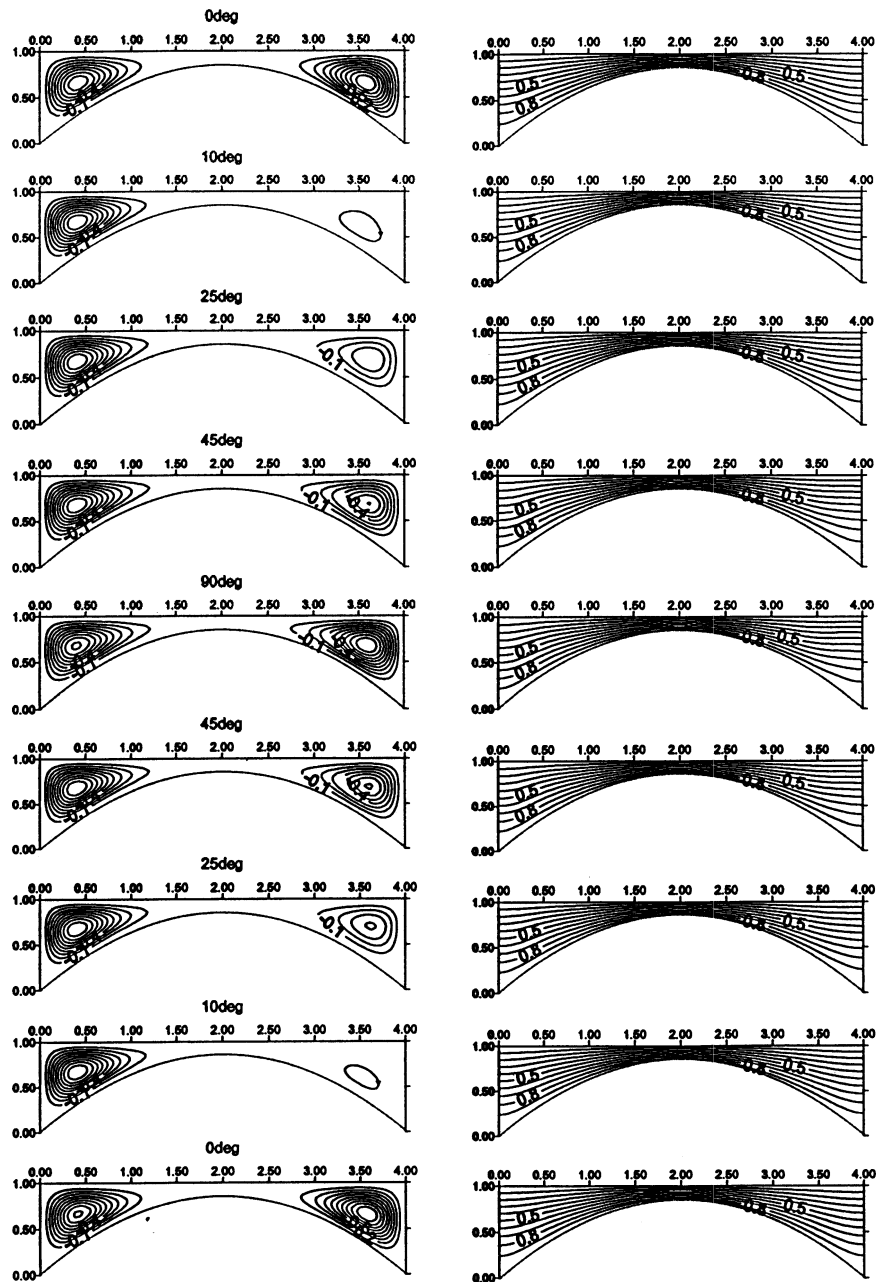


Fig. 5.24 Normalized streamlines and isothermal lines for AAC configuration at various angles of inclination for $Ra=1000$ and $SH=0.85$. Positive values indicate rotation in clockwise direction.

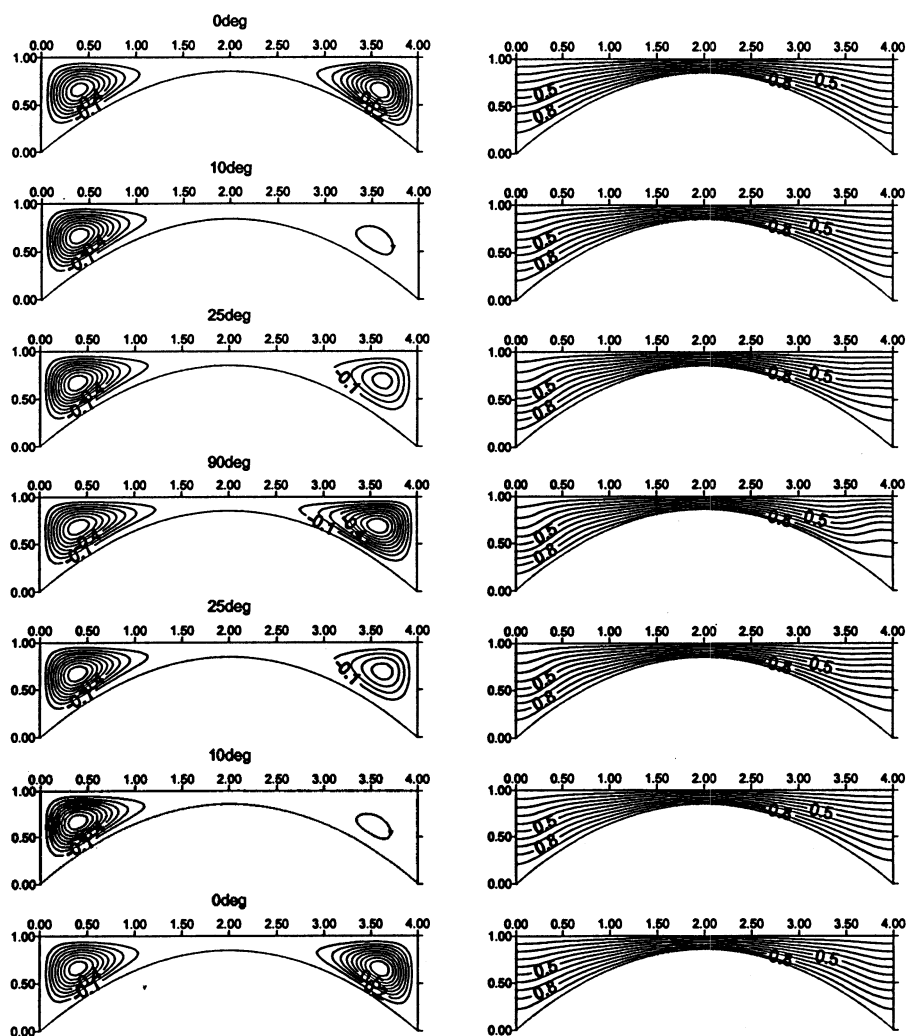


Fig. 5.25 Normalized streamlines and isothermal lines for AAC configuration at various angles of inclination for $Ra=3000$ and $SH=0.85$. Positive values indicate rotation in clockwise direction.

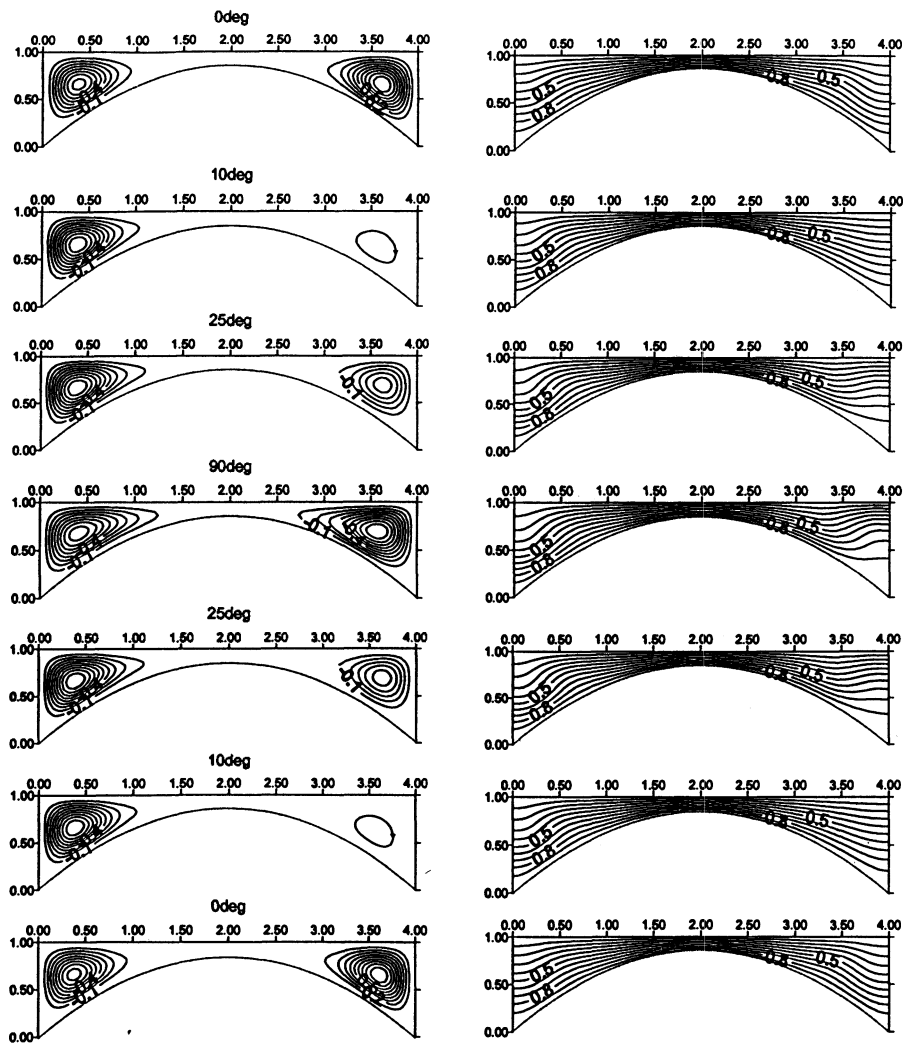


Fig. 5.26 Normalized streamlines and isothermal lines for AAC configuration at various angles of inclination for $Ra=5000$ and $SH=0.85$. Positive values indicate rotation in clockwise direction.

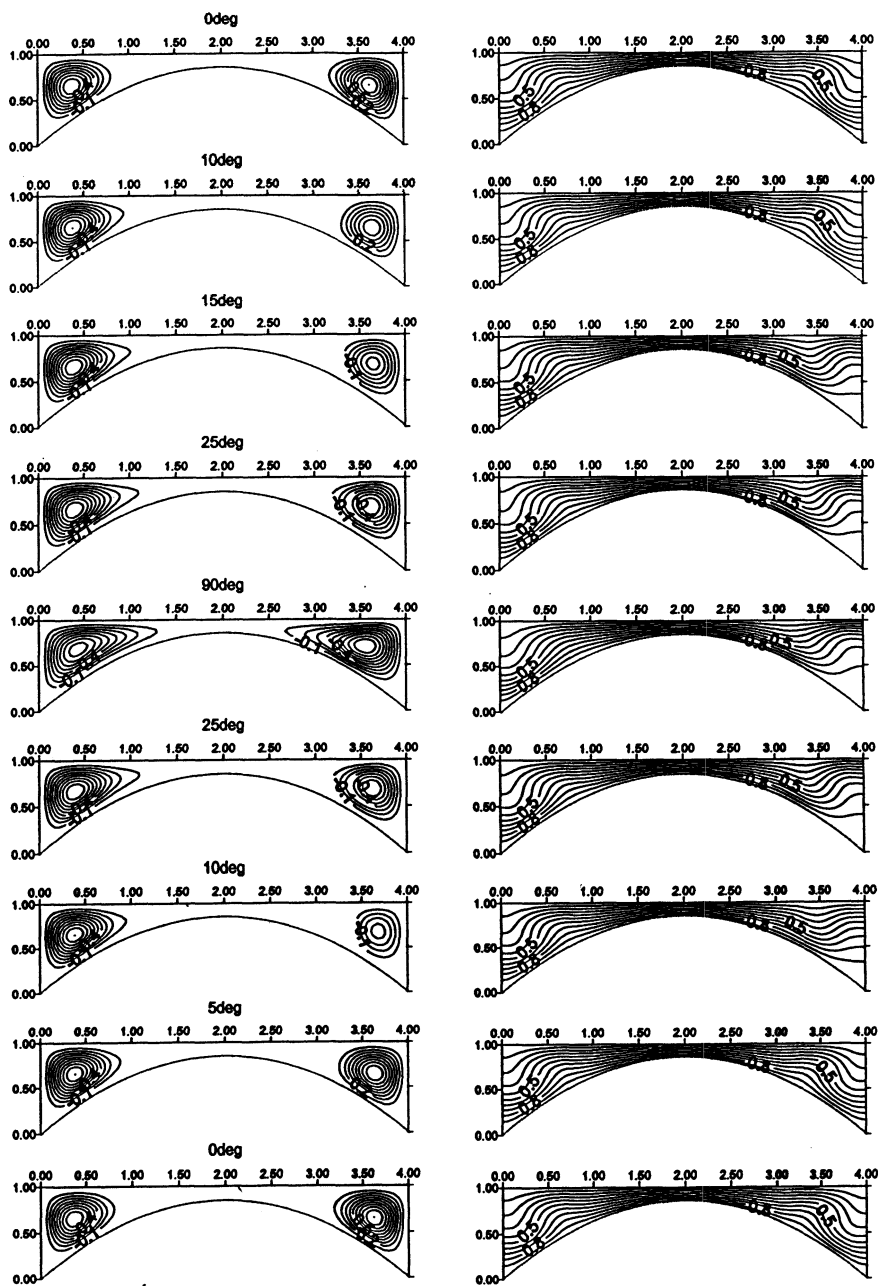


Fig. 5.27 Normalized streamlines and isothermal lines for AAC configuration at various angles of inclination for $Ra=10^4$ and $SH=0.85$. Positive values indicate rotation in clockwise direction.

5.5.2 Case of decreasing γ

No hysteresis phenomenon can be observed for all Ra numbers, except for $Ra = 10^4$, where a very slight difference in Nu number of the bottom wall is observed at hysteresis region between $\gamma = 5^\circ$ and 15° , Fig. 5.28.

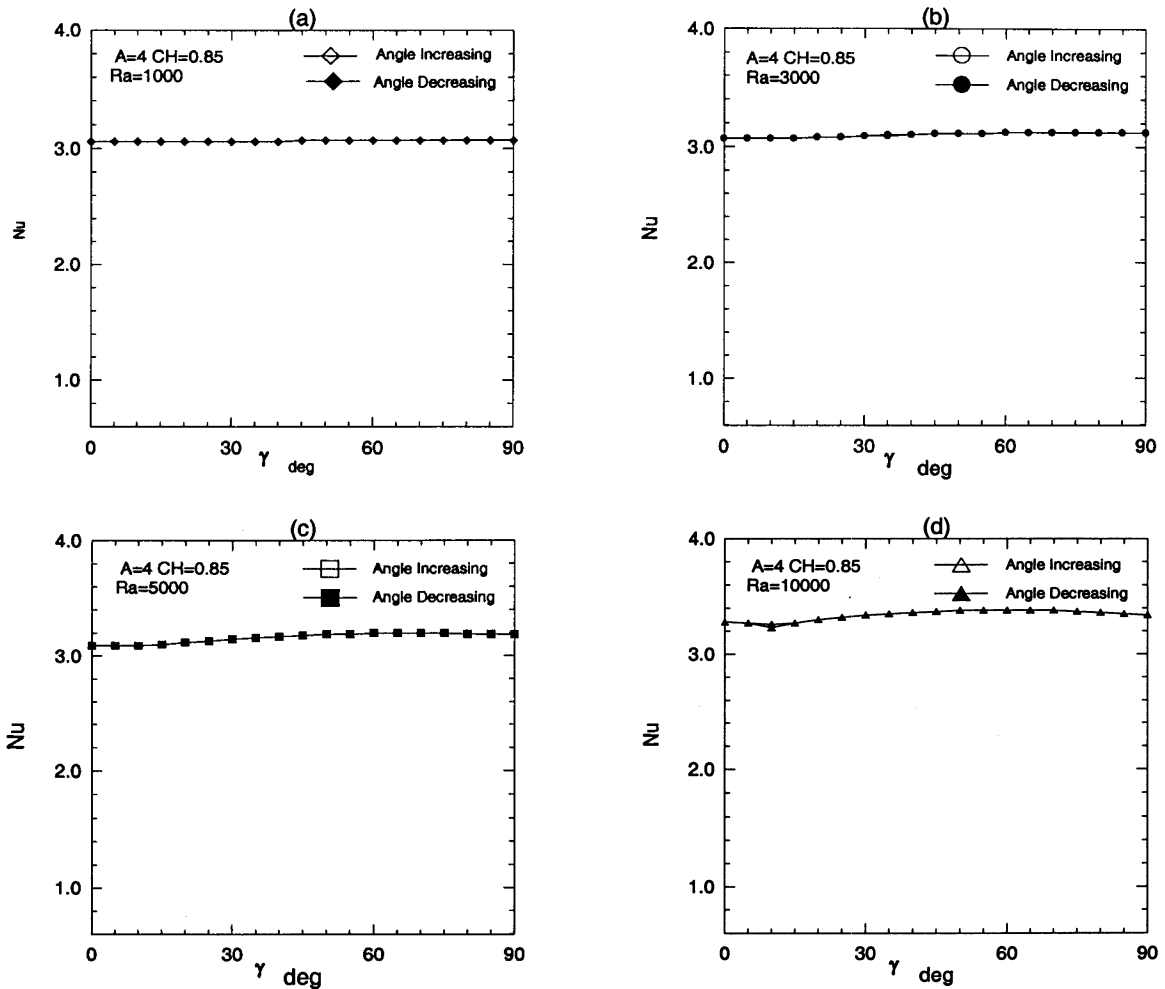


Fig. 5.28 Average Nu number (bottom wall) as a function of inclination angle γ for angle increasing and decreasing at various Ra numbers for AAC configuration and $SH=0.85$.

Chapter 6

Summary and Conclusions and Future Work

6.1 Summary and Conclusions

Flow mode-transition of steady, two-dimensional, natural convection in air-filled, inclined cavities, heated from below and cooled from top, has been numerically investigated using the finite-volume based SIMPLE numerical algorithm. Both regular, i.e., with flat walls, and curved bottom cavities have been considered in the present study.

In the case of regular cavities, seven different configurations of thermal conditions of cavity end walls have been considered. Temperature discontinuities at cavity corners have not been found to affect the predicted flow and internal thermal fields. However, results showed that these discontinuities have a significant effect on the predicted heat transfer rates of cavity walls, and hence a special numerical treatment of these discontinuities had to be implemented. Thermal conditions of cavity end walls have been found to have a significant effect on flow-mode transition of thermal convection flows inside inclined regular cavities. Results showed that it is quite possible to alter rates of heat transfer of various cavity walls by adjusting these thermal conditions and changing the cavity angle of inclination, which offers an important tool. Using such tool, one could control rates of heat transfer in many industrial applications where thermal convection flows play an important role.

Mode-transition and heat transfer effectiveness in inclined cavities with curved bottoms have also been investigated. At Ra numbers lower than critical values,

convection flows were observed, which resulted in a significant increase in the rate of heat transfer. Depending on the height of curvature and the value of Ra number, heat transfer rates can be increased or decreased, which indicates that the use of curved bottoms offers another tool to control the effectiveness of heat transfer inside inclined enclosures.

Hysteresis phenomenon encountered in inclined cavities heated from below and cooled from above has been investigated considering both regular and curved bottom cavities. Due to variations in initial conditions, more than one solution can be obtained. In the case of regular cavities, results indicated that changing thermal conditions of cavity end walls has a significant effect on mode-transitions and hence on hysteresis phenomenon developed in that case. In the case of curved bottom cavities with insulated end walls, depending on height of curvature, mode-transitions and hysteresis phenomenon can be eliminated. This conclusion is very useful for some engineering applications; where it might be desirable to avoid the occurrence of any sudden changes in rates of heat transfer inside the cavity.

6.2 Future work

As mentioned above, only steady two-dimensional situations have been considered in the present study. The following situations are of great relevance to the subject matter considered in the present study; and regarded as natural extension of the present work; and hence recommended as future work.

1. Consideration of three dimensional flows.

2. Time dependency or unsteady flows.
3. Considering variations of thermal boundary conditions in case of curved bottom cavities.
4. Cavities having more complicated geometries.

References

1. S. Ostrach, Internal viscous flows with body forces, Boundary layer research (H. Gortler, ed.) pp. 185-202, Springer Verlag, Berlin, 1958.
2. S. Ostrach, High speed aerodynamics and jet propulsion (F. K. Moore, ed.), Vol. 4, Chapter F, Princeton University Press, Princeton, 1964.
3. B. Gebhart, Heat transfer, McGraw-Hill, New York, 1971.
4. B. Gebhart, Natural Convection flows and stability, Advances in Heat Transfer (J. P. Hartnett and T. F. Irvin, Jr., eds.), Vol. 9, 1973.
5. W. Elenbaas, Heat dissipation of parallel plates by free convection, Physica, pp. 1 - 28, 1942.
6. G. De Vahl Davis, Laminar natural convection in an enclosed rectangular cavity, J. Heat and Mass Transfer, Vol. 11, pp. 1675 - 1693, 1968.
7. S. H. Yin, T. Y. Wung and K. Chen, Natural convection in an air layer enclosed within rectangular cavities, Int. J. Heat Mass Transfer, Vol. 21, pp. 307 - 315, 1978.
8. Orhan Aydin, Ahmet Ünal, Teoman Ayhan, Natural convection in rectangular enclosures heated from one side and cooled from the ceiling, International Journal of Heat and Mass Transfer, Vol. 42, pp. 2345 - 2355, 1999.
9. G. S. Shiralkar and C. L. Tien, A numerical study of the effect of a vertical temperature difference imposed on a horizontal enclosure, Numerical Heat Transfer, Vol. 5, pp. 185 - 197, 1982.

10. Hiroyuki Ozoë and Hiroshi Ukeba, Numerical analysis of natural convection of low Prandtl number fluids heated from below, Numerical Heat Transfer, Part A, pp. 26:363 - 374, 1994.
11. Marcelo M. Ganzarolli and Luiz F. Milanez, Natural convection in rectangular enclosures heated from below and symmetrically cooled from the sides, Int. J. Heat Mass Transfer, Vol. 38, No. 6, pp 1063 - 1073, 1995.
12. Massimo Corcione, Effects of the thermal boundary conditions at the sidewalls upon natural convection in rectangular enclosures heated from below and cooled from above, International Journal of Thermal Sciences, Vol. 42, pp.199 - 208, 2003.
13. G. K. Batchelor, Heat transfer by free convection across a closed cavity between vertical boundaries at different temperatures, Quarterly of Applied Mathematics, Oct. pp 209 – 233, 1954.
14. K. G. T. Hollands and L. Konicek, Experimental study of the stability of differentially heated inclined air layers, Int. J. Heat Mass Transfer, Vol. 16. pp 1467 - 1476, 1973.
15. T. E. Unny, Thermal instability in differentially heated inclined fluid layers, J. Appl. Mech., Vol. 39(1), pp. 41 - 46, 1972.
16. J. Hart, Stability of the flow in a differentially heated inclined box, J. Fluid Mech. Vol. 35(4), pp.775 - 798, 1969.
17. F. J. Hamady, J. R. Lloyd, H. Q. Yang and K. T. Yang, Study of local natural convection heat transfer in an inclined enclosure, Int. J. Heat Mass Transfer, Vol. 32, No. 9, pp. 1697 - 1708, 1989.

18. R. Ben Yedder and E. Bilgen, Laminar natural convection in inclined enclosures bounded by a solid wall, *Heat and Mass Transfer* Vol. 32, pp. 455 – 462, 1997.
19. J. N. Arnold, I. Catton and D. K. Edwards, Experimental investigation of natural convection in inclined rectangular regions of differing aspect ratios, *Journal of Heat Transfer*, Feb., pp. 67 – 71, 1976.
20. Symy M. Elsherbiny, Free convection in inclined air layer heated from above, *Int. J. Heat Mass Transfer*, Vol. 39, No. 18, pp. 3925 - 3930, 1996.
21. C. Y. Soong and P. Y. Tzeng, Numerical study on mode-transition of natural convection in differentially heated inclined enclosures, *Int. J. Heat Mass Transfer*, Vol. 39, No. 14, pp 2869 - 2882, 1996.
22. W. M. Lewandowski and M. J. Khubeiz, Experimental study of laminar natural convection in cells with various convex and concave bottoms, *transactions of the ASME*, Vol. 114, pp. 94- 98, February, 1992.
23. Yos S. Morsi and Subrat Das, Numerical investigation of natural convection inside complex enclosures, *Heat Transfer Engineering*, Vol. 24 (2), pp. 30 - 41, 2003.
24. Chin-Lung Chen, Chin-Hsiang Cheng, Buoyancy-induced flow and convective heat transfer in an inclined arc-shape enclosure, *International Journal of Heat and Fluid Flow*, Vol. 23, pp. 823-830, 2002.
25. S. V. Patankar, *Numerical heat transfer and fluid flow*, McGraw-Hill, New York, 1980.
26. M. Nansteel, S. Sadhal and P. Ayyaswamy, Discontinuous boundary temperatures in heat transfer theory, *Session on Significant Questions in Buoyancy Affected Enclosure or Cavity Flows*, ASME Winter Annual Meeting, December (1986).

27. G. de Vahl Davis and I. P. Jones, Natural convection in a square cavity: a comparison exercise, *Int. J. Numer. Meth. Fluids* Vol. 3, pp. 227 - 248, 1983.